Rocket Propelled Wind Tunnel

Fall Midterm Report

MAAE 4907P Engineering Design Project

Prepared For:

Dr. David MacPhee, Dr. Oren Petel, Dr. Jason Etele

Faculty of Engineering and Design
Carleton University

Date Submitted: November 1, 2024

Contents

List of Figures

List of Tables

1 Introduction

The 2024-2025 Rocket-Propelled Wind Tunnel (RPWT) is one of several ongoing capstone projects within the Carleton University Department of Mechanical and Aerospace Engineering. The RPWT team is a group of 21 fourth-year students who apply their engineering education to the design of a rocket engine powered launch vehicle. The co-leads of the project for this year are Jake Birkness and Philippe Charapov.

The mission of the RPWT team is to design a supersonic launch vehicle that incorporates an air-breathing test section [1]. This test section will incorporate an aerodynamic specimen and acts as a supersonic wind tunnel. The test section will experience Mach 3.0 flow for approximately 30 seconds, which is far longer than the test times of current supersonic wind tunnel designs. The launch vehicle will fly at an altitude of 70,000 ft is a common altitude for supersonic flight. To ascend to this altitude, the launch vehicle will be mounted to a launch rail that is tethered to stratospheric balloons.

To divide the design work on the RPWT, four sub-teams were created - Ascent System Design, Airframe Design, Propulsion & Control Systems Design, and Test Section Design. Each sub-team has a lead who organizes weekly check-in meetings and reports key information to Jake and Phil.

Two key design changes were considered this term - use of a plane-body design and integration of Schlieren imaging. The use of a plane-body was considered to allow for increased lift and stability of the launch vehicle, particularly during cruise. Further information on the plane-body airframe and control surfaces can be found in Sections 3.4, 3.5, and 4.7. The adoption of the plane-body has not yet been confirmed, but this decision will be made by the end of January 2025. A Schlieren imaging system was proposed as a novel application of Schlieren flow visualization within the launch vehicle. The design work on the Schlieren system will be explained in Sections 5.3 and 5.6. The adoption of a Schlieren imaging system has been confirmed and will drive the design choices for the rest of the launch vehicle, particular the size and location of the test section.

The following report outlines the individual contributions of members from each of the four sub-teams. Each sub-team section will provide background on the key developments from the term.

2 Ascent System Design

2.1 Ascent Subteam Introduction

The main goal of the ascent subteam is to develop mechanisms to ensure the rocket is safely delivered to its desired initial conditions prior to launch using a stratospheric balloon. The trajectory of the balloon will be critical to determine the rocket's position, launch path, and other parameters. A thorough understanding of the behavior of the balloon as it ascends in varying atmospheric conditions will allow for a more thorough planning of the rockets' trajectory. To avoid drifting away from the desired rocket flight zone, a system needs to be developed to control the position of the balloon and payload as it ascends. A potential solution alters the ascent rate of the balloon to utilize wind currents at different altitudes.

Improved dynamic modelling of the launch platform was implemented to account for the torque and sliding motion of the system when thrust and friction is produced from the rocket against the launch rail. This allows for a greater understanding of the dynamic motions of the launch system and the rocket.

It is important to control the launch attitude of the rocket about its pitch and yaw axes such that the flight-path and trajectory of the rocket are restricted to a desired path. Considerable progress was made this semester altering the previously designed launch platform and developing mechanisms to actively control the orientation of the rocket about its pitch and yaw axes.

2.2 Balloon Trajectory - Noah St-Amant

Peer Reviewed by: Doryan Saavedra-Zakikhani

The planning of the balloon trajectory includes many key variables that are analyzed. These parameters are the balloon's ascent rate, atmospheric density, the change in pressure during ascent, the temperature variations, drag forces, wind patterns, and various other environmental factors. These variables will largely influence the trajectory of the balloon. Hence, it is required to accurately predict and control these parameters to ensure that the rocket, or blended body, is deployed at the correct initial altitude and position.

2.2.1 Initial Balloon Sizing

Although the changing environmental factors are important in determining ascent properties of the balloon, the balloon sizing is also important. The selection of the balloon material, gas composition, shape, and size will also largely influence the desired goals of the balloon.

2.2.2 Balloon Material Selection

The selection of the material is important because different materials will provide different characteristics. The balloon's mission is to bring the rocket, or blended body, to an altitude of 70,000 ft, an elevated altitude that will have challenging environmental conditions. The other difficult challenge with the mission is the large payload mass. Hence, the selected material will need to possess high strength and durability, as well as be light in order to not further increase the total mass.

The material selected for the balloon is polyethylene. It is a widely known material selected for balloons with similar profiles of high-altitude and heavy-lift balloons [2]. NASA has used different polyethylene films for missions that have a payload of up to 5,000 kg, as well as an altitude of up to 30 km [2]. Polyethylene films are capable of having a mass of kilograms per thousand cubic meters [3]. The Institute of Space and Astronautical Science, and its balloon group had seen success in a polyethylene film with a mass of 6.8 kg for a balloon with a volume of 5000 m^3 [3].

2.2.3 Balloon Gas Selection

The gas selected for the ascent of the balloon is helium gas. It is widely used in many balloon applications [4]. Helium is the second-lightest gas, behind hydrogen. Although hydrogen has better properties for the mission, it is highly flammable as a very inert gas, which could cause the failure of our mission, if chosen in place of helium [4].

2.2.4 Balloon Shape

The balloon is currently modeled as a sphere. This is done to simplify the current progress of the trajectory code. This assumption will have to be undone with future progress in the design of the balloon.

Figure 1 shows a rendered model of the balloon at its maximum expansion volume of 16,500 m^3.

Figure 1: Rendered Balloon CAD

2.2.5 Analytical Balloon Model

An analytical model is initially developed to examine the forces acting on the balloon. The analytical model focuses only on the forces in the vertical direction, as it serves to determine first estimates of the required balloon properties. This is crucial to determine initial values and parameters for the balloon trajectory code, such as the required volume for the balloon, and mass limitations.

The initial analytical model is completed with many assumptions. The loaded mass for the rocket is 253.80 kg, using the information provided by the 2023-2024 rocket design team [1]. The launch platform is assumed to have a mass of 90 kg. The mass of the balloon itself is assumed to be 10 kg, as polyethylene allows for the possibility of being a few kilograms for a volume of 1000 m^3 [3]. Hence, the total mass for the analytical model is 353.80 kg. The coefficient of drag is 0.47, as described in MIT's fluid dynamics textbook [5].

The volume and velocity of the balloon are difficult to determine, as these values change drastically during the ascent of the balloon. As this is a first iteration, the volume of the balloon is assumed to be constant, as we are only trying to determine the volume at max expansion, which is the volume of the balloon at

its highest value. The velocity is also assumed to be constant, as balloons follow a linear trend, and it does not change drastically during flight. The volume of the balloon is assumed to be 5000 m^3 and the ascent speed is assumed to be 3 m/s. By performing the initial analytical model, the chosen volume can be studied to verify if it is large enough to achieve the desired altitude of 70,000 ft. This entire process can be iterated until the desired altitude is achieved.

Figure 2 shows a free body diagram representing the three primary forces acting on the balloon while only studying the forces in the vertical direction.

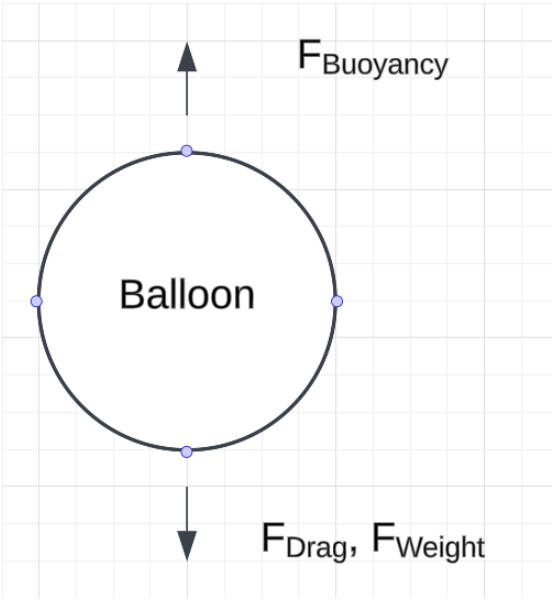

Figure 2: Analytical Balloon Free Body Diagram

The forces shown in Figure 2 are defined as follows:

$$F_{\mathrm{B}} = \rho_{\mathrm{air}} \cdot V_{\mathrm{Balloon}} \cdot g \tag{1}$$

$$F_{\mathrm{W}} = m \cdot g \tag{2}$$

$$F_{\mathrm{D}} = \frac{1}{2} \cdot C_d \cdot A \cdot \rho_{\mathrm{air}} \cdot v^2 \tag{3}$$

$$F_{\mathrm{Net}} = F_{\mathrm{B}} - F_{\mathrm{W}} - F_{\mathrm{D}} \tag{4}$$

Where:

- F_{B}: Buoyant force (N)
- F_{W}: Gravitational force (N)
- F_{D}: Drag force (N)
- ρ_{air}: Density of air (kg/m^3)
- V_{Balloon}: Balloon volume (m^3)
- g: Gravitational acceleration, 9.81 m/s^2
- m: Total mass of the system (kg)
- C_d: Drag coefficient
- A: Cross-sectional area of the balloon (m^2)
- v: Velocity of the balloon (m/s)

Using the described vertical force balance, which considers the vertical forces acting on the balloon, the net force is calculated. Based on this analysis, the balloon reaches a maximum altitude just below the initial goal of 70,000 ft. To achieve the desired altitude goal, variables will be adjusted in following iterations, such as an increase in maximum volume.

2.2.6 Balloon Trajectory Code

Analyzing the balloon trajectory is challenging due to constantly changing environmental conditions. A balloon trajectory code enables the study of the balloon's flight path and position while accounting for these variations during its ascent.

The mission involves launching the rocket to an altitude of 70,000 ft (21,336 m). To achieve this, the trajectory code must consider three atmospheric boundaries, each with distinct atmospheric profiles, as shown in Table 1.

Layer	**Altitude Range (m)**
Troposphere	0 to 11,000
Tropopause	11,000 to 20,000
Stratosphere	20,000 to 47,000

Table 1: Atmospheric Boundaries and Respective Altitude Ranges [6]

The trajectory code uses an ascent loop to calculate many properties at each time step. The code operates with a time step of 0.1 seconds, determining the changing properties within each atmospheric boundary as the balloon ascends. The pressure and temperature are computed in each boundary as follows:

- **Case 1:** If Altitude $< 11,000\,\mathrm{m}$ (Troposphere)
  - Temperature:

$$T = T_0 - L \cdot \text{Altitude} \tag{5}$$

  - Pressure:

$$P = P_0 \cdot \left(\frac{T}{T_0} \right)^{\frac{g}{R_{\text{air}} \cdot L}} \tag{6}$$

- **Case 2:** If $11,000\,\text{m} \leq \text{Altitude} < 20,000\,\text{m}$ (Tropopause)
  - Temperature:

$$T = 216.65\,\text{K} \tag{7}$$

  - Pressure:

$$P = 22650 \cdot \exp\left(-\frac{g \cdot (\text{Altitude} - 11,000)}{R_{\text{air}} \cdot T} \right) \tag{8}$$

- **Case 3:** If $\text{Altitude} \geq 20,000\,\text{m}$ (Stratosphere)
  - Temperature:

$$T = 216.65 + 0.003 \cdot (\text{Altitude} - 20,000) \tag{9}$$

  - Pressure:

$$P = 5474.89 \cdot \left(\frac{T}{216.65} \right)^{-\frac{g}{R_{\text{air}} \cdot 0.003}} \tag{10}$$

The results from the ascent loop are shown in Figure 3.

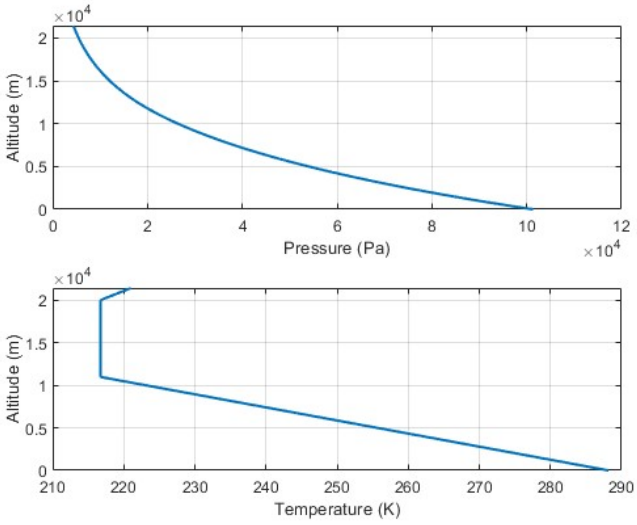

Figure 3: Pressure and Temperature Variation with Altitude

These results are identical to the International Standard Atmosphere [7], as shown in Figure 4.

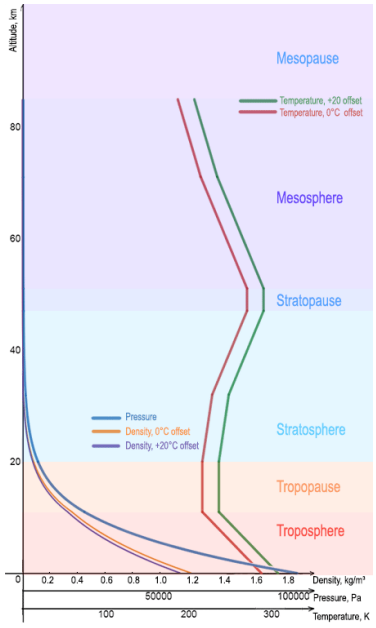

Figure 4: International Standard Atmosphere Model

As shown in Figure 4, the data is based on the International Standard Atmosphere [7].

The pressure and temperature at each atmospheric layer are crucial to determine many of the balloon's properties, as well as environmental properties affecting the balloon's ascent. Two values that are changing throughout the ascent are the density of the air surrounding the balloon and the density of the helium inside the balloon.

$$\rho_{\text{air}} = \frac{P}{R_{\text{air}} \cdot T} \tag{11}$$

$$\rho_{\text{helium}} = \frac{P}{R_{\text{helium}} \cdot T} \tag{12}$$

The variables used in the pressure and temperature equations for the three atmospheric layers, as well as in the densities, are as follows.

- T: Temperature at the balloon's altitude (K).
- P: Pressure at the balloon's altitude (Pa).
- Altitude: Altitude above sea level (m).
- T_0: Sea-level temperature (K).
- P_0: Sea-level pressure (Pa).
- L: Temperature lapse rate in the troposphere (K/m).
- g: Acceleration due to gravity ($\mathrm{m/s^2}$).
- R: Specific gas constant ($\mathrm{J/(kg \cdot K)}$).

Figure 5 demonstrates the results obtained for the density and altitude relationship.

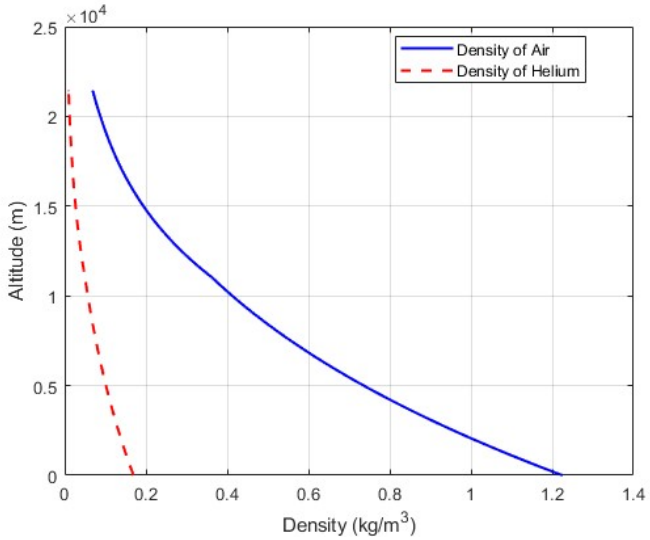

Figure 5: Density Variation with Altitude

In the analytical model, the total mass of the system was based on previously determined information and assumptions. As the team progressed, additional masses were added and determined. The masses used in the current iteration of the code are shown in Table 2.

Component	Mass (kg)	Source
Rocket Mass	253.80	2023-2024 Team [1]
Balloon (Material) Mass	20.00	Assumption from earlier [3]
Launch Platform Mass	520.00	From Jake [Section 2.4]
Control System Mass	183.70	From Doryan [Section 2.2]
Helium Mass	161.00	Iteration
Total Mass	**1138.50**	Sum of all masses

Table 2: Breakdown of Balloon System Masses

The process in order to determine the helium mass required to reach the desired altitude, as well as the expansion of the balloon, is obtained through the use of the following three equations.

$$V_{\text{min}} = \frac{m_{\text{helium}} \cdot R_{\text{helium}} \cdot T_0}{P_0} \tag{13}$$

$$V_{\text{max}} = \frac{m_{\text{helium}} \cdot R_{\text{helium}} \cdot T_{\text{altitude}}}{P_{\text{altitude}}} \tag{14}$$

$$m_{\text{helium}} = \frac{V_{\text{max}} \cdot P_{\text{altitude}}}{R_{\text{helium}} \cdot T_{\text{altitude}}} \tag{15}$$

Where:

- P_{altitude}: Pressure at the balloon's current altitude (Pa)
- T_{altitude}: Temperature at the balloon's current altitude (K)

These equations demonstrate that the values are interdependent; hence, they are obtained through iteration. An initial maximum expansion volume of the balloon is assumed and the helium mass is determined using Equation (15). The simulation is then continuously used to determine if the balloon can reach the desired altitude of 70,000 ft. The process of the iteration can also be done in reverse order, assuming a helium mass, although it can allow for a maximum volume size that is infinite and not realistic.

Once the process of iteration is complete, the maximum expansion volume of the balloon is determined to be 16,499.5 m^3, and the corresponding helium mass to be 160.86 kg. The values are rounded up for simplicity of the code, as the balloon will still be able to ascend for a short period of time while reaching its maximum expansion volume. The maximum balloon volume is 16,500 m^3, and the helium mass is 161 kg. Using the values obtained, the initial balloon size at sea level is 950.96 m^3, according to Equation (13).

During ascent, the balloon's volume will vary between the initial and maximum volume of the balloon. The balloon must increase in volume to maintain equilibrium due to the external atmospheric pressure decreasing with altitude. In order to determine this value, a volume loop is constructed in the code.

The MATLAB code calculates the balloon volume using the ideal gas law. It then determines the volume of the balloon based on the specific altitude conditions determined in the ascent loop described earlier.

The volume of the balloon:

$$V_{\text{balloon}} = \frac{m_{\text{helium}} \cdot R_{\text{helium}} \cdot T_{\text{altitude}}}{P_{\text{altitude}}} \tag{16}$$

- **Case 1:** If $V_{\text{balloon}} < 950.96\,\text{m}^3$
  - $V_{\text{balloon}} = 950.96\,\text{m}^3$.
  - $A_{\text{balloon}} = 467.66\,\text{m}^2$.
- **Case 2:** If $950.96\,\text{m}^3 \leq V_{\text{balloon}} \leq 16500\,\text{m}^3$
  - The balloon volume and area are recalculated at each time step, 0.1 seconds.
- **Case 3:** If $V_{\text{balloon}} > 16500\,\text{m}^3$
  - $V_{\text{balloon}} = 16500\,\text{m}^3$.
  - $A = 3134.3\,\text{m}^2$.

The results for the balloon volume during ascent, is shown in Figure 6.

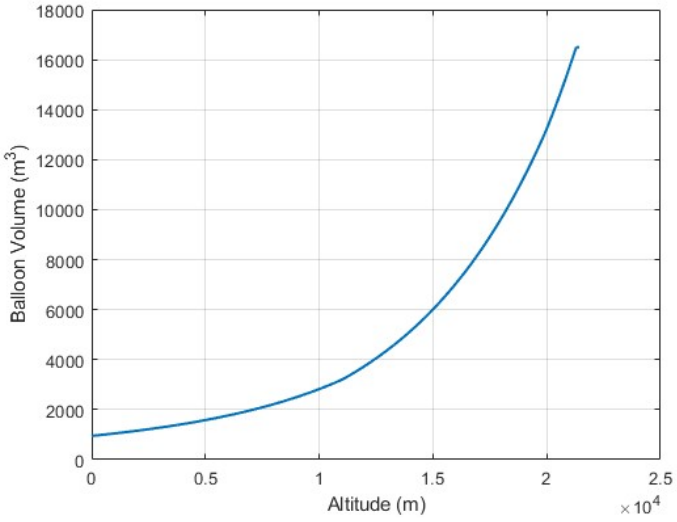

Figure 6: Balloon Volume during Ascent

With the changing atmospheric and balloon properties determined at each time step, a study of the kinematics of the balloon can be accomplished in the vertical (z) direction. Similar to the initial analytical approach, the net force acting on the balloon is computed at each time step in the code, using Equation (4) (Net Force). This is accomplished using the accompanying equations in that section: Equation (1) (Buoyancy Force), Equation (2) (Gravitational Force), and Equation (3) (Drag Force).

The results for each of these forces during ascent can be seen in Figures 7, 8, 9, and 10.

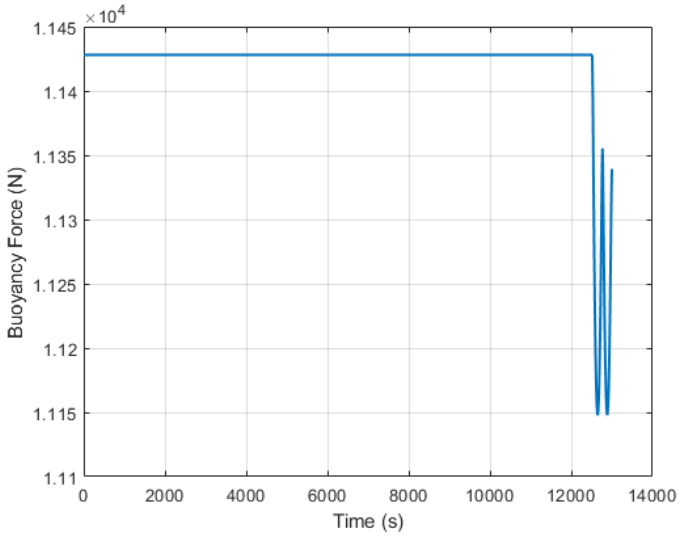

Figure 7: Buoyancy Force with Time

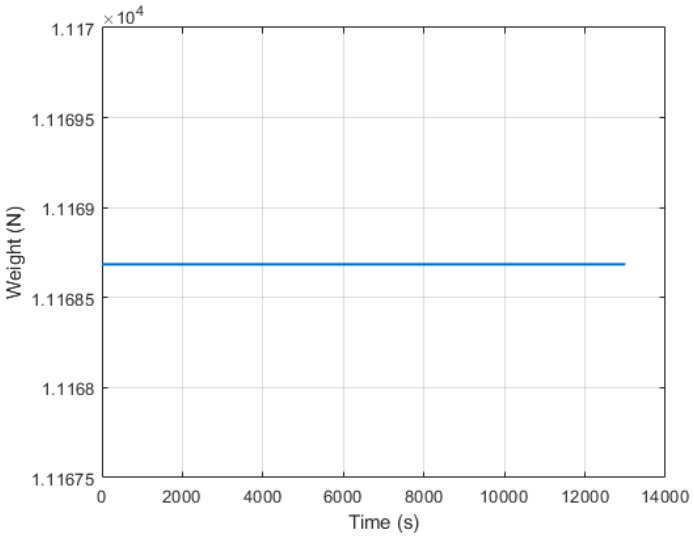

Figure 8: Gravitational Force with Time

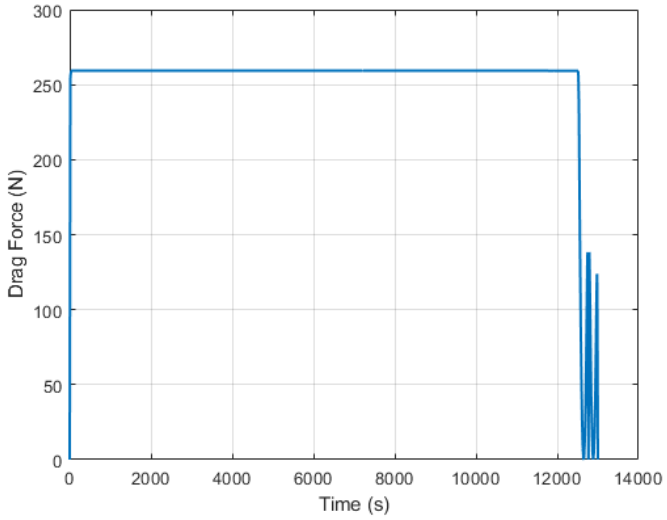

Figure 9: Drag Force vs Time

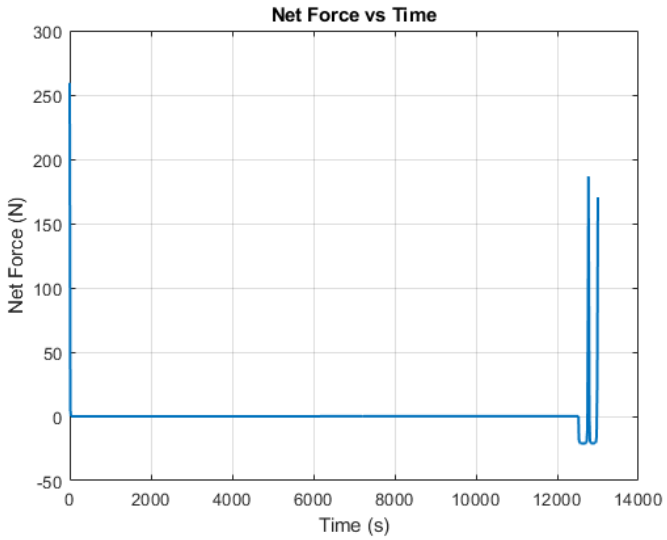

Figure 10: Net Force with Time

As seen in the three figures: Figure 7 (Buoyancy Force), Figure 9 (Drag Force), and Figure 10 (Net Force) oscillations are present past 12,500 seconds. This represents the time in the ascent where the balloon has reached its maximum altitude and will burst without a control system to allow the balloon to slowly

drift back to sea level. This would pose a significant issue with the heavy payload after the rocket ignites, although in Section 2.2, Doryan will be discussing his control system design.

The net force acting on the balloon is crucial in determining the kinematics of the balloon. The following three equations are used to determine the vertical velocity, as well as the position of the balloon as it ascends.

$$a = \frac{F_{\text{Net}}}{m_{\text{total}}} \tag{17}$$

$$v = v_{\text{initial}} + (a \cdot \Delta t) \tag{18}$$

$$z = z_{\text{initial}} + (v \cdot \Delta t) \tag{19}$$

Where:

- a: Acceleration (m/s^2).
- F_{Net}: Net force acting on the balloon (N).
- m_{total}: Total mass of the balloon system (kg).
- v: Velocity of the balloon (m/s).
- v_{initial}: Initial or previous velocity of the balloon (m/s).
- z: Current altitude of the balloon (m).
- z_{initial}: Initial or previous altitude of the object (m).
- Δt: Time step (s).

The results for the velocity and position of the balloon as it ascends with time are shown in Figures 11 and 12.

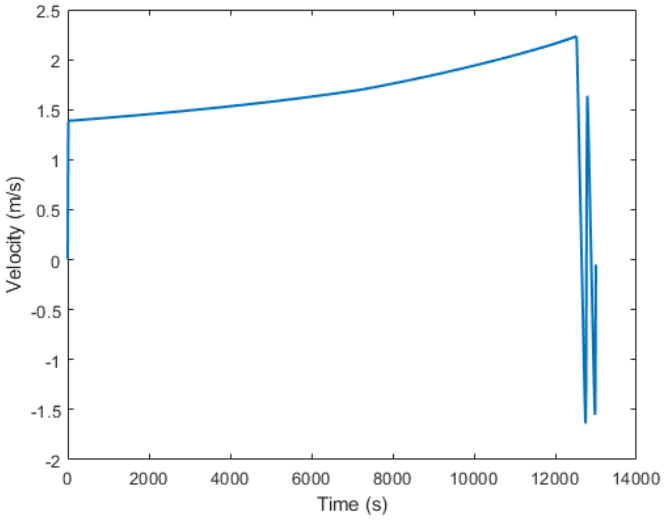

Figure 11: Balboon Velocity with Time

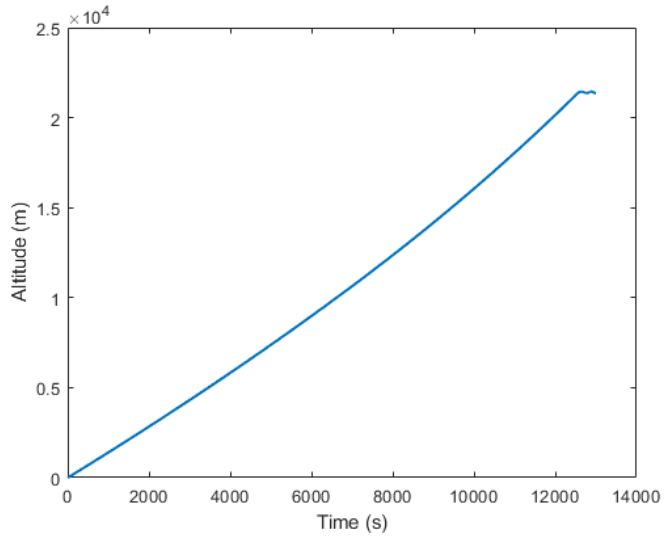

Figure 12: Balloon Altitude with Time

Similarly, the oscillations begin once the balloon reaches its burst point. As shown in Figures 11 and 12, the velocity increases rapidly once the ascent begins and slowly increases for nearly the entire duration of the ascent. The balloon reaches the desired altitude of 70,000 ft, or 21,336 m, in 12,500 seconds.

To this point, only the vertical (z-axis) of the balloon is considered. To continue, the horizontal (x-y axis) must be considered. At this iteration of the trajectory code, it considers the wind speeds and drag in the horizontal direction.

The wind speeds are found using data from previous days, available from Copernicus Climate Data Store [8]. This is to see how wind speeds would affect the trajectory of the balloon if launched on a previous day.

In order to simulate and determine the wind speeds on the day of the launch, a smaller balloon can be sent up prior to the main balloon launch. This would be a separate, unique design, that may be seen in the later half of the year.

Copernicus Climate Data Store offers the wind speeds based on the pressure at each altitude [6]. These values are shown in Table 3.

Pressure Level (hPa)	**Altitude (m)**
1000	Sea level (0 m)
925	760 m
850	1,500 m
700	3,000 m
500	5,500 m
400	7,000 m
300	9,000 m
250	10,500 m
200	12,000 m
150	14,000 m
100	16,000 m
70	18,500 m
50	20,000 m
30	23,000 m
20	26,000 m
10	31,000 m

Table 3: Pressure Levels and Associated Altitudes [6]

Due to the mission profile, only the wind speeds up to the altitude of 23,000 m are required. The wind speeds between these values are assumed linear and interpolated between these values. The pressure at each altitude from the ascent loop is used to determine the wind speeds.

The wind speed data is collected on two separate days in 2024: October 7 and November 7. The wind speeds as a function of pressure levels can be seen in Figures 13 and 14.

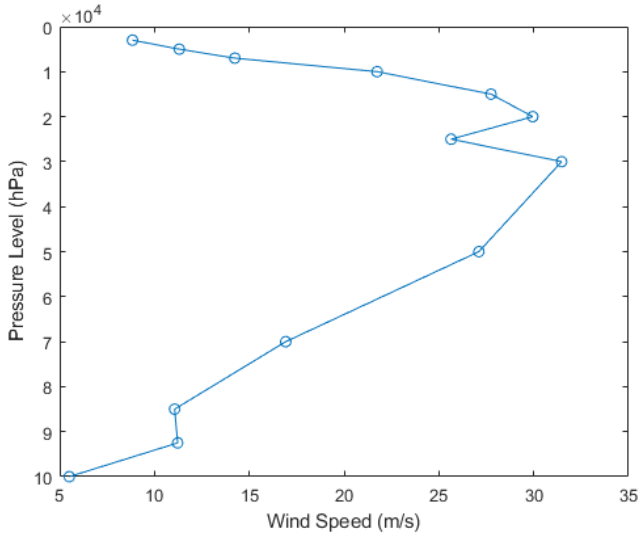

Figure 13: October 7, Wind Speed Data

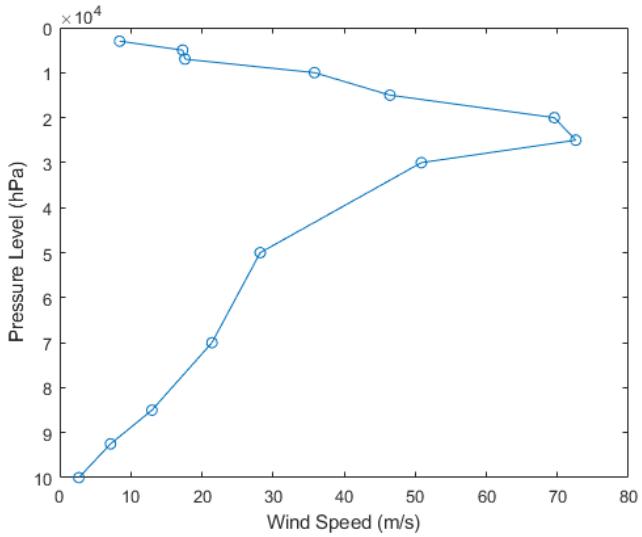

Figure 14: November 7, Wind Speed Data

Using the wind speed data, the horizontal velocity and position of the balloon are determined in a process similar to the vertical axis, calculated at each time step.

$$F_{\text{drag},x} = 0.5 \cdot C_d \cdot A \cdot \rho_{\text{air}} \cdot v_x^2 \tag{20}$$

$$F_{\text{drag},y} = 0.5 \cdot C_d \cdot A \cdot \rho_{\text{air}} \cdot v_y^2 \tag{21}$$

The velocity in the horizontal directions are determined by:

$$v_x = v_{x,\text{initial}} - \left(\frac{F_{\text{drag},x}}{m_{\text{total}}} \right) \cdot \Delta t \tag{22}$$

$$v_y = v_{y,\text{initial}} - \left(\frac{F_{\text{drag},y}}{m_{\text{total}}} \right) \cdot \Delta t \tag{23}$$

The position in the horizontal directions are determined by:

$$y_{\text{position}} = y_{\text{position}} + v_{\text{y}} \cdot \Delta t \tag{24}$$

$$x_{\text{position}} = x_{\text{position}} + v_{\text{x}} \cdot \Delta t \tag{25}$$

The wind speeds from two different days are used to simulate the ascent of the balloon: October 7, 2024, and November 7, 2024. The results of the balloon position during ascent are shown in Figures 15 and 16.

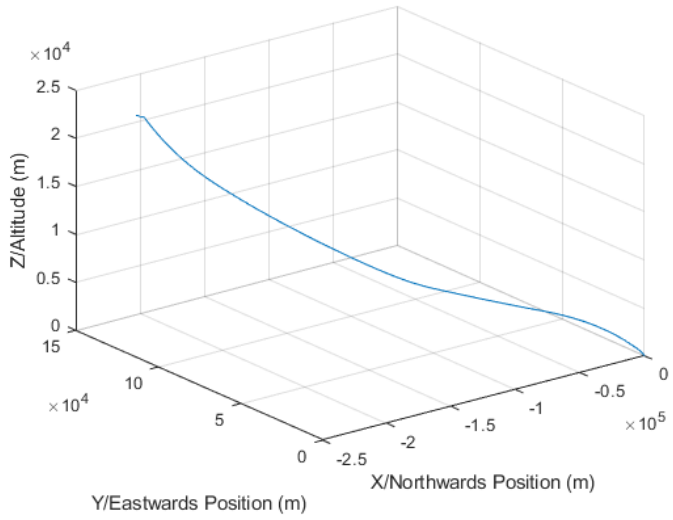

Figure 15: Balloon Ascent on October 7, 2024, with Wind Speeds

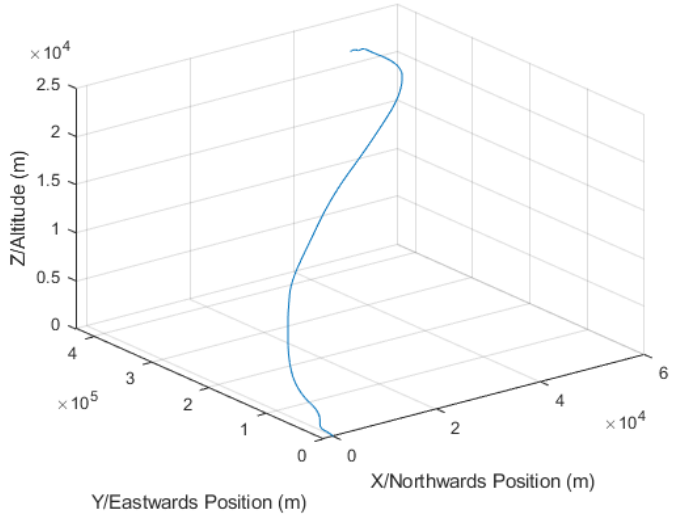

Figure 16: Balloon Ascent on November 7, 2024, with Wind Speeds

The two balloon trajectories are significantly different. As mentioned previously, the wind speeds are higher in magnitude on November 7, and this is reflected in the final position of the balloon on that date.

2.2.7 Future Work

In terms of future work, the balloon trajectory code has many assumptions that need to be removed, in order to provide a more accurate representation of the balloon ascent. The drag coefficient is currently assumed to be constant, which is not the case. Although closely familiar, the balloon is also not a sphere, which it is currently being modeled as, to ease the simplification of the current iteration of the code. There are also many other assumptions that need to be removed.

In the following semester, the idea of a second, probe balloon will be proposed. If approved, the probe balloon would ascend prior to the primary balloon. This probe balloon would collect data, such as wind speeds on the day of launch, allowing for a control launch, working closely with Doryan's work, to control the ascent of the balloon using wind currents.

2.3 Ascent Control System - Doryan Saavedra-Zakikhani

Peer Reviewed by: Noah St-Amant

2.3.1 Introduction

As the high altitude balloon ascends, it is subjected to wind forces that change depending on the time of day and altitude. As a result of these wind forces, the balloon and payload will usually end up considerably further from the initial launch site and potentially outside of the permitted flight zone. According to National Weather Service, weather balloons can drift over 125 miles (201 km) when ascending to 100,000 ft (30,480 m) due to wind [9].

A simple, yet effective way of controlling the position of the balloon is to ride the wind currents that vary with altitude. The ascent rate can be adjusted so the balloon remains at an altitude with favorable wind conditions to push it back to the initial launch site. This control concept was proposed in a paper by H. Du et al [10]. By actively controlling the altitude of the balloon, the position can also be controlled as illustrated in Figure 17. Wind data for the day of launch will need to be obtained from forecasts and weather stations in order to determine a suitable flight path for the balloon. A solution for controlling the ascent rate of the balloon and payload will be presented in this section of the report.

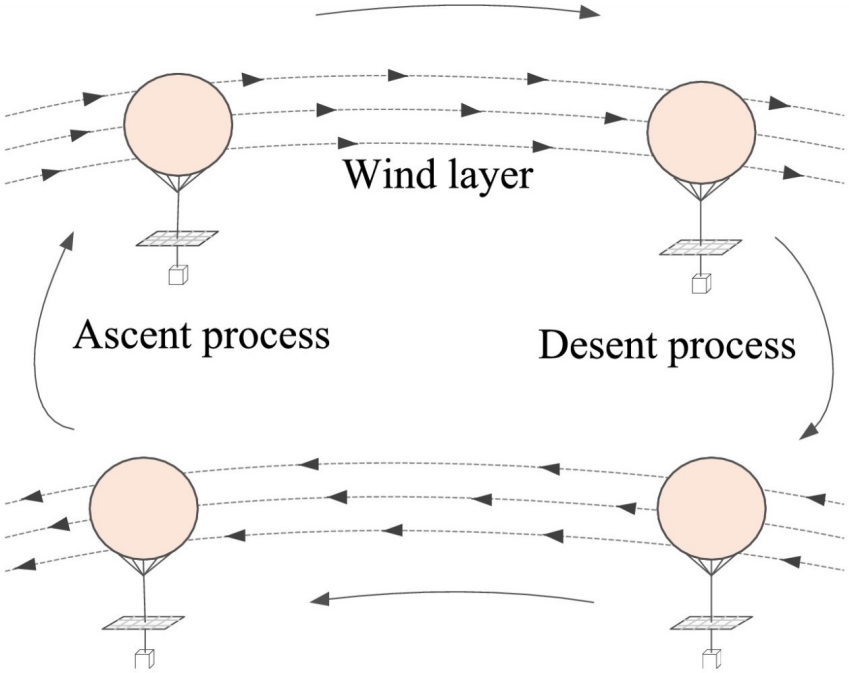

Figure 17: Balloon and Payload Position Control Concept by Changing Altitude [10]

2.3.2 Methods of Controlling Ascent Rate

There are several researched methods of controlling the ascent rate of a high altitude weather balloon. Each method relies on either increasing the weight of the system or decreasing the buoyancy force. Increasing the weight of the system requires adding mass. This can only be achieved at high altitudes by storing the surrounding air in a pressurized tank. However, adjusting the buoyancy force requires changing the volume of the balloon or internal gas density as shown by Archimedes Principle (see Eq 26) [11].

$$F_B = (\rho_{atm} - \rho_{He})V_{Balloon}g \tag{26}$$

Where:

F_B : Buoyancy force (N)

ρ_{atm} : Atmospheric air density at current altitude (kg/m^3)

ρ_{He} : Density of helium at current altitude (kg/m^3)

$V_{Balloon}$: Volume of the balloon (m^3)

g : Acceleration due to gravity [9.81 m/s^2]

Since helium was chosen as the weather balloon gas, the only method of controlling the buoyancy force is to change the volume. A few proposed and researched methods of controlling the ascent rate of a weather balloon is summarized in Table 4 along with their advantages and disadvantages.

Table 4: Methods of Controlling Balloon and Payload Altitude

Method	Advantage	Disadvantage
Increasing payload mass by compressing air [10]	- Simple tank and compressor system - No method to adjust the balloon volume is needed	- Time to fill tank increases with altitude - Large adjustments to the descent rate can take between a few minutes to over an hour
Increasing payload mass by compressing helium from the balloon	- Compressing helium from the balloon into a tank reduces the balloon volume	- The time to fill a tank with helium is extremely long due to the low density of helium - Constantly changing the volume of the balloon could cause significant wear in the balloon and may burst
Decrease balloon volume by mechanically compressing the balloon [12]	- Quick method to change the balloon volume - The capability to change ascent and descent rate quickly could allow for a more accurate trajectory analysis.	- A large, heavy, complex system is needed that can forcefully reduce the balloon volume - Since the mass of helium does not change, the internal balloon pressure will increase significantly - Limited range of altitudes were it is effective
Discharge helium from the balloon	- Quickly change the volume of the balloon to hover and descend - Significant reduction in payload mass due to simplicity of the design	- Impossible to recover lost helium, therefore, this method can only be used to hover at a specific altitude or to descend

Ultimately, the decision was made to design a system that can store and discharge air to control the ascent rate and altitude of the weather balloon and payload. Although the other options could be effective, they either proved too complex or provided poor performance. A sketch of the proposed control system is shown in Figure 18.

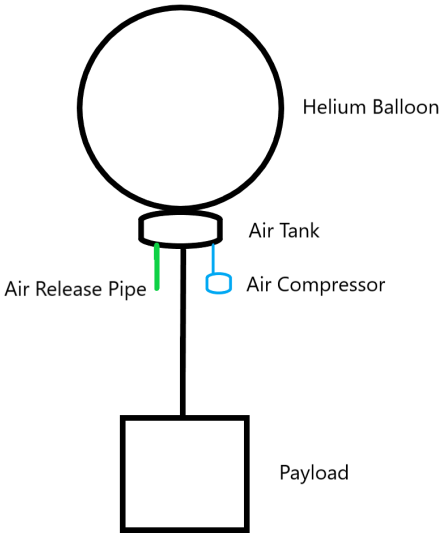

Figure 18: Ascent Control System Draft Concept

Two configurations of storing air in the tank will be explored in this report. The first is using a gas powered engine to spin an air pump that fills the tank. The second configuration will use an electric air compressor powered by onboard batteries.

2.3.3 Ascent Control System Sizing

2.3.3.1 Mass of Air Required

Hovering of the balloon and payload (reduce ascent speed to 0 m/s) can be achieved by balancing the buoyancy and gravity forces as shown in Eq 27.

$$F_B = F_g \tag{27}$$

Where:

F_g : Force due to gravity (N)

An important consideration is that a tank filled with air will produce its own buoyancy force. Therefore the total buoyancy force on the system comprises the force due to helium and due to air. However, adding air to the tank also increases the mass of the system. There are two components to the additional gravity force, air at atmospheric conditions and the excess compressed air. The first component occurs in the empty condition, with only uncompressed air in the tank (which has pressure, temperature, and density conditions equal to the surrounding atmosphere). The second component of the gravity force occurs

due to the excess compressed air in the tank. Combining the buoyancy and gravity force considerations yields Eq 28.

$$F_{B(He)} + F_{B(air)} = m_t g + m_{air_{atm}} g + m_{air_{excess}} g \tag{28}$$

Where:

$F_{B(He)}$: Buoyancy force due to helium tank (N)

$F_{B(air)}$: Buoyancy force due to air tank (N)

m_t : Total payload, balloon, and helium mass (kg)

$m_{air_{atm}}$: Mass of air in tank at ISA conditions (kg)

$m_{air_{excess}}$: Excess mass of air in tank (kg)

An interesting observation is that the buoyancy force of uncompressed air is equivalent to its mass. This is shown in Eq 29 and is due to the fact that the density of the uncompressed air is equivalent to the density of the surrounding atmosphere. This condition is true at all altitudes.

$$F_{B(air)} = m_{air_{atm}} g = \rho_{atm} V_{tank} g \tag{29}$$

Where:

V_{tank} : Volume of air tank (m^3)

Due to the observation shown in Eq 29, the Buoyancy force and gravity force of uncompressed air can be eliminated. We can then rearrange Eq 28 to isolate the mass of the excess air to give Eq 30.

$$m_{air_{excess}} = \frac{F_{B(He)} - m_t g}{g} \tag{30}$$

The excess mass of air required to reduce the descent rate to 0 m/s is given in Eq 30. This formula will give the mass required for hover at all altitudes. Since the buoyancy force was found to remain constant at all altitudes, the mass required to hover is constant at 4.34 kg.

2.3.3.2 Tank Size Analysis

The size of the air tank plays a crucial role in the performance of the altitude control system. The ability to store more air in the tank allows the weight of the payload to increase, which increases the descent rate of the balloon. However, most air pumps have a limit on the maximum tank pressure that they can operate. For the gas powered configuration, the pump that was chosen for this

analysis has a tank pressure limit of 155 psi (see Section 2.3.3.3). However, the electric air compressor has a pressure limit of 200 psi (see Section 2.3.3.3). The minimum tank size used must be able to store enough excess air mass to allow the balloon to hover without exceeding the pressure limit.

To start the analysis, the total pressure in the air tank (155 psi or 200 psi) is equal to the atmospheric air pressure combined with the pressure of the excess air required to hover as described in Eq 31.

$$P_{total} = P_{air_{excess}} + P_{air_{atm}} \tag{31}$$

Where:

P_{total} : Total pressure in air tank (Pa)

$P_{air_{excess}}$: Pressure due to excess air in the tank (Pa)

$P_{air_{atm}}$: Pressure due to air at the current altitude (Pa)

The excess air pressure can be modeled with the ideal gas law as shown in Eq 32. A simplifying assumption is made that the temperature in the tank is equal to the temperature of the surrounding atmosphere. This assumption is reasonable since the balloon and payload system will take a few hours to reach the desired altitude.

$$P_{air_{excess}} = \frac{m_{air_{excess}} R T_{atm}}{V_{tank}} \tag{32}$$

Where:

R : Gas constant of air [287 J/(kgK)]

T_{atm} : Temperature at ISA conditions (K)

Substituting Eq 32 in Eq 31 and isolating for the air tank volume gives Eq 33.

$$V_{tank} = \frac{m_{air_{excess}} R T_{atm}}{P_{total} - P_{air_{atm}}} \tag{33}$$

As the atmospheric pressure and temperature changes with altitude, so does the minimum required air tank volume.

Gas Powered Air Compressor Configuration

The gas powered air compressor and pump can only fill a tank up to 155 psi. Using this requirement, the minimum required air tank volume at each altitude is plotted in Figure 19.

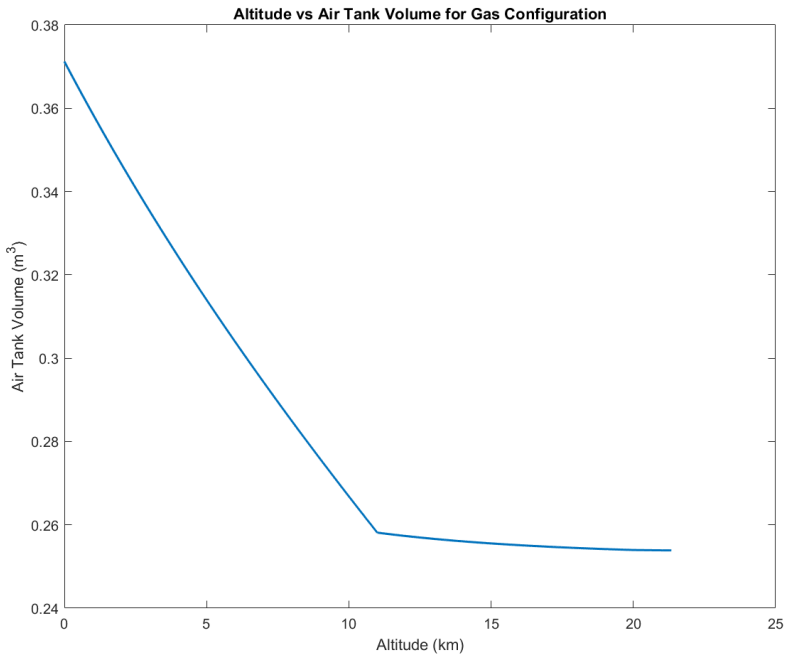

Figure 19: Air Tank Volume Change at Different Altitudes for Gas Powered Engine Configuration

There are many off the shelf compressed air tanks available on the market. However, their sizes are standardized. From the figure, it can be seen that at sea level, the required tank size is 0.37 m^3 (97.7 gallons). The nearest suitable tank size on the market is 120 gallons.

However, a closer analysis of the plot in Figure 19 will reveal that the required tank size decreases considerably at higher altitudes. Another standardized air tank size that can be easily purchased is 80 galloon. This is a significant reduction in tank size which translates to a reduction in weight.

It can be observed that at 6.12 km (20,079 ft), the required tank volume drops to 0.30 m^3 (80 gallons). The major disadvantage with using the smaller tank is that the balloon will be unable to descend below 6.12 km (20,079 ft). However, as seen in Noah's discussion (Section 2.1), the wind speed changes directions at much greater altitudes. Therefore, it is feasible to utilize the smaller tank size and set a restriction on the minimum operating altitude of the ascent control system. It is possible to choose a tank size between 80 and 120 gallons, however, they are not easily found for purchase and must be custom made. For the current iteration of the balloon control system, a tank size of 0.3 m^3 (80 gallons)

was chosen.

Electric Air Compressor Configuration

Due to the electric air compressor's capability to operate at a higher pressure of 200 psi, the tank size requirements are significantly reduced. Figure 20 shows the tank size at all altitudes using the electric air compressor.

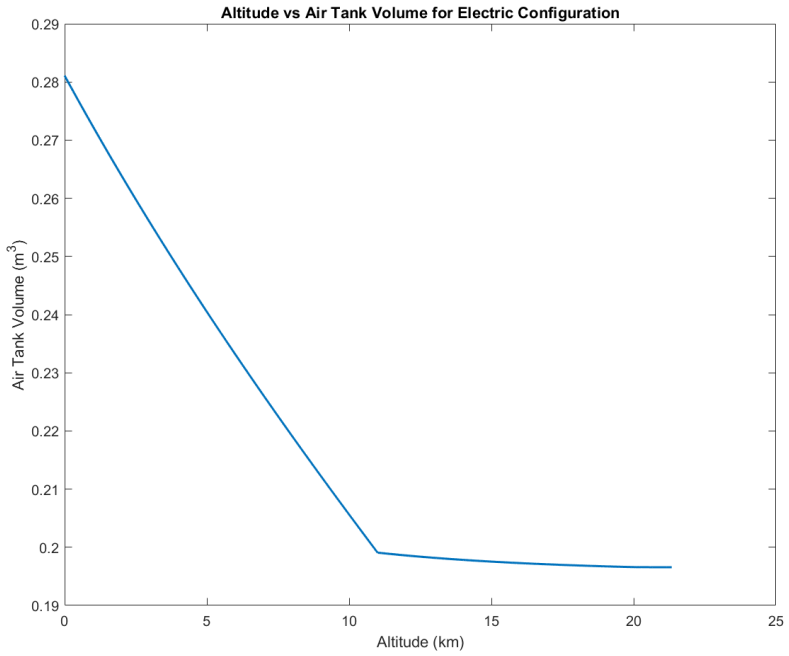

Figure 20: Air Tank Volume Change at Different Altitudes for Electric Configuration

From Figure 20, it can be seen that the required tank size at sea level is 0.28 m^3 (74 gallons). This means that the 80 gallon tank chosen for the gas powered configuration would work at all altitudes when using the electric air compressor. When looking at the minimum tank size for an operating altitude of 6.12 km (20,079 ft), the required tank size is 0.23 m^3 (61 gallons). In this case, a lighter tank may be used to reduce the overall weight of the system. However, for this configuration, the 80 gallon tank will be used. This will allow for a more equal comparison between the gas and electric configuration.

2.3.3.3 Chosen Components

In the performance analysis section of the report (Section 2.3.4). Two methods of filling the air tank are compared. The first is using a turbocharged gasoline engine that powers an air pump. The second method uses an electric compressor to power the air pump and fill the tank.

Both methods have advantages and disadvantages. A gas power engine has a considerably greater power density that batteries. This reduces weight by eliminating the need for heavy batteries. However, these engines experience considerably performance losses at high altitudes. This will result in increased time to fill the air tank. On the other hand, the electric air compressor, which requires heavy batteries, will be able to operate at all altitudes without a performance drop. Furthermore, it may be possible to use solar panels to reduce the size of the batteries required.

A suitable compressed air tank is shown in Figure 21. This tank can safely store air at a pressure of 200 psi [13]. This is fits the requirement for the maximum tank pressure that will be experienced during operation. Furthermore, the tank includes a mounting plate for the compressor system.

Figure 21: 80 Gallon Air Tank With Mounting Plate [13]

The performance analysis of the gas powered system utilizes an Industrial Air 4.7 hp single stage pump capable of a volumetric flow rate of 14 CFM, it is shown in Figure 22 [14].

Figure 22: Industrial Air 4.7 hp Single Stage Pump [14]

To power the pump, a Honda GX200 engine capable of producing 5.8 hp was selected as shown in Figure 23 [15]. A slightly more powerful engine than required was selected in order to delay the performance drop seen in the pump due to lower engine performance at higher altitudes [16].

Figure 23: Honda GX200 Engine [15]

For the electric configuration, the air compressor used for the performance analysis is shown in Figure 24. This compressor was chosen due to its high volumetric flow rate (8 CFM) and its ability to operate with a 12V battery [17].

Figure 24: Oasis XDM3000-12 Air Compressor [17]

The chosen air compressor requires 12V and 180 amps of current to operate at maximum volumetric flow rate. In order to operate for 1 hour, a 180 Ah battery is needed. An example of a suitable battery is shown in Figure 25. This battery has a mass of 42.4 kg (93.5 lb) [18]. The number of batteries required depends on the desired compressor operating time. For example, 10 hours of operation requires 425 kg (935 lb) worth of batteries. It is a significant increase when compared to the 10.2 kg (22.5 lb) of gasoline required to power the Honda GX200 engine for the same amount of time.

Figure 25: IDEALPOWER 12V 180A Battery

A summary of the components and masses are summarized in Table 5. Note that the electric air compressor configuration weighs over three times as much as the gas powered configuration.

Table 5: Mass of Ascent Control System Components

Component	Mass
Gas Engine Configuration	
Air Tank [13]	119.8 Kg (264.1 lb)
Industrial Air Pump [14]	30.8 kg (67.9 lb)
Honda GX200 Engine [15]	16.1 kg (35.5 lb)
Fuel for Honda Engine (10 hours of operation)	10.2 kg (22.5 lb)
Additional Components Estimate (Sensors, pipes, etc)	6.8 kg (15 lb)
Total	183.7 kg (405.0 lb)
Electric Motor Configuration	
Air Tank [13]	119.8 Kg (264.1 lb)
Electric Air Compressor System [17]	28.1 kg (62.0 lb)
Batteries (10 hours of operation) [18]	424 kg (935 lb)
Additional Components Estimate (Sensors, pipes, etc)	6.8 kg (15.0 lb)
Total	578.7 kg (1276 lb)

2.3.4 Performance Analysis of Control System

2.3.4.1 Tank Discharge Performance

The time it takes for the tank to discharge all of the excess air allows us to know the speed at which we can alter the ascent rate of the balloon. Furthermore, the thrust force felt on the control system due to the air discharge will be analyzed. The chosen 80 gallon tank contains a drain port with a diameter of 0.01905 m (0.75 in) [13]. This value will be used for the analysis. The mass of air in the tank used for this analysis will be 4.34 kg, which is the mass of air required to hover at a desired altitude. Since the air mass and tank size do not change between configurations, the results in this section will be the same for the gas and electric air compressor systems.

For the purpose of this analysis, since the tank pressure is large, compressible flow will be assumed. To start, the system needs to be analyzed to determine if the flow will be choked. From Frank White's Fluid Mechanics textbook, the flow is chocked if the back pressure is equal to or greater than the critical pressure [19]. Since the outlet does not consist of a diverging nozzle, if the flow is choked, it will remain at Mach 1 in the pipe. The absence of a diverging nozzle means that the flow cannot accelerate further. The critical pressure for Mach 1 can be found using the relation shown in Eq 34 [19].

$$\frac{P^*}{P_o} = 0.5283 \tag{34}$$

Where:

P^* : Critical Pressure (Pa)

P_o : Stagnation Pressure (Pa)

The flow is chocked when the back pressure is less than or equal to the critical pressure as described in Eq 35. Note that the critical pressure depends on the stagnation pressure in the tank. Therefore, as the tank discharges, the critical pressure decreases and at some point the flow will no longer be choked [19].

$$if P_b <= P^*, Ma = 1 \tag{35}$$

Where:

P_b : Back pressure (Pa)

Ma : Mach number at pipe exit

For choked flow, the formula to calculate the mass flow rate at the throat of a converging-diverging nozzle is given by Eq 36 [19]. Since there is no diverging nozzle in the system, this equation will give the mass flow rate at the exit of the pipe.

$$\dot{m} = \frac{0.6847 P_o A_e}{(RT_o)^{\frac{1}{2}}} \tag{36}$$

Where:

$\dot{m}$: Mass flow rate (kg/s)

A_e : Exit area (m^2)

T_o : Stagnation temperature (K)

When the exit pressure is greater than the critical pressure, as described in Eq 37, the flow is no longer choked and will be subsonic [19].

$$if P_b > P^*, Ma < 1 \tag{37}$$

However, even for the subsonic case, compressible flow will be assumed. This results in Eq 38 being used to describe the mass flow rate of air at the pipe exit [19].

$$\dot{m} = \frac{A_e P_o}{\sqrt{RT_o}} \sqrt{\frac{2k}{k-1} \left(\frac{P_e}{P_o}\right)^{\frac{2}{k}} \left[1 - \left(\frac{P_e}{P_o}\right)^{\frac{k-1}{k}}\right]} \tag{38}$$

Where:

k : Specific heat ratio of air [1.4]

The only unknown in the above formulas is the tank pressure and temperature which changes as a function of time. From the ideal gas law form that uses mass and volume, we can determine the change in pressure as simply the change in mass. Since the change in mass is equal to the mass flow rate multiplied by a time step, dt, we can obtain Eq 39.

$$dP_o = -\frac{\dot{m}RT_o}{V_{tank}}dt \tag{39}$$

Where:

dP_o : Change in stagnation pressure (Pa)

If we assume isentropic conditions, we can use the relation shown in Eq 40 to obtain the new stagnation temperature after a certain amount of air is discharged from the tank [19].

$$T_o = T_{initial}\left(\frac{P_{o_{new}}}{P_o}\right)^{\frac{k-1}{k}} \tag{40}$$

Where:

$T_{initial}$: Initial stagnation temperature in the tank (K)

$P_{o_{new}}$: New stagnation pressure in the tank (Pa)

For the analysis, we will assume that the mass of the tank does not change at small time intervals (0.001 second). The mass of air that discharges from the tank is given in Eq 41.

$$\Delta m_{air} = \dot{m}\Delta t \tag{41}$$

Where:

Δm_{air} : Change in air mass (kg)

Δt : Change in time (s)

At each time interval (0.001 s) the mass of air is reduced by the change in mass determined in Eq 41. Then Eq 34 - Eq 40 are used to determine the new mass flow rate. This is repeated until the air in the tank is empty and only the uncompressed air at the current atmospheric condition is left.

The time to discharge a full tank of air is plotted in figure 26 starting from sea level up to 21,336 m (70,000 ft). Note that the control system for the gas powered configuration can only operate starting at 6.12 km (20,079 ft).

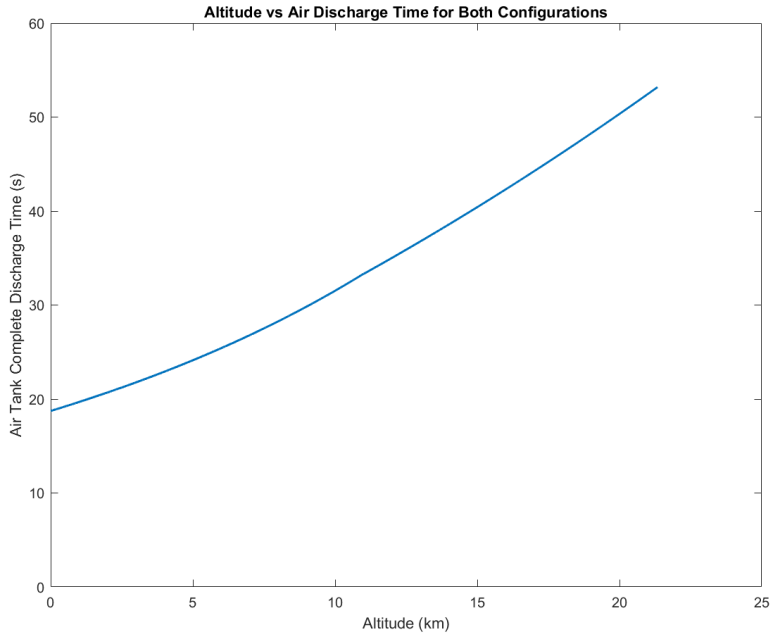

Figure 26: Altitude vs Air Discharge Time

The time to discharge the tank is relatively quick. At sea level, it takes 18.7 seconds for a full discharge while at 21,336 m (70,000 ft) the time increases to 53.2 seconds.

Due to the relatively high speed air discharge from the tank, it may induce a significant thrust force that could affect the position of the balloon and payload. To analyze this thrust force, Eq 42 will be used [20]. Note that the velocity at the exit for choked flow is simply Mach 1.

$$T = \dot{m}V_e + A_e(P_e - P_{atm}) = \dot{m}Ma\sqrt{kRT_e} + A_e(P_e - P_{air_{atm}}) \tag{42}$$

Where:

T : Thrust (N)

V_e : Exit velocity (m/s)

T_e : Temperature at pipe exit (K)

P_e : Exit pressure (Pa)

In Eq 42, the exit temperature is needed which is a function of Mach number as described by Eq 43 [19].

$$T_e = \frac{T_o}{1 + 0.2Ma^2} \tag{43}$$

Also needed for the thrust equation is the pressure at the pipe exit. This can be modeled using Eq. 44 [19].

$$P_e = \frac{P_o}{(1 + 0.2Ma^2)^{3.5}} \tag{44}$$

When the flow transitions to subsonic, Eq 45 must be used to determine the Mach number to be used in Eq 42 , Eq 43 [19], and 44.

$$Ma = \sqrt{5\left[\left(\frac{P_o}{P_e}\right)^{\frac{2}{7}} - 1\right]} \tag{45}$$

At 21,336 m (70,000 ft) the thrust produced over time is plotted in Figure 27 for both configurations.

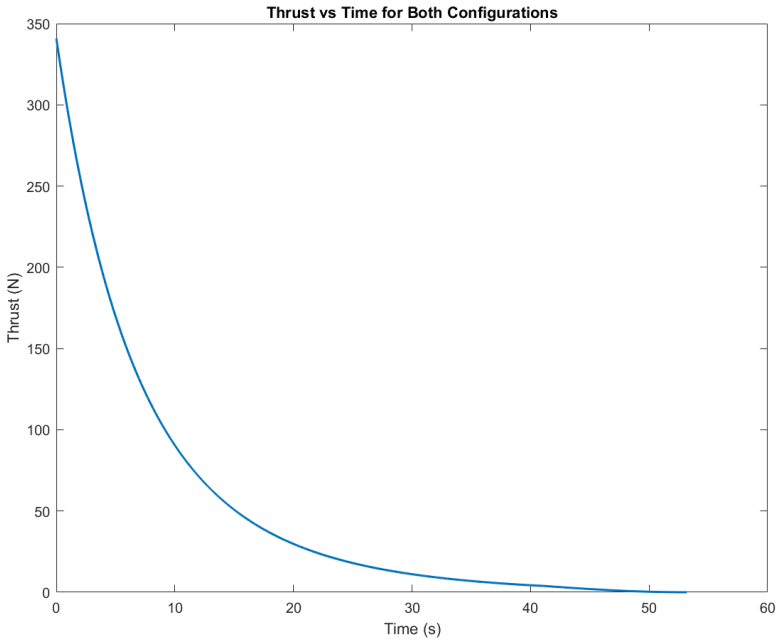

Figure 27: Thrust Change Over Time at 21,336 m (70,000 ft)

When discharging air at 70,000 ft, over 340.8 N of force is produced. This force gradually reduces to 0 N over a period of 53.2 seconds. The force is significant and can cause lateral and rotational motion of the launch mechanism depending where the tank and discharge valve is placed. This force could potentially be used to strategically maneuver the balloon and payload system. Especially since the tank can be pressurized multiple times to increase maneuverability.

2.3.4.2 Tank Filling Performance

The time to fill the air tank to the required mass in order to hover is an important performance parameter. If the time to fill the tank is long, then more power is required (gas or battery) and a longer wait time will be necessary before launching the rocket.

For the gasoline engine, the power produced decreases significantly with increased altitude due to the air density reduction [16]. It is possible to turbocharge the engine to allow the power produced to remain constant up to the critical altitude. While no design has been done on a turbocharger for the Honda GX200 engine, the Gudmundsson textbook reports that it is possible for some turbochargers to operate up to 7620 m (25,000 ft) [16]. Therefore, for the purpose of the performance analysis, the critical height of 7620 m (25,000 ft) will be assumed.

After the critical height is reached, the reduction in engine power can be determined using the Gagg-Ferrar Model as decribed by Gudmundsson and shown in Eq 46 [16].

$$P = P_{SL}(1.132(1 - 0.0000068756(h - h_{crit}))^{4.2561} - 0.132 \tag{46}$$

Where:

P : Engine power at altitude (hp)

P_{SL} : Engine power at sea level (hp)

h : altitude (ft)

h_{crit} : Critical altitude of the turbocharger (ft)

Furthermore, the volumetric flow rate of the pump is linearly related to the engine power. [21] Therefore, as the engine power decreases with altitude, so does the volumetric flow rate delivered by the air compressor. This can be modeled with Eq 47. Where the constant value is the volumetric flow rate (in m^3/s) per horsepower.

$$\dot{Q} \approx 0.0014 * P \tag{47}$$

Where:

$\dot{Q}$: Volumetric flow rate of air (m^3/s)

It should be noted that Eq 47 does not apply for the electric air compressor since the performance does not depend on altitude.

We can then obtain the mass flow rate of air through the pump at each altitude with Eq 48.

$$\dot{m}_{air} = \rho_{atm}\dot{Q} \tag{48}$$

Where:

$\dot{m}_{air}$: Mass flow rate of air (kg/s)

After determining the mass flow rate, the time to fill the air tank with the required mass to hover can be found using Eq 49. Note that this assumes that we are filling the tank at constant altitude which results in a constant mass flow rate.

$$t_{fill} = m_{air_{excess}}/\dot{m}_{air} \tag{49}$$

Where:

t_{fill} : Time to fill tank (s)

The time to fill at all altitudes beginning at the minimum operating altitude of 6.12 km (20,079 ft) is shown for the gas engine configuration in Figure 28.

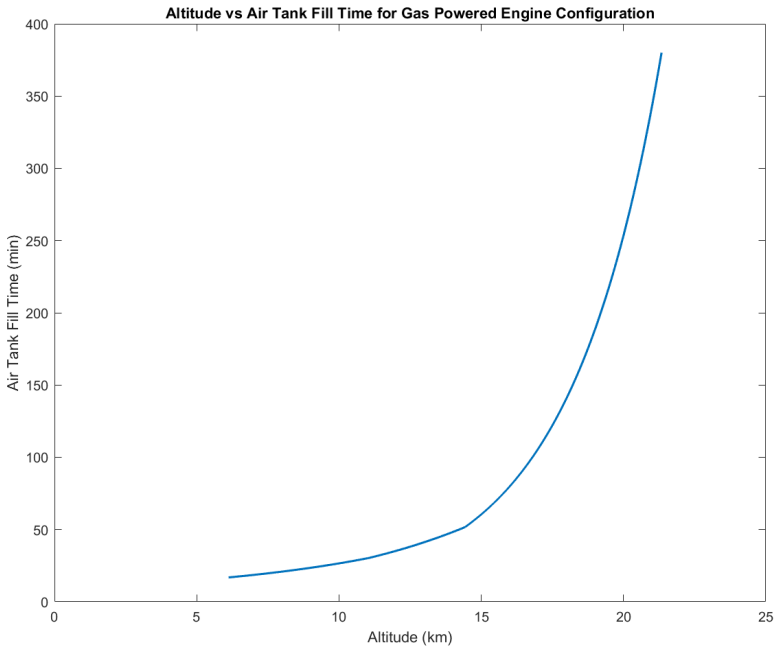

Figure 28: Air Tank Fill Time For Gas Powered Engine Configuration

The gas powered air compressor can fill the air tank in just 16.8 minutes at the minimum operating altitude. However, due to the large decrease in engine performance at high altitudes, the fill time increase significantly. At 21,336 m (70,000 ft), the time to fill the air tank is 380 minutes (6.3 hours).

For the electric compressor configuration, the tank can be filled at all altitudes. The time to fill the tank is shown in Figure 29. Note that with the electric air compressor, the volumetric flow rate does not change with altitude.

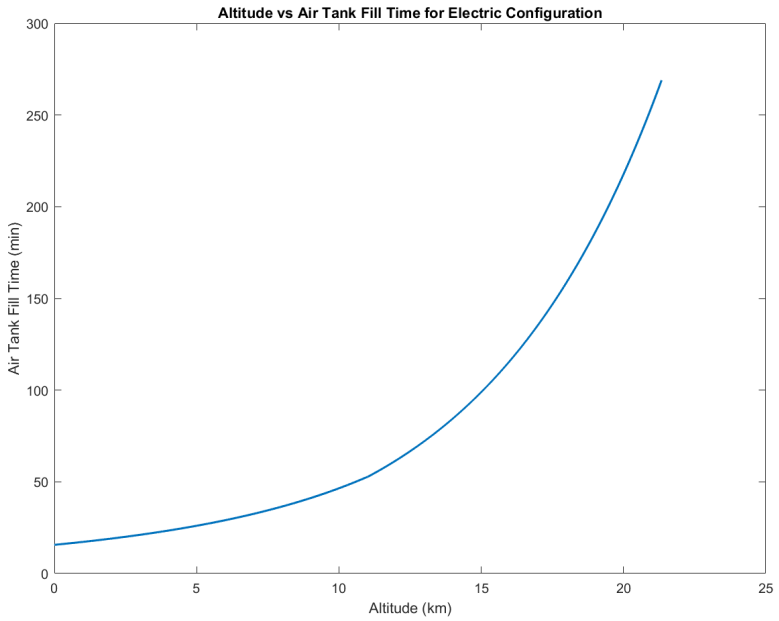

Figure 29: Air Tank Fill Time For Electric Configuration

At sea level, the time to fill the tank with the electric air compressor is 15.6 minutes. At the target altitude of 21,336 m (70,000 ft) the fill time increases to 269 minutes (4.5 hours).

Although the electric air compressor fills the tank faster at higher altitudes compared to the gas configuration, the time is still several hours long. One potential solution to mitigate this problem is to compress air as the balloon is rising to 70,000 ft. This would allow the tank to slowly fill and potentially contain the mass required to hover exactly at 70,000 ft.

2.3.5 Conclusion

From the preliminary analysis, controlling the balloon and payload position is feasible using an altitude control system. By adjusting the mass of air in a tank, the weight of the launch system can be changed resulting in control of the ascent/descent rate. Two methods of filling the tank were considered. The gas powered air compressor weighs significantly less than the electric configuration but takes significantly longer to fill the tank at high altitudes. The benefits of the electric air compressor is that it allows the control system to operate at all altitudes and fills the air tank quicker. However, there is a significant thrust

produced when the air is discharged. This may be leveraged in future designs for position and/or yaw control of the launch platform.

2.3.6 Future Work

Further work is required on integrating all the required components to the launch platform. It is also worth analyzing the feasibility of using solar panels to charge the batteries that power the electric air compressor. There are other systems on the rocket and launch mechanism that will require power, meaning solar panels may reduce the weight of batteries required. By examining how the ascent control system will be attached to the launch platform, a final decision can be made on the configuration to use (gas or electric). Analysis should be done on methods of utilizing the thrust produced by discharging air in order to control the launch mechanism. This could include adding a diverging nozzle to further increase the thrust produced. Furthermore, a computer system and electrical system that can control each component also needs to be developed. For the analysis of the electric system, the battery performance reduction due to decreased temperatures is ignored. Therefore, if this method is chosen, a battery heating system will need to be developed.

2.4 Dynamic Analysis of Launch System - Chaanasya Gowda

Peer Reviewed by: Sebastien Grondin

2.4.1 Launch Dynamics Introduction

The objective of this section is to address and obtain equations, along with solutions for the launching dynamics of the rocket using a weather balloon. The launch mechanism consists of a weather balloon, tethered at 4 points to the launch platform. The launch platform has the purpose of providing movability to set a specific launch angle. The platform is connected to the launch rail, where the rocket is held onto by lugs in the front and back for stable gliding across the rail.

The first task in performing a launch dynamic analysis on this system is to obtain the deflection angle from which the rocket departs the launch rail. This is done in order to determine how severe the deflection angle might result into, and if it is possible to be countered. This section will cover the approach to a more true representation of the free-body diagram of the launch mechanism, the mathematical theory, and the attempt performed to obtain differential equations representing the dynamic motion.

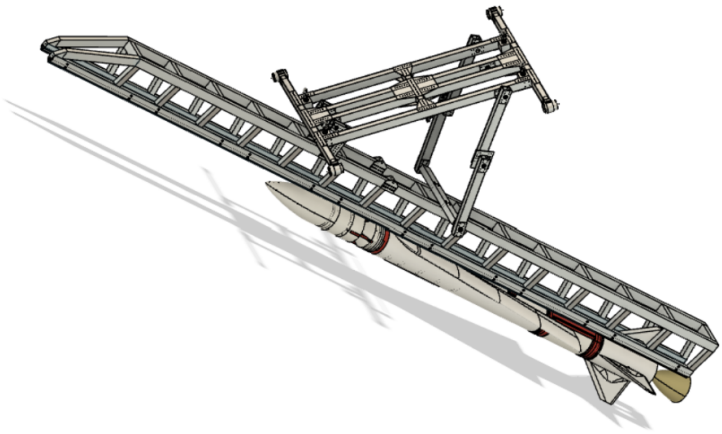

Figure 30: Launch platform, launch rail, and rocket design [22]

2.4.2 Free Body Diagram Comparison

In last year's report document, a free-body diagram was constructed with the assumptions that the rail and platform are a rigid solid piece. This assumption eliminates important dynamic motions that would have been produced as a result of the rockets' travel along the launch rail, and provides a simple free-body diagram as showcased in Figure 31. When thrust is applied by the rocket, it

moves along the launch rail, going against the friction produced by the rail and lugs on the rocket. When the rocket departs the rail, the thrust produces rotational movement (torque) from the center of mass of the entire system (including the balloon, launch platform and launch rail). This causes the rocket to leave at a deflected angle. Additionally, this dynamic model requires the calculation of the sliding motion of the rocket within the launch rail resulting from the applied thrust. This results in a more complicated dynamic analysis. The first goal in performing this dynamic analysis is to calculate the rocket's deflection angle, presenting a free-body diagram dedicated to finding that angle, as seen in Figure 32.

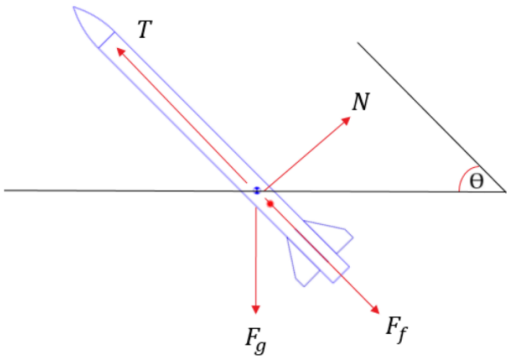

Figure 31: Last year's FBD for dynamic analysis [22]

The assumptions made while creating the free-body diagram were built upon from last year's report. However, the assumption of the launch platform being perfectly rigid and stable during the launching phase no longer applies in the new free-body diagram.

The assumptions for the new free-body diagram showcased in Figure 32 are as follows [22]:

- The thrust produced by the rocket is instantaneous and remains constant during the launch
- The thrust produced by the rocket is greater than the friction created by the guide rail against the rocket
- Ignoring air resistance and wind effects during the ascent phase
- "L" represents the length of the lever arm between the center of mass of the platform, rail, and balloon to the line of action (thrust)

- Link "L" is rigidly connected to the slider
- The 4 tethers that are connected to the platform and balloon act as a part of the rigid link
- Gravity at 70,000 ft is $9.81 m/s^2$ ($-0.006 m/s^2$ difference in gravitational acceleration is neglected)

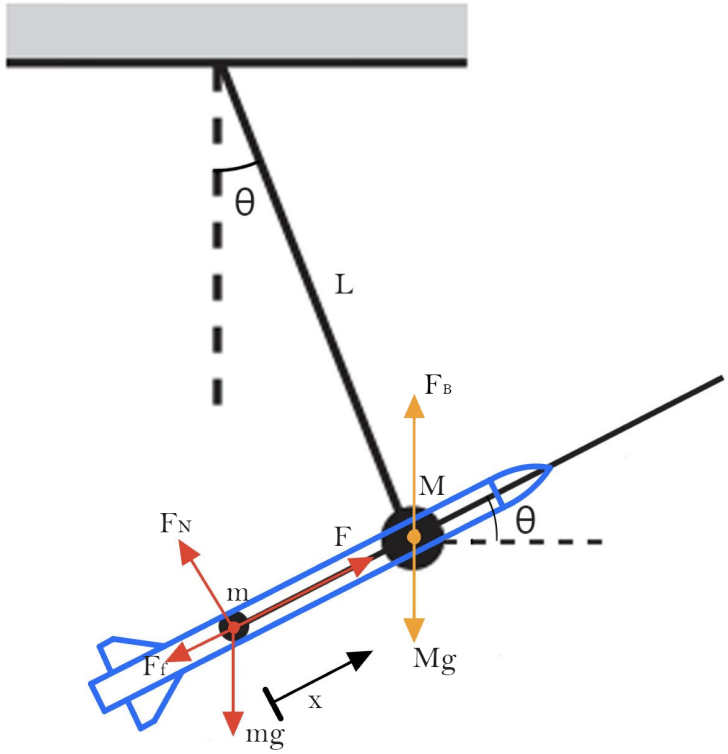

Figure 32: FBD to find the deflection angle (modified) [23]

Where:

- L: is defined as the length of the lever arm between the combined center of mass (balloon, platform and launch rail) and the thrust's line of action
- M: is defined as the combined mass of the balloon, platform, and launch rail
- m: is defined as the mass of the rocket
- g: is defined as gravity
- F: is defined as the thrust force

- F_N: is defined as the normal force of the rocket
- F_f: is defined as the coefficient of friction along the launch rail
- F_B: is defined as the bouyancy force
- θ: identifies as the angle of deflection of the rocket
- x: identifies as the distance travelled by the rocket across the launch rail

To clarify the direction of F_N, the rocket is held onto by lugs from the launch rail, therefore indicating that there is an upward force preventing the rocket from free-falling. This upward force would be defined as the normal force, F_N.

2.4.3 Theory and Analytical Solution

Newtonian Mechanics

Upon analyzing the free body diagram presented in Figure 32 it becomes evident that attempting a Newtonian method of solution would be difficult. This is due to the nature of solutions that are required by Newtonian mechanics. Using this method would require force calculations acting on the pendulum, specifically the gravitational force, and tension. Additionally, the thrust and gravitational forces acting on the slider mass (represented as the rocket) and the slider rod's (represented as the launch rail) gravitational force would have to be considered. Taking into account all these different force applications, further calculations and relations would have to be performed in order to understand how the forces would be applied to the pendulum and the slider, and slider rod simultaneously.

Lagrangian Mechanics

In order to solve the free-body diagram presented in Figure 32 above, the use of Lagrangian Mechanics would be beneficial. Lagrangian Mechanics works with the application of a generalized coordinate system. This allows dynamic motions to be defined through kinetic and potential energies only. In this system, the kinetic energy would include the dynamic motion of the pendulum and slider simultaneously, while the potential energy would account for the gravitational energy produced by the pendulum, slider and slider rod. An important fundamental principle to acknowledge concerning Lagrangian mechanics is the principle of stationary action (or Hamilton's principle), which states that the particle always follows the path of least energy consumption [24]. The basic Lagrangian equation is the defined as the difference between the kinetic and potential energies, as stated in Equation 51.

Force Application and the Rayleigh Dissipation Function

An important point to note is that Lagrangian Mechanics does not directly account for forces, it only focuses on the kinetic and potentional energy of a system. Acknowledging that in this system, there is an external force (thrust) being applied on the rocket, a buoyancy force and a friction force being produced against the launch rail and rocket. However, it should be emphasized that the friction force in particular is a non-conservative force that dissipates energy. Non-conservative forces that dissipate energy cannot be directly applied into a Lagrangian equation, but rather be applied through the use of the Rayleigh dissipation function.

The Rayleigh dissipation function, shown in Equation 50 represents how the friction would be applied to fit the dynamic motion equations. Variable "s" is expressed as the damping coefficient. Acknowledging that the damping coefficient is not currently known, the friction force will be treated as a non-dissipative non-conservative force. This will be demonstrated in the solution below. Thrust and buoyancy force on the other hand increases the energy within a system, and does not dissipate, and can therefore be implemented as is after obtaining the Lagrangian equations. Considering that the friction would be treated the same as the thrust and bouyancy force, the friction force would also be added as is. The solution to the free-body diagram represented in Figure 32 is given below.

The Rayleigh Dissipation Function:

$$F_{diss} + \frac{1}{2} s\dot{x}^2 \tag{50}$$

The Lagrange Equation:

$$L = KE - PE \tag{51}$$

With the guidance of a Harvard solution (modified), equations for positions of the masses and their speeds can be obtained [23]:

$$(x, y)_M = (L\sin\theta - L\cos\theta)$$

Their velocities are defined as the derivative of x with respect to time:

$$(x, y)_m = (L\sin\theta + x\cos\theta, -L\cos\theta + x\sin\theta)$$

$$v_M^2 = L^2 \cdot \dot{\theta}^2$$

$$v_M^2 = v_{M,x}^2 + v_{M,y}^2$$

$$v_{M,x}^2 = \frac{dx}{dt}((L\sin\theta)^2 = L\dot{\theta}\sin\theta$$

$$v_{M,y}^2 = \frac{dy}{dt}((-L\cos\theta)^2 = -L\dot{\theta}\cos\theta$$

$$v_M^2 = (L\dot{\theta}\sin\theta)^2 + (-L\dot{\theta}\cos\theta)^2 = L^2 \cdot \dot{\theta}^2$$

$$v_m^2 = v_{m,x}^2$$

$$v_{m,x}^2 = \frac{dx}{dt}((L\sin\theta + x\cos\theta)^2 = L\dot{\theta}\sin\theta + \dot{x}\dot{\theta}\cos\theta$$

$$v_m^2 = (L\dot{\theta}\sin\theta + \dot{x}\dot{\theta}\cos\theta)^2 = \left(L\dot{\theta} + \dot{x}\right)^2 + x^2\dot{\theta}^2$$

Solving for kinetic and potential energy:

$$KE = \frac{1}{2}mv^2, PE = mgh$$

$$KE = \frac{1}{2}ML^2\dot{\theta}^2 + \frac{1}{2}m((L\dot{\theta} + \dot{x})^2 + x^2\dot{\theta}^2)$$

$$PE = MgL\cos\theta + mg(-L\cos\theta + x\sin\theta)$$

This produces the Lagrangian Equation:

$$L_{lag} = \frac{1}{2}ML^2\dot{\theta}^2 + \frac{1}{2}m\left(\left(L\dot{\theta} + \dot{x}\right)^2 + x^2\dot{\theta}^2\right) + MgL\cos\theta + mg\left(L\cos\theta - x\sin\theta\right) \tag{52}$$

Applying thrust, friction and buoyancy forces into the equation and solving for the Euler-Lagrange equations:

$$Q_x = F - c\dot{x}$$
$$Q_y = F_B$$

$$\frac{d}{dt}\left(\frac{\partial L}{\partial \dot{x}}\right) - \frac{\partial L}{\partial x} = Q_x$$

$$\frac{d}{dt}\left(\frac{\partial L}{\partial \dot{\theta}}\right) - \frac{\partial L}{\partial \theta} = Q_y$$

After applying the Euler-Lagrange equations, the final 2 dynamic motion equations are obtained:

$$\ddot{x} = \frac{F}{m} - L\ddot{\theta} + x\dot{\theta}^2 - g\sin\theta - \frac{c}{m}\dot{x} \tag{53}$$

$$\ddot{\theta} = \frac{LF - 2mx\dot{x}\dot{\theta} - mLx\dot{\theta}^2 - mLg\sin\theta - Lc\dot{x} - (M+m)gL\sin\theta - mgx\cos\theta + F_B L\sin\theta}{(M+m)L^2 + mx^2} \tag{54}$$

The constant values and variable definitions can be summarized as followed:

Variables:

- x: Horizontal displacement of the slider [m]
- $\dot{x}$: Velocity of the slider in the horizontal direction $[m/s]$
- $\ddot{x}$: Acceleration of the slider in the horizontal direction $[m/s^2]$
- θ: Angle of pendulum measured from vertical $[rad]$
- $\dot{\theta}$: Angular velocity of the pendulum $[rad/s]$
- $\ddot{\theta}$: Angular acceleration of the pendulum $[rad/s^2]$

Constants:

- L: length of the lever arm between the combined center of mass (balloon, platform and launch rail) and the thrust's line of action $[2.59m]$
- M: Combined mass of the balloon, platform, and launch rail $[634.2kg]$
- m: Mass of the rocket $[164.53kg]$
- g: Gravity $[9.81m/s^2]$

- c: Coefficient of friction along the launch rail [0.2] [1]
- F: Thrust force acting on m in the slider direction [10653N]
- F_B: Buoyancy force acting on M [11428N] (Provided by Noah)

2.4.4 MATLAB - Simulink Solutions

From Equations 53 and 54 derived from the Lagrange, SimuLink was used and a model was created to express the two equations. Based off this model and the constant values provided above, the simulation was performed against multiple initial launch angles from the horizontal. Figure 33 portrays the Simulink diagram resulting from Equations 53 and 54.

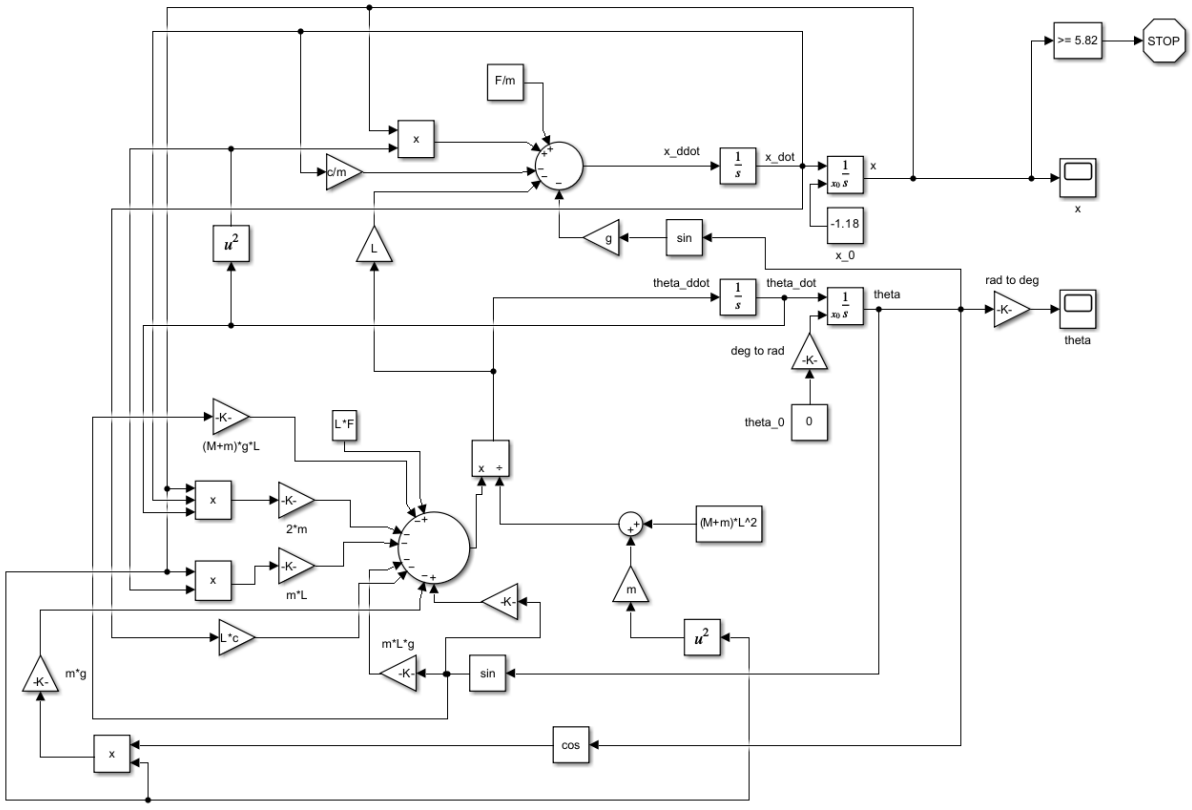

Figure 33: Simulink Diagram from Equations 53 and 54

Through this solution, various initial launch angles were inputted into Simulink

and was executed to obtain various deflection angles that would result from the thrust, friction, gravitational, and buoyancy forces. Figure 34 below provides the scope output of an initial launch angle of 0° from the horizontal. Additionally, Figure 35 presents various initial launch angles that are plotted against resultant angles (when the rocket departs).

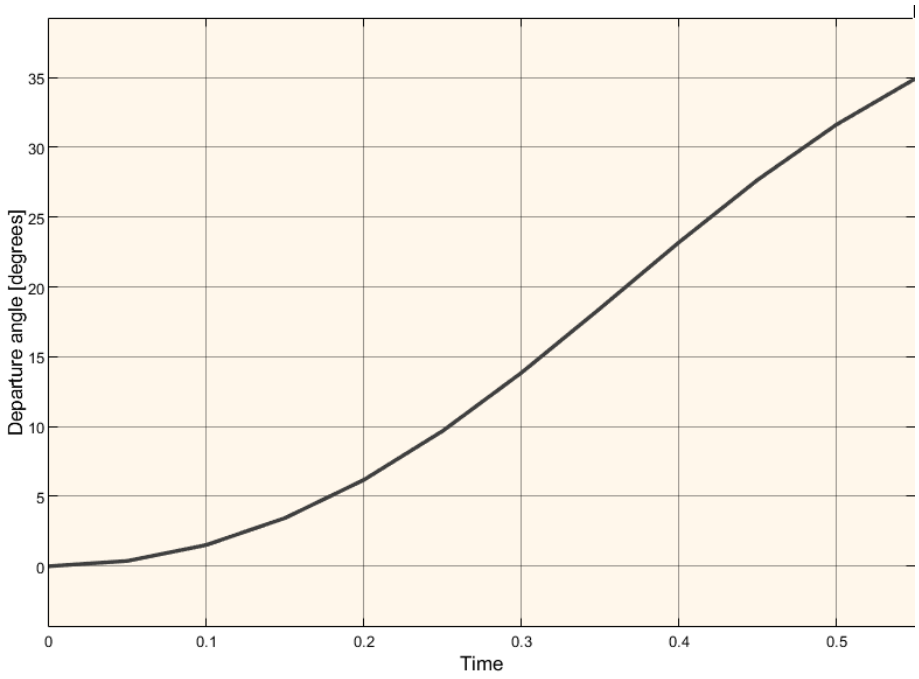

Figure 34: Resultant angle (rocket leaving launch rail) from a 0° initial angle

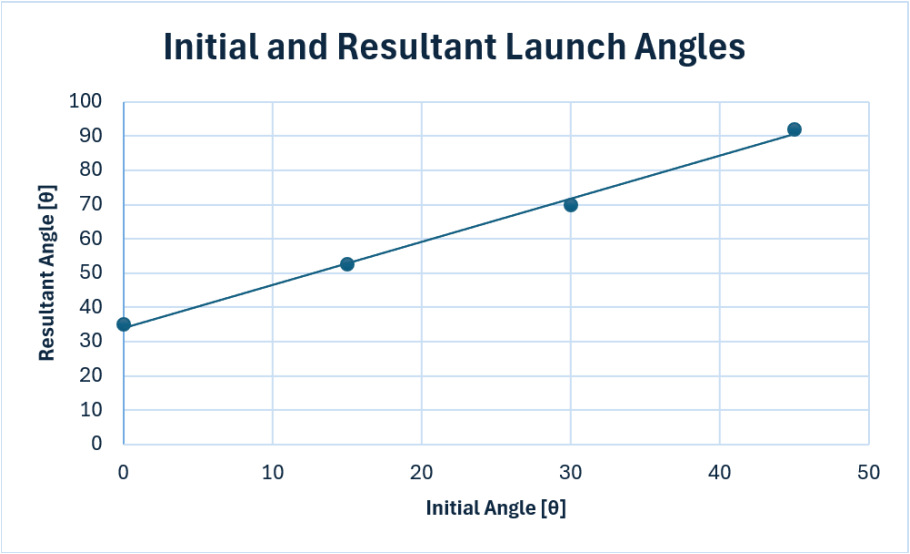

Figure 35: Resultant angle (rocket leaving launch rail) from initial launch angles of 0°, 15°, 30°, and 45°

.

2.4.5 Future Work

The Next Step:
The next step to obtain a more accurate dynamic representation of the rotation of the launch system is to incorporate the Rayleigh Dissipation Function for friction into the analysis. Currently, the friction force is applied as a non-conservative non-dissipative force, and should be replaced to ensure the accountability of dissipative energy within the system. This requires obtaining a damping coefficient which will be the main goal for next term.

Countering the Deflection:
In terms of the deflection of the launch system, from Figure 35, it can be noticed that the launch rail deflection angle is significant. To prevent this deflection, there are a few ways to counteract it. The first solution would be to have a counter plate that the thrust of the rocket would push off on. This would apply a force onto the rail pushing it backwards as the rocket leaves the rail. This would potentially reduce the deflection angle produced by the thrust and friction produced by the rocket against the launch rail. However, analysis is yet to be done to asses the extent of its impact in reducing the deflection.

The second, more straightforward solution would be to start at a lower angle, so that the rocket can reach the desired launch angle by the time it leaves

the launch rail. However, due to the simplifications and assumptions made for this analysis, it would be difficult to accurately estimate the starting launch angle to obtain the final departure angle of the rocket leaving the launch rail. This solution however would be simple as it would not require additional materials implemented onto a heavy launch system design. In the future, more analysis, research and calculations can be perform to figure out the most feasible and efficient solution.

2.5 Launch Platform Structure - Jake Birkness

Peer Reviewed by: Tristan Osena

The focus of this report will be on the structure of the launch platform and launch rail. A discussion of the design of the launch platform and launch rail will be provided, as well as a strength analysis of certain launch platform components.

2.5.1 Introduction to Launch Platform Structure and Analysis

The launch platform refers to the assembly that mounts to the launch rail and is tethered to the ascent balloon with swivel hoists. The launch platform is shown in an isolated view and mounted to the launch rail in Figure 36 (A) and (B) respectively.

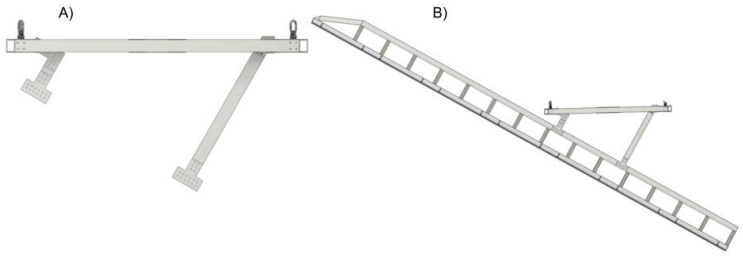

Figure 36: Launch Platform Isolated (A) and Mounted to Launch Rail (B)

The key component names that will be mentioned in this report are outlined in Figure 37 below. Please refer to Figure 37 if there is any uncertainty about the component being discussed for the remainder of this report.

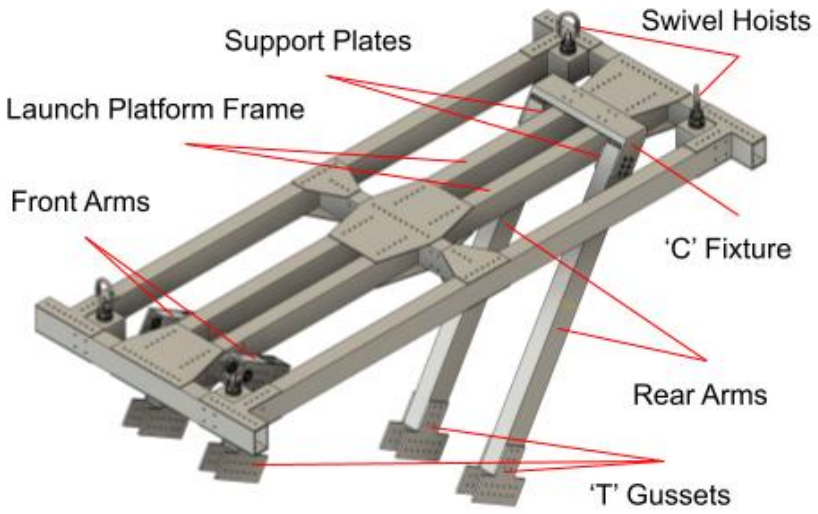

Figure 37: Labelled Components of Launch Platform

This report will first explain a significant design change that was made to the launch platform, which involved the removal of the deployment mechanism in favor of fixed mounting at the desired launch angle.

The first analysis done on the launch platform is a tensile stress analysis of the 'C' fixture. Next, an analysis of buckling in the frame of the launch platform will be discussed, involving both analytical and simulation models.

Finally, this report will discuss the addition of mounting holes and bolts to the launch rail to allow for the assembly of cross-beams and endplates. The strength of these fixtures will not be analyzed, but this will be investigated in the future.

2.5.1.1 Summary of Midterm Report Conclusions

The midterm report focused on the strength of two components, the swivel hoists and the rail guides. The swivel hoists are shown in Figure 37 above, and the rail guides are shown in Figure 38 below.

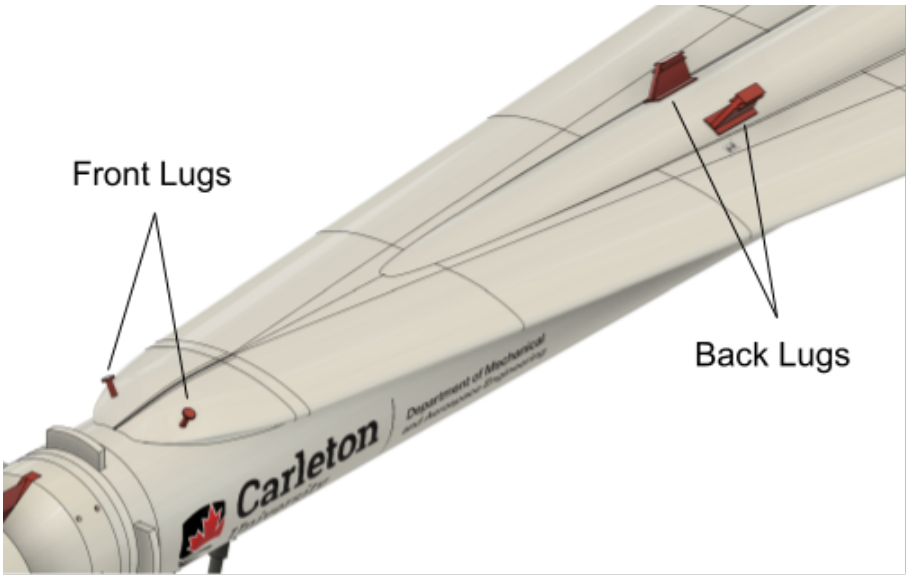

Figure 38: Front and Back Rail Guides on Rocket

The shear strength of the swivel hoists was analyzed under tension from the balloon tethers and complete launch assembly. This was done because the distributor of the swivel hoists did not provide justification for the weight limit of the hoists. Though the swivel hoist material and shear strength was difficult to accurately obtain, a relatively low shear strength of steel was assumed. This low strength was sufficient for the current tensile load expected in each swivel hoist. The distributor provided a weight limit of 1050 lbs (476 kg) [25], and the shear strength analysis provided a weight limit of approximately 1670 lbs (757 kg). The discrepancy is likely due to a different failure method of the swivel hoists driving the distributor's weight limit, as well as sources of error due to simplifying assumptions in the analytical model (e.g., perfect material microstructure).

The strength of the rail guides was only considered in tension for the midterm report. This was because the initial configuration had the rocket and launch rail stowed along the horizontal during the ascent phase. However, since the rocket will be stowed in an angled configuration with the new fixed launch platform, shear stress will need to be taken into account. The strength of the rear rail guides will likely depend on the strength of the fixtures used to mount the rail guides to the body of the rocket. Currently, they are welded to the rocket frame. Once the rocket frame has been updated for this year's design, the strength of the weld or modified fixture will be investigated.

2.5.2 Fixed Launch Platform

The main design change that was implemented this term is the removal of the deployment mechanism used to lower the launch rail from a horizontal, stowed position to an angled position that is ready for launch. This mechanism was replaced with a fixed structure that holds the rocket at the desired launch angle. This section will first discuss three reasons for the design change. Then, the new design will be explained and the important components that were modified or added will be discussed. Finally, the implementation of launch angle control will be discussed in connection with the work done by Tristan Osena in Section 2.5 of this report.

2.5.2.1 Reasons for Fixed Launch Platform

Justification for Previous Year's Design

To investigate the need for the deployment mechanism, the justification used for the mechanism from the previous year's report was obtained. One justification provided was that, "the folding structure allows the launch platform to take up less space when compared to a fixed structure." [1]. While this may simplify the process of assembling the launch assembly to the balloon, it would not change the effect of gust loads, as the surface area of the launch assembly is the same.

Another justification used in the previous year's report was that, "for a fixed structure, the launch rail would have to be held up at the launch angle by an external structure to allow for the launch platform to remain parallel to the ground." [1]. While it is difficult to understand the specific reason of how this conclusion was determined, one possible reason is due to concern over the location of the center of gravity of the combined launch rail and rocket. If the center of gravity is offset from the center of the launch platform, as shown in Figure 39, the launch platform would want to rotate to align the center of gravity with the center of the launch platform, so that the weight is distributed equally onto the four balloon tethers.

This behaviour could possibly be prevented by ensuring equal lengths of the balloon tethers, which would deliver a large amount of tension to each of the swivel hoists on the launch platform and prevent any pitch rotation of the launch platform. Regardless, the center of gravity should still be aligned with the center of the launch platform during ascent to attempt to keep the tension in each tether relatively equivalent. However, this can simply be accomplished by shifting the location where the launch platform is mounted to the launch rail based on the location of the center of gravity of the combined launch rail and rocket. This shift is shown in Figure 39 below. The center of gravity of the combined launch rail and rocket was not considered in the launch assembly design for this term, but it will be considered once the mass distribution of the rocket is updated.

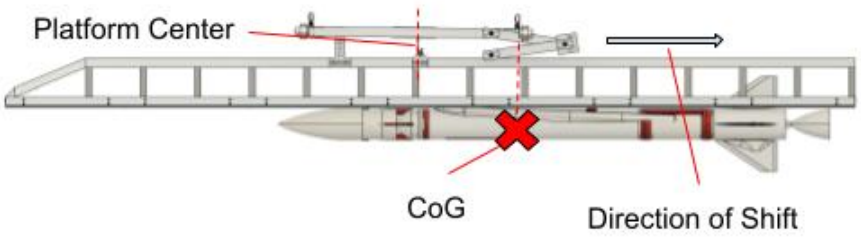

Figure 39: Shift of Launch Platform Position and CoG Alignment

Complexity of Manufacturing and Assembly

One of the clear benefits of using a fixed launch platform is the reduction of manufacturing and assembly complexity. The previous year's deployment mechanism used 30 bearings, which each required bored holes with precise tolerances to allow a tight fit. The new fixed launch platform uses only 8 bearings, which are kept to allow the future addition of the pitch control mechanism designed by Tristan Osena. This will be discussed further in Section 2.4.2.2. While the fixed platform does involve more bolts and support plates (gussets), the holes required and installation process for these fixtures is simpler than the installation of the bearings.

Another simplification that the fixed launch platform allows for is the removal of the pins and hooks used to keep the launch rail in the stowed, horizontal position. There is currently no mechanism for actually removing the pins, which would need to be designed and added to the platform. It is important to consider that if the release of a single pin fails, then the rocket would have to be launched without an initial angle, which could cause significant issues in the trajectory control of the rocket. The fixed launch platform does not involve any mechanisms for an initial launch angle to be achieved.

Increased Load of Deployment Impulse

One of the major design concerns of the previous year's deployment mechanism was the shock load caused by the sudden deceleration of the falling launch rail and rocket. It is difficult to estimate the precise impulse load caused by the lockout of the deployment mechanism. However, to demonstrate that there would be a considerably large impulse loaded on the launch platform, a simplified model was developed. This model only considers a deceleration and impulse in the vertical direction.

The first step is to estimate the velocity of the combined launch rail and rocket when the mechanism reaches its maximum length. To do so, it is assumed that the center of gravity would be in the center of the launch platform. The vertical

distance travelled by this point can be measured by finding the distance between the launch platform and the launch rail in both the horizontal and angled configurations. These measurements were found to be 177.8 mm and 1021.6 mm respectively, as shown in Figures 40 and 41 below. Please note that the rocket body appears to be in the center of the launch platform, but this would not be the case if the launch platform is mounted to the rail along the center of gravity of the assembled launch rail and rocket. This is because the launch rail is much heavier than the rocket.

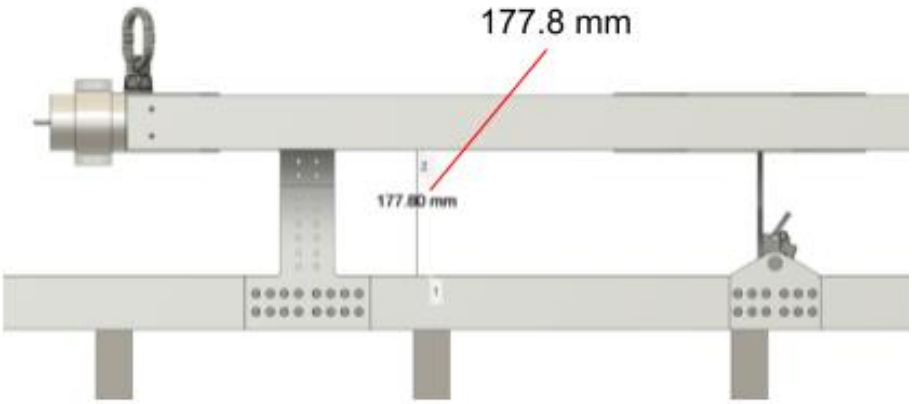

Figure 40: Stowed Distance Between Launch Platform and Rail

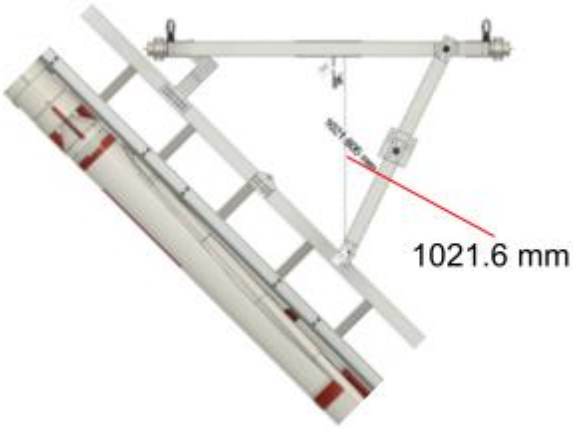

Figure 41: Deployed Distance Between Launch Platform and Rail

From the measured distances, the launch rail can be estimated to travel 843.8 mm, or 0.8439 m. The vertical velocity of the launch rail can be calculated using the kinematic equation shown in Equation 55 below. The launch rail is assumed to accelerate at 9.81 m/s^2, and the resultant velocity is estimated to be 4.07 m/s.

$$v_z = \sqrt{2 * a_z * \Delta z} = \sqrt{2 * (9.81\ m/s^2) * (0.8438\ m)} = 4.07\ m/s \tag{55}$$

Next, the impulse delivered to the launch platform by the sudden deceleration of the launch rail can be estimated using the impulse-momentum theorem, which is shown in Equation 56 below [26]. The impulse was estimated to be 2702 $kg * m/s$.

$$J_z = m\Delta v_z = (664\ kg) * (4.07\ m/s) = 2702\ kg * m/s \tag{56}$$

Using this impulse, the average force can be estimated. This calculation is difficult because the actual duration of the deceleration is unknown. However, for the purpose of demonstrating that the impulse-load would introduce significant design concerns, the duration of the deceleration is assumed to be 0.1 s. This is assumed based on the lack of damping in the deployment mechanism, which would cause a very rapid lockout of the mechanism. The average force caused by the estimated impulse with a duration of 0.1 s is estimated to be 27 kN, as shown in Equation 57 below.

$$F_{ave} = \frac{2702\ kg * m/s}{0.1\ s} = 27020\ N \cong 27kN \tag{57}$$

While this average force cannot be used to inform structural design because of the simplifying assumptions made, it is roughly four times the static load on the launch platform from the combined weight of the launch rail and rocket. This means that to achieve the same factor of safety for the strength of the launch platform, the beams, support plates, and fixtures would have to be increased in size or number. Another option would be to introduce damping into the deployment mechanism by having part of the mechanism surrounded by a viscous fluid. This would result in substantial complexity of assembly. The thermal considerations of the fluid would also have to be considered.

Summary of Reasons for Fixed Launch Platform

In conclusion, the deployment mechanism of the launch platform has been re-

placed with a fixed launch platform that is mounted to the launch rail at the desired launch angle. This was done because of limited justification provided for the need of the mechanism, because of the reduced design complexity of the fixed platform, and because of the elimination of the impulse caused by the sudden deceleration of the launch rail.

2.5.2.2 Preliminary Fixed Launch Platform Design

The changes to the design of the launch platform are primarily to the rear arms of the launch platform, as shown in Figure 37. The coupled arms used in the previous year's design were replaced with single rigid arms that are fixed to the launch platform frame at the top and to the launch rail at the bottom. The preliminary fixed launch platform holds the launch rail at an angle of 30 degrees, which is the angle used in the dynamic launch analysis performed by Chaanasya Gowda in Section 2.3. This can easily be adjusted by changing the length of the rear arms.

The rear arms are cut at 30 degrees on one end to allow clearance when mounting to the launch frame. A chamfer was added to the cut end to remove the sharp edge, as this could become dangerous for the person doing the launch platform assembly. The chamfered edge of a single rear arm is shown in Figure 42 below.

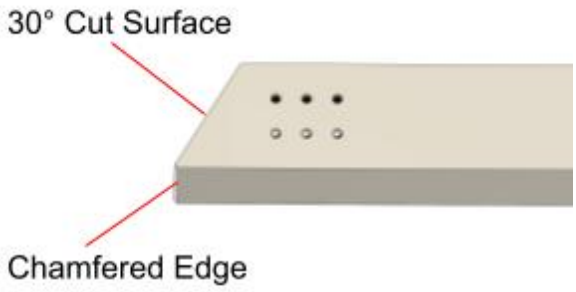

Figure 42: Chamfered Edge of Cut Surface on Rear Arm

The arms were previously mounted to the launch rail using a rigid connector bar. This connector bar was replaced with four T-gussets, in the same configuration used for the front arms in the previous design. As discussed in Section 2.4.2.1, the location where the gussets are bolted to the launch rail can be adjusted to keep the center of gravity of the combined launch rail and rocket at the center of the launch platform frame during ascent. The mounting of the front and rear launch platform arms to the launch rail is shown in Figure 43 below. Though

they are not shown, the gussets are mounted using 1/4" bolts and locknuts.

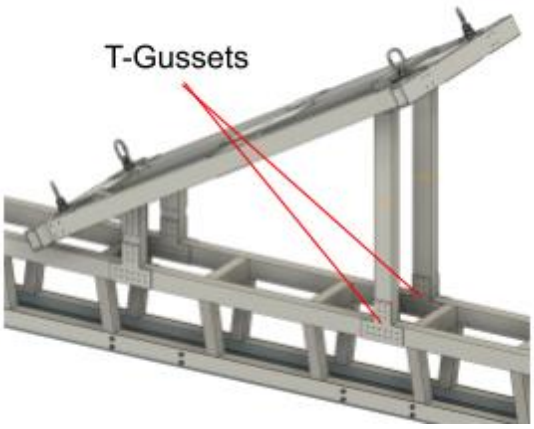

Figure 43: T-Gussets Used for Mounting Launch Rail to Launch Platform

The rear arms were previously mounted to the launch platform frame using pinned bearings on each side. These bearings have been replaced with a 'C'-shaped fixture to which the rear arms are bolted, as shown in Figure 44. Six bolts on each arm were used to mount the arms to the 'C' fixture. This number is the same as the fixtures used in the mounting to the launch rail. However, the number of bolts used may be refined based on future strength analysis. A chamfered edge was added to the 'C' Fixture to remove the sharp edge and make the assembly process safer.

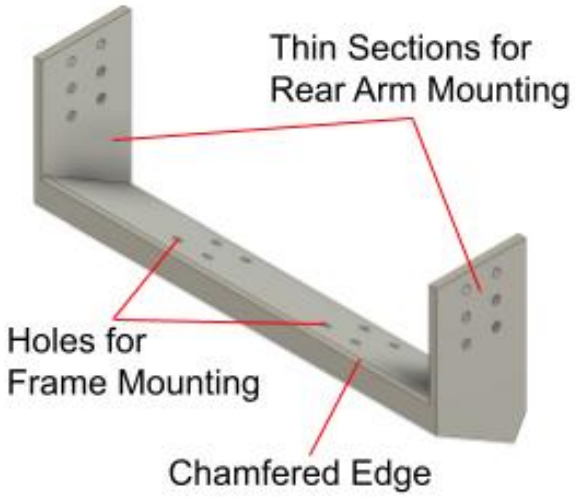

Figure 44: 'C' Fixture Used for Mounting Rear Arms to Launch Platform Frame

It is unlikely that the stainless steel bolts will experience shear failure. Instead, the bolts would likely tear through the weaker and thinner aluminum. To prevent bolt tear, the recommendations for bolt hole locations and spacing from AISC were followed [27]. The key recommendation followed is for the hole locations to be at minimum 1.5x the hole diameter from any adjacent edges. Since the holes used are 1/4" diameter, the bolt holes in the rear arms and 'C' fixture are located 3/8" from the nearest edges.

To increase the distribution of the compressive stress imposed on the aluminum rear arms by the bolts and locknuts, a support plate is used on either side, in a similar method to the sets of T-gussets used to fix the arms to the launch rail.

The 'C' shape allows the load of the combined launch rail and rocket to be distributed on the launch platform frame. The 'C' fixture is currently fixed to the launch platform frame using four bolts on each side. These bolts provide support in the horizontal directions, while the launch platform frame bears the vertical load. The load on the frame is considered in Section 2.4.4 of this report to ensure the hollow frame beams will not buckle under compression.

While the 'C' fixture is currently rigidly mounted to the launch platform frame, this can be changed to allow for a small amount of launch angle, or pitch angle, control. This will be accomplished by replacing the rear arms with the actuator mechanism being designed by Tristan Osena, as discussed in Section 2.5. Due to this future design change, the front arms were left with bearings in the same configuration as the previous design to allow for angular movement of the

launch rail.

2.5.3 Tensile Analysis of 'C' Fixture

For this analysis, and all future analyses in this report, the combined mass of the launch rail and rocket is estimated to be 664 kg. This is based off of the previous year's launch rail and wet rocket masses. The load is estimated to be 1630 N, which is approximately 1/4 of the combined weight of the launch rail and rocket. This assumes that the weight is evenly distributed on each of the four launch platform arms. This assumption may not be accurate as the center of gravity shifts after engine ignition, or even based on the static load distribution during ascent. However, if a large enough factor of safety is obtained, this would allow the conclusion that the failure mode being investigated will not occur.

A portion of the combined weight of the launch rail and rocket is loaded in tension onto the sides of the 'C' fixture, as shown in the free body diagram in Figure 45 below.

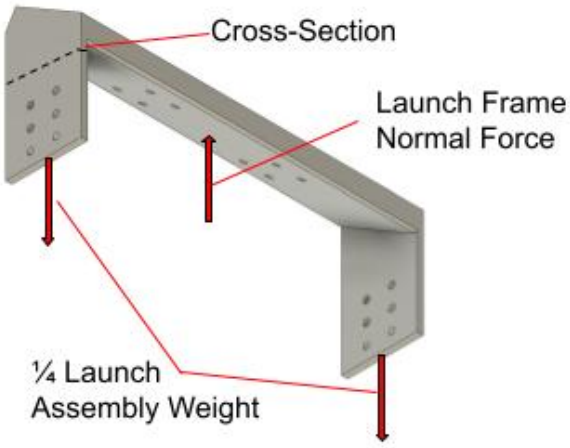

Figure 45: Tensile Loads on 'C' Fixture

To ensure that the width of the thin sides of the 'C' fixture is sufficient to bear the tensile stress of the launch assembly weight, an analytical stress analysis was conducted. The load is assumed to pass perpendicularly to the cross section.

The tensile stress can be calculated based on the area of the cross-section and the load specified. The tensile stress in this thin section was estimated to be 3.37 MPa, as shown in Equation 58 below.

$$\sigma = \frac{F_{tension}}{A_{cross\ section}} = \frac{1630\ N}{(76.2\ mm) * (6.35\ mm)} = 3.37\ MPa \tag{58}$$

This tensile stress provides a factor of safety of 82, based on a yield strength of Aluminum 6061 of 276 MPa [28]. This factor of safety is substantial, and it can be concluded that the thin sections of the 'C' fixture will not experience tensile failure.

2.5.4 Buckling Analysis of Launch Platform Frame

The 'C' fixture imposes a compressive load on the launch platform frame, as shown in the free body diagram in Figure 46 below.

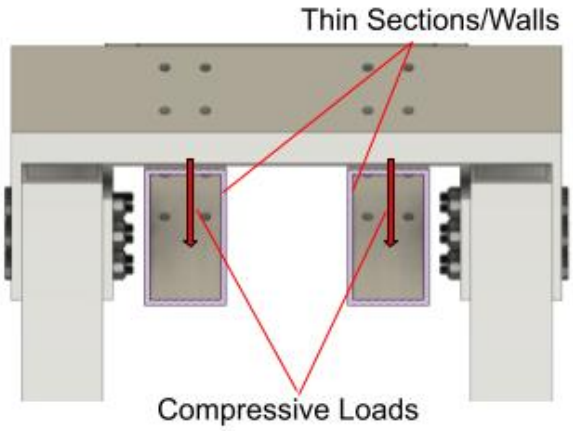

Figure 46: Compressive Loads on Launch Platform Frame

Due to the compressive load, a buckling failure of the thin walls of the aluminum frame becomes a concern. A buckling analysis was conducted to determine the factor of safety of the frame under the static load of the combined weight of the launch rail and rocket.

2.5.4.1 Analytical Model of Launch Platform Frame Buckling

An analytical buckling model was conducted by assuming that the thin walls of the frame are simply-supported plates. The simply-supported plate model is shown in Figure 47 below.

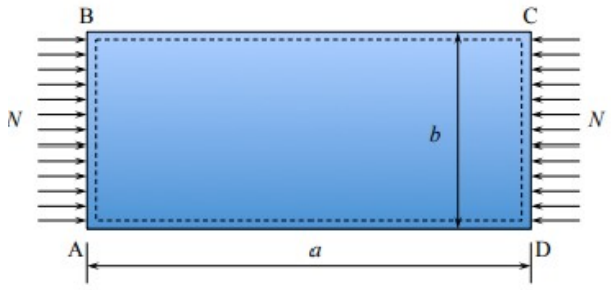

Figure 47: Simply-Supported Plate Under Compression [29]

This model ignores the support provided by sections of the frame that are not directly loaded by the 'C' fixture, but provides a method of estimating the load under which the walls will buckle. The parameters shown in Figure 47 above, as well as the material properties of the frame are the following:

- $a = 69.85\ mm$
- $b = 87.99\ mm$
- $N = 814\ N$
- $thickness\ (t) = 3.175\ mm$
- $v = 0.33$
- $E = 68.9\ GPa$

The critical force per meter that will cause the walls to buckle can be calculated using the formula shown in Equation 59 below [29].

$$N_c = k_c \frac{\pi^2 D}{b^2} \tag{59}$$

The 'D' term in Equation 59 is the flexural rigidity of the simply-supported plate. The flexural rigidity can be calculated based on the elastic modulus and moment of inertia, as shown in Equation 60 below. This formula is based on the moment of inertia of a rectangular cross-section. The flexural rigidity of the frame is estimated to be $20.36\ N * m^2$.

$$D = \frac{E}{(1 - v^2)} * \frac{bt^3}{12} = 20.36\ N * m^2 \tag{60}$$

It is important to note that only the first buckling mode (1/2 wavelength) is considered for this analysis. This is because the ratio of the plate length ('a' parameter) to the plate width ('b' parameter) is less than 1. With this ratio, the maximum number of half waves that will fit into the buckling failure is 1 [29]. The k_c term in Equation 59 is the buckling coefficient, which is calculated to be 4.22, as shown in Equation 61 below.

$$k_c = (\frac{b}{a} + \frac{a}{b})^2 = (\frac{87.99}{69.85} + \frac{69.85}{87.99})^2 = 4.22 \tag{61}$$

These values can be used to estimate the critical load that will cause buckling of the frame. The critical load was estimated to be 9.63 kN, as shown in the calculation below.

$$N_c \; per \; m = k_c \frac{\pi^2 D}{b^2} = 4.22 \frac{\pi^2 * 20.36 \; N * m^2}{(0.08799 \; m)^2} = 109470 \; N/m \tag{62}$$

$$N_c = (N_c \; per \; m) * (b) = (109470 \; N/m) * (0.08799 \; m) = 9632 \; N \cong 9.63 \; kN \tag{63}$$

The factor of safety can be estimated by comparing the compressive load of the launch assembly on the launch frame to the critical load calculated above. The factor of safety based on the analytical buckling model was found to be 11.8.

2.5.4.2 Simulation Model of Launch Platform Frame Buckling

The next step in the buckling analysis is to conduct a finite element analysis simulation of the compressive loading on the launch frame. Two models were considered in simulation to support the results of the analytical buckling model. Both models were simulated using the Structural Buckling feature in Fusion 360.

First, a rectangular plate was simulated in the same configuration as the load and constraints shown in Figure 47 above. This plate geometry is the same as the thin wall of the launch frame. The load applied is 815 N, which is approximately 1/8 of the combined weight of the launch rail and rocket. This simulation converged to a factor of safety above the applied load of 283.8. Figure 48 below shows the deformation experienced by the plate under the compressive load.

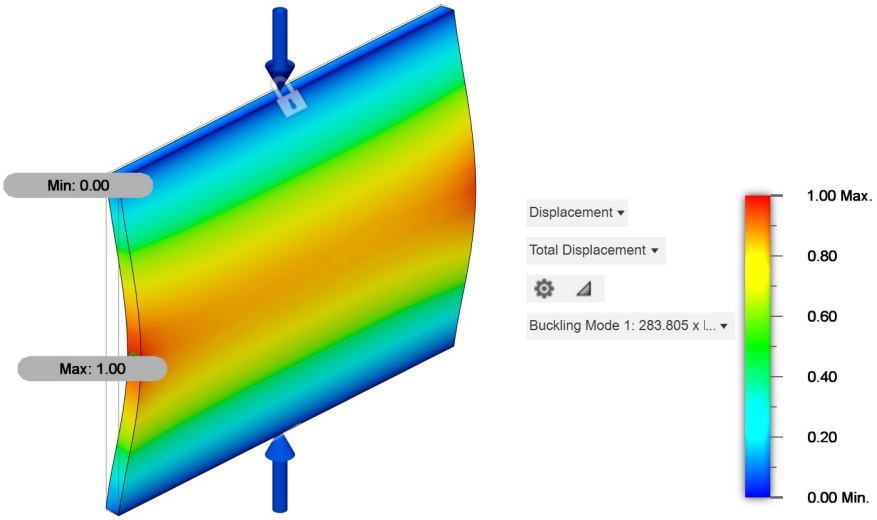

Figure 48: Buckling Deformation of Simply-Supported Plate in Simulation

The second model that was simulated under buckling conditions was a full section of the launch frame. This model considers the dissipation of stress along the top and bottom surfaces of the launch frame, not just the walls. The cut faces of the frame were constrained in this simulation, to mimic the parts of the launch platform frame that are not directly loaded. The load applied to the top and bottom surfaces is 1630 N for this simulation, which is approximately 1/4 of the combined weight of the launch rail and rocket. This simulation converged to a factor of safety above the applied load of 567.8. Figure 49 below shows the deformation experienced by the frame section under the compressive load.

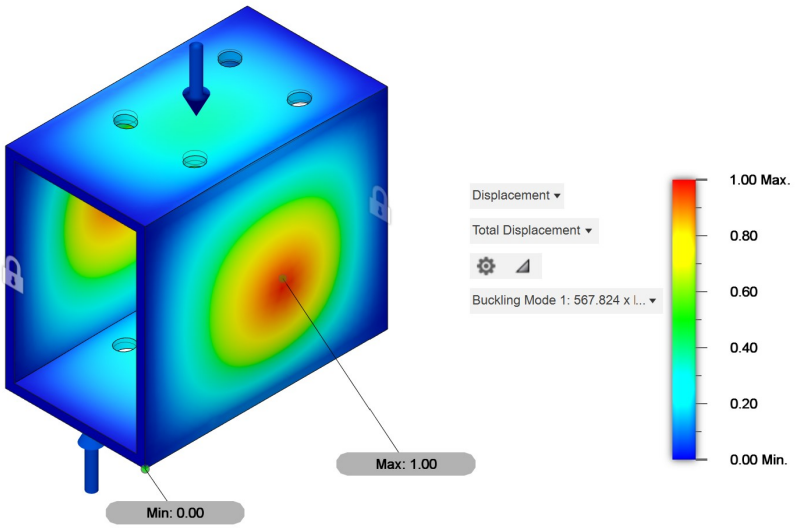

Figure 49: Buckling Deformation of Frame Section in Simulation

2.5.4.3 Comparison of Analytical and Simulated Buckling Models

These differences may be a result of a number of sources of error present in the models. In particular, the stress distribution in the simulation models may dissipate some of the load, which increases the load the walls can withstand before buckling. Another source of error present in both of the models is the effect of the remainder of the launch frame, which also dissipates some of the stress on the section under compression.

Despite the deviation between the simulated and analytical models, both provide a factor of safety that is considerably larger than the minimum 1.5 factor of safety recommended by NASA [30]. Based on these results, it is determined that the launch frame will not experience buckling failure under the compressive load of the 'C' fixture. This can be further confirmed through future structural testing of the launch frame beams.

2.5.5 Addition of Mounting Holes to Launch Rail Endplates

Another concern that was noticed was the lack of a structure that will prevent the rocket from slipping off the end of the rail. Two endplates and associated mounting fixtures were added to accomplish this. There were two endplates used at the rear of the launch rail to keep the guide rails in place, but they did not extend to the guide rail opening (where the rocket slides on and off). These end plates will be manufactured from 304 Stainless Steel, which is a common grade of Stainless Steel [31]. Steel is preferred to aluminum for these fixtures,

as they will experience a large load due to the rocket weight. Stainless steel was chosen to provide corrosion resistance to the launch environment, as was done for the selection of the bolt and locknut material.

A single 1.4" bolt is mounted to a threaded hole in the solid launch rail. This size is the same as the bolts used to mount the arms of the launch platform to both the 'C' fixture and launch rail. The strength of the endplate was not analyzed this term, but the shear stress imposed on the endplate by the rear rail guides of the rocket will need to be investigated to ensure the endplates do not tear during loading. The updated model of the launch rail with mounted endplates is shown in Figure 50 below.

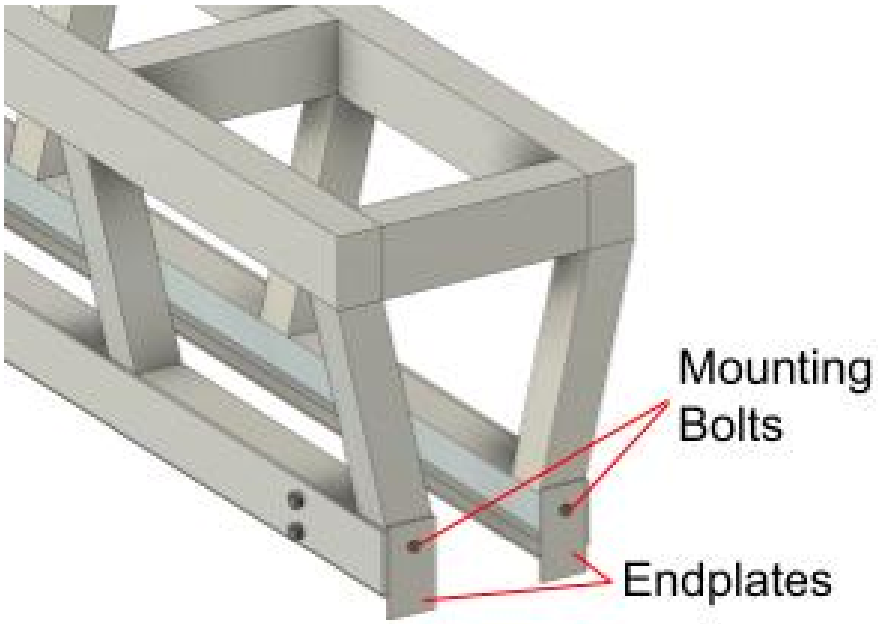

Figure 50: Mounted Endplates to Prevent Rocket Detachment

2.5.6 Launch Platform Structure Conclusion

In conclusion, the launch platform was modified from a deployable mechanism to a fixed design that holds the combined launch rail and rocket at a 30 degree elevation angle.

The fixed launch platform was investigated for tensile and buckling failure. Despite some deviation between analytical and simulated results, there were substantial factors of safety calculated for both of these failure scenarios, and

no design changes were made based off the results.

Endplates with mounting holes were added to the rear of the launch platform to prevent the rocket from detaching from the guide rails during ascent.

2.5.6.1 Future Work on Launch Platform Structure

Due to the desire for small adjustments to the launch angle, future work will involve the addition of the pitch control mechanism outlined in Section 2.5. This will result in the replacement of the rear arms of the launch platform with adjustable length arms that are being designed by Tristan Osena.

In terms of structural analysis of the launch platform, there is considerable work left to be done. An important analysis next term will be to analyze the strength of the bearings that connect the front arms of the launch platform to the launch platform frame. In addition to the bearing analysis, a strength analysis will need to be conducted on the bolted sections to determine if the current number of bolts is sufficient, or if the number needs to be adjusted.

Finally, it would be desirable to conduct an analysis of the launch rail as the rocket moves after ignition. It may be possible to reduce the complexity of the launch rail, as well as the number of structural members that are used.

2.5.6.2 Thank You and Contact Information

Thank you for taking the time to read this report on the launch platform structure used in the 2024/2025 Rocket-Propelled Wind Tunnel capstone project. Please provide any feedback to Jake Birkness at jakebirkness@cmail.carleton.ca.

2.6 Launch Platform Attitude Control - Tristan Osena

The initial state of a rocket at launch is imperative when designing a mission. The Rocket-Propelled Wind Tunnel (RPWT) will fly above Canada's controlled airspace at 70,000 ft and descend through controlled airspace during landing, thus it is necessary to precisely specify the initial pitch and yaw of the rocket to ensure that it closely follows a desired flight-path. The roll-pitch-yaw rocket-fixed axis is used to characterize the attitude of the rocket in three dimensions, as shown in Figure 51.

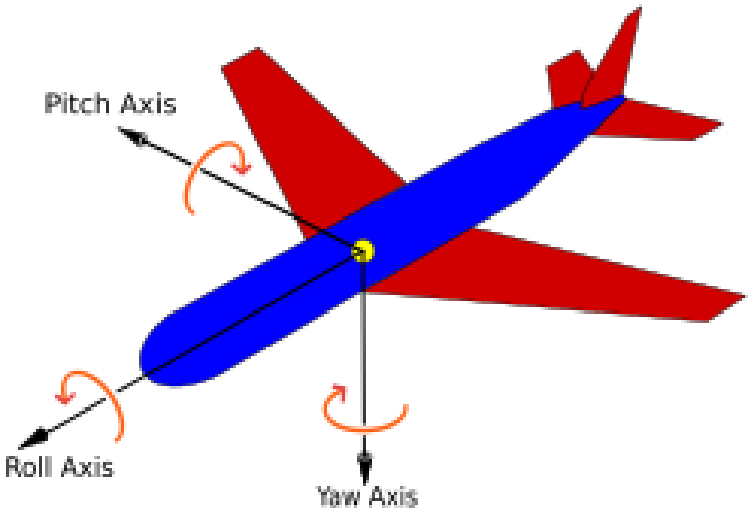

Figure 51: Roll-Pitch-Yaw Principle Axes for Rocket [32]

The RPWT will ascend to altitude using a stratospheric balloon, the launch rail and rocket will be mounted below the balloon at a known pitch-angle. During ascent, atmospheric perturbations such as gusts of wind will influence the attitude of the launch platform. It is assumed that the launch platform will be oriented at a random yaw angle once it reaches altitude, and the pitch angle of the rocket may need to be influenced to achieve the desired trajectory. Improved initial attitude control mechanisms are necessary for the rocket to re-orient due to attitude perturbations during ascent. During the Fall 2024 semester, the design of pitch and yaw control mechanisms was initiated to implement on the launch platform.

2.6.1 Launch Pitch Control

The previous launch platform design does not include any active pitch control. However, it introduced a mechanism to drop the rocket from horizontal to a 45° pitch attitude prior to launch. The stated purpose of the mechanism is to

allow the launch assembly to be more compact during ascent while allowing for a launch at 45° from horizontal [33]. Jake Birkness' design report, presented in section 2.4, provides analyses of the launch platform finding that an impulsive force of $27,000N$ is to be expected on the center of mass of the rocket due to the falling launch rail. Large impulsive forces acting on the rocket have the potential of damaging the internals of the rocket prior to launch, this would have to be reduced using mechanically complex damping mechanisms.

To allow for active pitch control of the rocket prior to launch, the design of twin linear actuators was initiated. The Actuators are designed to replace the rear arms of the launch platform to allow for variable extension and retraction, thus controlling the pitch-angle of the rocket at launch.

2.6.1.1 Linear Actuator Design Parameters

Linear actuators convert rotary motion into linear motion through the use of a lead screw and flange. An electric motor and gearbox apply a torque about the lead screw, the rotation of the lead screw is related to the linear motion of an extension arm through the pitch of the thread. The pitch of a thread is given to be the distance between consecutive threads, as a threaded screw makes one full rotation, the threads will move a linear distance equal to the pitch.

Figure 52 shows a close-up view of the designed lead screw and extension arm mechanism. As the central screw rotates fully, the connected threaded flange is forced to translate a distance equal to the pitch.

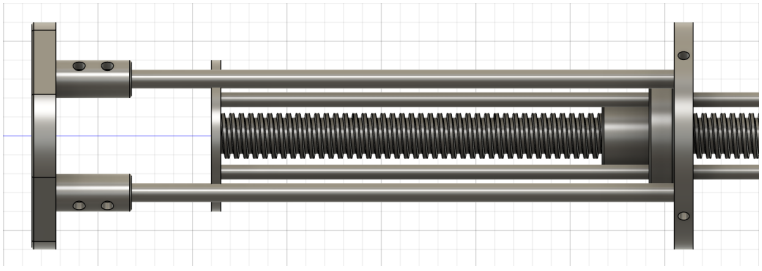

Figure 52: Lead Screw Extension Mechanism

The linear actuators were designed for a maximum extension of 300 mm, from the geometry of the launch platform, it was determined that an extension of 300 mm corresponds to a maximum pitch angle of approximately 12° above horizontal. An M24 lead screw was selected with a pitch of 5 mm from McMaster-Carr [34]. The M24 screw was selected as it was the smallest sized threaded rod available in 5 mm pitch.

The linear actuators must be designed to manipulate the loads applied by the launch platform and rocket. A safety factor must be introduced such that the devices do not fail when lifting the maximum desired load. The mass of the

launch rail and rocket combined was determined to be 664.1 kg, assuming the previous years' calculated loaded mass of 253.8 kg [33]. The maximum axial load on the lead screw was calculated using the weight of the mechanism above, and the angular deflection of the actuators at max extension. The load was calculated to be 6592.4 N.

The necessary driving torque was calculated by scaling the power applied by an assumed system efficiency factor of 0.5.

$$P_{out} = \eta * P_{in} \tag{64}$$

$$\tau * \omega * \eta = F_{load} * \frac{\omega * Pitch}{2\pi} \tag{65}$$

$$\tau = \frac{F_{load} * Pitch}{2\pi\eta} \tag{66}$$

Equations 64 to 66 describe how the necessary driving torque was determined. Power is known to be the product of force and velocity, in the case of angular systems that is torque and angular velocity. The power applied to the lead screw is equal to the driving torque multiplied by the driving speed. The power required by the extension arm is the product of the load applied and linear velocity. The linear velocity of the extension arm can be found by multiplying the lead screw pitch distance by the angular velocity converted to revolutions per second. The conversion is made simply by dividing the angular velocity by 2π.

Using the values selected and calculated above, the maximum driving torque was found to be 10.5 $N*m$. A drylin® E-stepper NEMA34 motor was selected for usage on each linear actuator. The motor has a high rated holding torque of 5.9 $N*m$, and a dynamic torque of 4.25 $N*m$ operating at 90 rpm [35]. Figure 53 displays the torque-angular speed characteristic curve of the selected motor driven at 24 and 48 Volts.

It is shown that the selected motor has a high torque-output of approximately 5.3 $N*m$ at low angular speeds. During the linear actuator design, it was necessary to consider how fast the mechanism can extend or retract, the speed at which the mechanism can actuate is limited by the maximum speed at which necessary torque is accomplished.

This motor is desirable as it can be geared above the necessary torque using a simple 2.5 gear ratio, the motor also comes in a compact package, weighing 3.3 kg [35]. The motor requires a $24V$ $4.8A$ power source for continuous operation, a CANBAT Lithium-Iron-Phosphate $25.6V$ power source was selected, the battery is equipped with $12A*h$ charge capacity [36]. Operating at $4.8A$, the power source allows for 1.25 hours of continuous use of two motors. The battery has a weight of 2.72 kg.

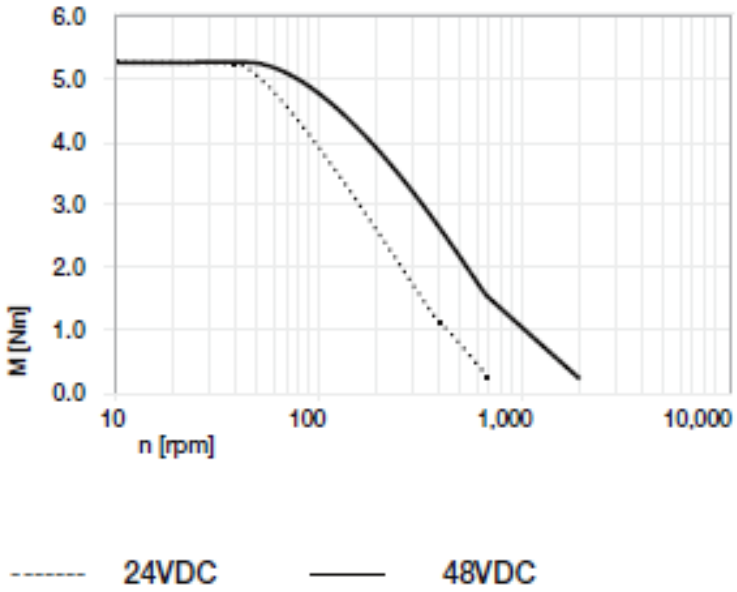

Figure 53: Drylin Motor Torque-Speed Characteristic [35]

2.6.1.2 Summary of Design Specifications

Table 6, below, summarizes the design requirements for the linear actuators, using the drylin®motors and CANBAT power source.

Table 6: Linear Actuator Design Parameters

Max. Axial Load	6592.4 N
System Efficiency	0.5
Max. Torque Required	10.5 $N * m$
Motor Torque (@ 90 rpm)	4.25 $N * m$
Desired Gear Ratio	2.5
Max. Driving Torque	10.625 $N * m$
Lead Screw Diameter	M24
Lead Screw Pitch	5 mm

2.6.1.3 Mechanical Design of Actuators

The linear actuator was designed in 3 stages; the extension arm, the lead screw assembly and the drive assembly. The extension arm attaches to the lead screw and lower launch rail, the lead screw assembly joins the extension arm to the drive assembly, and the drive assembly joins the lead screw to the upper launch platform.

To achieve the required mechanical advantage to drive the lead screw, two

McMaster-Carr gears were selected and implemented. A 2.5 gear ratio was achieved using a driven 20-tooth gear driving a 50-tooth gear which is fixed to the lead screw.

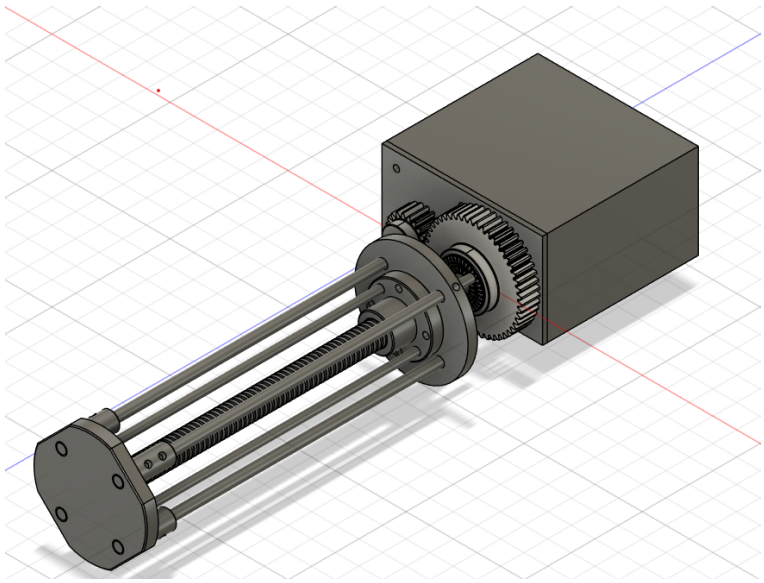

Figure 54: Assembled Linear Actuator Mechanism

Figure 54 shows the designed linear actuator in the retracted configuration. The actuator has an overall length of 635 mm, extending fully to 915 mm, allowing for a total of 280 mm extension.

In Figure 54, the gears are exposed while the remainder of the drive assembly is concealed within a housing. A housing will be made that encompasses the gears and pins the linear actuators into the launch platform.

The lead screw transmits force to the extension arm through the threaded flange. The flange is post-machined to bore holes for guide rods. The guide rods restrict the motion of the flange to a single degree-of-freedom sliding motion.

Figures 55 and 56 show the top view of the linear actuator with the housing removed. The M24 lead screw is machined to a 17 mm diameter shaft, such that a 50 tooth gear can slide on and bolt to the shaft. The 50-tooth gear is mounted on concentric thrust roller bearings within the gearbox housing, enabling it to rotate smoothly under high loads. An additional thrust bearing is attached further down the 17 mm shaft, the bearing sits within the drive assembly housing to support axial and tangential loads on the lead screw.

The lead screw, flange, gears and bearings are all sourced from McMaster-Carr. The drive assembly housing can be manufactured from 5 mm and 10 mm sheet metal. A table of selected components and associated costs is presented in Table

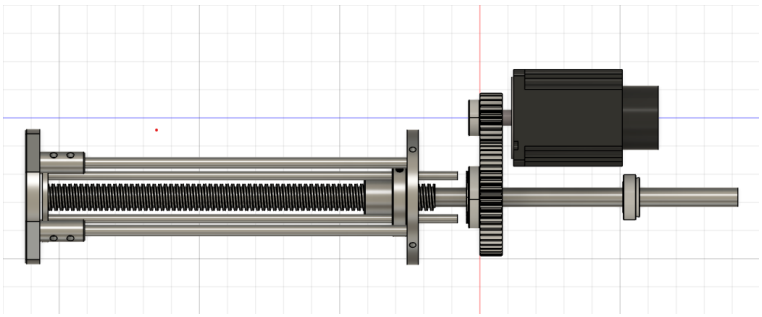

Figure 55: Extension Mechanism Retracted

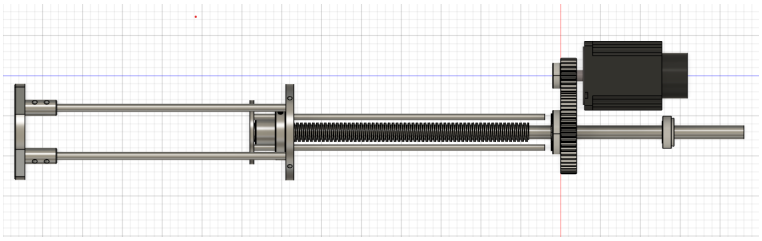

Figure 56: Extension Mechanism Extended

7. Note that the list does not account for the costs of fasteners or certain custom machined components.

Table 7 finds that the total cost of major components for each linear actuator will be $ 1072.64. Nearly 50 % of the cost is associated with the electric motor, it may be beneficial to examine more cost-efficient stepper motors providing similar performance.

2.6.1.4 Future Work

Next steps for the linear actuator are to complete the design for the connecting points between the actuators and the platform, and performing computer-aided simulations to verify the performance of the mechanism and determine an efficiency value for the system.

2.6.2 Launch Platform Yaw Control

When participating in civil rocketry, it is necessary to actively control the yaw-angle of the rocket at launch in order to restrict the initial trajectory of the rocket. The previously designed launch platform included four electric motors equipped with propellers, each mounted at a corner of the launch platform. The propeller actuators were predicted to be ineffective at accurately controlling the yaw, as thrust provided about the yaw axis is dependent on the varying

Table 7: Linear Actuator Components

Component	Cost (CAD)
500 *mm* M24 Lead Screw	43.02
M24 Threaded Flange Nut	99.21
50 Tooth Module 2 Round-Bore Gear	82.00
20 Tooth Module 2 Round-Bore Gear	22.68
Drylin NEMA 34 E-Stepper Motor	532.25
CANBAT 25.6V 12 Ah Battery	249
17 *mm* Shaft Tapered-Roller Thrust Bearing	31.73
17 *mm* Shaft Needle-Roller Thrust Bearing	5.47
30 *mm* Shaft Needle-Roller Thrust Bearing	7.28
Total Component Cost	1072.64

density of air during ascent. The propeller actuators will be replaced with a Control Moment Gyroscope (CMG) mechanism which works to actuate the vertical yaw-axis of the launch platform by altering the angular momentum of spinning wheels.

A technical journal article was found in which a group of researchers experimented using control moment gyroscopes to actuate and stabilize the yaw of the launch platform [37]. Their design uses a mechanism placed above the launch platform centre of gravity with the CMGs placed equidistant from the centre. The apparatus designed and tested by *Shoyama et. al* is displayed in Figure 57.

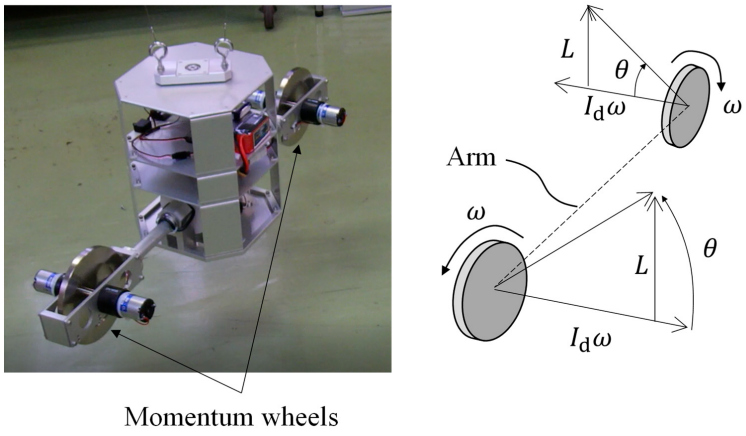

Figure 57: Experimental CMG Yaw Control Mechanism [37]

The control moment gyroscopes are initially positioned vertically as shown in Figure 57. In the vertical configuration, the angular momentum of each wheel

cancels out, however, as both wheels rotate about the arm their angular momentum increases about the yaw axis.

2.6.2.1 Control Moment Gyroscope Dynamics

The launch platform can be torqued about its yaw axis by altering the total angular momentum about the yaw axis. The angular momentum contributed by both CMGs is modeled using the relation below. The variable ω represents the angular velocity of the CMG wheels and θ represents the elevation of the angular momentum vector with respect to the horizontal [37].

$$h_{yaw} = 2 * I_{wheel} * \omega * sin(\theta) \tag{67}$$

In the equation above, I_{wheel} denotes the moment of inertia of each CMG wheel. The total angular momentum would be equal to $2 * L$, as depicted in Figure 57. It should be noted that L is equivalent to h_{yaw}, presented in the equation above.

Torque about an axis is equal to the time-derivative of the angular momentum about the same axis, thus, the torque contributed by the CMG apparatus can be determined by taking the derivative of the above equation.

$$\tau_{yaw} = \frac{d}{dt}(2 * I_{wheel} * \omega(t) * sin[\theta(t)]) \tag{68}$$

$$\tau_{yaw} = 2I_{wheel}(\dot{\omega} sin(\theta) + \omega\dot{\theta} cos(\theta)) \tag{69}$$

Within the CMG apparatus, the angular velocity and elevation of the wheels are both time-variable. The total torque contributed about the yaw-axis consists of two terms, the first term is related to the angular acceleration of the wheels at a non-zero elevation angle, whereas the second term is a function of the wheel angular velocity and the rate of change of the elevation of the wheels.

While both wheels are aligned vertically, their angular momentum cancels out and the wheels can spin up without interfering with the attitude of the platform. At a constant velocity, the wheels can be tilted at a constant angular velocity from the horizontal plane to induce a torque about the yaw axis.

2.6.2.2 Launch Platform Yaw Dynamics

The sum of torques about the yaw axis is equal to the angular acceleration of the platform scaled by the total moment of inertia about the axis, as shown in the relation below.

$$\Sigma\tau_{yaw} = I_{tot_{yaw}} * \dot{\omega}_{platform} \tag{70}$$

The objective of the CMG mechanism is to counteract any atmospheric torques and correct any drift which occurs from the desired azimuth angle, the angle can be determined by integrating the angular acceleration twice, as shown below.

$$\Sigma \int \tau_{yaw} = I_{tot_{yaw}} * \int \dot{\omega}_{platform} \tag{71}$$

$$\theta_{platform} = \frac{\int \int \tau_{yaw} dt dt}{I_{yaw}} \tag{72}$$

2.6.2.3 Yaw Control System Design

The dynamics for the CMG and launch platform must be implemented within a feedback-controlled system to achieve and stabilize the yaw angle of the platform at a desired setting. Next steps for this project involve developing and simulating the control system within Simulink. The simulations will be run with varied CMG inertia and wheel speed, allowing a wheel mass and geometry to be selected in addition to a reasonable angular velocity for a desired system response.

Using the wheel mass, geometry and velocity constraints, a structural base will be designed to attach the CMG mechanism to the top of the launch platform, connecting between the balloon and the launch platform. The structural element must be able to support the load of the launch platform and rocket, and must be able to rotate with respect to the balloon.

The implementation of a feedback-controlled system will require the implementation of gyroscopic sensors on the launch platform. Future work will involve implementing and verifying the performance of gyroscopic sensors for use on the launch platform

2.7 Ascent Subteam Recap

The ascent subsystem was developed through the design work outlined above. The key developments of the ascent system from the term include preliminary sizing of the launch balloon, devised control systems for altitude and attitude, an improved dynamic model of launch, and the proposed fixed launch platform design.

Next term, the ascent sub-team will work to integrate the initial conditions for launch with the control system design. It is vital that the initial conditions from launch can be estimated to ensure initial dynamic stability of the launch vehicle. In addition, further design work and analysis will be done to integrate the altitude and pitch control mechanisms with the launch platform.

3 Airframe Design

3.1 Airframe Subteam Introduction

The airframe project for the rocket design project (RDP) capstone has been a build-off of the previous year's work, including the rocket design, wing design, and test section design. The group has been broken into two working teams to focus on the rocket design of the 2024 launch vehicle and a newly proposed blended wing design which will be designed around a test section; putting a larger emphasis on obtaining accurate in-flight test results.

Additionally, a Schlieren imaging system will be integrated into the launch vehicle. This is an integral feature of the Rocket-Propelled Wind Tunnel as it will provide high-speed flow visualization. Integrating this system is mission-critical and is a key focus of both design groups.

Figure 58: RDP 2024 Final Airframe Design [1]

The goal of the Airframe Subteam is to adapt and improve upon the previous model of the rocket airframe. The newly added Schlieren imaging system will require a structural analysis update of the outer mold to mitigate any failures. Adapting the rocket airframe model includes the redesign of several different flagged components from the previous year design, such as nosecone, landing gears, and wing deployment system.

The Blended Wing concept idea originated from the conclusions reached in the 2024 RDP term report. Which stated the design was incomplete as the deployable wings as shown in the 2024 design in *Figure* 58 did not generate adequate glide performance along with a large Angle of Attack (A.O.A.) required during cruise largely nullifying any opportunity to capture flow normal to the test section inlet.

The landing gear design of the previous year was determined to require work to improve capabilities of surviving landing. This, alongside the addition of internal space with respect to the new airframe considerations, allowed for a

new design approach towards the landing gear mechanism to be used in the aircraft mold.

The addition of a shock absorber mechanism also analyzed the damping method and simulation, and the addition of a worm gear to rotationally deploy and self-lock the landing gear in order to develop a new landing gear mechanism. With respect to the cover analysis absent from 2024 RDP term report,

a thermal analysis method was required to be developed to analyze temperature change of rocket body during entire flight, and design thermal control strategies for required rocket components. A simulation model would be developed to determine the thermal issues presented in each design, and passive and active thermal control strategies could be proposed to reduce these factors.

3.2 Rocket Body Design and Analysis - Graham

Peer Reviewed by: Wissam Aldouri

3.2.1 Review of previous model

With the addition of a Schlieren imaging system, more internal space is required indie the rocket to allow for the imaging system to properly fit inside the rocket outer frame. This analysis aims to determine a thickness of the outer mold with respect to the increased diameter that will achieve similar failure analysis compared to last year report. A review of the previous report concluded that the decision for airframe outer mold consisted of a 2-meter-long metal tube of outer radius of 127 millimeters, or 5 inches, and a 5-millimeter thickness. [1]. An FEA analysis was conducted on the test section outer cylinder tube, which led to similar analysis values to apply to the airframe tube [1]. From analysis with respect to lens, camera, and focal lengths, it was concluded that a schlieren imaging system would not properly fit inside the inner tube without significant reduction to test sample size. As a result, an allowable 6 inches, or 152-millimeter radius was given for analysis purposes, but may be required to change with respect to updated data and requirements.

3.2.2 Rocket Body Design comparison of materials

A review of manned and unmanned solid rocket motor aircraft provided information towards key considerations of airframe design and analysis, in addition to common structural materials and practices. Designs which were analyzed commonly include aluminum, titanium, steel, and carbon fiber reinforced polymers [38]. A referenced design included the Boeing X-51 Waverider [38]. While scramjets are not considered for usage in the solid rocket motor design currently in usage, referencing the internal design and shape of the rocket provided insight into analysis considerations of rocket shaped aircraft in addition to bay sectioning and assembly methods [39]. Unfortunately, information regarding

different manufacturing methods and equations for analysis regarding different design remains classified.

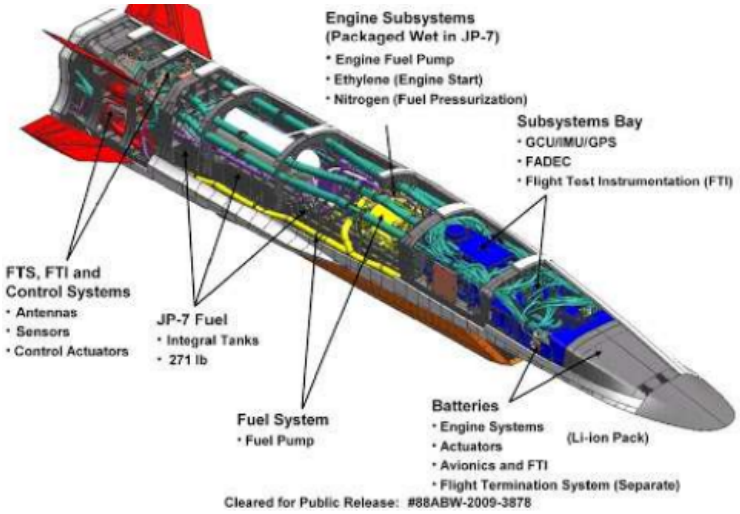

Figure 59: FEA Analysis of Boeing X-51A [39]

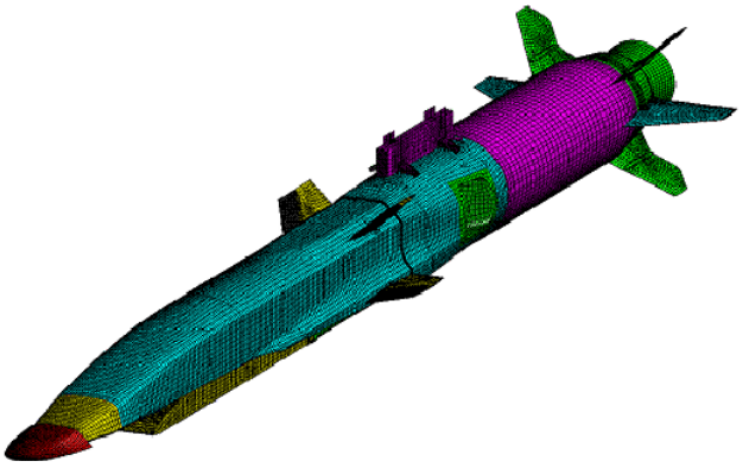

Figure 60: Generalization of X-51A Internal Sections [38]

3.2.3 Axial Compression Analysis

Considering an upscaled airframe, the thickness of the frame may be insufficient with respect to the bigger diameter as smaller thickness to diameter ratios can

compromise the mold's structural integrity. To determine this, a structural analysis of thin-walled cylinders was performed to determine a value of thickness which will not fail under flight loads, while reducing weight and required thrust load. From flight, two major loads will be applied to the outer mold: buckling due to axial compression and deformation due to bending loads.

3.2.4 Axial Compression Analysis

To determine the required thickness of the airframe, the material properties were used to determine the amount of stress experienced by the structure before an isothermal cylinder would buckle under axial compression. This equation is given by Eq.73 where; E is Young's modulus (Pa), ν is Poisson's ratio, γ is the buckling knockdown ratio, and t and r are the thickness (m) and radius (m) respectively [40] [41] [42]. The equation considers local bending which may occur in the cylinder as length is not included in the equation. The buckling knockdown factor added to the equation, is a method of which can determine the difference between theoretical and testing critical bending stresses. This value incorporates the usage of axial half wave and circumferential full waves that denote how sections of the cylinder may buckle [40] [43]. Considering the amount of information currently present and the lack of bulkheads being considered, the buckling coefficient can be set to 1.0 to consider theoretical values. The calculation for the buckling knockdown coefficient can be seen through equations Eq.74 through Eq.75 [40].

$$\sigma_{cr} = \frac{\gamma E}{\sqrt{3(1-\nu^2)}} * \frac{t}{r} \tag{73}$$

$$\gamma = 1 - 0.901(1 - e^{-\phi}) \tag{74}$$

$$\phi = \frac{1}{16}\sqrt{\frac{r}{t}} \tag{75}$$

3.2.5 Bending Analysis

Bending analysis considers both ends to be simply supported. For sufficiently long cylinders, the equation can be defined by Eq.76 where; E is Young's modulus (Pa), ν is Poisson's ratio, and t and r are the thickness (m) and radius (m), respectively [40]. This analysis is performed with respect to a cross-sectional collapse due to side loading away from structural supports. Thereby preventing the circular cross-section design from deforming into an oval shape from a uniform bending load [40]. A future analysis will include a moment-bending analysis of the weight of the test section against the airframe during turning for level flight at 70,000 ft.

$$M_{cr} = 0.987 * \frac{Ert^2}{\sqrt{1-\nu^2}} \tag{76}$$

3.2.6 Analysis and Model of Rocket Outer Mold

Preliminary model was created with information gathered from calculations. A comparison of the previous outer mold frame and new model frame is illustrated in Figure 61. To achieve similar axial compression critical strengths to the previous model, the thickness of the airframe would be required to increase to 6 mm for similar axial compression forces for a structural steel frame. This would cause the airframe to weigh approximately 93.54 kg, or roughly 30 kg more than the previous model.

Table 8: Structure Critical Stress and Weight Analysis

Outer Radius Model	thickness (mm)	σ_{cr} (GPa)	Weight (kg)
10”	5	5.0039	61.41
12”	6.0	5.0038	93.54

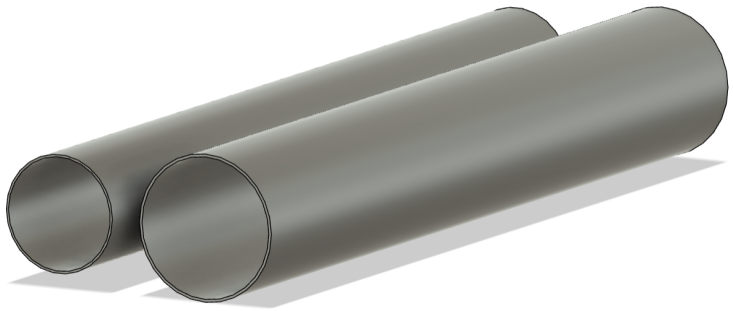

Figure 61: Comparison of Previous Airframe and New Airframe Outer Molds

3.2.7 Conclusion and Future Works

The analysis of structural integrity of thin-walled cylinders under axial compression and bending has produced an outer mold geometry which can be used for assembly and sizing for components. Should a design change be necessary, analysis methods will be performed again to ensure proper sizing. The research carried on different aircraft has assisted in the determination of proper materials and thickness-to-diameter ratios for the completion of the calculations and model.

The preliminary design inner radius is subject to change depending on Schlieren imaging apparatus and requirements, as such the methods used above can redefine new airframe geometry to accommodate for the updated information. Future work will focus on the creation of bulkheads and mounting framework on the interior of the rocket body. This will include mounting for the test section, respective electronic hardware and areas for

motor housing.In addition, with the information presented by the nose cone development, an aerodynamic analysis could be performed to determine updated drag and lift forces which act on the face of the rocket, and the development of shock waves along the surface of the mold.

3.3 Rocket Body Deployable Wings - Graham

3.3.1 Design Comparisons and Considerations

In the last year's design, a proposal for deployable wings on the rocket body was created to provide a method of lift post-burnout for landing. This system consisted of two wings with similar deployment mechanisms which would swing the wings from the back of the rocket to perpendicular to the rocket body [1]. As a result, the rocket would have a more streamlined surface that would decrease drag during the testing phase of flight but provide additional lift to the rocket when landing[1]. This proposal was ultimately reconsidered for fairings and stowed wings, as the deployment mechanisms would take up too much space on the rocket body [1]. From this decision, no analysis was performed with respect to drag and lift values to determine if the wings would function as expected.

With the increase in rocket body size, the reconsideration of deployable wings would be plausible with proper analysis and can become a consideration to the rocket body versus lifting body design choice. This would require the usage of CFD analysis to determine the coefficients of drag and lift, in addition to the center of pressure, to determine the drag and lift forces acting on the wing as a method of solving for actuation moments. This can then be used to determine the maximum moment required to open the wings with respect to aircraft speed and altitude and compared with the position of the rocket during flight with trajectory analysis values. From this analysis, it can be concluded whether the wings are applicable or would require a design change consideration.

3.3.2 Review of Last Year's Model

From last year's report, set design goals and physical constraints were set, as seen in 9 The deployable wings consisted of two flat wings which would be attached to 4-bar rocker mechanisms[1]. The rocker bar would be deployed by a linear actuator bar that would pull on the bar system to swing the wing from the tip facing the back of the rocket, to being perpendicular to the rocket [1]. The rocker bar mechanism would assist in the distribution of forces and reduce the amount of actuation required to open the wings to their desired position[1].

Table 9: Parameters set in ANSYS Fluent CFD

Feature	Dimension
System length	1.75 [m]
System width (above body)	0.325 [m]
System height (above body)	0.1 [m]
Vehicle mass at burnout	77 [kg]

3.3.3 Drag/Lift Forces Forces

To determine the the maximum actuation torque, the wing will be analyzed as a fixed support and free end beam with a force application creating a bending moment. It will be assumed that the maximum force applied to the wing is at the point where the wings are fully deployed and perpendicular to the rocket body. As such, the rocket actuation magnitude must be equal to or greater than the calculated moment forced caused by the forces opposing wing movement. These forces will be compromised of the drag of the air on the wing. The general equation of drag forces can be defined as Eq.77 [44] where C_D is the coefficient of drag, A is the reference area, ρ is the density, and V is the velocity of the object [44].

$$D = \frac{1}{2} * C_d * \rho * S * U_\infty^2 \tag{77}$$

$$L = \frac{1}{2} * C_l * \rho * S * U_\infty^2 \tag{78}$$

$$C_d = C_{d,0} + C_{d,l} \tag{79}$$

$$C_{d,0} = C_{d,f} + C_{d,w} \tag{80}$$

$$C_{d,l} = C_{d,i} + C_{d,v} \tag{81}$$

$C_{d,0}$ and $C_{d,l}$ are representative of the coefficient of drag with zero-lift and with lift respectively. These can then be determined by the coefficients of surface friction drag ($C_{d,f}$) and wave drag ($C_{d,w}$) for zero-lift, and the induced ($C_{d,i}$) and viscous ($C_{d,v}$) drag coefficients for lift [44]. these values were determined through simulation of the airfoil as seen in the CFD Analysis .

From the forces gained, the actuation can be determined by evaluating a moment force acting along the plane yaw axis. A center of pressure has not been determined for the wing shape from the previous year, and for the current work performed. As such, it will be estimated that the center of gravity, or the center of the wing, will be the point of application for the resultant force. While this method is not entirely accurate towards the final value, it will provide a sufficient estimate of the forces required to open the wings.

$$M_a = D * d_c \tag{82}$$

The method of which to apply altitude to these equation involves the Mach number. The mach number is defined as the ratio between an objects speed and the speed of sound of a surrounding medium, and can be solved for using Eq.83 where v is the velocity of the object and a is the speed of sound. With respect to the medium, the speed of sound can be calculated as Eq.83 where γ is the ratio of specific heats (1.4 for air), R is the specific gas constant (287.05 J/kg K), and T is the temperature of the surrounding air [45]. From the International Standard Atmosphere (ISA) model, the values for temperature, pressure, and dynamic viscosity can be determined., which thereby gives the mach number, free stream velocity, and Reynolds number that can be used in the CFD simulation and are tabulated in Figure 62.

$$M = \frac{v}{a} \tag{83}$$

$$a = \sqrt{\gamma * R * T} \tag{84}$$

Chord [mm]	263.158	Area [m2]	0.092479687	Length [m]	1.75
Altitude [ft]	Temperature [K]	Pressure [Pa]	Density [kg/m3]	Speed of Sound [m/s]	D. Viscosity [kg/ms]
70000	217.9146	4487.7	0.071742	295.9294	0.000014286
60000	216.65	7231.2	0.11628	295.0695	0.000014216
50000	216.65	11664	0.18756	295.0695	0.000014216
40000	216.65	18823	0.30267	295.0695	0.000014216
30000	228.7994	30149	0.45904	303.2301	0.000014876
20000	248.564	46601	0.65312	316.056	0.000015917
10000	268.3475	69695	0.90477	328.3929	0.000016922
0	288.15	101330	1.225	340.294	0.000017894

Figure 62: Air Properties for Different Altitudes [46] [45] [47]

These properties are determined with respect to the altitude of the object in the air, relative to sea level [45]. These values are also required in order to determine the drag as seen in Eq.77. Where Re is the Reynolds number, U_∞ is the velocity of the free-stream, ρ_∞ is the density of the free-stream air, μ_∞ is the dynamic viscosity of the free-stream air, and c is the chord length of the airfoil.

$$Re = \frac{\rho_\infty * U_\infty * c}{\mu_\infty} \tag{85}$$

3.3.4 CFD Analysis

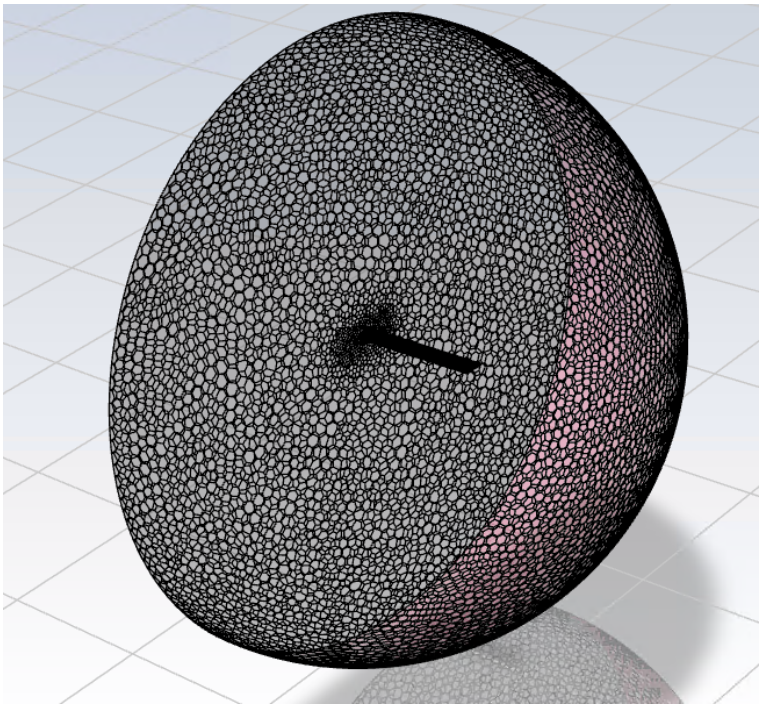

Figure 63: Mesh of Fluid Boundary and Wing Shape

To determine coefficient of drag and coefficient of lift values, the wing will be analyzed using ANSYS Fluent computational fluid dynamics (CFD). This will allow for the computation of drag and lift forces which act on the wing. Due to symmetry, only one wing will be analyzed. CFD analysis will be performed at different mach numbers and height values [47], which will be changed through varying density and pressure values for air. A model of the wing is required in order to perform the calculation, unfortunately a legacy file was not found in the previous years files or network drives. As such, a wing was made by using the airfoil shape of the final rocket design Fusion 360 file, by projecting and sketching the airfoil to extrude out to the size set by the design constraints. This model was placed into ANSYS with a half circle shape representative of the fluid domain and a polyhedral mesh was generated as seen in Figure 63. The parameters set in the solution folder can be seen in Table 10, where air is solved as an ideal gas density with Sutherland viscosity at higher mach numbers (=>0.7), and is set to constant density at lower mach numbers (<0.7). Pressure and air density values were taken with respect to altitude as per tabulated values in Figure 62 In the analysis, the pressure far field was set to project mach 3 conditions into the front of the airfoil, with reference air density and operating

pressure being set to height values of 10,000 feet intervals. To ensure proper value acquisition from the CFD analysis, a reference shape with coefficient values available is the best method to ensure correct values. However, the last year report did not specify a wing or airfoil shape. It was concluded that the best assumption for similar airfoil shape seen in the fairing design was a 6 percent thick supercritical airfoil [48]. Performing a geometrical analysis of the sketched airfoil, it was found that the thickness to cord ratio is 0.11. Unfortunately, mach numbers of drag and lift values solely exist up to mach numbers of 0.84. As such, the best method performed to ensure proper values was to take a reference shape with a similar boundary condition to the generated mesh of the airfoil and perform simulations to ensure proper data collection with expected shape values.

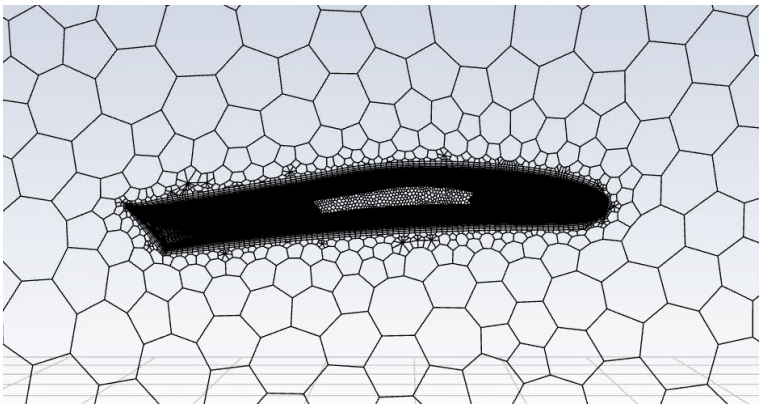

Figure 64: Mesh of Airfoil Face

Table 10: Parameters set in ANSYS Fluent CFD [49] [50]

ANSYS Fluent Parameters
Steady State
Pressure Based
Spalart-Allmaras
Energy Equation On
Air - Ideal gas, Sutherland viscosity
Pressure far field boundary inlet
Slip wall connected to object
Second order spatial discretization

From the analysis simulations were performed at height intervals of 10,000 ft for mach number intervals of 0.25. These simulations would yield the C_D, which could be used with the known air properties and air speed values to determine

F_D.

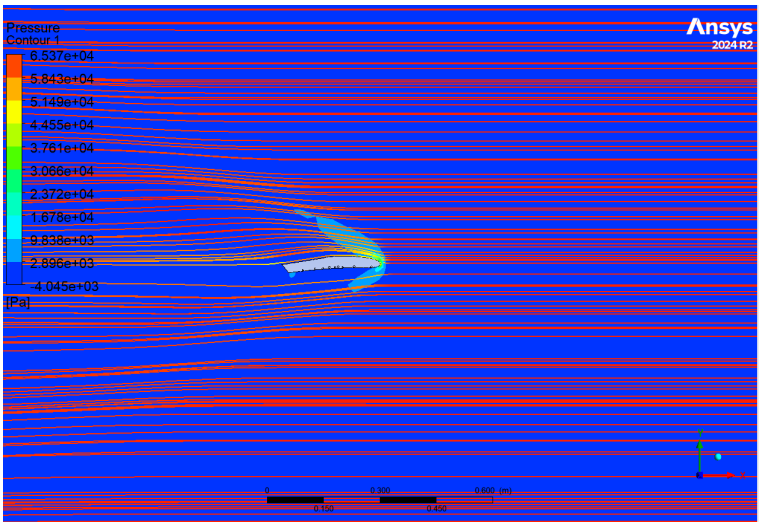

Figure 65: Streamline Velocity and Pressure Contour, 0 degree AoA

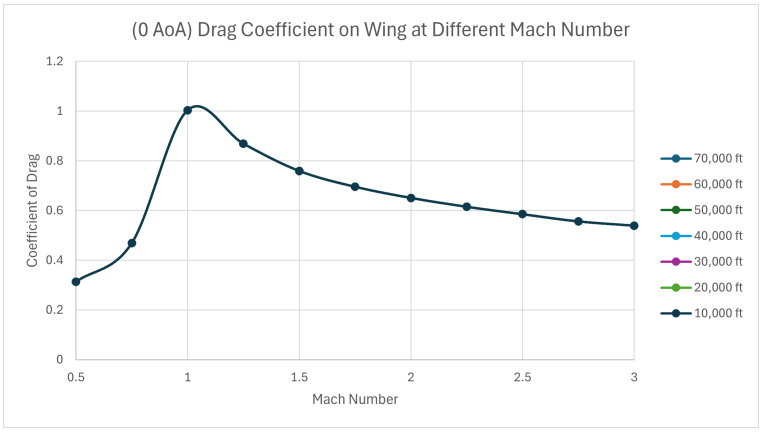

Figure 66: C_D of Airfoil at 70,000 ft, 0 degree AoA

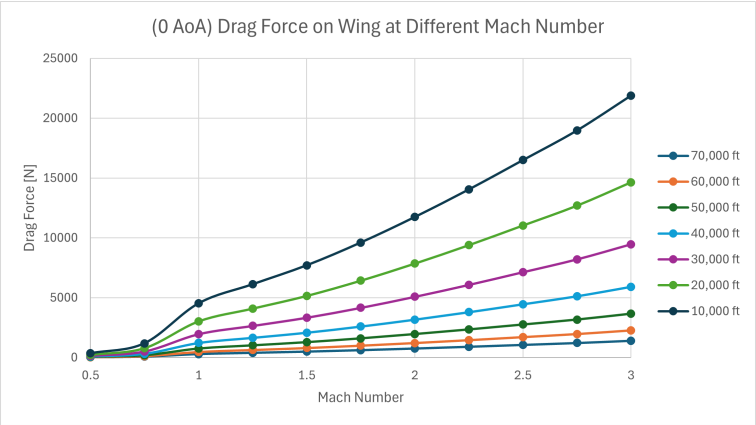

Figure 67: C_D of Airfoil at 70,000 ft, 0 degree AoA

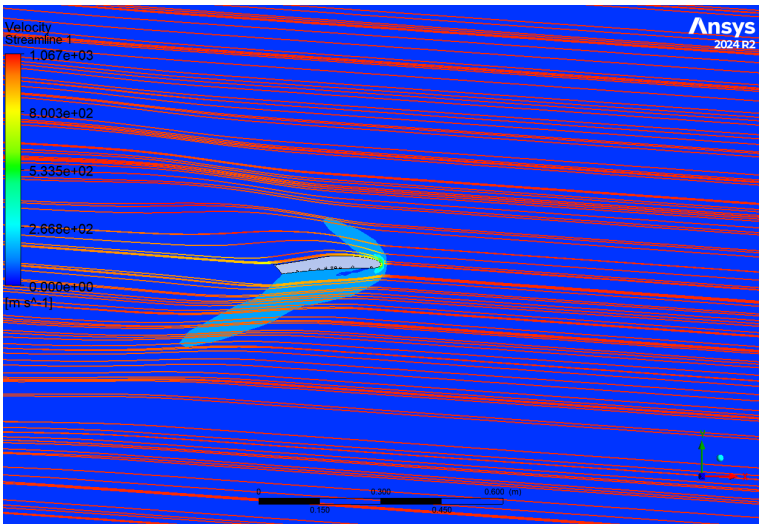

Figure 68: Streamline Velocity and Pressure Contour, 4 degree AoA

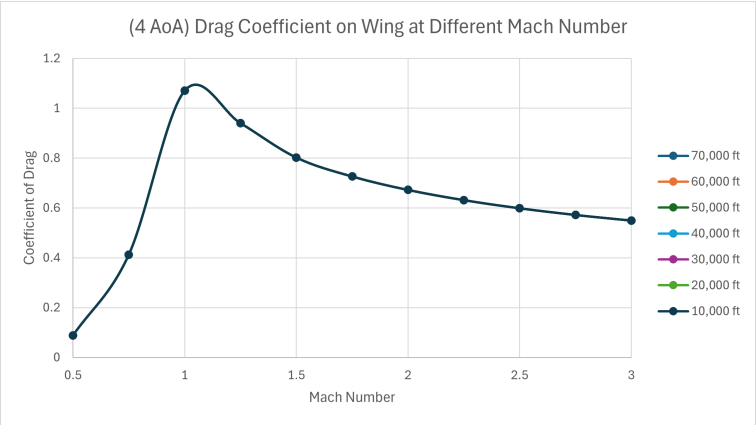

Figure 69: C_D of Airfoil at 70,000 ft, 4 degree AoA

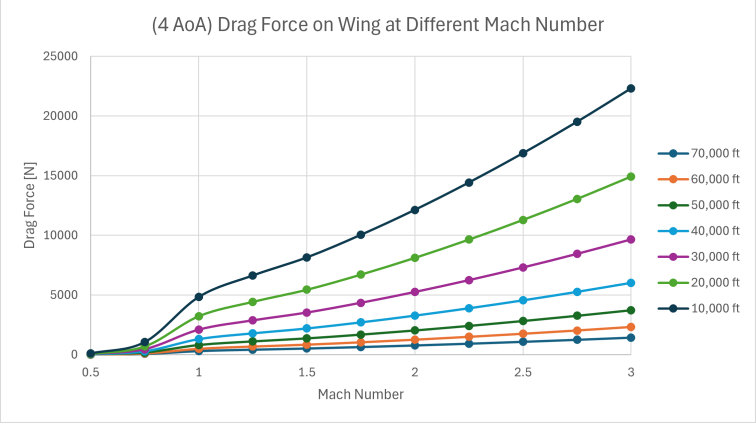

Figure 70: F_D of Airfoil at 70,000 ft, 4 degree AoA

From simulation, it was found that the differences in coefficient of drag with respect to altitude are relatively small. As such, the coefficients of drag will be analyzed from on set of values and applied to the drag force equation Eq.77. These coefficients of drag are representative of the total summation of drag coefficients described in Eq.79. By applying the drag force equation and moment equations, the total actuation of the point can be determined. As seen in the the coefficient of drag graph 69, the trend of drag coefficient with respect to mach number drastically increases around Mach 1. This is due to the creation of shock waves along the surface of the wing [48]. From these drag coefficients, Eq.77 was used to calculate the drag force, which is then used to estimate the moment force acting on the wing with respect to the center of pressure.

3.3.5 Conclusions

The drag values serve as a representation of force required along the wing arm in order to open the wings and maintain their position. Ideally, the wings would open at the highest position possible to decrease air density, and the lowest speed possible to ensure lowest free-stream velocity of air, both of which contribute to drag force as per Eq.77. This information can be compared with trajectory analysis numbers to obtain best points of flight. These values are estimations with respect to the center of gravity.

3.3.6 Conclusion and Future Works

The conclusion of the applicability of deployable wings in the rocket body system is incomplete. This requires the determination of the center of pressure on the wing, which can be completed with a simulation of the moment and forces acting on the wing. Once this is completed, the values can be used to find an actuator that can handle the deployment forces during flight. This information can reference the trajectory analysis to determine the point where the actuator can open and if the position during flight seems reasonable. An analysis regarding the partial opening of the wings will also be performed. This will be done by utilizing the structural bar method described and used throughout the deployable wing section, with a force angled with respect to the sweep angle of the wing. This will assist with deployment mechanics and analysis of the deployable wings. If the conclusion is that the deployable wings are applicable, then the deployment mechanism can be examined further to reduce size. This will apply calculations regarding the dynamics of machinery and bar mechanism force analysis. If the deployable wings are concluded to be non-applicable, research into different mechanisms or deployable wing systems can be performed. One prospect could include the experimental ND-1 aircraft designed by NASA which features an oblique wing capable of rotating to different sweep angles [51]. These wings are designed to reduce wave drag, making them capable of maneuvering at high speed, while still having large wing lengths which can generate lift in subsonic travel [51].

3.4 Blended Wing Conceptual and Preliminary Design - Philippe Charapov

Peer Reviewed by: Nathan Bolduc

3.4.1 Background

The objective of this project component is to create a blended wing design to achieve more favorable condition for flight during the cruise and glide portion of the flight. Rather than the previous design where a rocket body was adapted to house a test section and wings to achieve a lifting body during cruise; this design is meant to be built around the test section.
The primary goal being to avoid the deflection of flow at the exit of the test

section. In Figure 71 is shown a comparison of the previous test section flow path lines versus the proposed test section flow.

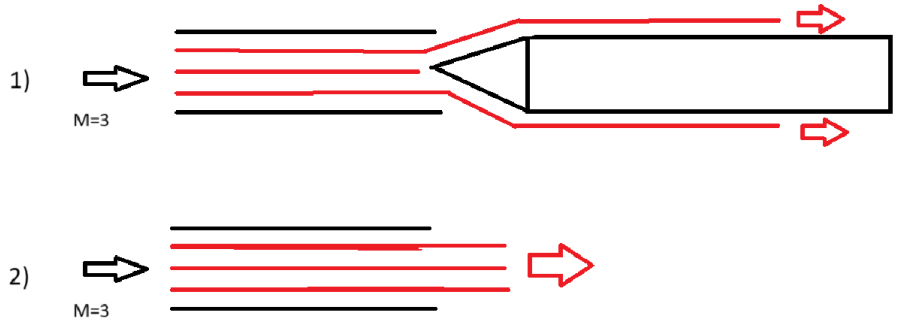

Figure 71: Test Section Location Comparison: 1) 2024 Section Flow - High Drag Design, 2) Blended Wing Underbody Design - No Flow Deflection

This effort begins with evaluating the feasibility of an underbody test section as opposed to it being concentric to the circular body.
The following report will describe the Objectives, Design, Methodology and Analysis of Blended Wing design feasibility compared to the previous rocket body conceptual design.[1]

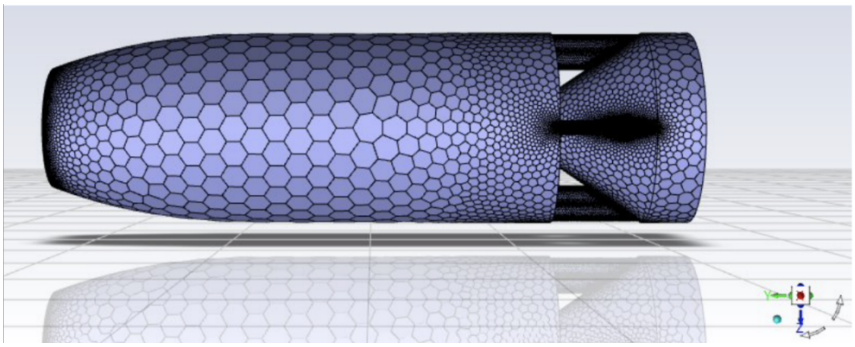

(a) 2024 Test Section Profile [1]

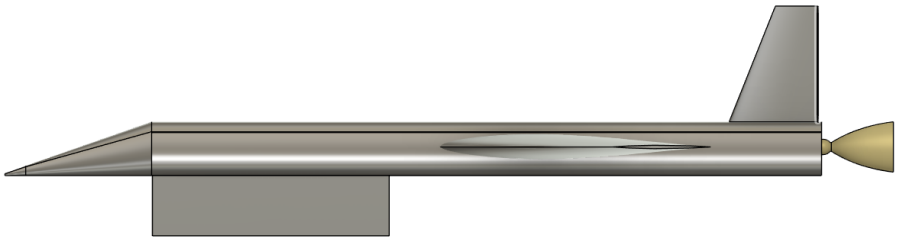

(b) Blended Wing Airframe Profile

Figure 72: Comparison of 2024 & 2025 Test Sections

3.4.2 Objective

The scope of work for the Fall 2024 term has been to design and develop an improved design of the previous airframe with the primary distinguishing factor being the test section location: it will be placed under the launch vehicle such that there is unimpeded through flow through the test section. This design is referred to as the "Blended Wing Airframe".

This is a systems engineering and design exercise, with the goal of a late-January Go/No-Go decision. To move forward with the blended wing airframe or retain the previous rocket airframe concept.

3.4.3 Design

3.4.3.1 Known Variables and Assumptions

3.4.3.2 V_∞ and Atmospheric conditions

Incoming airspeed can be determined based off of atmospheric conditions and the mach relations. To find the speed of sound at 70 000 ft at ISA conditions[45], see *Equation* 86 [52].

Relevant atmospheric properties are described in *Table* 11.

$$M = \frac{V_\infty}{\sqrt{\gamma R T_\infty}} \tag{86}$$

Table 11: Relevant Atmospheric Conditions at $70kft$

Density$[\frac{kg}{m^3}]$	0.07131
Temperature $[K]$	216.65
Speed of Sound $[\frac{m}{s}]$	295.04
Gravitational Acceleration $[\frac{m}{s^2}]$	9.5979

3.4.3.3 Airfoil Selection:

Referring to the previous year's report [1], it can be determined that a NASA Supercritical series airfoil was used [1] [48]. Specifically the NASASC2-0706 [53] was used for this iteration.

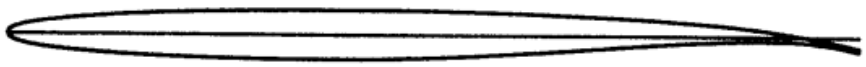

Figure 73: Example NASA Supercritical Airfoil (NASASC(2)-0706) - $6\%\frac{t}{c}$, $c_d = 0.7$ [48]

This transonic-specific airfoil is characterized by NASA between $0 < M < 0.82$ and has a significant increase in drag as the incoming airspeed approaches sonic conditions. Figure 74 depicts the change in the drag coefficient of an 11% thick supercritical airfoil. Lift coefficient or aerodynamic efficiency data cannot be determined analytically.

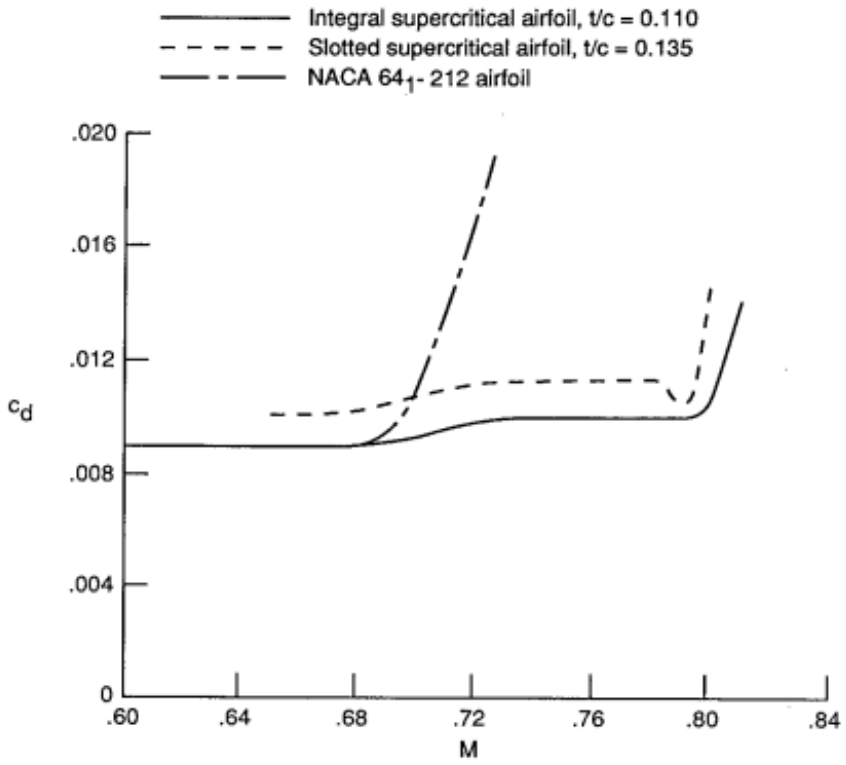

Figure 74: Test Section Location Comparison: 1) 2024 Section Flow - High Drag Design, 2) Blended Wing Underbody Design - No Flow Deflection [48]

The selected NASA SC(2)-0706 airfoil does not appear to adequately combine the cruise and glide phases of flight. Further analysis of this airfoil, and the potential selection of an alternative, will be left as future work. This is a significant task requiring experimental testing or computational simulations to provide conclusive results.

3.4.3.4 Thin Airfoil Assumption:

To proceed with the analysis, a thin airfoil assumption will be used, approximating the airfoil as a flat plate. While not entirely accurate due to the current baseline airfoil's positive camber and non-zero frontal area, this approximation is valid for supersonic conditions because of the 6% thickness-to-chord ratio ($\frac{t}{c}$). The assumption holds under the following conditions:

- The airfoil thickness is small relative to the chord length.

$$\frac{t}{c} << 1 \tag{87}$$

- The airfoil has a small A.O.A.

$$\alpha << 1 \tag{88}$$

- The airfoil's camber deviation from the centerline is minimal.

This simplification enables the estimation of lift parameters but does not account for lift at zero AoA due to camber. A flat plate approximation will be used to evaluate lift and drag coefficients, leveraging the low camber nature of the NASA supercritical airfoil series. Using the free body diagram of a flat plate (Figure 75), lift and drag forces in one-dimensional flow can be derived from the Navier-Stokes equations, shown in Equations 89-92. Under the assumption of infinitesimal thickness, at $\alpha = 0$, the lift coefficient (C_l) and wave drag coefficient ($C_{d_{wave}}$) both become zero.

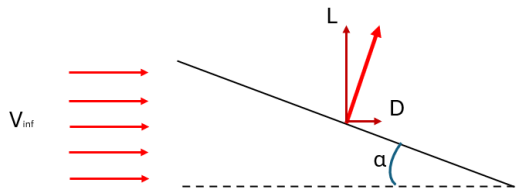

Figure 75: Free body diagram of flow over an angled flat plate

Wing performance characteristics required for the blended wing aircraft being designed by the airframe group. These are derived from the Navier-Stokes equations of fluid motion (see Equations 89-92).

$$\frac{\delta\rho}{\delta t} + \nabla\ (\rho\mathbf{V}) = 0 \tag{89}$$

$$\frac{\delta(\rho\ u)}{\delta t} + \nabla\ (\rho u * \mathbf{V}) = -\frac{\delta p}{\delta x} + \frac{\delta\tau xx}{\delta x} + \frac{\delta\tau yx}{\delta y} + \frac{\delta\tau zx}{\delta z} + \rho f_x \tag{90}$$

$$\frac{\delta(\rho\ v)}{\delta t} + \nabla\ (\rho v * \mathbf{V}) = -\frac{\delta p}{\delta y} + \frac{\delta\tau yx}{\delta x} + \frac{\delta\tau yy}{\delta y} + \frac{\delta\tau zy}{\delta z} + \rho f y \tag{91}$$

$$\frac{\delta(\rho\ w)}{\delta t} + \nabla\ (\rho w * \mathbf{V}) = -\frac{\delta p}{\delta z} + \frac{\delta\tau xz}{\delta x} + \frac{\delta\tau yz}{\delta y} + \frac{\delta\tau zz}{\delta z} + \rho f z \tag{92}$$

The lift and drag characteristic equations of an angled flat plate can be derived as the following relations, only wave drag terms are considered for the drag coefficient term for now as skin friction data is unavailable. These will be added in the future.

$$C_l = \frac{4\alpha}{\sqrt{M^2 - 1}} \tag{93}$$

$$C_d = \frac{4\alpha^2}{\sqrt{M^2 - 1}} \tag{94}$$

It is critical to note that Equation 93, the thin airfoil lift coefficient equation, is independent of the airfoil shape as this equations is specific to a flat plate. The flat plate drag coefficient, Equation 94, Is specific to the flat plate and any modification to the thin airfoil will modify the wave drag generated by the body cross-section.

3.4.3.5 Coefficient of Lift:

Previously the target lift coefficient was $C_l = 0.35$, this has proven unrealistic as we do not need to achieve this. Mainly the target Lift coefficient was obtained for transonic conditions for a deployable glide wing with a large aspect ratio. Recall, the NASA SC(2)-0706 airfoil was only characterized up to a Mach number of 0.82, as shown in Figure 74.

Using thin airfoil and flat plate assumptions, Table 12 shows updated lift coefficients for various AoAs, providing stricter constraints for the wing design until detailed parameters are refined through CFD and experimental methods. The lift and drag coefficients, respectfully, in Table 12 are determined using Equation 93 and Equation 94, shown above.

Table 12: Lift and Drag Coefficients at Various Angles of Attack from Thin Airfoil Approximations

Angle of Attack (α) (deg)	**α (radians)**	**C_L**	**Wave Drag ($C_{D_{wave}}$)**	**Induced Drag ($C_{D_{induced}}$)**	**Total Drag (C_D)**	**Aerodynamic Efficiency**
0	0	0	0.0000	0.0000	0.0000	/
1	0.0175	0.025	0.0004	0.0001	0.0005	46.74
2	0.0349	0.049	0.0017	0.0004	0.0021	23.44
3	0.0524	0.074	0.0039	0.0009	0.0047	15.61
5	0.0873	0.123	0.0108	0.0024	0.0132	9.37
10	0.1745	0.247	0.0431	0.0096	0.0526	4.69

Using this information, the $C_{l\alpha}$ plot can be created, this relates the lift coefficient to the angle of attack of the aircraft (ref Figure 76), $C_{l\alpha}$ being the slope of this plot. Experimental results will see a non linear portion at larger AoA's due to flow separation causing loss of lift and stall. In this case, from Figure 76, $C_{l\alpha} = 1.4142$.

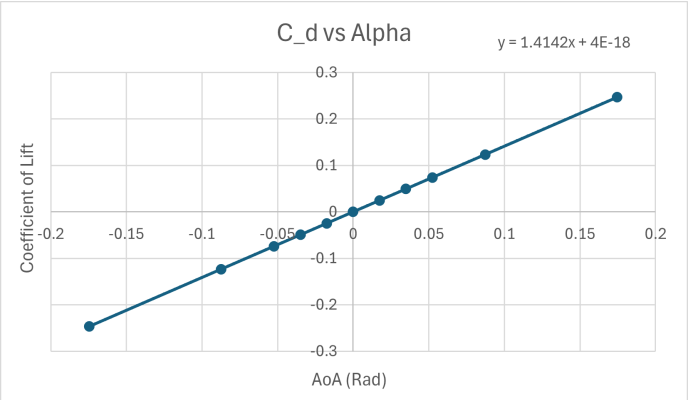

Figure 76: Effect of AoA on the Lift Coefficient of a Thin Airfoil

3.4.3.6 Coefficient of Drag:

Using the flat plate drag relation shown in Equation 94, the wave drag of the supersonic thin airfoil was estimated for various AoA's in Table 12. Although this wave drag estimation does not consider crucial factors such as induced drag, and skin friction drag. As skin friction drag cannot be calculated due to the immaturity of the design and material choices it will be left out for the time being.
The second component, induced drag, is relatively simple to calculate and can be determined with Equation 95

$$C_{d_{induced}} = C_{d_pmin} + kC_l^2 \tag{95}$$

The minimum drag polar term is dependent on the aircraft geometry, this term was set to zero until this parasitic drag can be determined using computational methods. Because of this. In the subsequent portions of this project it will be assumed that: $C_{D_pmin} = 0$.
Summing these drag terms together provides a simplified view of the drag parameters of the wing of the aircraft for cruise and glide portions of the flight. These drag values for various AoA's are shown in Table 12. The total drag coefficients are plotted against AoA in Figure 77. Due to the uncambered assumption, the drag polar is symmetrical, unlike that of significantly cambered airfoils.

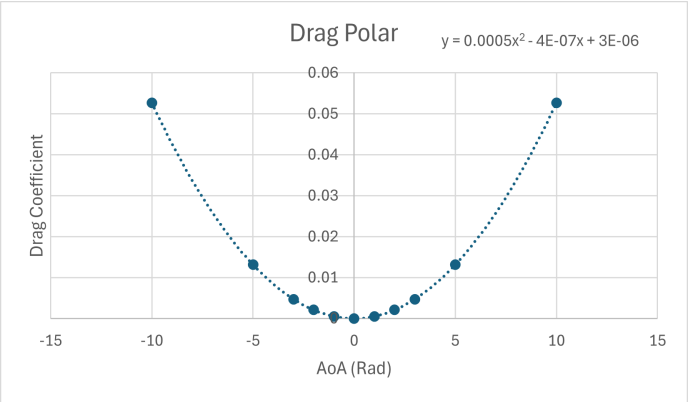

Figure 77: Drag Polar of Supersonic Thin Airfoil

3.4.3.7 A.O.A.:

The angle of attack of the wing to the incoming airflow will determine the amount of lift generated by the aircraft. This is closely coupled to the total area of the lifting surfaces as a small A.o.A., therefore lower C_l, can be compensated by a larger lifting surface area. Additionally, a large enough wing surface area needs to be used such that gliding performance is adequate for a return to home maneuver. Maximizing Aerodynamic efficiency, E, is critical for flight, for a small aircraft such as the one currently being designed, an efficiency between $5 - 15$ can be targeted.

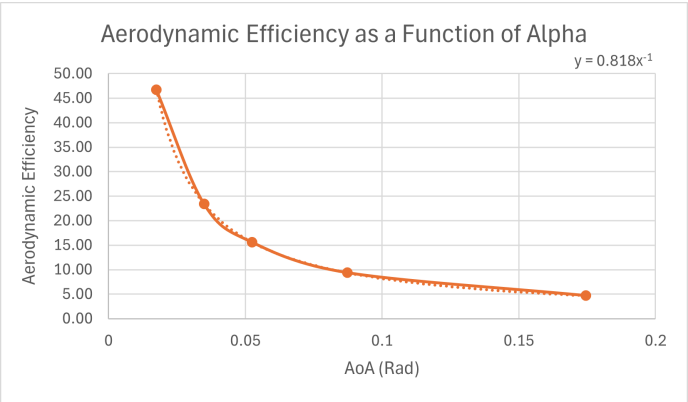

Figure 78: Effect of AoA on Aerodynamic Efficiency

From Figure 78 and Table 12, a 3 deg A.o.A. was selected to balance the lift required and the glide performance. See Table 13, a summary of the flight parameters at a 3 deg A.o.A..

Table 13: Airfoil performance parameters at a 3 deg angle of attack

α $[rad]$	0.0524
Lift Coefficient (C_l)	0.074
Total Drag Coefficient (C_d)	0.0077
Aerodynamic Efficiency $[E]$	9.57

3.4.3.8 Lift estimation:

A numerical integration method was used to obtain the total lift of the non-constant cross-section wing shown below in Figures 79 and 80.
The trapezoidal shape which can be solved analytically without integration is used to validate the integration methodology. This is done to confirm the validity of the method and all calculations and code written to achieve this objective. This can then be expanded on to contrast an compare multiple wing shapes, areas and airfoil characteristics. Such contrasting and comparisons will be left up to the following semesters work to effectively use this foundation for detail wing design.
The following, Equation 96, mathematically describes the numerical integration of the lift per unit span (L'_y). For numerical integration this integral form can be transformed to the summation shown in Equation 97 for a constant segment size.

$$L = \int_0^{b/2} L'_y dy \tag{96}$$

$$L = 2\ \Delta y \sum_{i=1}^{\frac{b}{2}-1} \frac{1}{2}\rho V_\infty^2 c(y_i) C_l(y_i) \tag{97}$$

A similar relation can be written for calculating the drag components.

$$D = 2\ \Delta y \sum_{i=1}^{\frac{b}{2}-1} \frac{1}{2}\rho V_\infty^2 c(y_i) C_d(y_i) \tag{98}$$

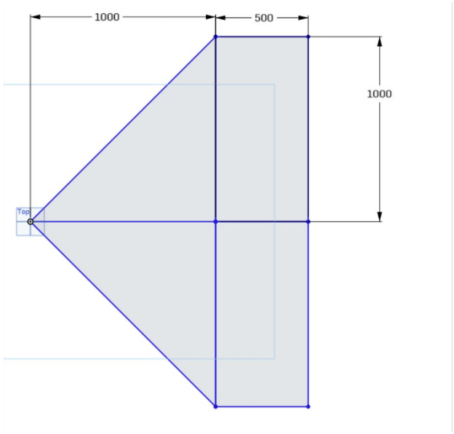

Figure 79: Plan form Area of Delta style wing ($2m^2$)

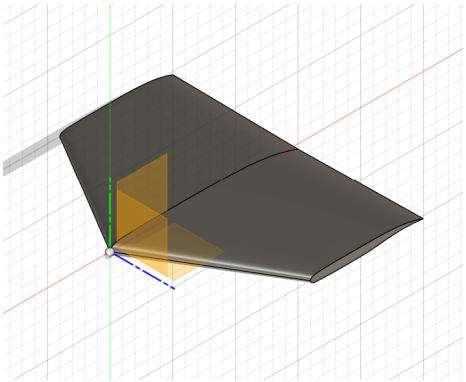

Figure 80: Isometric View of Delta Style Wing

This numerical integration was performed for the following segment sizes: 0.01, 0.02, 0.05, 0.1. See Table 14. The resultant of both the drag and lift convergence analysis showed a linear relation to segment size and the resultant lift and drag forces. See Figures 81 & 82, as such the nul segment size value can be estimated using a linear trend line, see Table 14.

Table 14: Lift and Drag Results as a Function of Segmentation Size Using a Numerical Integration Method

Convergence Comparison					
Segment Size $[m]$	0.1	0.05	0.02	0.01	[HTML]ADADAD0
Lift $[kN]$	3.93	4.04	4.10	4.12	[HTML]ADADAD4.14
Drag $[N]$	46.2	47.4	48.1	48.4	[HTML]ADADAD48.6

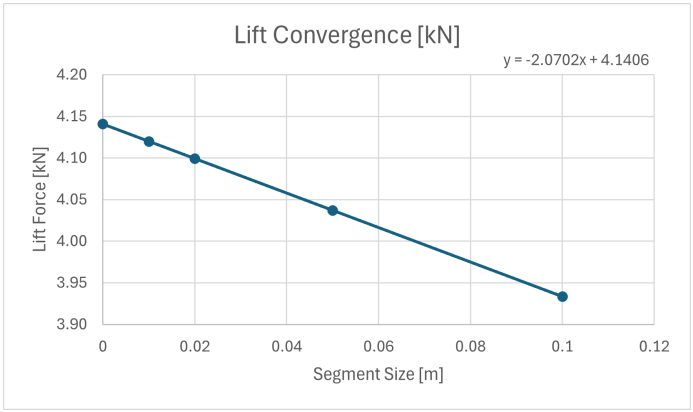

Figure 81: Segment Wise Convergence of Lift

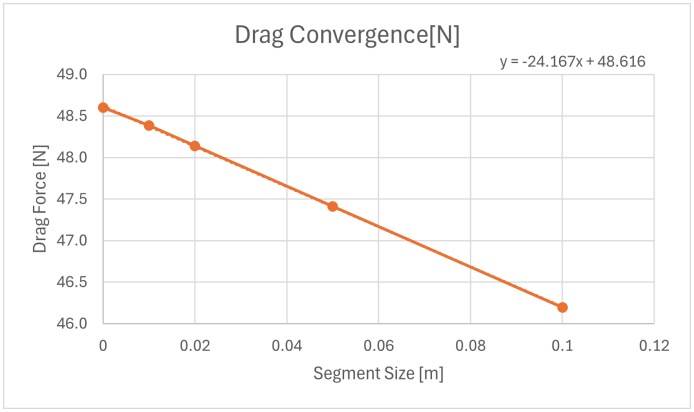

Figure 82: Segment Wise Convergence of Drag

$$L = \frac{1}{2}\rho V_\infty^2 S C_L \tag{99}$$

To validate these results the governing equations of lift and drag were used with identical parameters, see Table 15 below.

Table 15: Airfoil Performance Validation at a 3 deg AoA

/	Numerical Integration	Analytical	% Difference
Lift $[kN]$	4.141	4.140	0.02
Total Drag $[N]$	48.6	29.8	63.4

3.4.3.9 Continued Work

Having validated the methodology the next steps of this project are to determine the wing lift and shape while maintaining parity with the Controls and Avionics groups. All this with the goal of a a Go/No-go decision on direction to proceed with the design of this vehicle and focus the teams efforts in a singular direction.
To achieve this before the the end of January 2025, some key steps to take are performing CFD analysis to validate the use of the NASA supercritical airfoil previously selected. Key intermediate steps involve fine tuning the analytical drag values to include skin friction terms, to validate the CFD parameters.

Working in conjunction with Wissam and Graham, to perform a comprehensive comparison of the lifting body and rocket designs for the Go/No-go decision.

3.5 Lifting Body Structural Design - Wissam Aldouri

3.5.1 Introduction

The work presented in this section focuses on the design and analysis of a supersonic lifting body vehicle, specifically tailored for the mission profile involving steady cruise at Mach 3 and subsequent unpowered descent and recovery. The design process integrates mass and volume budgeting, aerodynamic optimization, and structural analysis to ensure a feasible layout and reliable performance throughout the mission phases.

3.5.2 Mass and Volume Budget

A mass and volume budget was established for the vehicle's primary systems to ensure a feasible internal layout and precise placement of the center of gravity (CG). Table 16 provides an overview of the estimated dimensions, volumes, and masses of the six major components. These values are derived from a combination of last year's data [1] and updated estimates tailored to this year's system requirements.

Table 16: Mass and Volume for Vehicle Systems

No.	Component Name	Dimensions (m)	Volume (m^3)	Mass (kg)
1	Propulsion System	Diameter: 0.244, Length: 1.99	0.093	194.6
2	Battery Bay	0.3 x 0.15 x 0.1	0.005	4.5
3	Avionics Bay	0.5 x 0.2 x 0.15	0.015	5.5
4	Front Landing Gear	0.5 x 0.15 x 0.1	0.008	5.5
5	Back Landing Gear	0.5 x 0.15 x 0.1	0.008	5.5
6	Test Section	12"x12", Length: 1.2	0.111	41.6

The propulsion system dimensions, with a diameter of 0.244 m and a length of 1.99 m, correspond to a volume of 0.093 m^3 and a mass of 194.6 kg. These values

were sourced from last year's report *page: 102* [1]. They remain consistent with the operational requirements for this year's design iteration until more defined values are obtained from the Trajectory Analysis subteam.

The battery bay is estimated at 0.3 m x 0.15 m x 0.1 m, resulting in a volume of 0.005 m^3 and a mass of 4.5 kg. These preliminary values reflect the power needs of the Schlieren imaging system, including the camera, light source, and data acquisition systems. Refinement of these estimates will depend on the finalized power system requirements and hardware selections.

The avionics bay, with dimensions of 0.5 m x 0.2 m x 0.15 m (volume: 0.015 m^3, mass: 5.5 kg), is essential for housing control systems and potential required future sensors.

The front and back landing gear are both estimated at 0.5 m x 0.15 m x 0.1 m each, contributing a volume of 0.008 m^3 and a mass of 5.5 kg per unit. These are preliminary estimates with further refinements expected as structural and mechanical analyses are completed.

The test section is going to be designed to accommodate the Schlieren imaging setup and is currently sized at 12 inches by 12 inches with a length of 1.2 m. These dimensions correspond to a volume of 0.111 m^3 and the mass of 41.6 kg is sourced from last year's report and spreadsheet as a baseline. These estimates ensure sufficient space for the optical system (total focal distance of 1 m) and its components. However, as the design progresses and imaging requirements are refined, the cross-sectional area and length of the test section are likely to decrease.

3.5.3 Internal Layout and Space Allocation

The internal layout of these components, shown in Figure 83, balances the propulsion system, test section, and avionics for optimal CG positioning. Placing the avionics and battery bay close to the test section is advantageous for several reasons. First, it minimizes the length of wiring required to connect the bays together, reducing potential signal losses and the overall weight of cabling. Shorter connections also improve reliability by reducing the risk of connection failures and electromagnetic interference (EMI) that could affect sensitive electronics within the test section. Additionally, having these components in close proximity allows for efficient power distribution to the sensors and cameras in the test section, which is crucial for maintaining stable operation during high-speed flight.

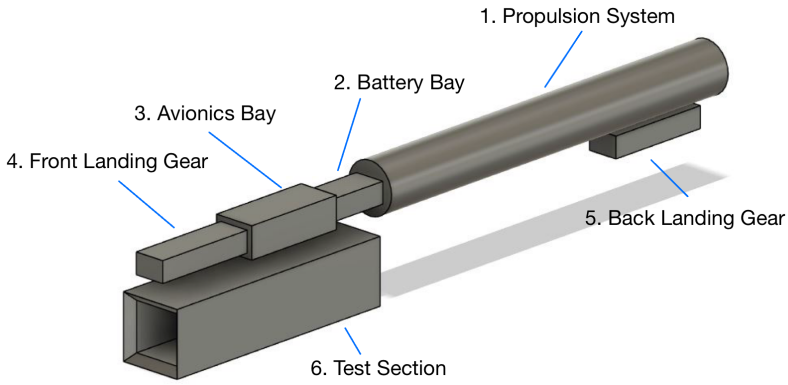

Figure 83: Internal Layout and Space Allocation

3.5.4 External Layout and Center of Gravity Analysis

The external layout and center of gravity are critical to achieving static stability for the vehicle. Both the initial center of gravity (wet mass configuration, CG_i) and final enter of gravity (dry mass configuration, CG_f) were determined based on the external layout, which is strongly influenced by aerodynamic performance and structural considerations. The CG_i is located at 2625 mm from the nose, while the CG_f is at 2293 mm from the nose. These positions are the result of iterative aerodynamic simulations and structural analyses to balance stability and performance.

The fuselage features a flat-bottomed cross-section, shown in Figure 84, to accommodate the test section and generate lift when the angle of attack (AOA) exceeds zero degrees for gliding purposes. The fuselage is constructed from Aluminium 6061 T6, chosen for its lightweight nature, favorable thermal properties, and a density of 2700 kg/m^3 [54]. This material has been widely used in aerospace applications due to its balance of structural strength, corrosion resistance, and machinability [55]. For the design speed and mission requirements, Aluminum 6061 T6 offers sufficient thermal resistance and strength-to-weight ratio to ensure the vehicle remains efficient during both cruise and unpowered gliding phases.

The structure incorporates two distinct thicknesses, 10 mm for the forward section (2.135 m) and 5 mm for the rear section (2 m), as determined in the Thermal Analysis section 3.7. This may make manufacturing of the fuselage difficult, but if done correctly it would have the benefit of removing the unwanted dead weight. These variations in thickness are done to handle the varying aerodynamic and thermal loads across the fuselage as discussed in the Thermal Analysis section 3.7. Based on these parameters, the total mass of the fuselage is calculated to be 84.915 kg using Equation 100:

$$m = \rho V = \rho A L \tag{100}$$

where A is the cross-sectional area, L is the length, and ρ is the density. Table 17 summarizes the key parameters used for the mass calculation.

Table 17: Fuselage Design Parameters

Section	**Thickness (mm)**	**Cross-sectional Area (m^2)**	**Length (m)**
Front	10	0.01	2.135
Back	5	0.005	2.000

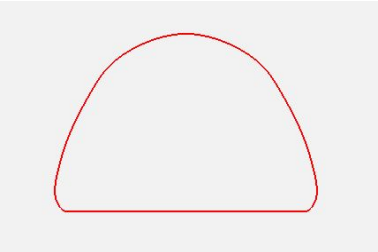

Figure 84: Flat-Bottom Fuselage Cross-Section

The fuselage incorporates a nose cone designed to position the test section as far forward as possible, minimizing internal shock waves and meeting the requirements of the Schlieren imaging subteam. The relationship between the shock wave angle (β) and the Mach number (M) for an attached shock is given by [56]:

$$\beta = \sin^{-1}\left(\frac{1}{M}\right) \tag{101}$$

For $M = 3$, the shock wave angle is calculated to be 19.5°. To optimize aerodynamic performance, the nose cone angle should ideally align closely with this value. A larger nose cone angle, such as the current 29°, causes the formation of a detached bow shock, increasing wave drag and creating unfavorable pressure gradients. Conversely, aligning the nose cone angle closer to 19.5° would minimize wave drag and allow for smoother flow attachment.

However, the 29° nose cone angle enables the test section to be positioned farther forward, which is critical for the Schlieren imaging system's functionality. A compromise can be achieved by reducing the nose cone angle to 21°, maintaining compatibility with the shock wave angle while ensuring that the wings remain behind the shock for aerodynamic stability. This trade-off balances the

objectives of minimizing drag, maintaining stability, and accommodating the forward placement of the test section.

Further analysis and simulations are necessary to finalize the nose cone angle, ensuring that it achieves a balance between aerodynamic efficiency and system integration requirements.

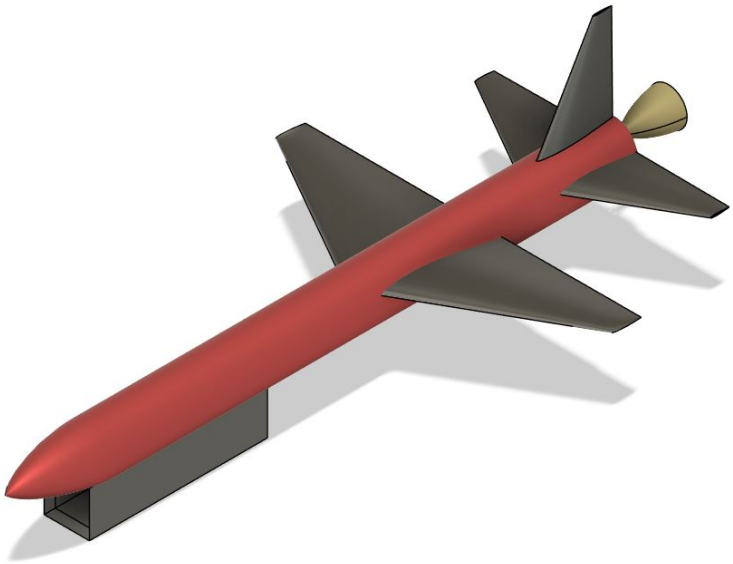

Figure 85: CAD Model of the Lifting Body

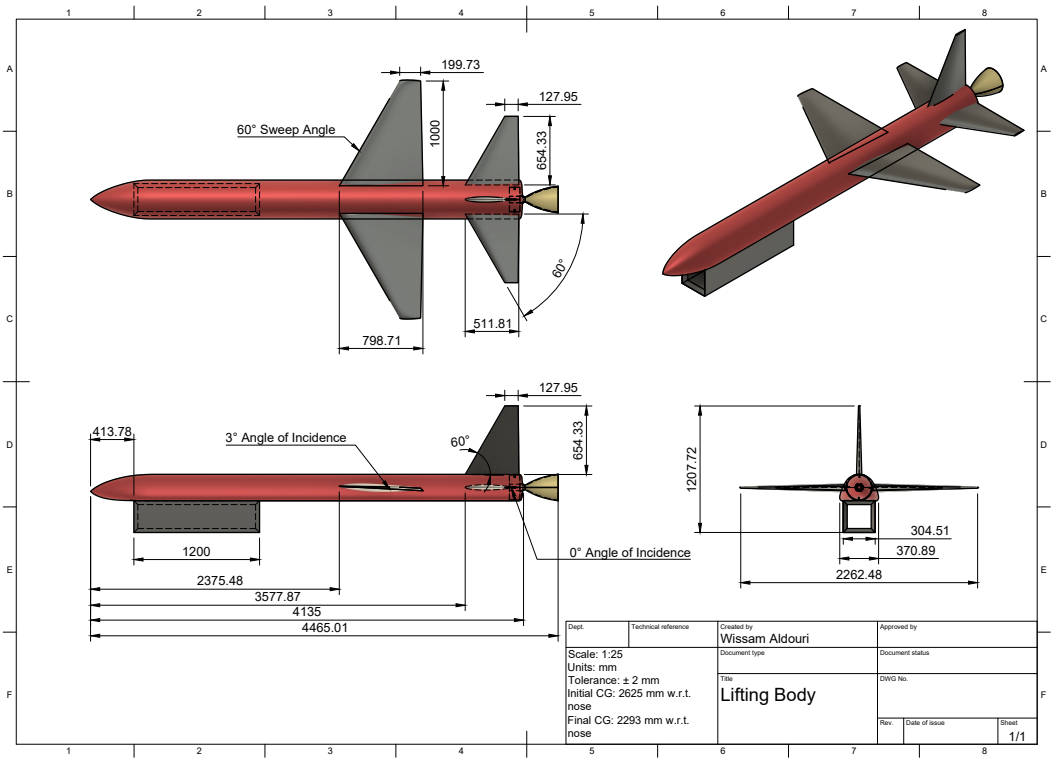

Figure 86: Lifting Body Engineering Drawing

The wings and control surfaces shown in Figure 86, are sized to provide the required lift and static stability during cruise, as discussed in the Aerodynamic Analysis section 3.5.5.

The wing design uses a NASASC2-0714 airfoil [57], chosen last year, and incorporates a 3-degree angle of incidence. The wings are positioned at 2.375 m from the nose, ensuring that changes in CG due to fuel consumption do not significantly affect the pitching moment. Additionally, the wings are designed with a 60-degree sweep angle. This design strikes a balance between supersonic performance at Mach 3 during the 30-second test duration and subsonic gliding requirements for the unpowered descent and landing.

Unlike a delta wing, which performs well at high speeds due to its high sweep angle and low drag at supersonic conditions, the chosen swept wing design has several advantages for this mission. Delta wings are less efficient at subsonic speeds and exhibit higher induced drag during glide, reducing the vehicle's horizontal range and making unpowered landings less effective [58]. The 60-degree swept wings ensure sufficient supersonic performance during the cruise phase while maintaining better lift-to-drag characteristics at lower speeds, crucial for

maximizing the glide distance after burnout. This is particularly important given the mission's dual requirements of achieving steady flight at Mach 3 and enabling an effective glide for unpowered recovery.

Furthermore, a Blended Wing Design is being investigated as an alternative approach to further enhance aerodynamic efficiency. Blended wings offer the potential to integrate the control surfaces and stabilizers more seamlessly with the fuselage, resulting in improved lift-to-drag ratios and reduced wave drag. This design could also enhance overall stability during the mission's critical phases, such as supersonic cruise and unpowered descent.

The horizontal stabilizers, employing a symmetric airfoil of NACA 63A010 [59], are set at a 0-degree angle of incidence and positioned at the end of the fuselage, as shown in Figure 85, to ensure static pitching stability. The symmetric airfoil ensures minimal pitching moment contribution during steady-level flight while providing sufficient authority to counteract pitch disturbances.

The vertical stabilizer, also using a NACA 63A010 airfoil, has dimensions that are currently assumed to provide adequate yaw stability. However, these dimensions are subject to further refinement based on detailed aerodynamic analyses. For now, the masses of the wings and control surfaces are estimated at 70 kg and 30 kg, respectively.

This design choice reflects a deliberate compromise between high-speed aerodynamics and subsonic glide performance, ensuring the vehicle's ability to meet both its test objectives and recovery requirements effectively.

The center of gravity for the entire vehicle is calculated using the following equation:

$$x_{\text{CG}} = \frac{\sum(m_i x_i)}{\sum m_i} \tag{102}$$

where:

- x_{CG} is the center of gravity location from the reference point (nose of the vehicle),
- m_i is the mass of the i-th component,
- x_i is the distance of the i-th component's CG from the reference point.

The calculated x_{CG} values, along with the mass and CG contributions of individual components, are presented in Table 18.

Table 18: Overall Mass and CG Analysis of Vehicle

Component	Mass (kg)	Length (m)	CG Distance from Nose (m)	$m_i \cdot x_i$ (kg-m)
Propulsion System	194.600	1.990	3.140	611.044
Battery Bay	4.500	0.300	1.995	8.978
Avionics Bay	5.500	0.500	1.595	8.773
Front Landing Gear	5.500	0.500	1.095	6.023
Back Landing Gear	5.500	0.500	3.500	19.250
Test Section	41.600	1.200	1.013	42.141
Fuselage	84.915	4.135	2.068	175.562
Wings	70.000	0.800	2.775	194.250
Control Surfaces	30.000	0.500	3.885	116.550
TOTAL Wet Mass	442.115	—	—	CG_i: 2.625 m from the nose
TOTAL Dry Mass	268.715	—	—	CG_f: 2.293 m from the nose

The preliminary mass and CG data ensure that the vehicle layout supports aerodynamic and structural requirements while attempting to maintain static stability. The CG_i is located at 2625 mm from the nose, while the CG_f shifts to 2293 mm from the nose. This shift is attributed to the consumption of propellant during flight, reducing the mass of the propulsion system from 194.6 kg to 21.2 kg after burnout, based on last year's analysis, results in a 268.7 kg dry mass. This change significantly alters the mass distribution.

A detailed engineering drawing can be found in Figure 86. Further refinements will integrate results from ongoing aerodynamic simulations and material selections, ensuring precise alignment with mission requirements.

3.5.5 Aerodynamic Analysis

3.5.5.1 Assumptions

The aerodynamic analysis focuses on the cruise phase of the vehicle, assuming steady conditions at Mach 3 for a 30-second test duration. The final center of gravity, calculated as 2.293 m in the previous section and approximated to be zero in the vertical axis from the nose, was used for all simulations. The main goal of this analysis is to achieve the required lift for level flight while maintaining 0° angle of attack during cruise. This configuration ensures stable operation and minimizes disruptions to the test section.

3.5.5.2 Methodology and Tools

The simulations were conducted using Open Vehicle Sketch Pad (OpenVSP), a parametric tool for aerodynamic modeling [60]. OpenVSP was used to simulate the vehicle's aerodynamic performance, but the test section was excluded from the geometry due to OpenVSP's limitation with open geometries. Despite this, the test section's center of gravity was included in the analysis to maintain accuracy.

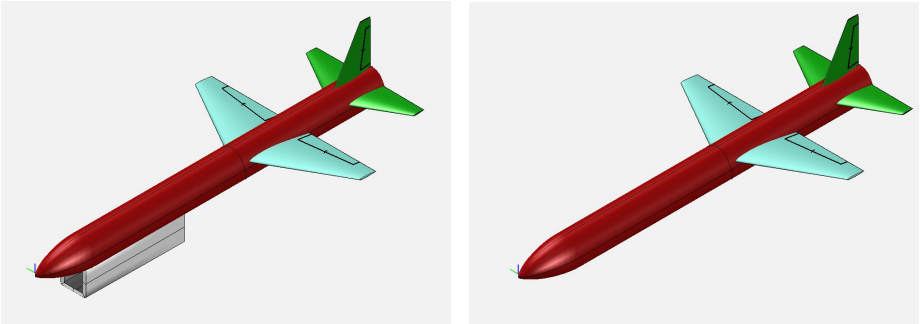

(a) OpenVSP Model Including Test Section

(b) OpenVSP Model Excluding Test Section

Figure 87: Comparison of OpenVSP Models With and Without the Test Section

Figure 87a and Figure 87b show the OpenVSP models with and without the test section, respectively. Iterative simulations were performed to ensure level cruise at 0° AOA, as this configuration is critical for stable imaging conditions.

3.5.5.3 Equations

To calculate the aerodynamic parameters for the cruise phase, the following equations were used:

1. Required Lift Steady Cruise:

$$L = mg \tag{103}$$

where:

- L: Lift force (N),
- m: Mass of the vehicle (kg),
- g: Gravitational acceleration.

The parameters used for the lift calculation are summarized in Table 19.

Table 19: Parameters for Lift Calculation

Parameter	**Value**	**Unit**
Vehicle Dry Mass (m)	268.72	kg
Gravitational Acceleration (g)	9.81	m/s^2
Lift Force (L)	2636.09	N

2. Lift Coefficient Equation [61]:

$$C_L = \frac{L}{0.5\rho V^2 S} \tag{104}$$

where:

- C_L: Coefficient of lift (dimensionless),
- L: Lift force (N),
- ρ: Air density (kg/m^3),
- V: Freestream velocity (m/s),
- S: Wing area (m^2).

The parameters used for the lift coefficient calculation are found in Table 20.

Table 20: Parameters for Lift Coefficient Calculation

Parameter	**Value**	**Unit**
Lift Force (L)	2636.09	N
Air Density (ρ)	0.07131 [62]	kg/m^3
Freestream Velocity (V)	885.12 [63]	m/s
Wing Area (S)	1.0	m^2
Coefficient of Lift (C_L)	0.0948	–

The taper ratio (λ) and the Mean Aerodynamic Chord (c_{MAC}) are calculated using the following equations:

3. Taper Ratio [64]:

$$\lambda = \frac{c_t}{c_r} \tag{105}$$

where:

- c_t: Tip chord length (m),
- c_r: Root chord length (m).

The calculated value of λ is shown in Table 21.

Table 21: Parameters for Taper Ratio Calculation

Parameter	**Value**	**Unit**
Tip Chord (c_t)	0.2	m
Root Chord (c_r)	0.8	m
Taper Ratio (λ)	0.25	–

4. Mean Aerodynamic Chord [64]:

$$c_{MAC} = \frac{2}{3} c_r \left(\frac{1 + \lambda + \lambda^2}{1 + \lambda} \right) \tag{106}$$

where:

- c_{MAC}: Mean Aerodynamic Chord (m),
- c_r: Root chord length (m),
- λ: Taper ratio (dimensionless).

The calculated value of c_{MAC} is shown in Table 22.

Table 22: Parameters for Mean Aerodynamic Chord Calculation

Parameter	**Value**	**Unit**
Root Chord (c_r)	0.8	m
Taper Ratio (λ)	0.25	–
Mean Aerodynamic Chord (c_{MAC})	0.56	m

5. Reynolds Number Equation [65]:

$$Re = \frac{\rho V c_{MAC}}{\mu} \tag{107}$$

where:

- Re: Reynolds number (dimensionless),
- ρ: Air density (kg/m^3),
- V: Freestream velocity (m/s),
- c_{MAC}: Mean Aerodynamic Chord (m),
- μ: Dynamic viscosity (Pa $\cdot$ s).

The parameters for the Reynolds number calculation are found in Table 23.

Table 23: Parameters for Reynolds Number Calculation

Parameter	**Value**	**Unit**
Air Density (ρ)	0.07131 [62]	kg/m^3
Freestream Velocity (V)	885.12 [63]	m/s
Mean Aerodynamic Chord Length (c_{MAC})	0.56	m
Dynamic Viscosity (μ)	1.421×10^{-5} [62]	Pa $\cdot$ s
Reynolds Number (Re)	2.49×10^6	–

The required coefficient of lift for steady cruise at 0° AOA is $C_L = 0.0948$, which ensures that the lift force matches the vehicle's weight during level flight. The Reynolds number for the cruise condition, calculated as $Re = 2.49 \times 10^6$, was used to set up the simulation parameters in OpenVSP.

3.5.5.4 Results and Discussion

The results of the aerodynamic simulations are presented in Figures 88, 89, 90, and 92, showcasing the vehicle's aerodynamic performance during cruise at Mach 3. These figures provide a detailed analysis of key parameters, including the pressure distribution over the vehicle's surface, the variation of lift, pitching moment coefficients, and the lift-to-drag ratio with angle of attack. Together, they validate the design's ability to achieve stable flight, maintain aerodynamic efficiency, and meet the mission's requirements of high-speed performance and unpowered recovery. Each figure highlights specific aspects of the design's effectiveness, offering critical insights into the interaction of aerodynamic forces with the vehicle's geometry.

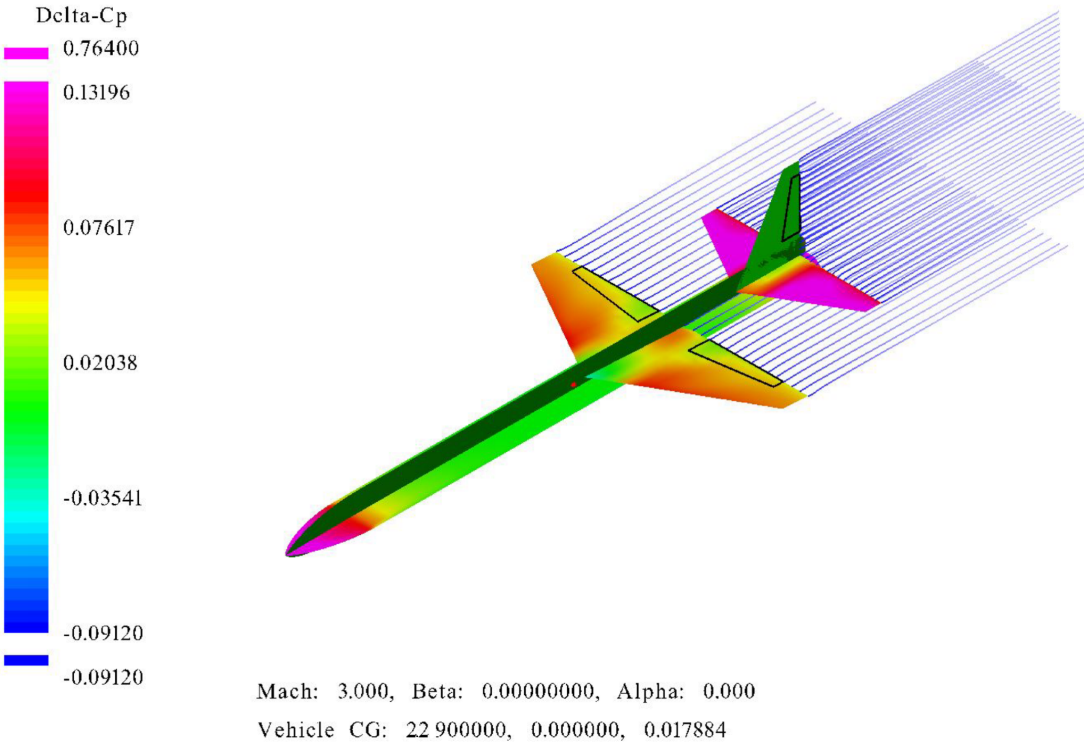

Figure 88: Pressure Distribution at Mach 3

Figure 88 illustrates the pressure distribution over the vehicle's surface during Mach 3 cruise. The high-pressure regions, shown in pink and red, are concentrated around the nose cone, where the initial shock compression occurs, and along the leading edges of the wings and horizontal stabilizers. These

high-pressure areas are consistent with the expected regions of maximum aerodynamic loading. The transition to lower-pressure zones, depicted in lighter colors, occurs smoothly across the midsection and trailing edges of the fuselage, confirming controlled airflow over these surfaces. The uniform pressure gradients in the figure also demonstrate that the wings and stabilizers are effectively positioned behind the primary shock wave, reducing aerodynamic interference and ensuring stable flight conditions.

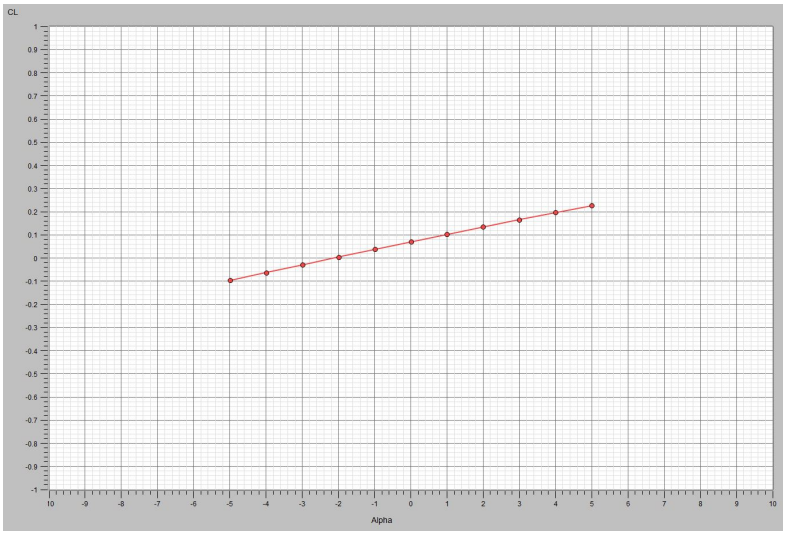

Figure 89: Lift Coefficient (C_L) vs. Angle of Attack (α)

Figure 89 depicts the variation of the lift coefficient (C_L) with the angle of attack (α). The linear relationship confirms stable lift generation. At 0° α, C_L is approximately 0.08, which is close to the required lift coefficient of 0.0948 for steady cruise at 0° α. However, further design refinement is necessary to achieve the exact C_L for better stability.

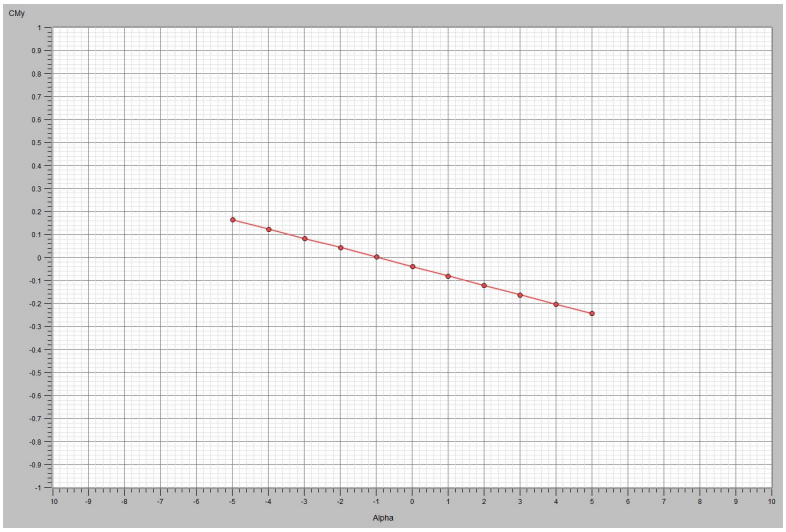

Figure 90: Pitching Moment Coefficient (C_{My}) vs. Angle of Attack (α)

Figure 90 shows the variation of the pitching moment coefficient (C_{M_y}) with α. The negative slope of the curve indicates stable pitching behavior, primarily due to the inclusion of horizontal stabilizers. A negative slope implies that the aircraft exhibits restoring moments in response to changes in pitch angle: if the nose pitches down, the negative slope causes C_{M_y} to increase, generating a moment that raises the nose back up. Conversely, if the nose pitches up, C_{M_y} decreases, producing a moment that pushes the nose back down. This self-correcting behavior is critical for static stability and ensures that the vehicle can naturally return to equilibrium after small disturbances. At $0°$ α, C_{M_y} is approximately -0.04, which, while stable, is not ideal. Achieving $C_{M_y} = 0$ at $0°$ α is a target for improved static stability, necessitating further design refinements and aerodynamic adjustments.

Prior simulations without horizontal stabilizers resulted in a positive slope as shown in Figure 91, which is detrimental to static stability, as it would amplify pitch deviations rather than counteract them.

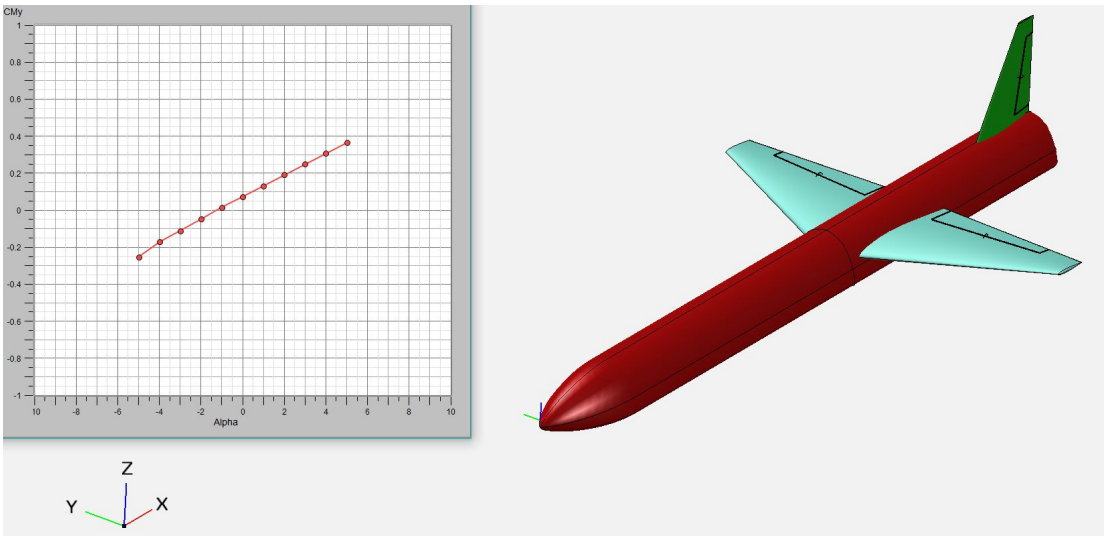

Figure 91: Pitching Moment Coefficient (C_{My}) vs. Angle of Attack (α) without Horizontal Stabilizers

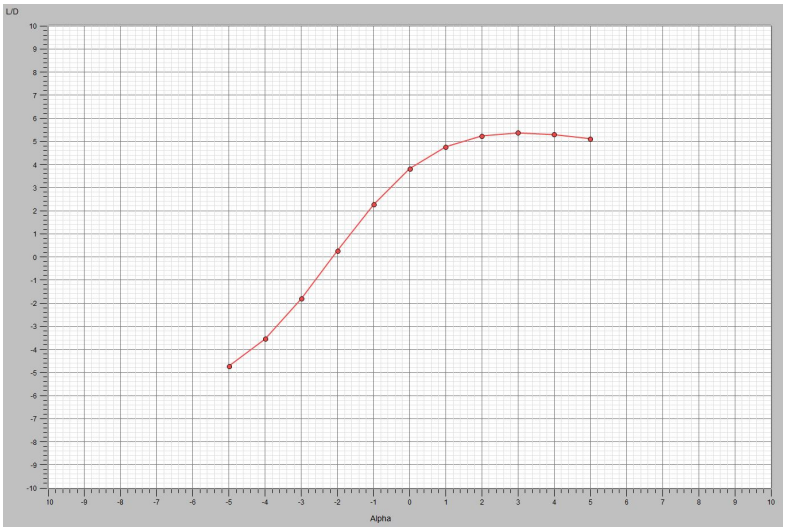

Figure 92: Lift-to-Drag Ratio (L/D) vs. Angle of Attack (α)

Figure 92 highlights the lift-to-drag (L/D) ratio across varying angles of attack. The maximum L/D ratio of 5.4 occurs at 3° α, which aligns with effective cruise efficiency. However, this value needs improvement to enhance the gliding performance and extend the horizontal distance covered during the vehicle's un-

powered landing phase. Achieving a higher L/D ratio would ensure the vehicle meets its operational range.

3.5.6 Conclusion and Future Work

The analysis presented in this section provides valuable preliminary insight into the vehicle's cruise performance, focusing on achieving stable lift and static stability. However, further work is essential to refine the design and ensure a holistic approach to all phases of the mission.

First and foremost, the test section must be incorporated into future aerodynamic analyses to ensure consistency and validate the overall performance. This step is critical to verify that the aerodynamic performance of the vehicle aligns with the functional requirements of the test section, particularly under the conditions of Mach 3 cruise.

Additionally, more detailed work is required to refine the aerodynamic characteristics of the vehicle. This includes: - Conducting comprehensive drag analyses, encompassing parasitic, wave, and shock drag contributions, to optimize the vehicle's aerodynamic efficiency across all mission phases. - Expanding the scope of analysis to include other mission phases, such as descent and recovery, to ensure the vehicle performs reliably throughout the entire mission profile.

The center of gravity placement must also be continually reassessed as the design evolves to maintain static stability across different configurations and mission phases. Iterative simulations and adjustments will be necessary to account for design changes and payload dynamics.

On the structural front, Finite Element Analysis (FEA) must be performed to evaluate the structural integrity of the vehicle under various loading conditions. This will ensure that the design is robust enough to withstand the extreme aerodynamic forces encountered during high-speed flight and other mission phases.

While the current results establish a foundation, additional work in aerodynamic, CG, and structural analyses is required to complete the design and prepare the vehicle for its intended mission.

3.6 Landing Gear - Ruxin Zhang

Peer Reviewed by: Yancheng Ding

3.6.1 Introduction

In this project, the design goal of the landing gear was to ensure that the rocket would be safer and more stable when it landed, thus enabling recycling. This not only means having the ability to support the rocket's dead weight, but also requires that when the rocket lands on the ground at high speed, the landing gear is able to effectively absorb and cushion the impact to avoid damage to

the rocket structure. The design of the landing gear needs to include shock-absorbing components, which can effectively disperse and absorb the impact energy, thereby minimizing damage to the rocket body. Moreover, in order for the landing gear not to take up too much space and reduce air resistance during the launch and flight of the rocket, the design also needs to consider its reasonable deployment and storage methods.

3.6.2 Research

I have looked up some information about the landing part of the rocket body which is not a traditional landing gear, but a landing leg.
If our rocket is a body shape, it is difficult to control the balance of the rocket body during landing with the traditional landing gear or the landing skid that was designed by the design team last year, and the rocket will be easily tipped over during the landing skid.
Referring to SPACEX's falcon 9 rocket, their rocket is divided into two stages, only the first stage is used for recovery, there are 4 landing legs in the first stage, the first stage rocket needs to be flipped by the cold gas thrusters, so that the bottom of the rocket is facing towards the earth, ready to enter the atmosphere. At this point, the rocket's motors perform a "return burn", i.e., a re-fire, in order to adjust their trajectory and begin the return to the launch site or landing platform [66]. Since we are a solid rocket, modeling this landing method may require additional engines to control the landing attitude of the rocket, making the design of the system more complicated.
If we design the landing of a rocket in the shape of an airplane, we can use the landing gear traditionally used for airplane landing, and the main design and deployment method of the airplane landing gear can also be used as a reference.

3.6.3 Shock Absorber

Due to the need to maintain fluid stability of the rocket in flight, the landing gear is to be designed to be retractable in order to maintain minimum drag during the flight of the rocket and to be deployed only during landing. Large airplane landing gear typically consists of multiple wheels. According to last year's report information, the empty weight of our rocket is at 80.34kg, my design is two wheels on one strut, this configuration is suitable for most light weight vehicles and can provide good stability and support.
The strut portion of the landing gear is designed as an oleo strut to provide better shock absorption. The shock strut uses two retractable cylinders, both of which are closed at the outer ends. The top cylinder is attached to the airplane and the bottom cylinder is attached to the landing gear. The bottom cylinder, often referred to as the piston, is also free to slide in and out of the top cylinder [67].

3.6.4 Landing gear model simplification

Landing gear fitted with oleo strut can be simplified to a mass-spring-shock absorber system, with the shock absorber acting as a spring and damper. The tires act as springs [68].A simplified diagram of the landing gear is shown in below figure.

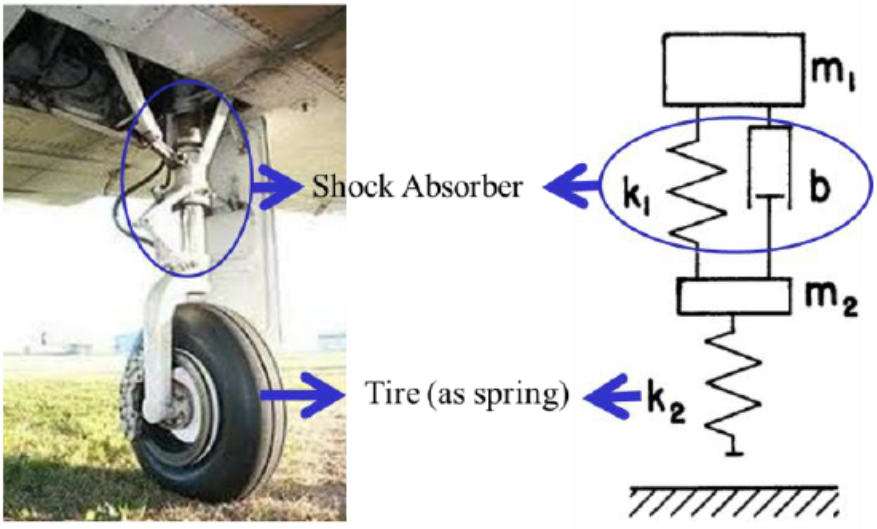

Figure 93: simplified diagram of the landing gear

3.6.5 Equation and modeling of Landing gear motion

Based on Newton's second law, the following equations can be listed to find the resultant force and displacement acting on the airframe[68].

$$F_1 = m_1\ddot{x}_1 = W_1 - F_(spring) - F_(damping) \tag{108}$$

$$F_2 = m_2\ddot{x}_2 = F_(spring, shockabsorb) + F_(damping) - F_(spring, tire) \tag{109}$$

$$m_1\ddot{x}_1 + k_1(x_1 - x_2) + b(\dot{x_1} - \dot{x_2}) = W_1 \tag{110}$$

$$m_2\ddot{x}_2 - k_1(x_1 - x_2) - b(\dot{x_1} - \dot{x_2}) + k_2x_2 = 0 \tag{111}$$

where:
b: Shock absorber damping coefficient
F_1: Net force acting on airframe
F_2: Ground reaction force
g: Gravity
k_1: Shock absorber spring constant
k_2: Tire spring constant

L: Lift force acting on aircraft
m_1: Aircraft mass (per landing gear)
m_2: Sum of wheel, tire and axle mass
V: Aircraft vertical speed (descent velocity)
W_1: Aircraft weight minus lift force
x_1: Displacement of shock absorber
x_2: Displacement of wheel
The model is built in MATLAB/Simulink based on the derived equation as shown below.

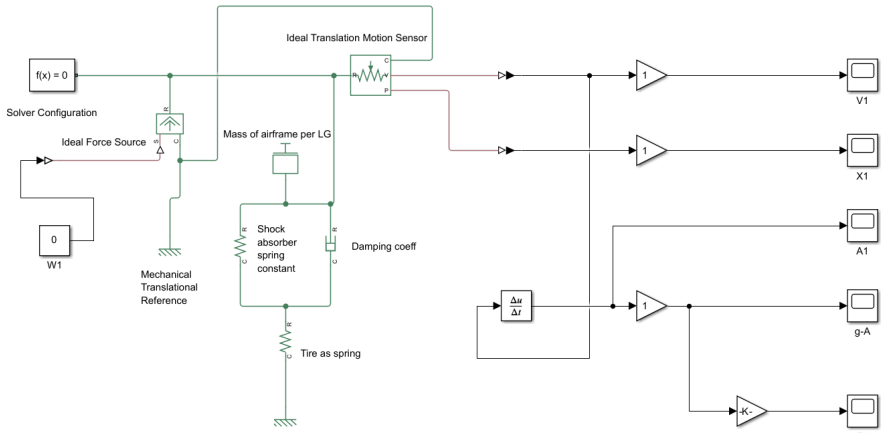

Figure 94: MATLAB/Simulink mode of the landing gear

In this model, the required inputs are k1: shock absorber spring constant, b: shock absorber damping coefficient, k2: tire spring constant, m1: fuselage mass (for each landing gear) and V: vertical velocity of the aircraft (descent velocity). The most important outputs are F1: net force acting on the fuselage and x1: shock absorber displacement.

3.6.6 MATLAB/Simulink model operation

The model will be run using the following parameter data as inputs.
k_1=3000N/M
k_2: 5000N/M
b: 200N*s/M
m_1: 27KG
V: 3m/s
The plots of F1: Net force acting on the airframe and X1: Displacement of shock absorber are shown below.

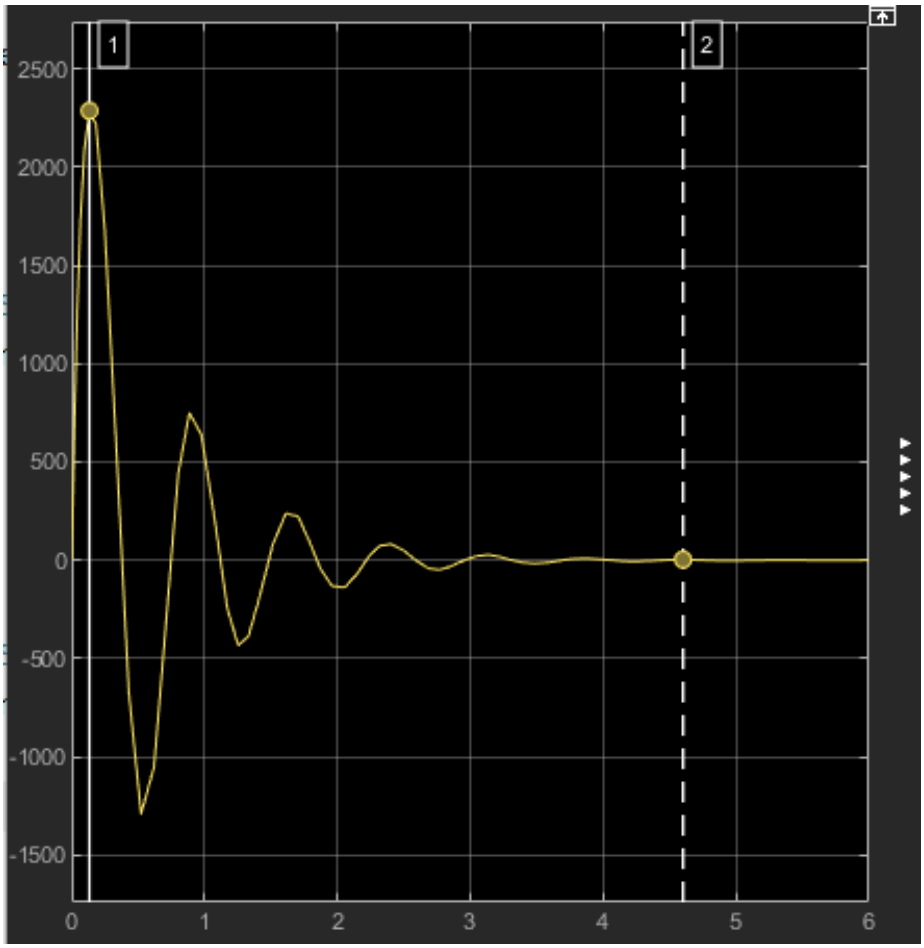

Figure 95: Plot of F1(net force acting on the fuselage)

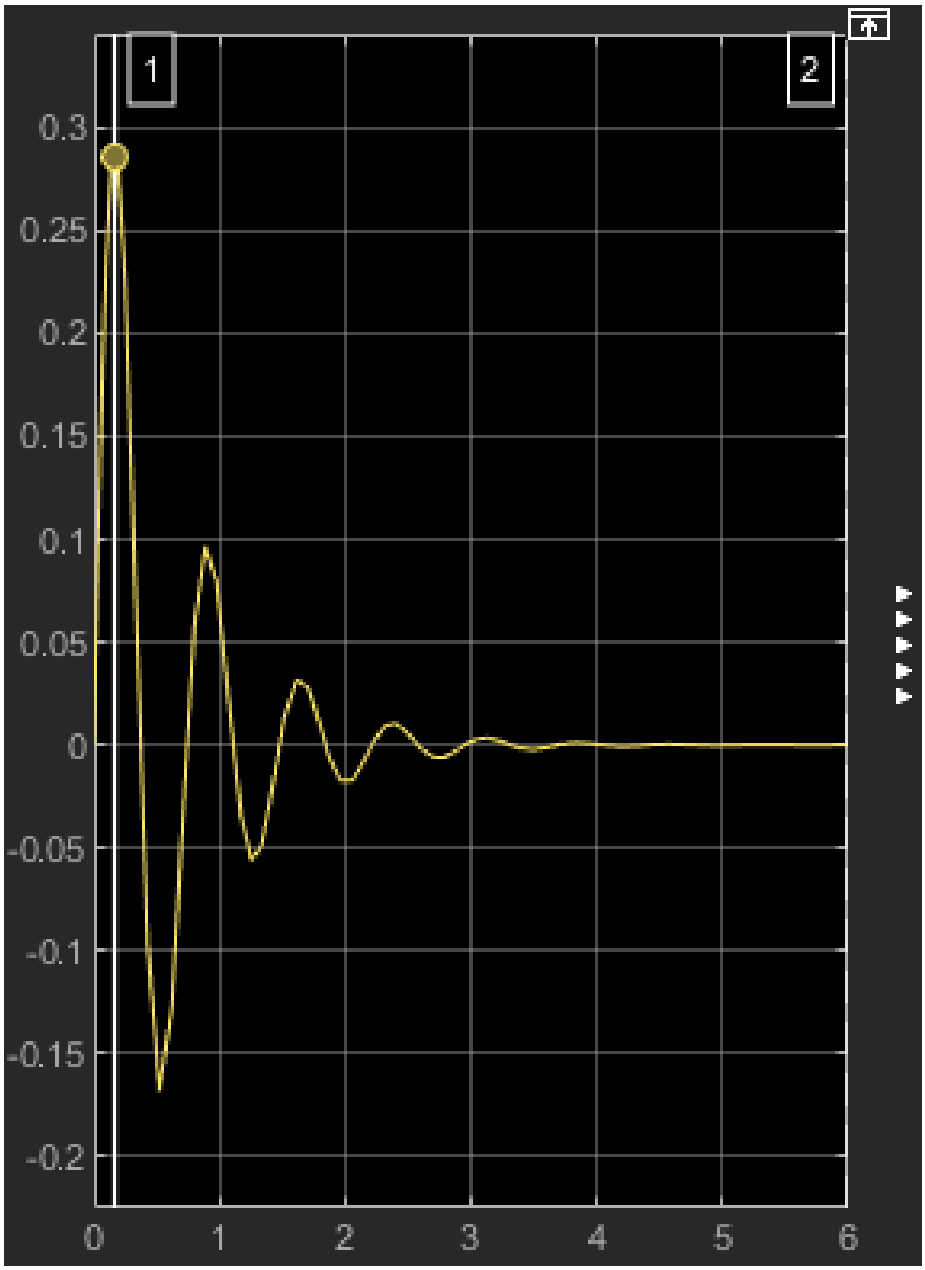

Figure 96: Plot of x1(Displacement of shock absorber)

As can be seen from these two graphs, the maximum net force acting on the airframe by the landing gear is analyzed to be 2,290N at touchdown, and the maximum displacement of the shock absorber (oil-pressure strut) is 0.2875m

3.6.7 Sensitivity Study

With the values of m1 and V fixed to change b, k1 and k2 go for a sensitivity study. The two outputs, F1 and x1, are observed by varying only one parameter of these three at a time.The sensitivity analysis obtained is shown below.

Case Number	Input design parameters						Output parameter			
	b(N*s/m)	change	k1(N/m)	change	k2(N/m)	change	max x1(m)	change	max F1(N)	change
baseline	200		3000		5000		0.2875		2290	
1	180	-10%	3000		5000		0.2953	2.71%	2261	-1.27%
2	220	10%	3000		5000		0.2833	-1.46%	2328	1.66%
3	200		2700	-10%	5000		0.2914	1.36%	2227	-2.75%
4	200		3300	10%	5000		0.2845	-1.04%	2338	2.09%
5	200		2700		4500	-10%	0.2965	3.13%	2244	-2%
6	200		2700		5500	10%	0.2809	-2.30%	2325	1.53%

Figure 97: sensitivity analysis

From this sensitivity analysis, it can be observed that the input design parameters b, k1 and k2 are all proportional to the force F1, but inversely proportional to the displacement of the strut x1.By adjusting these three parameters we can trade-off the two outputs F1 and X1.

3.6.8 Self Locking Device

Regarding the self-locking result of the landing gear, I would like to use a worm gear transmission. A worm gear transmission is a gear mechanism that consists of two main components: a worm, which is a gear similar to a screw, and a worm wheel, which is a gear similar to an ordinary gear whose teeth mesh with the threads of the worm. Worm gears are used to transmit motion and torque between two non-intersecting, non-parallel shafts, usually at an angle of 90 degrees. Worm gears are commonly used in applications requiring high reduction ratios and compact designs, such as conveyors and cranes. A distinctive feature of worm gears is that the worm can drive the worm wheel, but the worm wheel cannot drive the worm. This feature makes them self-locking [69].

3.6.9 Selection of thread configuration

Regarding threads for gears, ISO metric trapezoidal thread is a good choice. This thread is commonly used in mechanical systems that require efficient power transmission, such as lead screws and main shafts. Trapezoidal threads have a trapezoidal profile, which provides better load distribution and higher durability than square threads. They are often used in applications that require movement and precise positioning.[70]. I will be using ISO metric trapezoidal thread with specification TR30*10, i.e., a thread configuration with a thread angle of 30 degrees, a major diameter of 30mm and a pitch of 10mm.

3.6.10 Modeling of worm gears

By modeling the worm gear in Fusion 360, the worm gear is modeled as shown in the following figures.

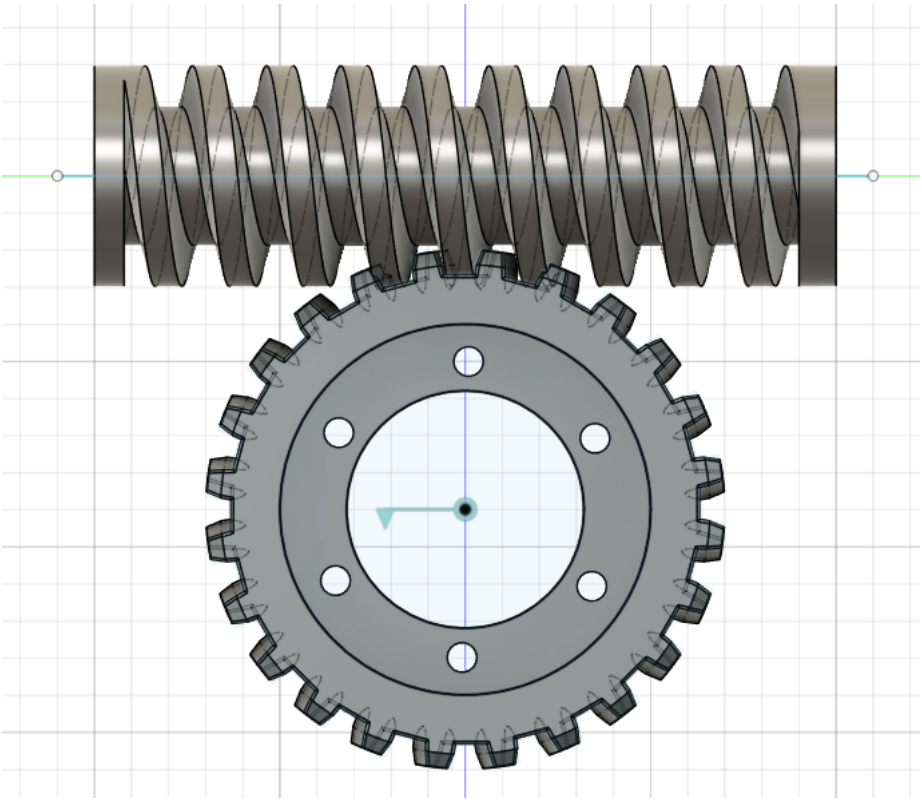

Figure 98: worm gear

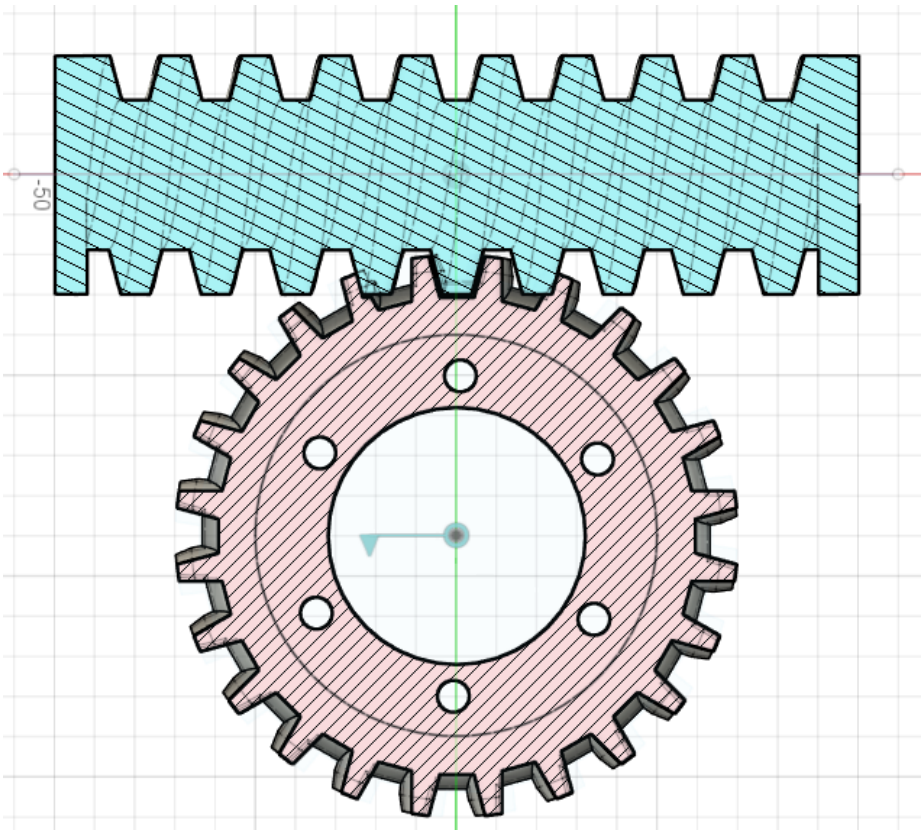

Figure 99: worm gear section view

3.6.11 Modeling of Landing gears

In the midterm report, it was learned that the space for storing the landing gear was a rectangle of 0.5m*0.15m*0.1m with a volume of approximately $0.008m^3$. The landing gear was redesigned according to this space limitation, and a worm gear was incorporated as the driving device for the landing gear and also as the locking device when the landing gear is fully vertical.
Multiple views of the landing gear fully retracted are shown in the following figures.

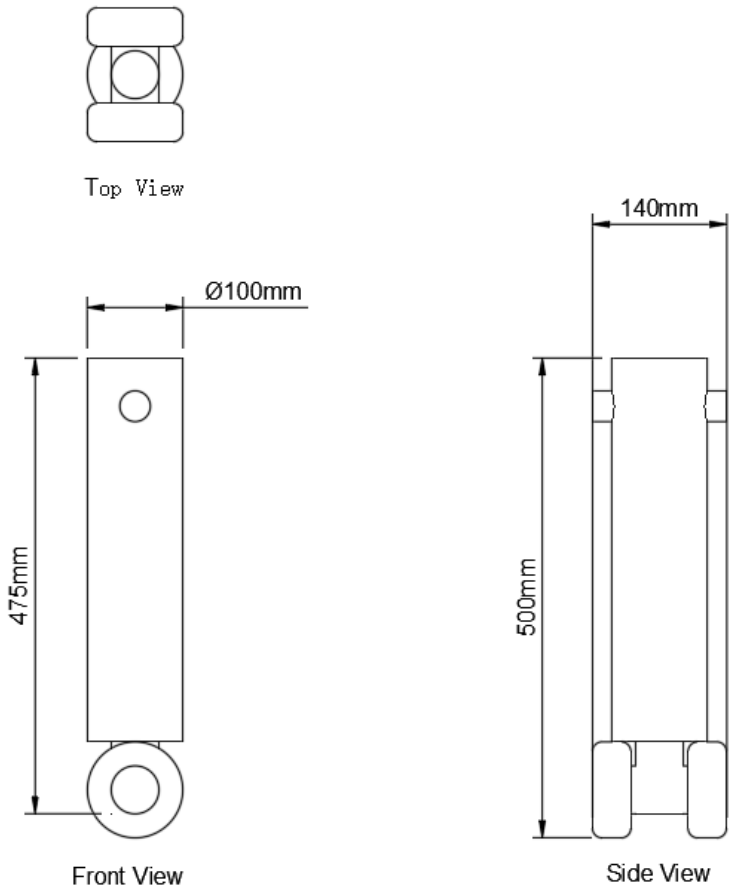

Figure 100: Landing Gear Fully Retracted Three-Dimensional View

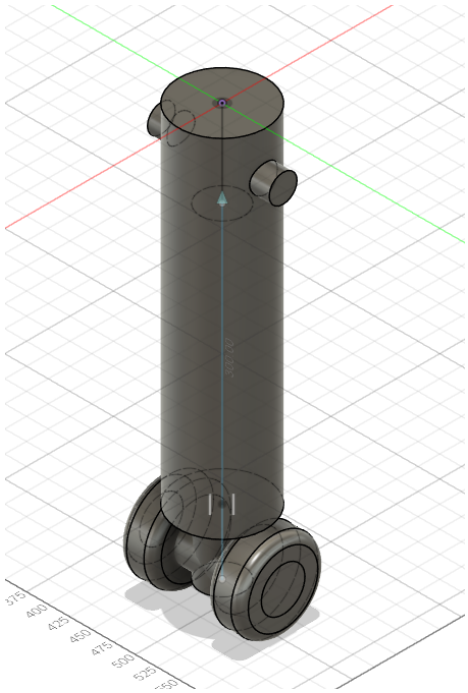

Figure 101: Landing Gear Fully Retracted Isometric View

As shown above, the dimensions of this landing gear when fully recovered are 500 mm in length, 140 mm in width, 100 mm in height, and the capacity of the space it occupies is $0.007m^3$. It can be put into the reserved space.
Multiple views of the landing gear (with worm gear) fully retracted are shown in the following figures.

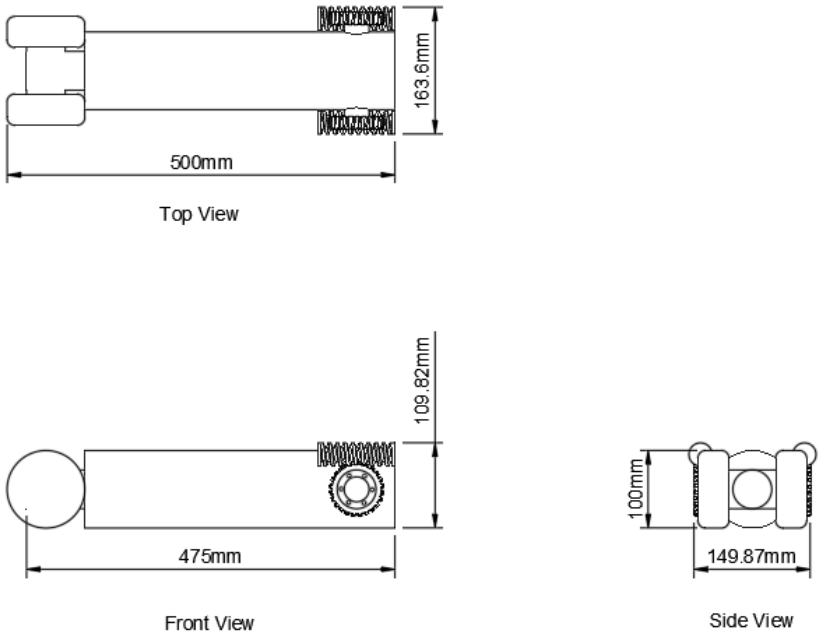

Figure 102: Landing Gear (with worm gear) Fully Retracted Three-Dimensional View

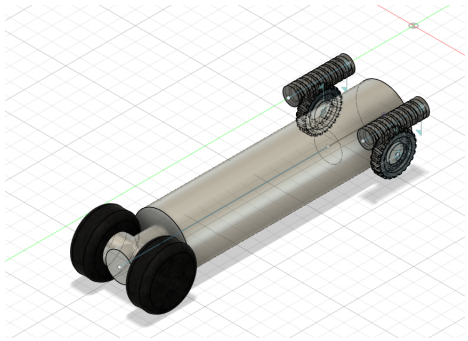

Figure 103: Landing Gear (with worm gear) Fully Retracted Isometric View

Multiple views of the landing gear (with worm gear) fully deployed are shown in the following figures.

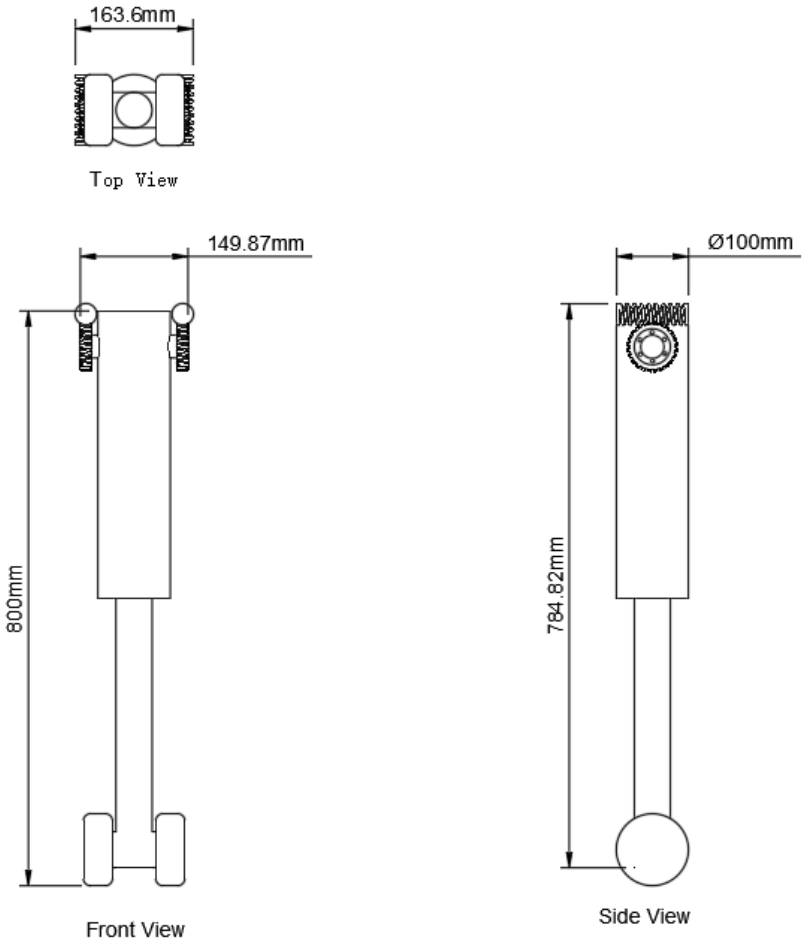

Figure 104: Landing Gear (with worm gear) Fully Deployed Three-Dimensional View

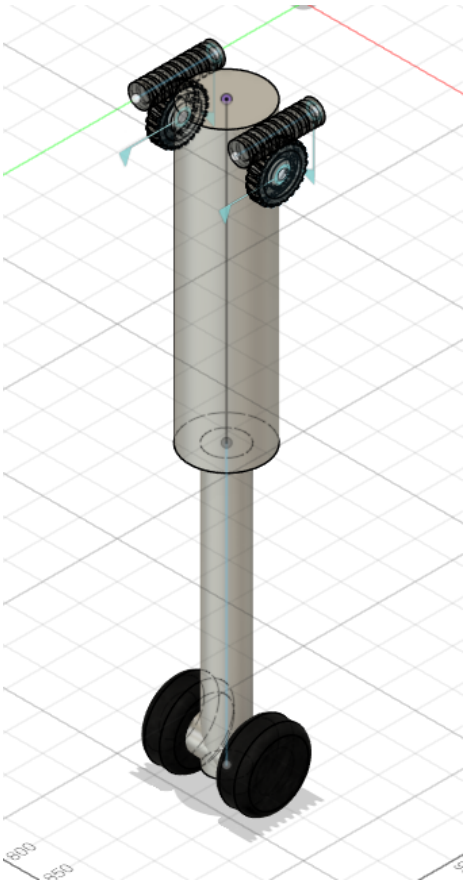

Figure 105: Landing Gear (with worm gear) Fully Deployed Isometric View

As shown above, this landing gear can be up to 800 mm long when fully deployed, a value that can be adjusted depending on the minimum ground clearance required for the test section

3.6.12 Motor Configuration

The worm gear can be deployed by the motor driving the worm and then rotating the worm wheel to rotate the landing gear which is expected to have a weight of 5.5kg. The landing gear requires 90 degrees of rotation to go from a horizontal to a vertical position, and from the modeling in fushion360 it is known that six 360-degree rotations of the worm will result in one 90-degree rotation of the worm wheel, and this information can be used to know the gear ratio (i).
In order to analyze the RPM and output power required by the motor, it is necessary to know the time required to deploy the landing gear. A simple force analysis and equations to be used is shown below.

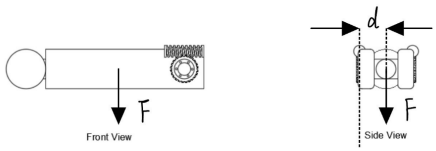

Figure 106: Simple Force Analysis

$$F = W = mg \tag{112}$$

$$T_o = F * d \tag{113}$$

$$i = 6/(1/4) = 24 \tag{114}$$

$$T_i = T_o/(\eta * i) \tag{115}$$

$$\omega_(worm) = 2\pi * (6/t) \tag{116}$$

$$RPM = \omega_(worm) * (60/2\pi) \tag{117}$$

$$P = T_i * \omega_(worm) \tag{118}$$

where:
m: Mass of the landing gear in 5.5 kg
d: Distance from the center of gravity of the landing gear to the axis of rotation of the worm wheel, in 0.062 m
g: Gravity, takes the value of $9.81 m/s^2$
F: Turning force on the landing gear
T_o: Torque of the worm wheel that rotates the landing gear, in N*m
i: Gear ratio
T_i: Torque of the worm, driving the worm wheel, in N*m
η: Worm gear efficiency
$\omega_(worm)$: Angular velocity of the worm
t: Time required for landing gear to be fully deployed
RPM: RPM of the motor
P: Output power of the motor
In the current worm gear design, the gear ratio is 24, according to the following chart [71], the worm gear efficiency is about 75 percent, we need to know the parameter t, then the RPM and the output power of the motor can be calculate.

Worm Gear Ratio	Efficiency
10:1	82~85%
20:1	78~82%
30:1	73~76%
40:1	69~75%
50:1	67~72%
60:1	65~70%

Figure 107: Worm Gear Efficiency

Suppose t is 3 seconds, that is, the time to fully deploy the landing gear is 3 seconds. The calculated RPM of the motor is 120 and the output power is 2.34 watts.
The above calculations are for a motor configuration when there is only one worm gear driving the landing gear, if there are two, with one worm gear on the left and one on the right, which is the current design, two motors are required. If the distance from the center of gravity of the landing gear to the axis of rotation of the two worm wheel is the same, then the torque of the worm gears needs to be divided by two, resulting in an output of 1.17 watts per motor.

3.6.13 Conclusion

At different placement of landing gear, the distribution of fuselage mass on each landing gear is different, so that the combined force on the fuselage and the displacement of the shock absorbers are also different, which can be predicted by using MATLAB/Simulink model and by adjusting the spring coefficients and damping coefficients to get the desired output.
The current design uses a worm gear to achieve rotational deployment of the landing gear and can stop the movement of the worm gear after the landing gear has been deployed. Due to the nature of the worm gear transmission, the worm wheel cannot drive the worm, so self-locking can be achieved and there will be no movement other than the up and down linear movement of the landing gear when it is fully deployed for landing. By knowing the required landing gear deployment time, the RPM and power output of the driving worm gear motor can be calculated.
In the future, the connection point between the landing gear and the fuselage as well as the placement of the landing gear on the fuselage will need to be studied. The above calculations of the combined fuselage force at landing, the shock absorber displacement distance and the configuration of the drive motor may have to be adjusted later as well

3.7 Thermal Analysis - Yancheng Ding

Peer Reviewed by: Ruxin Zhang

3.7.1 Introduction

Thermal analysis aims to simulate, analyze and visualize the temperature changes that occur during the entire rocket flight. In the previous year of work, the thermal distribution was not analyzed due to the limit of time. This year, the goal of the work is to analyze the temperature change within each subsystem of the rocket body, determine the thermal deformation, and design the required thermal control.

3.7.2 Atmosphere Modeling

For the modeling of the pressure and temperature of the atmosphere, the following properties are expected: ambient temperature and pressure, air density, dynamic viscosity, and thermal conductivity. These parameters are expected to be obtained with a simple input of altitude. The last year's report has done analysis and ambient temperature and pressure from 0 to 30000m altitude, and the rest data are collected from U.S. Standard Atmosphere Supplements, 1966 [72]. For automatic analysis, a MATLAB function is written for calculating the parameters, with altitude in meters as input and the desired parameters as output. For visualizing the data, plots are generated for each parameter, from height of 0 to 30000m:

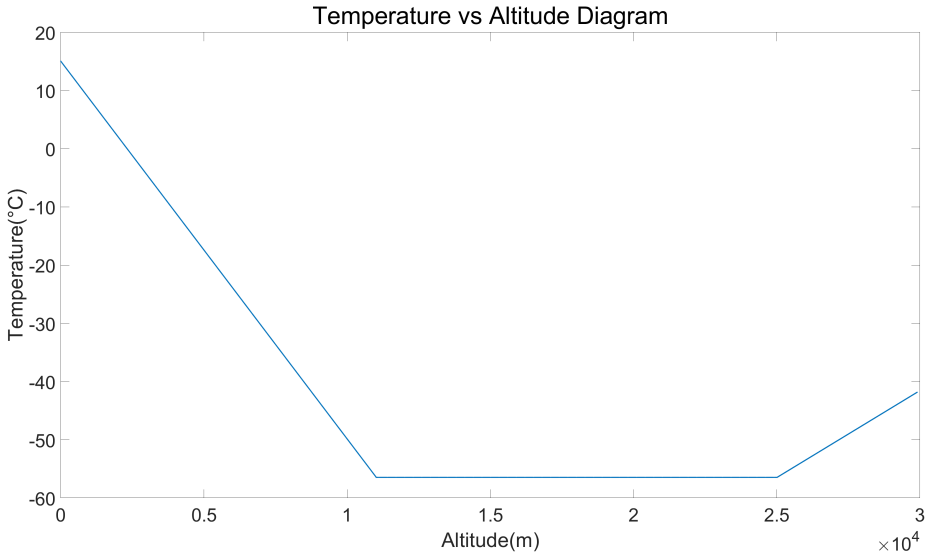

Figure 108: Temperature vs Altitude

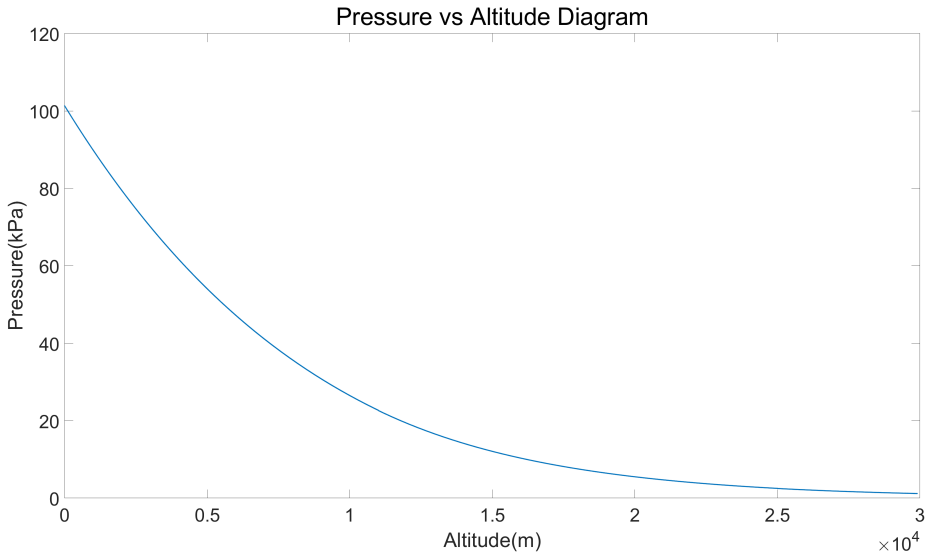

Figure 109: Pressure vs Altitude

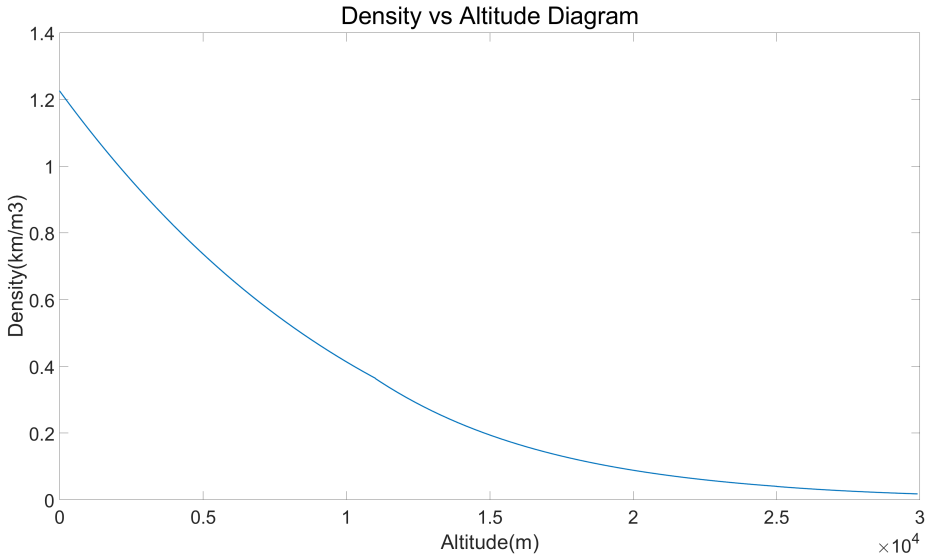

Figure 110: Density vs Altitude

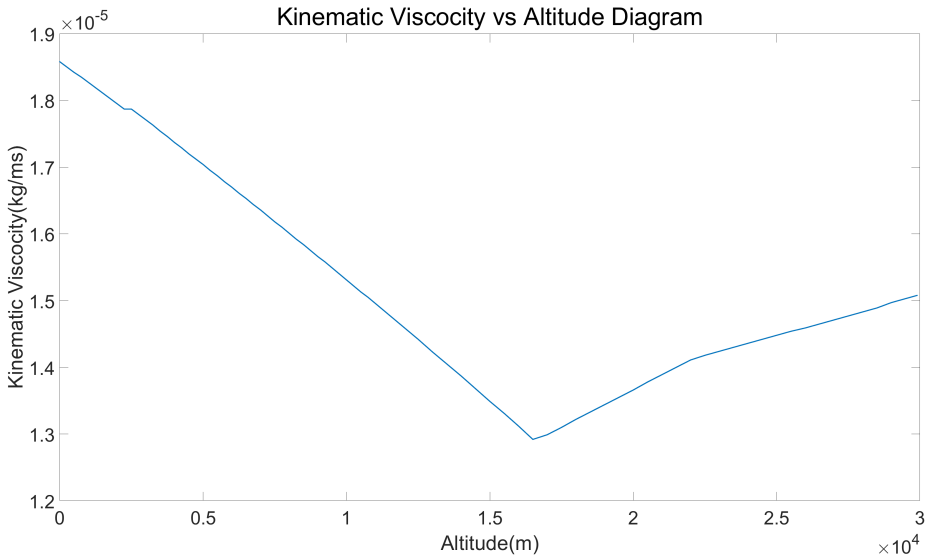

Figure 111: Kinematic Viscosity vs Altitude

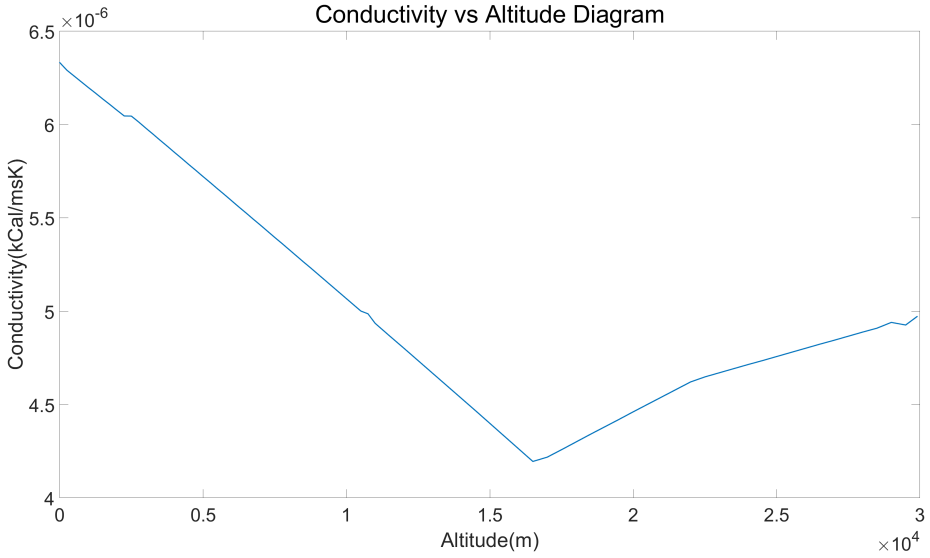

Figure 112: Conductivity vs Altitude

3.7.3 Thermal Geometry Forming & Boundary Conditions

The geometry of rocket body is analyzed before thermal analyzing. Based on design from midterm report [73], the outer diameter of the rocket shell is 12" with $6mm$ thickness, the nose cone has an angle of 19.5 degrees, and the rest

geometry is assumed to be the same as of sizing from midterm report [73]. The material is assumed to be fully made of Al6061 T6, which was mentioned in previous year's report [1]. Based on these data, a CAD model is made for visualizing the cross section view of the rocket body:

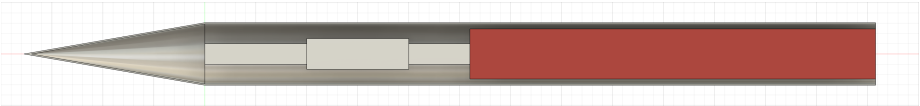

Figure 113: Cross Section View of Rocket Body for Thermal Analaysis

The surrounding pipe is the shell of the rocket body, the three blocks at the front of the rocket body represent the front landing gear, the avionics bay, and the battery bay. Since the designs to these parts are not done yet, they are assumed to have the same thermal properties as of Al6061 T6 for current simulation. The red part is the propulsion system. For current analysis, the test section and wings are not included since they have not been fully designed.

The roughness of the rocket body surface is assumed to be $0.01mm$, which is the error of Haas DM 1 [74], the CNC machine operating at Carleton University.

During ascending, convection takes place on the outer surface of the rocket body, including the convection between the outer surface of the rocket shell and the atmosphere, the same for the nose cone. Conduction takes place within the parts of the rocket body, among the landing gear, avionics & battery bay, and the propulsion system. For both conduction and convection, the equation below is used for calculating heat transfer:

$$\dot{Q} = hA\Delta T \tag{119}$$

where h is the conduction/convection coefficient in unit of W/mK, A is the surface area in unit of m^2, and ΔT is the difference of temperatures between two objects, in unit of °C.

During cruising, the nose cone is assumed to be fully immersed in the oblique shock, and the propellant burns with a constant chamber temperature of 3440K according to previous year's report [1]. To calculate the convection process during cruising, the following equations are used to determine heat transfer caused by high-speed compressible flow and surface friction: [75]:

$$Re = \frac{VL}{\mu} \tag{120}$$

$$Pr = \frac{\mu C_p}{k} \tag{121}$$

$$r = Pr^{\frac{1}{3}} \tag{122}$$

$$T_r = T_\infty + r\frac{V^2}{2C_p} \tag{123}$$

$$C_f = \frac{0.026}{Re^{\frac{1}{7}}}(1 + B\frac{k_s}{L}) \tag{124}$$

$$h_c = 0.5C_f\rho\frac{V^3}{T_\infty} \tag{125}$$

where:
Re: Reynolds number
V: Flow velocity $[m/s]$
L: Characteristic length $[m]$
μ: Kinematic viscosity $[kg/ms]$
Pr: Prandtl number
Cp: Specific heat capacity $[J/g°C]$
k: Conduction coefficient $[W/mK]$
r: Recovery factor
T_r: Recovery temperature $[°C]$
T_∞: Ambient temperature $[°C]$
C_f: Friction coefficient
B: Constant, equals to 20
k_s: Surface roughness $[m]$
h_c: Convection coefficient $[W/mK]$
ρ: Density, unit $[kg/m^3]$
The recovery temperature, by definition, is the temperature of air flow after impacting the object and has transferred all kinetic energy into thermal energy. In other words, it is the temperature surrounding the surface of object during high speed cruising. The recovery temperature is used for calculating heat transfer during cruising.

Thermal radiation is neglected in calculating heat transfer of the rocket body.

3.7.4 Ascending & Cruising Analysis

For calculating the thermal changes on rocket body during ascending, a SIMULINK model is established for simulating temperature variations. Three major blocks act in the simulation: a block for calculating atmosphere conditions with respect to altitude, which comes from the atmosphere modeling in previous content, a convection block connected to the outer surface of the rocket body. The convection block links to the Rocket block, where it simulates the thermal conductions take place within the rocket body. The thermal properties of Al6061 T6 [76] and propellant [77] [78] [79] [80] are inserted as parameters. Illustration of SIMULINK blocks are shown below:

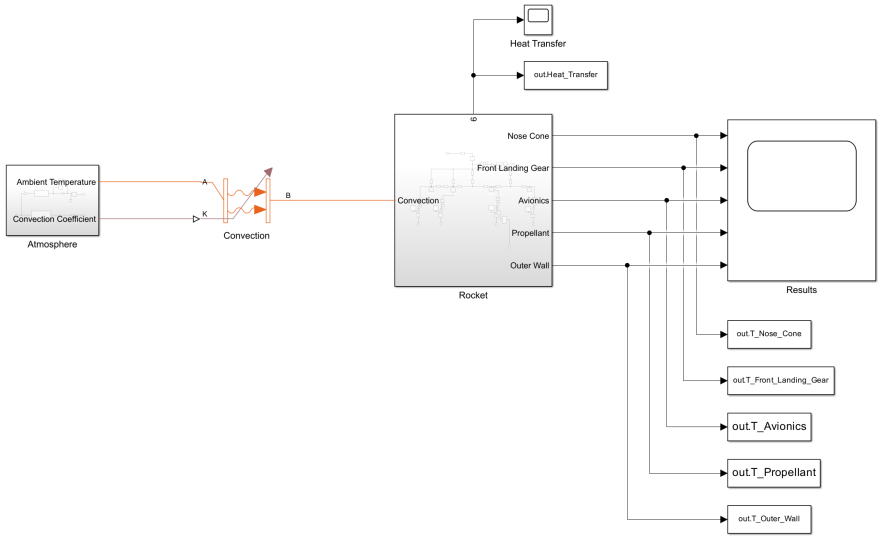

Figure 114: SIMULINK Blocks for Thermal Simulation

For ascending analysis, the ascending rate is stated to be between $3.5m/s$ to $3m/s$ from midterm report [73]. For worst case assumption, the ascending rate is assumed to be $3m/s$ for simulating the longest ascending duration, which indicates 7200 seconds of ascending period. The final temperature of the rocket body, after simulating the entire ascending process, are used as the initial temperatures of rocket parts for cruising simulation. The cruising period is stated to be 47 seconds from previous year's report [1]. For worst case assumptions, the cruising period is set to be 60 seconds with constant speed of Mach 3. Plots are generated below to show the temperature change of rocket parts over time during ascending and cruising:

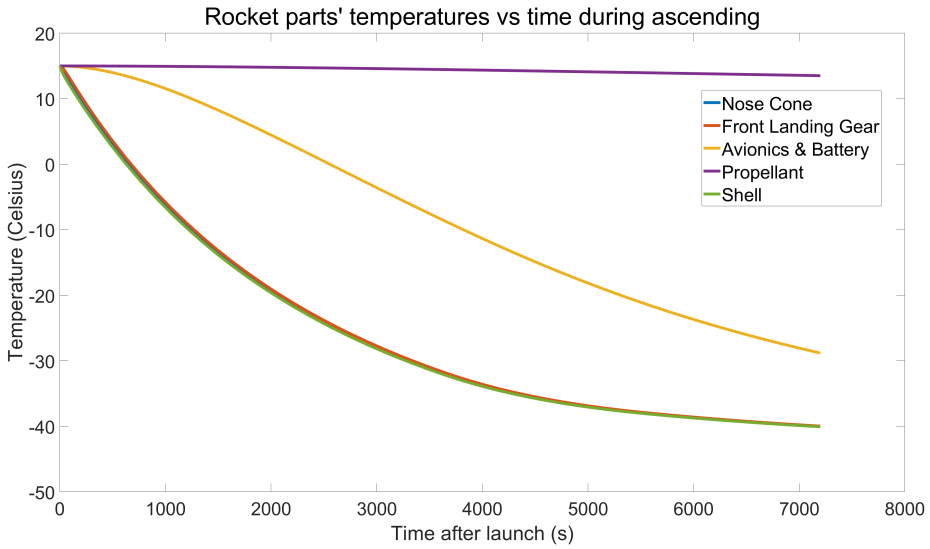

Figure 115: Ascending Thermal Simulation Results

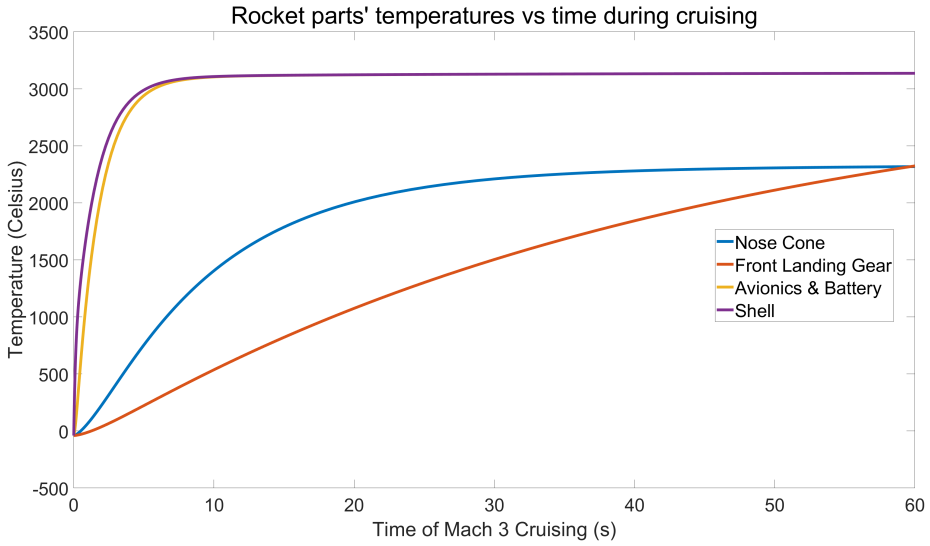

Figure 116: Cruising Thermal Simulation Results

The width of the lines indicates the error of calculation. For ascending thermal simulation results, the nose cone results are covered by other lines. The nose cone have the same temperatures as of rocket shell.

As viewed from the results, the avionics and battery bays dropped to -28 Celsius degrees by the end of ascending process, and soon heated to 3000 Celsius degrees

due to the burning of propellant. As mentioned, the chamber temperature is calculated to be $3440K$. The rest of rocket parts are also heated to higher than 1500 Celsius degrees after the cruising process. According to the ASM Data Sheet [76], the melting point of Al6061 T6 is 580 Celsius degrees, indicating that the entire rocket will melt after cruising. Also requested by Xuan from Recovery and Landing Control group, avionic and battery bays are required to operate normally at a constant temperature of 15 Celsius degrees. Considering these constrains, designs are done in following sections to solve the issues.

3.7.5 Insulation Layer Design

For selecting insulation material, it is required to have low thermal conductivity, high stiffness to survive under large acceleration during cruising, and good structural integrity to cover objects with different geometry. Carbon-phenolic composite is selected as it fulfills all three requirements above. According to research [81], carbon-phenolic composite has a thickness of $0.01m$ for a single layer, and thermal conductivity of $0.2W/mK$. It decomposites at around $1900°C$ degrees, but can survive shortly under $3440K$ [82]. For the design, two parts of the rocket needs to be covered with thermal layers: the avionics and battery bays, and the propulsion system. The avionics and battery system shares the same insulation layer since they have the same requirement to temperatures, and sharing insulation layer also reduces the mass of insulation required. The avionics and battery bays only require minimal insulation to maintain constant temperature, while the propulsion needs thick insulation to keep its temperature away from other parts of the rocket.

For avionics and battery bays, they are together covered by one single layer of insulation. For the propulsion system, it is covered 7 layers from the battery bay, and the gap between the propulsion system and the rocket shell is fully filled with insulation layer. The 7 layers are placed behind the battery bay, which results in 8 layers between the battery bay and the propulsion system. Since the thermal conductivity increases as carbon-phenolic layers compile [81], 8 layers offer the best conductivity while isolating the propulsion system from other parts of the rocket body. An updated cross section view of the rocket is shown below to visualize the insulation layers:

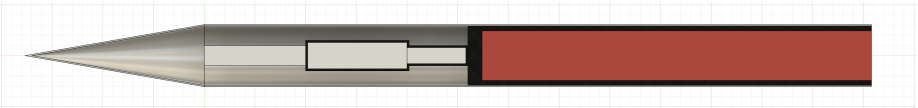

Figure 117: Cross Section View of Rocket Body with Insulation Layer

Due to the insulation layers, the usable volume is decreased, but providing extra thermal protection. Below is the plot of temperatures after insulation layers are added:

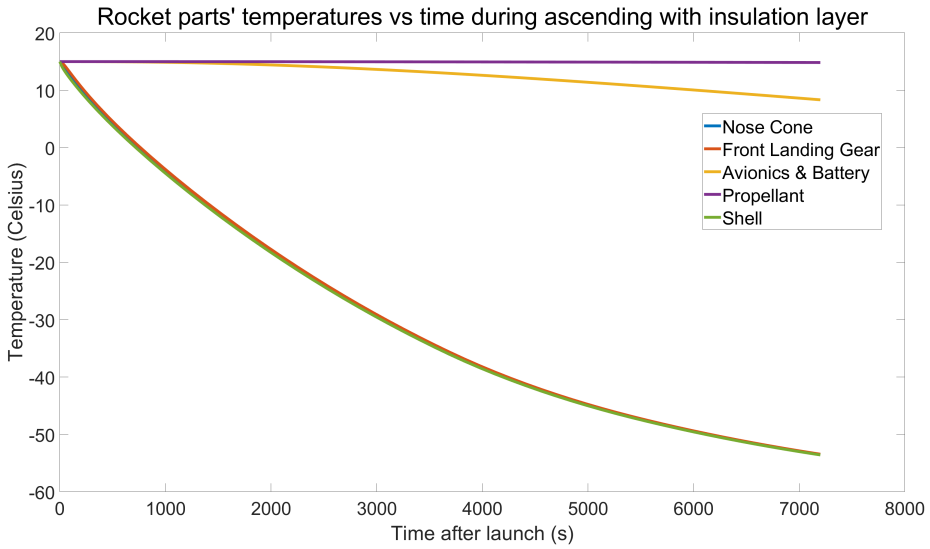

Figure 118: Ascending Thermal Simulation with Insulation

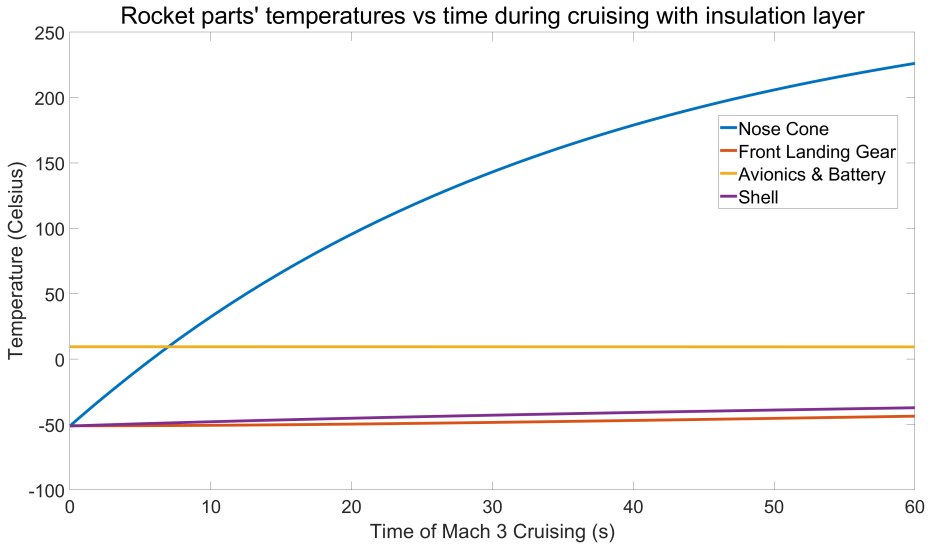

Figure 119: Cruising Thermal Simulation with Insulation

The width of the lines indicates the error of calculation. Again, for the ascending plot, the nose cone results are covered and are the same as the temperature of shell.

By applying insulation layers, the propulsion system's thermal effects on the

rocket body have been minimized. During cruising, the propulsion system heats the avionics & battery bays by increasing 0.084 Celsius degrees, which is negligible.

The avionics and battery bays drops by 6.6 Celsius degrees during ascending. Avoid temperature drop during ascending is impossible, since the surrounding air is constantly transferring heat out of the rocket. Passive methods cannot fully stop the temperature drop, active thermal control needs to be installed. Therefore, a heater is needed to be inserted in the avionics and battery bays, which is to be discussed in following section.

3.7.6 Active Thermal Control

To avoid temperature drop of avionics and battery bay, a thermal heater is to be inserted. To determine the maximum power output of the heater, the heat transfer of avionics & battery bays are exported and shown below:

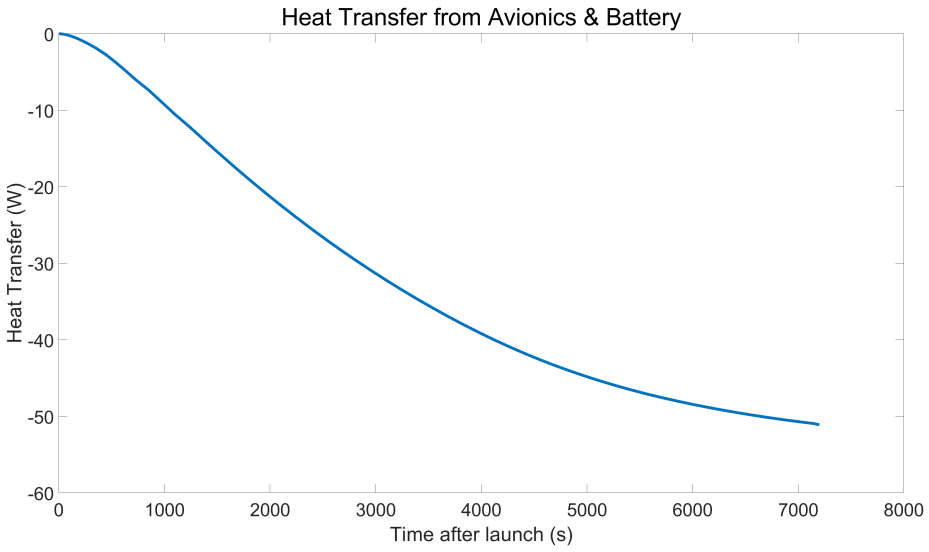

Figure 120: Heat Transfer of Avionics and Battery Bay during Ascending

As shown in the figure, the maximum heat transfer out of the avionics and battery bay is around -50W, therefore the heater requires power output no more than 60W. Required by Xuan from Recovery and Landing Control group, the heater should produce minimal magnetic field during heating to reduce influence on the magnetic sensors. Metallic heaters involve coils that would generate magnetic fields which is undesirable. Therefore, carbon film heater is selected. Carbon film heater is thin, with a minimal thickness of 70μm [83], while generating power output of maximum 60W. Due to its material of carbon, it generates almost no magnetic field during operating. This enables it to be placed any-

where in the avionics and battery bay, and heats the avionics electronic devices easily.

Simulation with heaters are updated with results shown below:

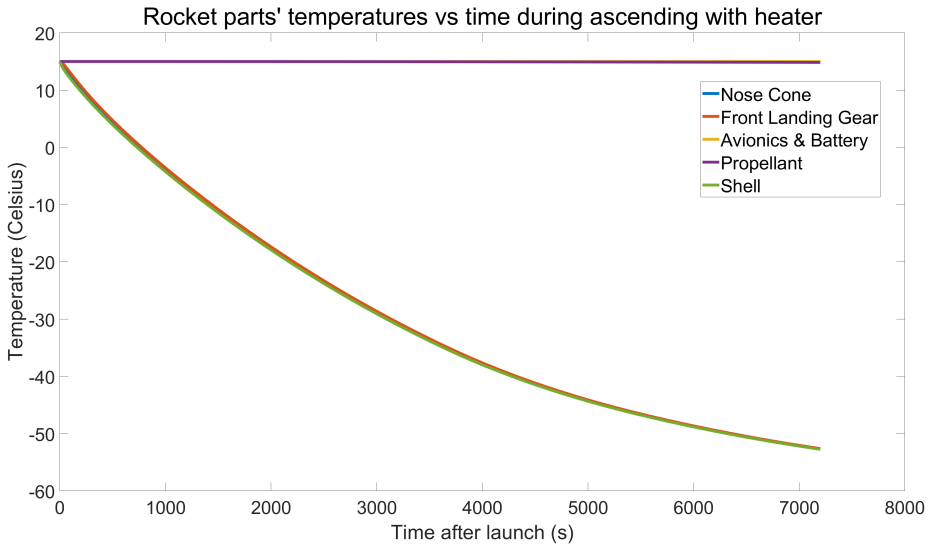

Figure 121: Ascending Thermal Simulation with Heater

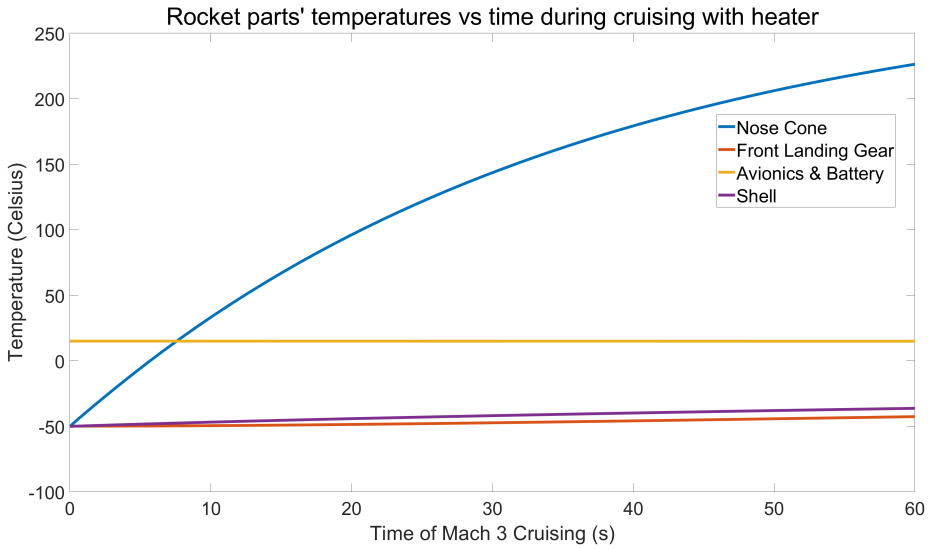

Figure 122: Cruising Thermal Simulation with Heater

The width of the lines indicates the error of calculation. The avionics & battery

system is covered by propulsion system, which is constantly $15°C$.

3.7.7 Thermal Expansion

During the entire flight of the rocket body, large thermal expansion is taking place. Since the avionics & battery bays are at constant temperature, and the propulsion system is also relatively stable in temperature changing, the most deformation takes place on the nose cone and the shell of the rocket body. The equation below is used to calculate thermal expansion [84]:

$$\Delta L = \alpha L_0 \Delta T \tag{126}$$

where:
ΔL: Deformation length $[m]$
α: Coefficient of linear thermal expansion $[m/m°C]$
L_0: Original length $[m]$
ΔT: Temperature difference $[°C]$
For current design, the rocket has a length of approximately $4.2m$ and diameter of 12", and the coefficient of linear thermal expansion is $25.2\mu m/m°C$ according to AMS Data Sheet [76]. Therefore, the thermal deformation in axial direction is $7mm$ maximum, and radial deformation is $0.5mm$, both shrinking down the length and diameter of the rocket. This could result in the airframe design, especially in connections between the rocket shell and inner systems. It is suggested to leave suitable space at the connection points to minimize the influence of thermal expansion. Also, considering the nose cone is experiencing high temperature change during cruising, it is suggested that the nose cone should not have direct contact with the rest of the rocket body, to avoid any thermal stress from the deformation of the nose cone.

3.7.8 Conclusion

In conclusion, the thermal simulation during ascending and cruising has been analyzed. Thermal layers and heater have been designed for the rocket systems to main the desired thermal stability of the rocket body. Thermal deformation has been calculated with suggestions to airframe designers. In future work, thermal analysis will be done with respect to further updates of rocket's geometry, with test section and wing included. Assistance on airframe design will be done with more precise thermal stress and strain calculated.

3.8 Airframe Subteam Recap

In this section, various sections and mechanisms regarding airframe components were analyzed. In the rocket body section, a larger outer mold was introduced to accommodate for the schlieren imaging system, without compromising structural integrity. In addition, the previous year's design of deployable wings was analyzed to determine the point of which they were able to fully deploy and under what actuation force they would be required to hold.

In the lifting body structure design, a new proposal for a lifting body design was introduced. This required preliminary analysis on a delta wing airfoil which would span the airframe to produce lift. This required an analysis of drag and lift to determine the wing area and the respective lift estimation. Analyses regarding the physical structure of the main lifting body airframe were performed as well. The aerodynamics of cruise flight at Mach 3, external and internal layout planning for different components were performed as well.

Newly developed landing gear was installed into the rocket body and the lift body. By analyzing the landing gear shock absorbers and studying the self-locking structure, a landing gear mechanism was designed that is retractable and can self-lock after deployment, further improving the survivability of the vehicle after burnout. Finally, a thermal analysis of airframes was performed to determine the thermal deformation which would occur during flight. Using methods of heat transfer and material skin friction, a thermal simulation was created to model the temperature change results of the aircraft with respect to flight time and develop methods of passive and active thermal controls to counteract these effects.

From this information, the main goal will be to determine the applicability of each aircraft body to the design goal of Mach 3 test section inlet velocity for 30 seconds, at 70,000 feet with the new implementation for Schlieren imaging design. The analysis consists of the airframe shape, wing design, landing and thermal implementations. This information will be used to weigh the benefits of each design to present to the rocket design project team, along with their respective research. From this, a final design direction will be concluded, and the team can focus on more specific design goals with respect to the final aircraft design.

4 Propulsion & Control Systems Design

4.1 Propulsion & Control Subteam Introduction

The propulsion & control systems design section delves into the development of an advanced propulsion system, integration of sophisticated control mechanisms, evaluation of control surface effectiveness, and trajectory simulation. The design process includes preliminary sizing of a solid rocket motor optimized for high-speed and high-altitude performance, complemented by a newly developed and validated trajectory prediction simulation. A pitch-hold autopilot system was implemented to maintain stability during ascent and cruise phases, while also addressing challenges encountered in last year's design, particularly in achieving rapid and precise convergence to the desired pitch angle during flight.

A major focus was placed on sensor calibration and data fusion, leveraging inputs from accelerometers, gyroscopes, and magnetometers to ensure accurate orientation and motion estimates. Techniques like Kalman filtering and complementary algorithms significantly enhance system reliability by reducing noise. Furthermore, control systems such as the airbrakes, dedicated to active throttling by increasing drag during cruise and descent, and fins, operating effectively across subsonic, transonic, and supersonic regimes, were also refined. The fins are the primary control surface during flight as they are used from launch to landing, and will have to be effective in the subsonic, transonic, and supersonic flow regimes. For a plane-like vehicle, elevons on a delta wing were evaluated using XFLR5 simulations to assess their performance in various flight conditions, especially during landing.

By integrating these technologies and control systems, this section showcases the potential to achieve precise trajectory control and navigation, even under demanding scenarios like supersonic trajectory adjustments and dynamic flight conditions.

4.2 Trajectory Analysis - Ahmed Moussa

4.2.1 Introduction

Trajectory simulations are necessary to estimate and validate the overall design's flight and thrust profiles with some degree of accuracy. In the prior year of work on this project, a simulation was developed in MATLAB. This simulation will be refered to as the legacy simulation for the remainder of this section. A new simulation is in development with the intention of providing more accurate results and resolving the shortcomings of the legacy simulation, which will be discussed. Since a constant thrust profile and a 45^o launch angle were selected in the prior year, it is hypothesized that the rocket will closely follow ballistic trajectory with a steeper descent relative to its ascent. The anticipated

launch height remains at 70'000ft (21.34km) as well as the loaded rocket mass of 253.80kg until a new mass budget is created.

4.2.2 Legacy Simulation

The rocket's altitude and Mach profiles were estimated by last year's trajectory prediction simulation in early 2024. Its results, plotted in Fig. 123., indicate that the rocket maintained an altitude between 20km and 23km during the 30s test period starting at the green line representing when Mach 3 flight is achieved. Upon reaching Mach 3, the simulated rocket did not maintain a constant speed; rather it continued to accelerate until burnout. This is undesireable and indicates that a re-evaluation of the thrust profile is necessary.

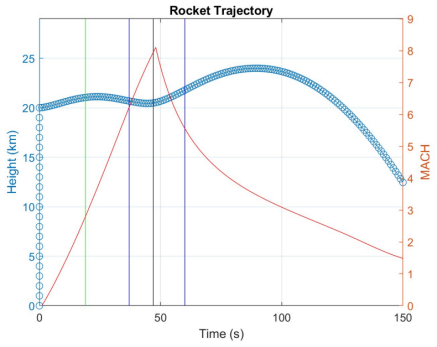

Figure 123: Altitude and Mach profile legacy simulation output. [1]

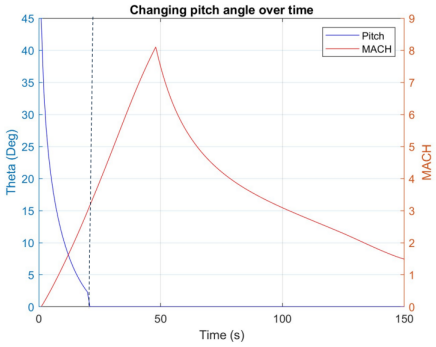

Figure 124: Pitch angle and Mach profile legacy simulation output. [1]

Last year's report [1, p.234] and the data plotted in Fig. 124 indicate that the pitch angle remains a constant 0^o once Mach 3 flight conditions are reached; however, as seen in Fig. 123., that cannot be the case due to the significant fluctuations in altitude. The legacy simulation's data invalidates itself and it is likely that the pitch was hardcoded beyond the Mach 3 point without mention. The launch height also appears to be set to 20km which is not what was specified in the report [1, p.13]. Retrieval control surfaces and the change in drag forces after nose cone detachment were not considered in the legacy simulation [1, p.241].

4.2.3 Updated Simulation

A new trajectory simulation program has been developed to replace the legacy program. This program follows a similar solving methodology described in the prior year's report [1, pp.230-233]. The net forces on the rocket body are computed at each time-step using Eq. (127) and (128) using a pitch angle with respect to Earth's normal. These forces are translated into accelerations using the total mass of the rocket and newton's second law of motion. Acceleration is

integrated for velocity which is integrated for the position of the rocket throughout its trajectory. The pitch angle is re-evaluated using the updated velocities following Eq. (129).

$$\sum F_x = F_T sin(\phi) - F_D sin(\phi) - F_L cos(\pi + \phi) \tag{127}$$

$$\sum F_y = F_T cos(\phi) - F_D cos(\phi) - F_L sin(\phi) \tag{128}$$

$$\phi = ATAN2(u_x, u_y) \tag{129}$$

The mass of the rocket changes with each time-step as fuel is burned to deliver thrust. The mass flowrate is computed by Eq. (130) using last year's estimated specific impulse of 260s [85]. A simple drag formula (131) is used to compute the drag force using an average of last year's simulated drag coefficient and the rocket cross-section area. Likewise, a simple lift formula (132) is used to compute the lift force using last year's rocket geometry to determine the lifting area beneath the rocket. The lift coefficient required is estimated in the following section on thrust profile evaluation. Atmospheric conditions are sourced from the International Standard Atmosphere model.

$$\dot{m} = \frac{F_T}{g_0 I_{sp}} \tag{130}$$

$$F_D = \frac{1}{2} C_D u^2 A_{ref} \tag{131}$$

$$F_L = \frac{1}{2} C_L u^2 A_{ref} \tag{132}$$

Fig. 125. contains a plot of both the newly computed altitude profile and Mach profile. Comparing these new results with the legacy simulation results, the altitude and Mach curves are similar prior to the rocket's burnout; however, the new results do not demonstrate a gradual increase in altitude post-burnout. Due to this inconsistency, it can be concluded that the legacy simulation results are invalid since there is no plausible explanation as to how the rocket could overcome drag and gravitational forces without generating sufficient thrust or lift. It is explicitly stated in the prior year's report that lift generated by wings and fins was not taken into account in the simulation [1, p.234], hence why lift forces cannot explain the observed phenomenon either.

4.2.4 Thrust Profile Evaluation

As noted prior, the thrust profile must be re-evaluated due to the constant acceleration leading to speeds far beyond the required Mach 3. Assuming the thrust vector is level with the horizon during cruise flight, the engine needs to generate enough thrust to offset any drag forces that would slow down the

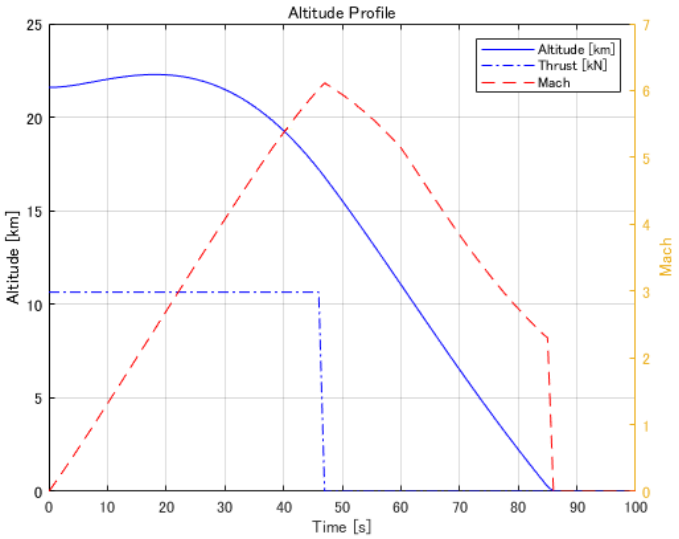

Figure 125: Altitude and Mach profiles determined by the new simulation.

vehicle. Lift forces from fins and wings at Mach 3 are expected to counter the weight of the body. During cruise, a drag force of 1282 N is estimated by the drag equation (131) using the arguments tabulated in Table 24. An equivalent constant thrust force is needed to oppose the drag and maintain 0 acceleration.

Table 24: Drag Equation Parameters Sourced from Last Year [1]

Parameter	**Value**
Drag Coefficient (C_D)	0.905
Air Density	0.0709 kg/m^3
Speed @ Mach 3	888 m/s
Cross Section Area	0.0507 m^2

A larger thrust is needed prior to the constant cruise thrust to accelerate the rocket to Mach 3. The acceleration thrust profile will be evaluated in 2025 when details on launch rail mechanisms and forces are avaialble. In the meantime, simulations using the cruise thrust profile for a rocket starting at Mach 3 can provide an estimated altitude profile plotted in Fig. 126 and 127.

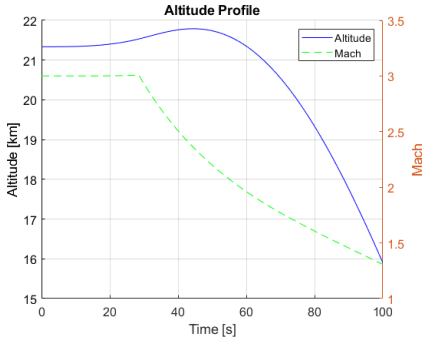

Figure 126: Altitude and Mach profile for cruise starting @ Mach 3.

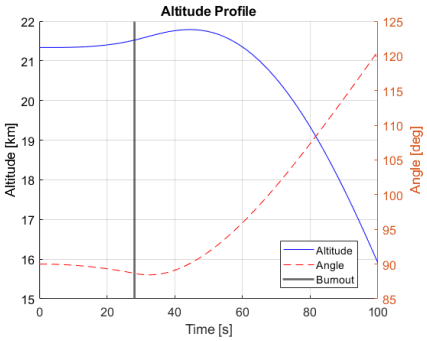

Figure 127: Altitude and pitch profile for cruise starting @ Mach 3.

4.2.5 Conclusions

The simulation demonstrates a near-constant Mach profile during cruise. The altitude of the rocket gradually increased by 257m during the burn and another 196m post-burnout. The increase can be attributed to the decrease in fuel mass as it is expent. The lift force which is designed to lift the full loaded weight of the rocket remains the same while the weight of the rocket decreases, resulting in an increasingly net positive force vertically. Whether this poses a significant problem for the test section has yet to be evaluated.

For future iterations of the simulator, it is important to take into account individual drag components. Wave drag and skin drag tend to vary significantly with Mach number. Furthermore, if a plane body is selected by the airframe design group, the total drag is likely to increase significantly due to the increased surface area of the wings. The next iteration will also include forces from vehicle control surfaces once they are defined.

The simulation will also take gravity turn into account once a rough estimate of the vehicle dimensions is available. Gravity turn may have significant effects on the trajectory of the rocket, especially during the early phases of the trajectory where the velocity is relatively low. The rate of change in pitch associated with gravity turn is inversely proportional to velocity as seen in Eq. (133) [85]. Consequently, the smaller the velocity, the greater the influence of gravity turn.

$$\frac{d\theta}{dt} = \frac{a_g \sin\theta}{V} \tag{133}$$

Due to the high speed involved in the simulation, it will be better to implement

a finer explicit solving algorithm such as RK4 rather than simply minimizing the time-step of the current forward-Euler solver. An RK4 solver will respond to changes in acceleration more effectively and reduce the computational load of the simulation. The effectiveness of the new solver relative to the current solver has yet to be quantified. In the present state of the simulator, it is sufficient to support the feasibility of the vehicle's mission. It provides a simplified analytical solution for the vehicle's trajectory involving estimates of all forces acting on the body.

4.3 Propulsion Systems - Ahmed Moussa

4.3.1 Introduction

Continuing on last year's rocket design iteration, the propulsion system consists of a solid rocket motor with a Rao contour nozzle. Constrained by last year's rocket dimensions, the combustion chamber can have a maximum diameter of 10in including a 5mm motor casing thickness. The airframe design group has provided a rough estimate that the system must be less than two meters long to be compatible with both rocket or plane models. The fuel composition and grain geometry must be re-evaluated to attain the desired flight profile.

4.3.2 Engine Configuration

There are two phases of flight that require thrust: the acceleration phase bringing the vehicle to a speed of Mach 3, and the cruise phase to maintain level flight and a constant speed during the supersonic test. A uniform fuel grain profile cannot meet the thrust requirements of both stages; therefore, a two-phase profile is proposed. Illustrated in Fig. 128, the first phase consists of an annular grain geometry. This provides a large burn surface area and consequently a higher combustion pressure and nozzle massflow to generate thrust. This is a progressive burn, meaning the combustion pressure increases due to the gradual increase in surface area as the tube's interior surface burns out. Once the first phase has completely burned out, there is a cylinder of fuel remaining in the combustion chamber. This is the second phase "end-burn" configuration which delivers a constant thrust to counteract drag forces.

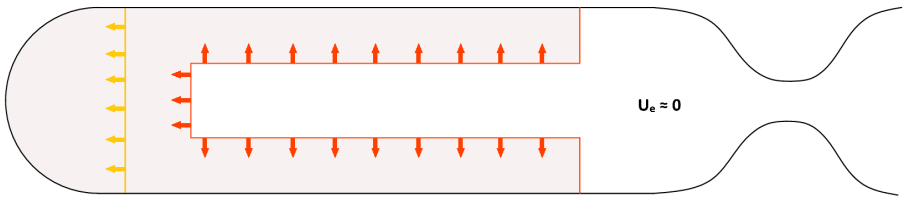

Figure 128: 2D illustration of the proposed two-phase fuel grain profile.

It is desirable that the fuel composition of both phases is identical to simplify manufacturing processes. The end-burn and annular geometries were also selected for ease of manfucaturing. There are other progressive and neutral grain geometries which may be either more or less effective than those selected; however, they are often much more challenging to manufacture and more prone to manufacturing errors.

4.3.3 Engine Sizing

The total thrust produced by a sounding rocket at a given altitude is defined by Eq. (134) below [85].

$$F_T = \dot{m} u_e + A_e \left(P_e - P_\infty \right) \tag{134}$$

In an "ideal" performance scenario producing the most thrust possible for a specific engine, the nozzle exit pressure is equal to the ambient pressure. This is dangerous since any increase in atmospheric pressure during flight can yield shocks within the nozzle, because the supersonic exhaust's pressure will be lower than the ambient pressure along the path of the thrust vector. To avoid shocks caused by over-expansion of the exhaust, the nozzle is designed to be slightly under-expanded ($P_e > P_\infty$) when operating at the test altitude of 70'000ft (21.34km). The desired exit pressure was arbitrarily selected as 4881.5 Pa which is 110% of the ambient pressure at the test altitude. This altitude is the ceiling and hosts the test body for the longest time, hence why it is a critical design point. For this reason, initial engine sizing is based on the requirements of the cruise phase of flight. Furthermore, the acceleration grain has many more flexible parameters such as its thrust, inner diameter, and time to Mach 3 while the cruise grain is far more rigid in terms of what's required and possible.

The exhaust mass flowrate and velocity are represented by Eq. (135) & (136) respectively [85]. These equations are valid for isentropic flow. The isentropic nozzle flow assumption is supported by last year's work which demonstrated a 2.6% difference between the thrust from an isentropic nozzle flow analysis versus a non-isentropic simulation [1]. Provided a fuel composition and its chemical properties, the density, ratio of specific heats (γ), gas constant (R), and flame temperature T_c are known. To simplify the analysis, the stagnation temperature (T_0) is assumed equal to T_c. This implies no energy is lost in the combustion process and complete combustion occurs.

$$\dot{m} = \frac{P_0 A_t \sqrt{\gamma}}{\sqrt{R T_0}} \left(\frac{2}{\gamma + 1} \right)^{\frac{\gamma+1}{2(\gamma-1)}} \tag{135}$$

$$u_e = \frac{2\gamma R T_0}{\gamma - 1} \left[1 - \left(\frac{P_e}{P_0} \right)^{\frac{\gamma-1}{\gamma}} \right] \tag{136}$$

Subsituting these equations into Eq. (134) yields Eq. (137) which has two unknown terms: P_0 and A_t. Nozzle exit area (A_e) is limited by the geometry

of the vehicle. The nozzle exit diameter will be maximized to deliver as much thrust as possible while ensuring it does not extrude out into the freestream flow. As of the mid-year point in time, no definite decisions have been made on the body of the test vehicle; hence the exit area of last year's nozzle which is constrained by a 10in diameter including a 5mm wall is used for this design [1]. While the required throat area can be plotted over various nozzle stagnation pressures, it isn't possible to arbitrarily select a stagnation pressure since it depends on fuel properties and surface burn area. The following section will expand on the stagnation pressure and further assumptions made.

$$F_T = \frac{2\gamma R T_0 P_0 A_t \sqrt{\gamma}}{(\gamma-1)\sqrt{RT_0}} \left(\frac{2}{\gamma+1}\right)^{\frac{\gamma+1}{2(\gamma-1)}} \left[1 - \left(\frac{P_e}{P_0}\right)^{\frac{\gamma-1}{\gamma}}\right] + A_e\left(P_e - P_\infty\right) \quad (137)$$

4.3.3.1 Sizing Methodology

For preliminary solid rocket motor design, the velocity of combustion products at the exit of the chamber are often assumed neglible. This leads to assuming the static and stagnation pressures are equal [85][86]. Since stagnation pressure does not change without shocks, work, or heat transfer, this assumption's validity is reinforced by the fact that constant chamber pressure is needed to achieve a constant thrust profile. This assumption is less stable for the increasing pressure of a progressive burn during the early stages of flight.

Solving for the static combustion pressure is possible using the conservation of mass and fuel properties.

$$\frac{dm_s}{dt} = \frac{dm_g}{dt} + \dot{m}_e \quad (138)$$

Equation (138) is a basic mass conservation model of the combustion chamber. The change in solid fuel mass $\frac{dm_s}{dt}$ as it burns is equal to the sum of the change in gas mass within the combustion chamber $\frac{dm_s}{dt}$ and the nozzle mass flowrate out of the chamber $\dot{m}_e$. The flowrate out of the nozzle has already been represented by Eq. (135). The solid mass change can be modeled by a simple massflow equation (139) which relies on fuel density, geometry, and surface burn rate $\dot{r}_{fuel}$.

$$\frac{dm_s}{dt} = \rho_s \dot{r}_{fuel} A_b \quad (139)$$

$$\frac{dm_g}{dt} = V_g \frac{d\rho_g}{dt} + \rho_g \frac{dV_g}{dt} \quad (140)$$

A gas' mass change is defined by Eq. (140) where V_g is the instantaneous gas volume and ρ_g is the instantaneous gas density [85]. As mentioned prior, the pressure of the combustion chamber must be constant to deliver constant thrust.

Referring back to existing assumptions, isentropic flow follows the ideal gas law $P = \rho RT$. Due to this analytical constraint and the assumption that $T_0 = T_c$, the change in density must be zero to maintain a constant pressure. Despite an increase in volume as the solid fuel burns, the second term of Eq. (140) can be neglected due to the relatively small density ($\rho_g << \rho_s$)[87]. In summary, the change in gas mass within the combustion chamber is neglible and can be negated in Eq. (138) for preliminary design work. Expanding the equation's remaining terms and re-arranging the equation for combustion pressure results in the following formula:

$$P_c = P_0 = \frac{\rho_s \dot{r}_{fuel} A_b}{A_t} \sqrt{\frac{RT_0}{\gamma} \left(\frac{\gamma+1}{2}\right)^{\frac{\gamma+1}{\gamma-1}}} \tag{141}$$

The square root portion of this expression is solely dependent on fuel properties and is refered to as the characteristic velocity C^*. Eq. (141) is reduced to Eq. (142) which is identical to the combustion pressure formula specified by NATO for preliminary solid rocket motor design [86]. While it could've been directly used from [86], it is important to understand the assumptions that were used to formulate this expression.

$$P_c = P_0 = \rho_s \dot{r}_{fuel} C^* \frac{A_b}{A_t} \tag{142}$$

$$\dot{r}_{fuel} = a P_c^n \tag{143}$$

$$P_c = P_0 = \left(a \rho_s C^* \frac{A_b}{A_t}\right)^{\frac{1}{1-n}} \tag{144}$$

The burn rate of a fuel is proportional to the combustion pressure. The most common approach to modeling the relationship between burn rate and pressure is Eq. (143) where n is a unitless parameter known as the pressure exponent and a is the temperature coefficient with units $\frac{m/s}{Pa^n}$ [85][87]. Both parameters are empirically determined. The pressure exponent value lies between 0 and 1. The sensitivity of the burn rate to pressure changes increases as the pressure exponent approaches unity. Subsituting Eq. (143) into Eq. (142) and re-arranging the formula yields a final equation (144) for combustion chamber pressure. Furthermore, substituting this equation as stagnation pressure into the thrust force equation (134) leaves us with two unknowns: A_b & A_t. With knowledge of the fuel's specifications, the required throat area can be plotted against burn area for a desired thrust.

4.3.3.2 Fuel Selection

Following last year's decision to use HTPB-based fuels due to their burn rate flexibility and high energy density, the required throat area to burn area for several HTPB mixtures are plotted in Fig. 129 using Eq. (137) & (144). Additional parameters such as the expansion ratio and combustion pressure with respect to the throat and burn area are plotted. All fuel properties used in Eq. (137) are sourced from textbooks and publications [87][88].

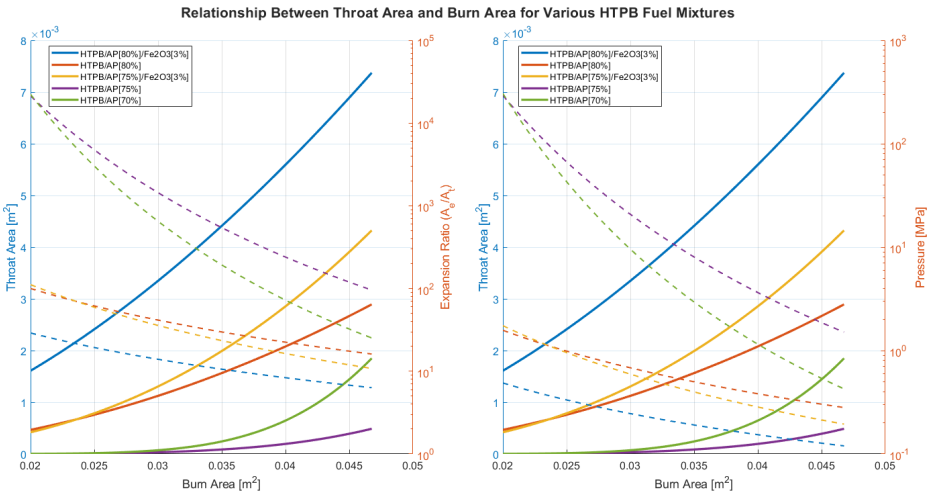

Figure 129: Altitude and Mach profiles determined by the new simulation.

A fuel composition with 80% ammonium perchlorate (AP) has been selected for preliminary design work. It appears to maintain a relatively stable combustion pressure over various burn areas; hence it offers good flexibility in its geometry and nozzle expansion ratio if needed when solving for the acceleration burn phase. The fuel and burn parameters are tabulated in Table 25.

Table 25: HTPB/AP-80% Fuel Properties & Parameters [87][88]

Fuel Parameter	**Value**
Ratio of Specific Heats (γ)	1.25
Density	1855 kg/m^3
Flame Temperature	3440 K
Burn Parameter	
Temperature Coefficient	10.19 $m/sPa^{0.433}$
Pressure Exponent	0.433

4.3.3.3 Results

Using the maximum burn area $0.0467m^2$, the throat area must be $0.00293m^2$ to produce 1.28 kN of thrust during the cruise phase of flight. This configuration results yields a nozzle expansion ratio of 15.9 and a combustion chamber pressure of approximately 0.28 MPa. The relatively smaller pressure compared to last year's design is due to the thrust being reduced to nearly 1/10th of its original value. It is likely that the acceleration phase will have a greater chamber pressure comparable to that of last year. Given the chamber pressure, Eq. (143) yields a burn rate of 5.88mm/s. To meet the 28s cruise time requirement at this burn rate, the end-burn grain must have a length of 0.1647m. At a density of $1855kg/m^2$, the total mass of the fuel required to maintain level flight at the cruise altitude is 14kg.

4.3.3.4 Subsequent Design Phase

In the following capstone term, the acceleration burn profie's geometry will be determined and a unique fuel igniter will be designed. Analyses on the early stages of operation post-ignition need to happen while considering the rapid change of gas mass within the chamber. In case a reasonable acceleration burn cannot be achieved with the current geometric constraints, Fe_2O_3 can be mixed with the fuel to increase the burn rate. Furthermore, the difference between the target exit pressure and ambient atmospheric pressure can be narrowed. Simulations of the combustion chamber will be performed to further refine the design considering thermal effects and non-isentropic flow.

4.4 Control Actuation System - Talha Nawaz

Peer Reviewed by: Tristan Fernandes

A Control Actuation System (CAS) is a system that integrates the actuators, control surfaces, electronics, and mechanisms which combined provide the control for Unmanned Aerial Vehicles (UAVs). Control Actuation Systems are commonly used in military applications, such as in the guidance of rockets, missiles, munitions, and aircraft [89].

Control Actuation Systems work with 2 main actuation methods, thrust vectoring and fin/canard control [90]. For our Rocket Design Project, we will be designing a fin-based CAS System based on the fins designed last year.

4.4.1 Industry Applications

There are multiple industry entities designing and producing Control Actuation Systems worldwide, including Lockheed Martin, Raytheon, Parker US, Marotta Controls, MPS Micro Precision Systems, and General Dynamics.

Of the aforementioned entities, the 2 providing the most information about their products (though still annoyingly little due to information confidentiality) are Marotta Controls and MPS Micro Precision Systems.

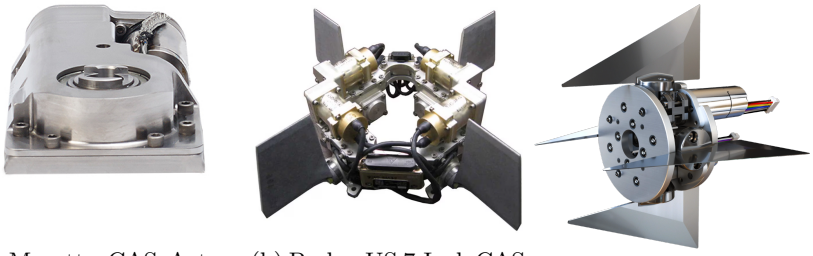

(a) Marotta CAS Actuator [89]

(b) Parker US 7-Inch CAS [90]

(c) MPS CAS [91]

Figure 130: CAS Systems Compared

Control Actuation Systems consist of DC Motors, speed reduction mechanisms, ballscrew/planetary roller screws, sensors, and linkages [91].
Most Control Actuation Systems use two actuation mechanisms, rotary and linear, with rotary mechanisms exerting up to and above 6000 in-lbf and linear mechanisms exerting up to 10,000 lbf [89].

These are the factors that are advertised in industry CAS Systems:

- Over 23 Hz response rate [89]
- High G tolerance [90]
- High temperature tolerance [90]
- No load slew rates of over 200°/sec [89]
- Position and velocity Hall-Effect sensors [90]
- Fin angular play under 0.1° root mean square [91]

All of which would be imperative aspects for our design of the CAS System.

4.4.2 Work from Last Year

Last year, Zak Sultan designed the fins. They prioritized a double wedge airfoil and clipped delta planform [1]. These are considered standard for supersonic fins [92], with the size of the fins being constrained by the launch rails and maximized in order to keep the small Angle of Attack (AoA) assumption valid

[1].

One aspect that did not appear to be justified is the thickening of the root chord of the fin as seen in Figure 131. It could be inferred that it is in order to provide greater structural integrity to the fin. However, this would only be the case if the fin were static and attached directly to the airframe. This is because with or without this bulge along the chord, the fin must anyways taper down to the same fin stem, resulting in the same load path and thus potential failure point.

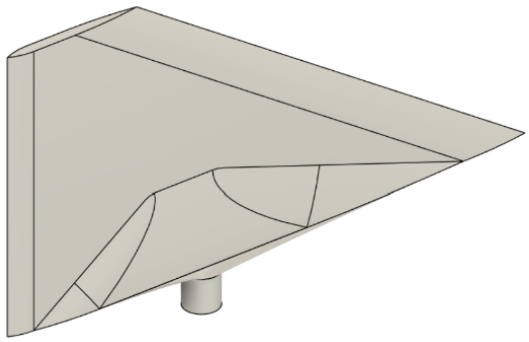

Figure 131: Fin CAD [1]

The other assumptions made by Zak during their analysis include simplifying the fins as thin flat plates, and assuming that the angle of attack during supersonic flight is low enough to generalise airflow as parallel to the plate. Zak also worked under the assumption of stable flight conditions, where gusts and weather would not affect the rocket [1].

Zak's recommendations for future work included the following:

- CFD analysis of the fins to validate fin performance
- Stability and performance analysis during landing phase
- Material selection for thermal and torsional tolerances
- Design of an actuation system

4.4.3 Lift and Drag Calculations

Using Zak's method for calculating C_L using a flat plate approximation, we get:

$$C_{L_\alpha} = \frac{4}{\sqrt{Ma^2 - 1}} \tag{145}$$

At Mach 3, C_{L_α} is calculated to be $= 1.41$. Then, using the equation:

$$C_L = C_{L_\alpha} \times \alpha \tag{146}$$

We get C_L to be $= 0.0984$ when $\alpha = 0.070$ rad, or $4.0°$.

In order to test the validity of the flat plate assumption for the calculation of C_L, we will use the theoretical equation from NACA for C_{L_α} below [93]:

$$\begin{aligned} C_{L_\alpha} = \frac{1}{\pi B\sqrt{m'^2 - 1}} \Bigg\{ \frac{[4m'k + A'(k-1)]^2}{2A'(k^2-1)} \Bigg[\frac{1}{k} \arccos\left(\frac{1}{m'}\right) + \frac{k\sqrt{m'^2-1}}{\sqrt{(km'+1)(km'-1)}} \\ \times \left(\arccos\left(\frac{-1}{km'}\right) - \arccos\left(\frac{4km'(A'-1) - A'(k+3)}{4km' + A'(k-1)}\right)\right)\Bigg] + \frac{[4m'k - A'(k-1)]^2}{4A'(k-1)} \\ \times \sqrt{\frac{m'+1}{k(km'+1)}} \arccos\left(\frac{4km'(1-A') + A'(3k+1)}{4km' - A'(k-1)}\right) + \frac{[4m'k + A'(1+3k)]^2}{4A'(k+1)} \\ \times \sqrt{\frac{m'-1}{k(km'+1)}} \arccos\left(\frac{4km'(A'-1) + A'(k-1)}{4km' + A'(3k+1)}\right) \Bigg\} \end{aligned} \tag{147}$$

Where:

$\lambda = \frac{C_t}{C_r}$
$A = \frac{6S}{C_r(1+\lambda)}$
$\phi = (\frac{\pi}{2}) - \arctan(\frac{S}{C_r - C_t})$
$m = \cot(\phi)$
$B = \sqrt{Ma^2 - 1}$
$k = \frac{BA(1+\lambda)}{BA(1+\lambda) - 4Bm(1-\lambda)}$
$m' = Bm$
$A' = BA$

The data in Table 26 denotes the geometry of the designed fins:

Table 26: Fin Geometry

Dimension	Meters
Root Chord (C_r)	0.508
Tip Chord (C_t)	0.127
Taper Ratio (λ)	0.25
Thickness	0.0104
Aspect Ratio	2.4
Center of Pressure x-Distance (Chord)	0.0635
Center of Pressure y-Distance (Span)	0.127

Using the Equation 147, we calculate the value of C_{L_α} to be 1.45. At the maximum Angle of Attack of 4.0°, we get $C_L = 0.101$. With a difference of only 2.8%, we can claim our value of C_L to be validated.

Using the NACA maximum Coefficient of Lift, we can calculate the maximum Lift Force (L) using the equation below:

$$L = \frac{1}{2} C_L \rho V^2 A \tag{148}$$

Using the Standard Atmospheric Model [6], we get $\rho = 0.07175\ kg/m^3$. Using the fin geometry, we get $A = 0.0807\ m^2$, and from the speed of Mach 3, we get $V = 887.4\ m/s$.

This provides us with a theoretical Lift Force of 231 Newtons, validating Zak's claims and providing a reference value for a free-standing fin.

The method we used for calculating supersonic drag force comes from the USAF DATCOM report [44]

$$C_D = C_{D_0} + C_{D_L} \tag{149}$$

$$C_{D_0} = C_{D_f} + C_{D_w} \tag{150}$$

$$C_{D_L} = C_{D_i} + C_{D_v} \tag{151}$$

$$C_{D_w} = \frac{K}{\beta} \left(\frac{t}{c} \right)^2_{eff} \frac{S_{bw}}{S_{ref}} \tag{152}$$

$$C_{D_L} = \left[\pi AR \frac{C_{D_L}}{C_L^2} \frac{p}{1+p} \right] \left(\frac{1}{\pi AR} \right) \left(\frac{1+p}{p} \right) (C_L^2) \tag{153}$$

where the symbols are:
C_D : Total Drag Coefficient
C_{D_0} : Zero-Lift Drag Coefficient
C_{D_L} : Lift Drag Coefficient
C_{D_f} : Skin Friction Drag Coefficient
C_{D_w} : Wave Drag Coefficient
C_{D_i} : Induced Drag Coefficient
C_{D_v} : Viscous Drag Coefficient
K : Supersonic Airfoil-Based Constant
$\beta = \sqrt{M^2 - 1}$: Cotangent of Mach Angle
t : Max Thickness
c : Chord Length
$\frac{t}{c}_{eff}$: Effective Thickness Ratio
$\frac{S_{bw}}{S_{ref}}$: Wing Area divided by Reference Area
AR : Aspect Ratio
p : Planform Shape Parameter
$\pi AR \frac{C_{D_L}}{C_L^2} \frac{p}{1+p}$: Output of Figure 4.1.5.2-58 [44]

From the equations 149 to 153 from [44], we reach a reasonable range of Drag Coefficients for our Fin. The value for C_D ranges from $0.15113 \leq C_D \leq 0.2939$ based on S_{ref}. Stating that S_{ref} is the area of the triangle that fully encompasses the planform, we get $\frac{S_{bw}}{S_{ref}} = 0.93745$, which gives $C_D = 0.2812$.

Finally, using this value, we can calculate the Drag Force at Mach 3 and AOA of 4°to be 55.3 Newtons.

4.4.4 CFD for Lift and Drag Values

Through multiple attempts, I finally replicated Dominik's CFD setup from last year [1], with the settings being provided in Table 27

Table 27: CFD Free Flow Solution Settings

Settings
Steady State
Pressure Based
K-Epsilon viscosity
Energy Equation On
Air modelled as ideal gas with Sutherland viscosity
Inlet + walls as far field pressure boundaries
Rhie-Chow momentum-based method
All second order spatial discretization

Using these values, we converge to the preliminary simulated values of $F_D = 43.2$ N and $F_L = 189.2$ N, and of $C_D = 0.22$ and $C_L = 0.083$. This results in a difference of 21.9% and 18.1 % respectively.

This difference in values can be caused by differences in what each method accounts for. For example, the Lift Calculation 147 does not account for the airfoil of the fin, assuming it is flat. Analytical results also do not account for viscosity changes in the air, which are significant due to our altitude. Finally, the effects of having a non-triangular wing, but rather a clipped delta wing, leads to greater tip effects, which are not necessarily accounted for analytically.

Therefore, I will reattempt with the following recommendation.

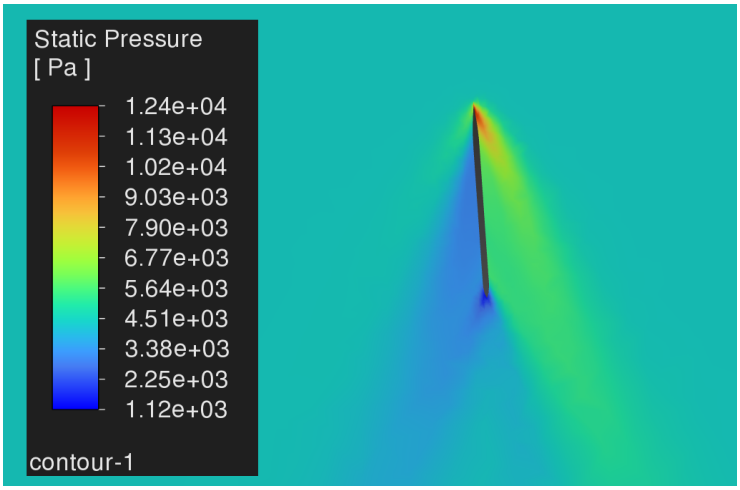

Figure 132: Fin Pressure Contour

I will conduct a simulation with an annular boundary condition representing the body tube of the rocket, allowing us to consider the boundary layer's influence on the fin's control authority and effectiveness as shown in Fig 134. This is a major factor affecting the viability of our fins as active control surfaces, as the boundary layer may be large enough to limit our control authority.

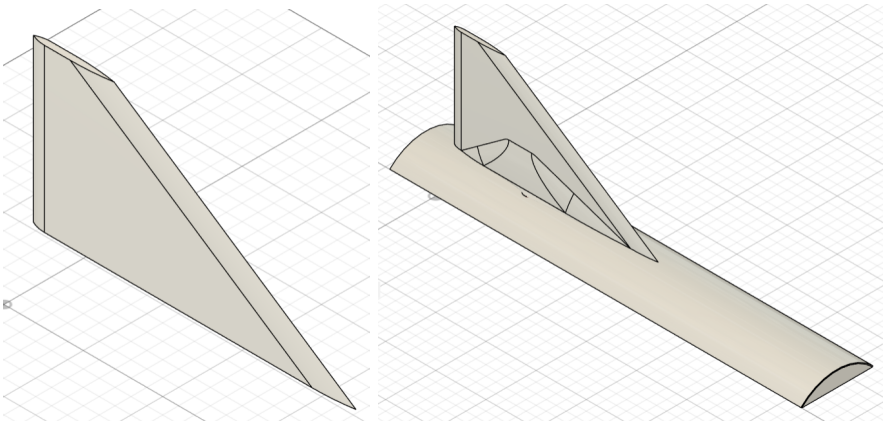

(a) Simplified Fin Model (b) Fin With Partial Body Tube

Figure 133: Fin CFD Models

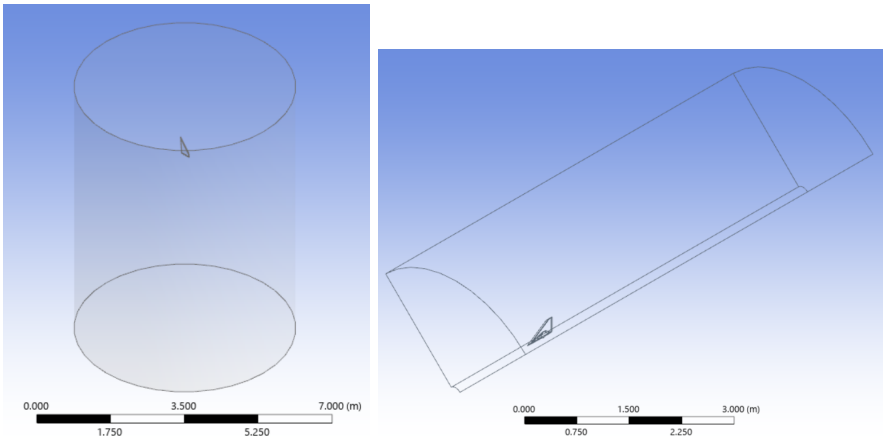

(a) Cylindrical Fin CFD Geometry (b) Annular Fin CFD Geometry

Figure 134: Fin CFD Geometry

4.4.5 Fin Stem Calculations

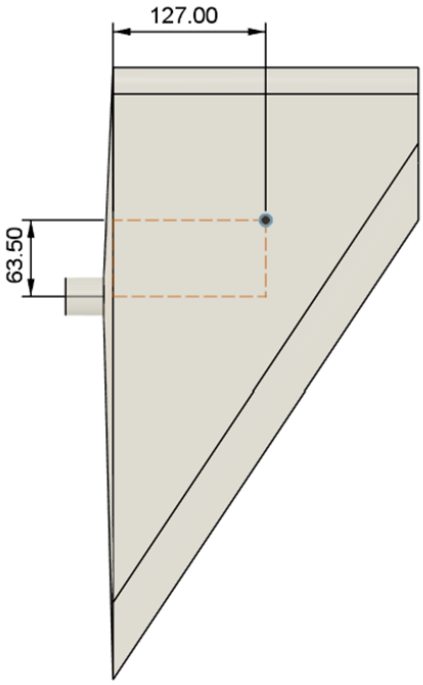

Figure 135: Fin Center of Pressure Location

Using Table 26, we have the values of C_P location for the fins as shown in 135. Using this information, we have the moment arms through which the Lift and Drag Forces are applied to the fin stem in Fig 136.

$$M = Fd \tag{154}$$

Using Eq 154, we calculate the moments being applied on the fin stem to be:

$M_D = M_{bending} = (231N)(0.127m) = 29.3Nm$
$M_L = M_{torsion} = (\sqrt{231^2 + 55.3^2}N)(0.0635m) = 15.1Nm$

Applying a Safety Factor of 2, this means our fin stem must be able to withstand torques of $M_{bending} = 59Nm$ and $M_{torsion} = 30.2Nm$.

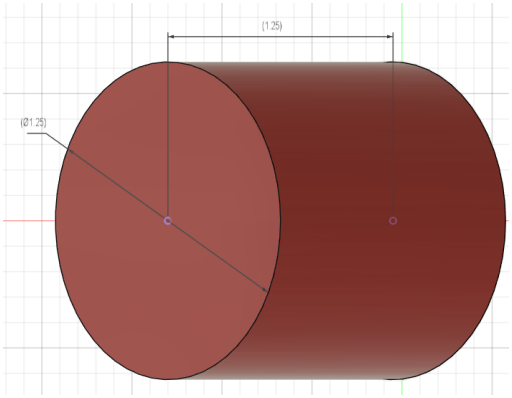

Figure 136: Fin Stem Dimensions

$$\tau_{Torsion} = \frac{rT}{J} = \frac{32rT}{\pi D^4} = \frac{16T}{\pi D^3} \tag{155}$$

$$\sigma_{Bending_{Max}} = \frac{Mc}{I} = \frac{32M}{\pi D^3} \tag{156}$$

$$V = \sqrt{\sigma_x^2 - (\sigma_x \sigma_y) + \sigma_y^2 + (3\tau_{xy}^2)} \tag{157}$$

Using Eqs 155 and 156 from [94], we calculate the Torsion Stress to be 15 MPa and Bending Stress to be 29 MPa. Finally, using Von Mises' Formula for equivalent Stresses (Eq 157), we get the Von Mises' Equivalent Stress to be 16.3 MPa. Von Mises' Equivalent Stress is the maximum stress withstood by a single point of an object made with ductile material, and is used for predicting ductile failure [94] As seen in Table 28, the fin stem is viable and feasible.

Table 28: Alloy Yield Analysis [55]

Material	**Yield Strength /MPa**	**Safety Factor**
Aluminium 6061-0	55	3.4
Aluminium 6061-T6	240	15
Aluminium 7075-T7	435	27

4.4.6 Actuator Requirement Calculations

From Zak's work, we find this graph of fin deflection vs time during cruise, in Figure 137:

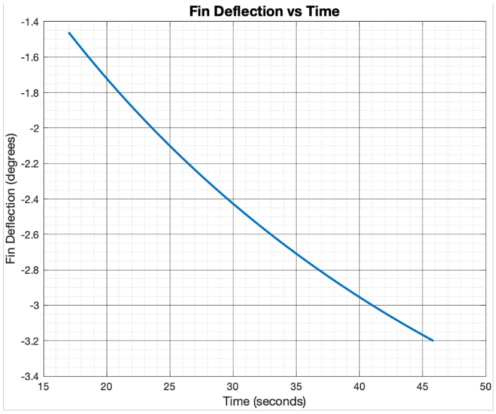

Figure 137: Fin Deflection vs Time During Cruise [1]

Figure 137 is produced under the assumption of steady flight, with no gusts or perturbations during Cruise. Under this assumption, we can identify that the maximum predicted angle of attack is 3.2°. For the purposes of designing the CAS system, it is adequate to round up to ±4°as the maximum Angle of Attack encountered during Cruise. This ensures that we work with the low Angle of Attack assumption, while still providing an envelope for counteracting disturbances.

For the landing flight section, we have two restrictions on the maximum deflection angle of the fins. First, is a restriction of the subsonic stall angle, which for our chosen double-wedge airfoil is over 13° [95]. Secondly, is the restriction of the assumptions for subsonic fin flight performance. This assumption restricts us to a maximum Angle of Attack of 12°, where between ±12°, the Coefficient of Lift curve is approximated as linear.

From Figure 137, we also notice that the moment of maximum angular velocity is at a time of 15 seconds. By taking the gradient of the curve at this point, we calculate the maximum estimated angular velocity with the no-gust assumption to be 0.084°/second.

From industry, CAS Systems can be expected to move at angular velocities >200°/sec [89] while under no load. This will act as a validation for the expected gear ratios for any given motor, where under no load:

$$RPM_{Motor}/GearRatio > 200°/sec \tag{158}$$

Table 29: Actuator Requirements

Requirement	Value	Source
No Load Slew Rate (ω_{noload})	$>200°$/sec	Marotta [89]
Loaded Slew Rate (ω_{load})	$>8°$/sec	Pitch Hold Auto Pilot
Maximum Angular Play	$\leq 0.1°$	MPS [91]
Maximum Cruise Angle of Attack	$\pm 4°$	Small AoA Assumption
Maximum Subsonic Angle of Attack	$\pm 12°$	Linear C_L Approximation
Maximum Torque (τ_{max})	$30.2Nm$	Max Torsion Analysis

4.4.7 Future Work

Finally, for the Winter semester, I hope to have a design for the CAS System completed, evaluated in terms of its form factor, frequency response, angular play, and requirements outlined in Table 29. These priorities will help to rule out and highlight specific design choices, such as rotary and linear actuation methods, as well as choosing gear reductions and motor specifications.

4.5 Airbrake Control System - Nevan Bulitka

Peer Reviewed by Ryan Heywood

Airbrakes are a control surface typically specific to solid rockets. They are specifically designed to increase the drag of the vehicle to either lower the apogee. They are often seen in hobby rocketry and student rocketry competitions where the rocket follows a ballistic trajectory, or in this case to decrease the velocity. Airbrakes are a flight critical system for the Rocket Propelled Wind Tunnel (RPWT) as they are the only system capable of active throttling, in this case by adjusting the drag coefficient.

4.5.1 Previous Years' Work

Last year an airbrake system was proposed and designed to fit within the avionics bay of the airframe. It was actuated by a NEMA 17 high torque stepper motor with a radial deployment design. A schematic of the 2023-2024 airbrake system can be seen in Figure 138. It is a 4 tab design, connected to the motor via the rotating center plate and a small link. The center rotating plate has a rotational limit of 45 degrees, where the airbrakes are at full deployment, while at 0 degrees they are flush to the rocket body, also known as the clean configuration.

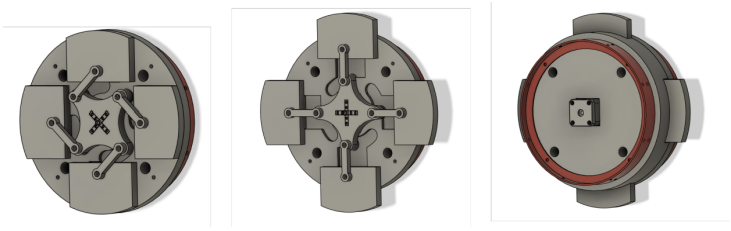

Figure 138: 2023-2024 Airbrakes Design [1]

4.5.2 Current Work

An analysis was performed on the previous design that resulted in the drag coefficient values shown in Table 30 below. Using Equation 159, drag values were calculated and also tabulated in Table 30. Since the drag coefficients were found for the whole vehicle, the difference in drag forces can be used as the "braking power" of the airbrakes. Determining the braking power is critical as it will be used to combat the variation in thrust specifically during cruise when a constant velocity is desired and the grain is in it's end burn.

Table 30: 2023-2024 Airbrake Effect on Vehicle Drag

Deployment Angle (^{o})	0	15	30	45
C_d	0.7889	0.8289	0.8665	0.8891
Drag (N)	1,195	1,256	1,313	1,343

$$D = \frac{1}{2}\rho v^2 C_d A \tag{159}$$

Where:

ρ: density

v: velocity

C_d: drag coefficient

A: reference area

With the introduction of the new Schlieren imaging system, an increase in diameter from 10" to 12" was deemed necessary for adequate space in the test section. As such, a scaled-up version of the previous airbrake design was made. The scaled-up version seen in Figure 139 is a preliminary design following the same methodology as the 2023-2024 design. It allows for variable deployment

from 0 to 45 degrees. When at full deployment, each airbrake extends, disrupting the flow, increasing the form drag.

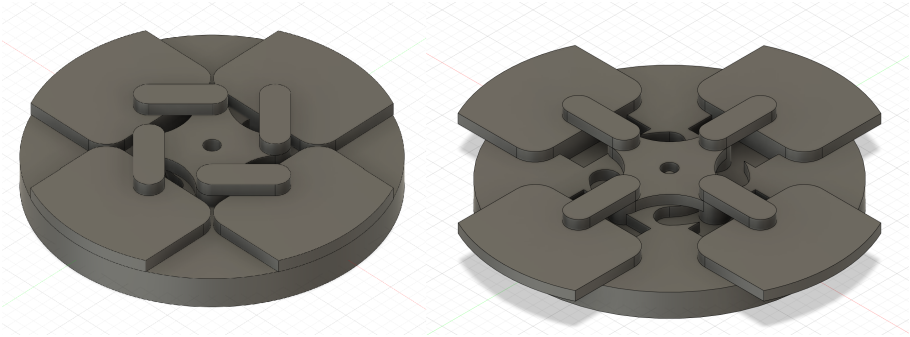

Figure 139: Updated Airbrake Design (12" diameter)

Stagnation Pressure is the pressure measured at a point in a fluid flow at which the fluid comes to rest. For compressible flows it can be determined using Equation 4.5.2. [96]

$$P_t = p(1 + \frac{\gamma - 1}{1} M^2)$$

$\gamma\gamma - 1(160)$

Where:

P_t: stagnation pressure

p: static pressure

γ: ratio of specific heats

M: mach number

A very loose approximation of drag can be obtained by multiplying the stagnation pressure by the reference area. This assumes that the streamlines end in stagnation points along the surface of the airbrake. Evidently, this is not the case, but for a first approximation it will suffice. The stagnation pressure at the flight conditions and resultant drag force per airbrake is shown in Table 31. Each tab was measured at protruding $29.9mm$, with a thickness of $9.9mm$, and an arc length of $132.9mm$. This resulted in an area of $3855mm^2$.

Table 31: Stagnation Pressure - Radial Airbrake Drag Estimation

Stagnation Pressure (kPa)	174.5
Drag Force Estimation (N)	673

The calculated $673N$ drag force per tab is far above even the total braking power calculated in Section 4.5.2 of $148N$. This braking force was found as mentioned before by the difference in drag force between the clean and fully deployed configurations. The C_d used were found through the use of computational fluid dynamics (CFD). One possible problem with this could be the mesh size, as it was a 3D simulation of the whole rocket, done on a student version of Ansys Fluent. An image of the surface mesh is shown below in Figure 140. It is apparent that the mesh on the surface of the airbrakes is far too coarse. This would have hindered the accuracy of the results and therefore, the braking force calculated above.

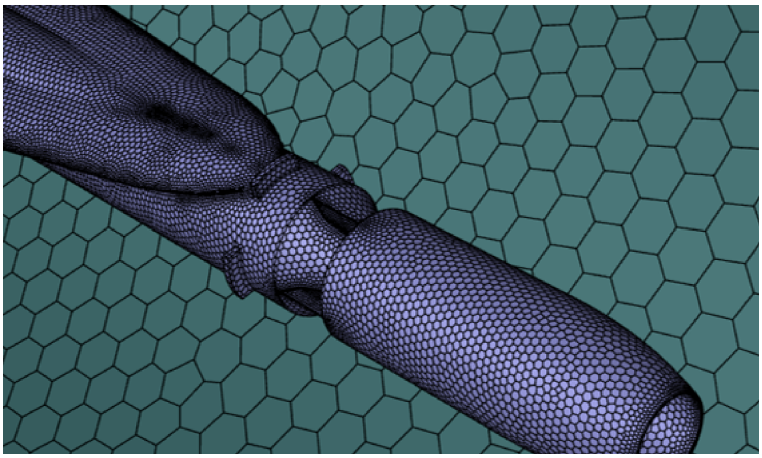

Figure 140: 2023-2024 Surface Mesh [1] (Image: 229)

4.5.3 Alternative Design

With the investigation into an alternative airframe design underway, namely a lifting body or blended wing, it presents the opportunity to fully redesign the airbrake system. An 'umbrella' style design could offer some key benefits that the current radially deploying airbrakes lack. This variation of the airbrake concept uses linear actuation and pushes the brakes out at an angle through the use of a small linkage. This concept was investigated last year but was determined to be too heavy, and complex with the linear actuation. However, it would provide a higher braking force as a larger airbrake could be used. An example of this airbrake is shown below in Figure 141. Although it is shown

on a rocket body, it could be designed for installation on the upper and lower surfaces of the lifting body as well.

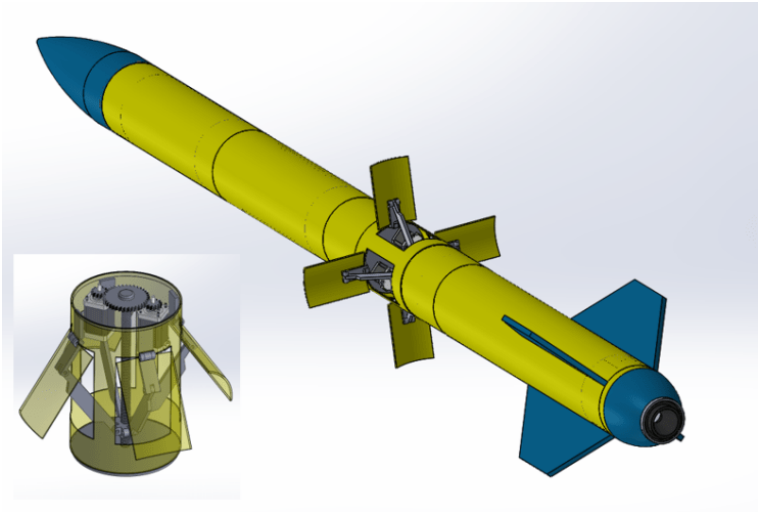

Figure 141: Linearly Actuated Airbrakes [97]

An estimated drag value for the this style of airbrake was also found using Equation 4.5.2. An arbitrary size of $15cm$ by $13.29cm$ was chosen to keep it to the same width as the radial airbrakes, while taking advantage of the additional space. An arbitrary 30° of deployment was chosen giving a total area of $19,935mm^2$, and projected area of $9,968mm^2$, a factor of 2.58 times larger per airbrake than the radial design. With a reduction from four airbrakes in the radial design to two in the 'umbrella' design, it still yields a 30% increase in area. This is seen below in Table 32.

Table 32: Stagnation Pressure - 'Umbrella Airbrake' Drag Estimation

Stagnation Pressure (kPa)	174.5
Drag Force Estimation (N)	1,740

4.5.4 CFD Comparison

In order to directly compare the two designs in more detail, they were both analyzed using CFD, in this case, Ansys Fluent was the application chosen. CFD uses numerical methods to solve the Navier-Stokes equations, continuity, the energy equation, and ideal gas equations. The last two equations are needed as the fluid is compressible, that is to say, density is not constant and constant viscosity cannot be assumed. The Navier-Stokes equations for an infinitesimally

small, moving fluid element are shown in Equations 161-163, for the x, y, and z components respectfully. The conservation of mass or continuity equation, shown in Equation 164. [98]

$$\frac{\partial(\rho u)}{\partial t} + \nabla \cdot (\rho u \boldsymbol{V}) = -\frac{\partial p}{\partial x} + \frac{\partial \tau_{xx}}{\partial x} + \frac{\tau_{yx}}{\partial y} + \frac{\tau_{zx}}{\partial z} + \rho f_x \tag{161}$$

$$\frac{\partial(\rho v)}{\partial t} + \nabla \cdot (\rho v \boldsymbol{V}) = -\frac{\partial p}{\partial y} + \frac{\partial \tau_{xy}}{\partial x} + \frac{\tau_{yy}}{\partial y} + \frac{\tau_{zy}}{\partial z} + \rho f_y \tag{162}$$

$$\frac{\partial(\rho w)}{\partial t} + \nabla \cdot (\rho w \boldsymbol{V}) = -\frac{\partial p}{\partial z} + \frac{\partial \tau_{xz}}{\partial x} + \frac{\tau_{yz}}{\partial y} + \frac{\tau_{zz}}{\partial z} + \rho f_z \tag{163}$$

$$\frac{\partial \rho}{\partial t} + \nabla \cdot (\rho \boldsymbol{V}) = 0 \tag{164}$$

Where:

ρ: density	p: pressure
u: x-speed	τ_{yx}: viscous stress (xz plane, in x direction)
v: y-speed	f: body forces
w: z-speed	t: time
∇: divergence operator	$\boldsymbol{V}$: velocity vector field

The energy equation simply states that the rate of change of energy inside a fluid element is equal to the sum of the net flux of heat into the element, and the rate of work done on the element due to pressure and stress forces on the surface. It has many terms and can be found in as Equation (15.26) in [98].

To begin, three simulations were done, one with only a flat plate acting as the rocket outer wall, a second with the radial airbrake design, and a third with the 'umbrella' airbrake design. All three simulations followed the same setup, with the same sized domain, initialization, and boundary conditions. These conditions are tabulated below in Table 33. All simulations were run up to a maximum of 1,000 iterations, however, they converged prior to reaching that.

Table 33: CFD Drag Analysis Settings

Steady State	Inlet: Velocity
Density Based Solver	Outlet: Pressure
K-Omega SST	Atmosphere Side: Far Field Pressure Inlet
Energy Equation On	Wall and Airbrakes: Wall
Air as Ideal Gas	Second Order Spacial Discretization
Sutherland Viscosity	High Speed Numerics
Solution Steering to Supersonic	Residuals: 10^{-5}

In order to determine a benchmark for the airbrake simulations, the flat plate simulation was done first. The mesh for the flat plate is shown below in Figure 142. It is a structured mesh with 26,600 elements, a max skewness of 0.029, and minimum orthogonal quality of 0.999, indicating a highly structured mesh. Although not optimized with a higher concentration of cells near the wall, the mesh size should be small enough to capture the boundary layer. Future work would involve mesh convergence and optimization.

Figures 143-145 show the temperature, pressure, and velocity contours.

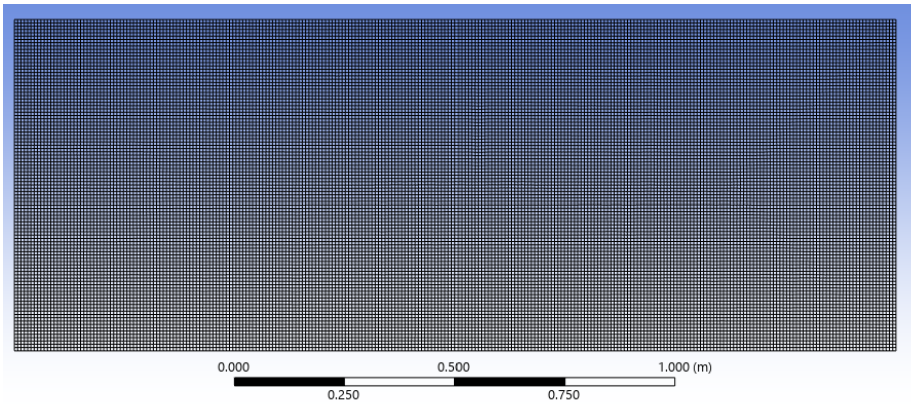

Figure 142: No Airbrake Mesh

Figures 143 to 145 show the temperature, pressure, and velocity contours. As expected the temperature and velocity contours show little change however, the pressure shows an increase from $4,750Pa$ up to around $7,300Pa$ far from the wall.

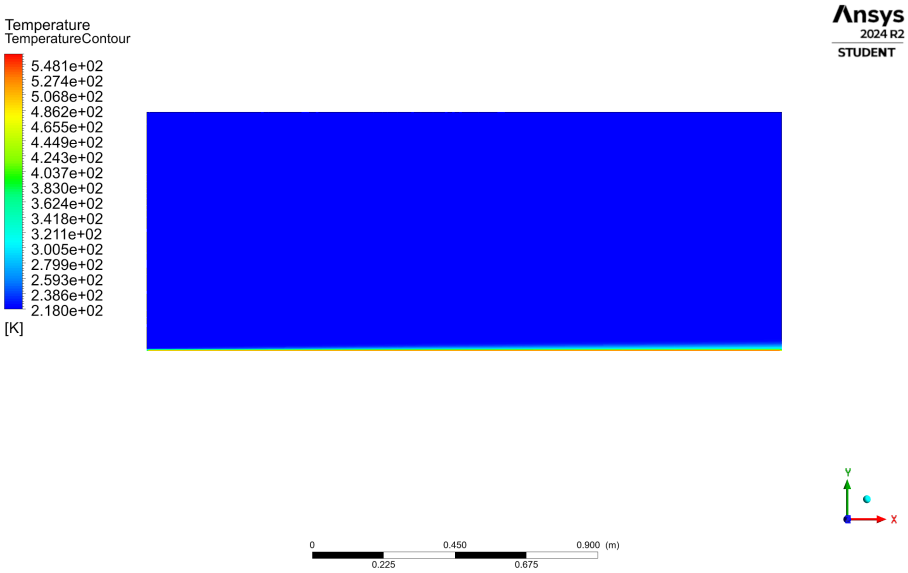

Figure 143: No Airbrake Temperature Contour

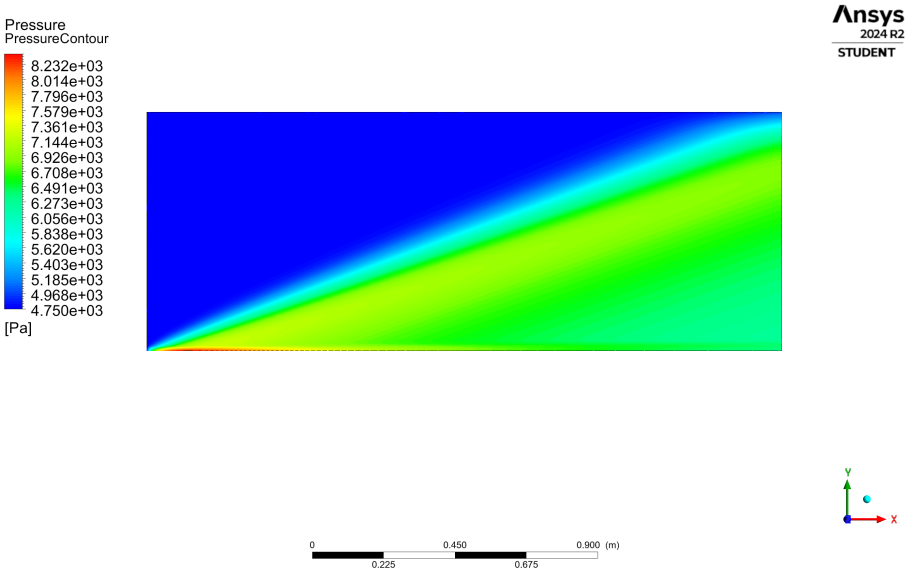

Figure 144: No Airbrake Pressure Contour

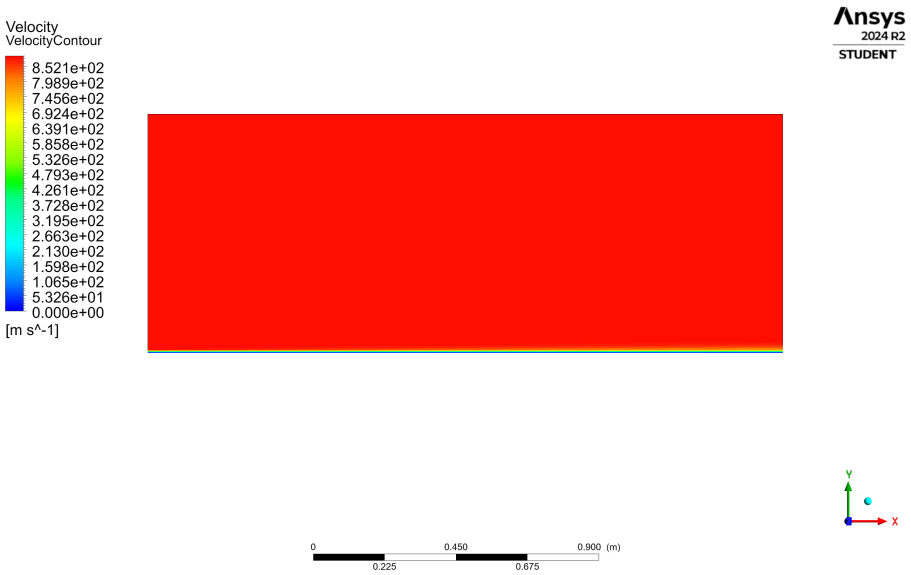

Figure 145: No Airbrake Velocity Contour

Similarly, the radial airbrake design was simulated, with the mesh shown below in Figure 146. It again is a structured mesh with 165,581 elements, with a maximum skewness of 0.350 and a minimum orthogonal quality of 0.884.

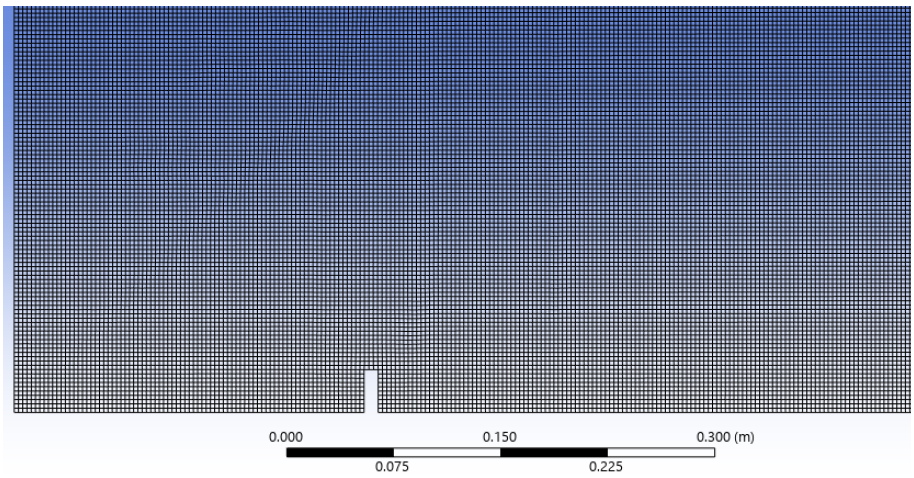

Figure 146: Radial Airbrake Mesh

Figures 147-149, show the temperature, pressure, and velocity or the flow past

the radially deploying airbrake.

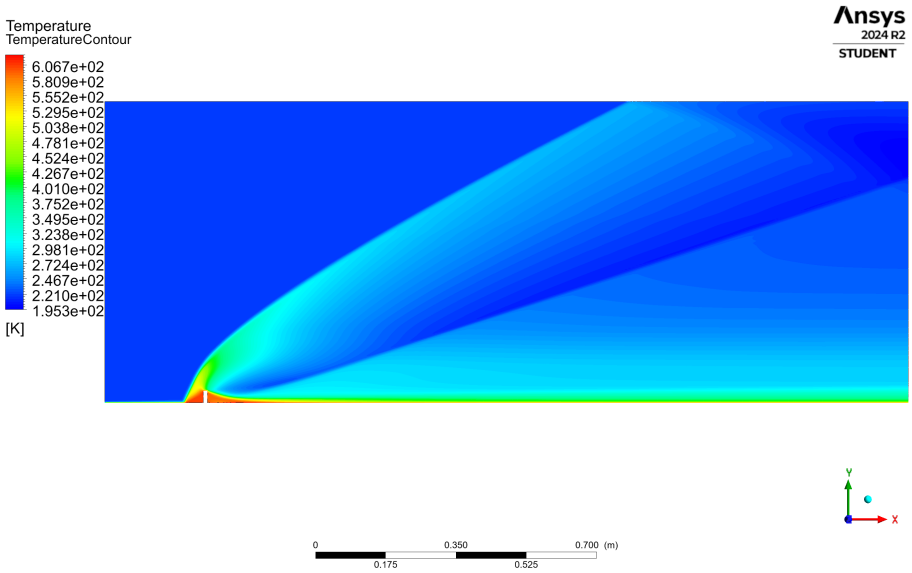

Figure 147: Radial Airbrake Temperature Contour

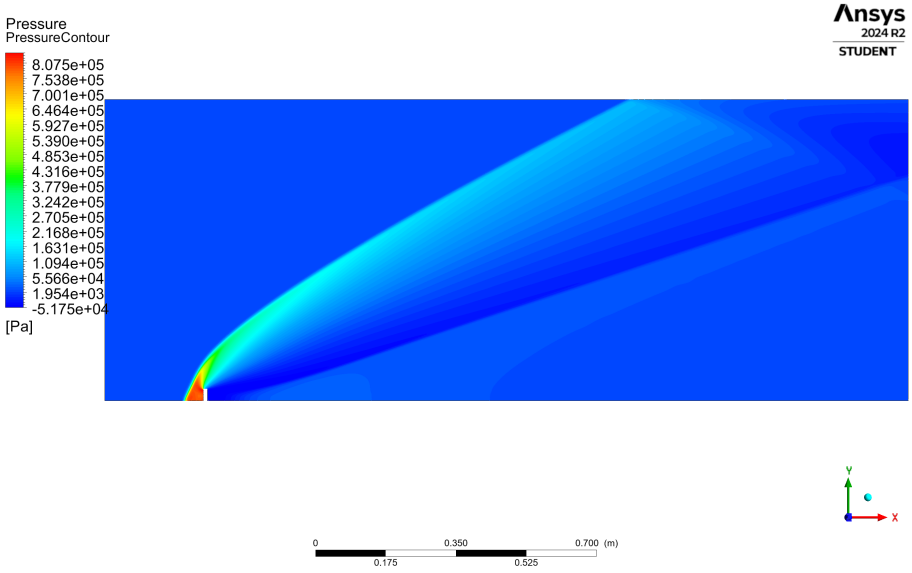

Figure 148: Radial Airbrake Pressure Contour

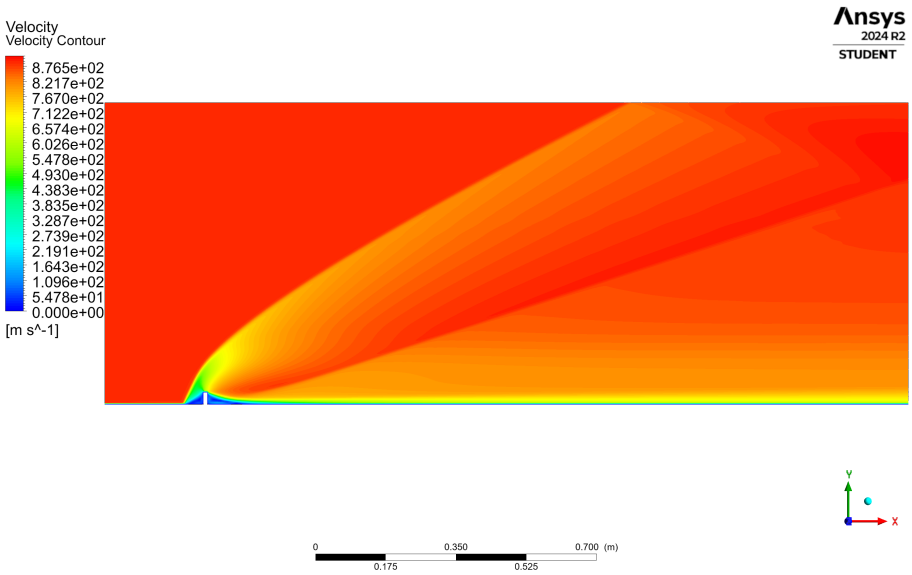

Figure 149: Radial Airbrake Velocity Contour

Finally, the 'umbrella' airbrake design was simulated, with the mesh shown below in Figure 150. It again is a structured mesh with 165,048 elements, with a maximum skewness of 0.647 and a minimum orthogonal quality of 0.664.

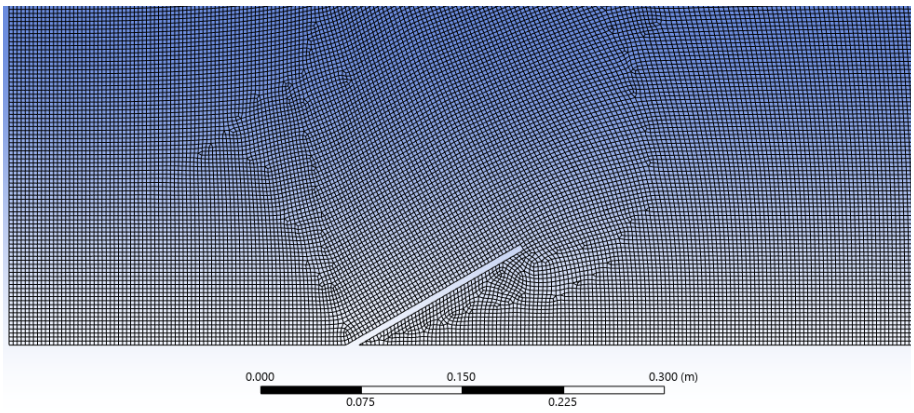

Figure 150: Linear Airbrake Velocity Contour

Figures 151-153, show the temperature, pressure, and velocity or the flow past the linearly actuated airbrake.

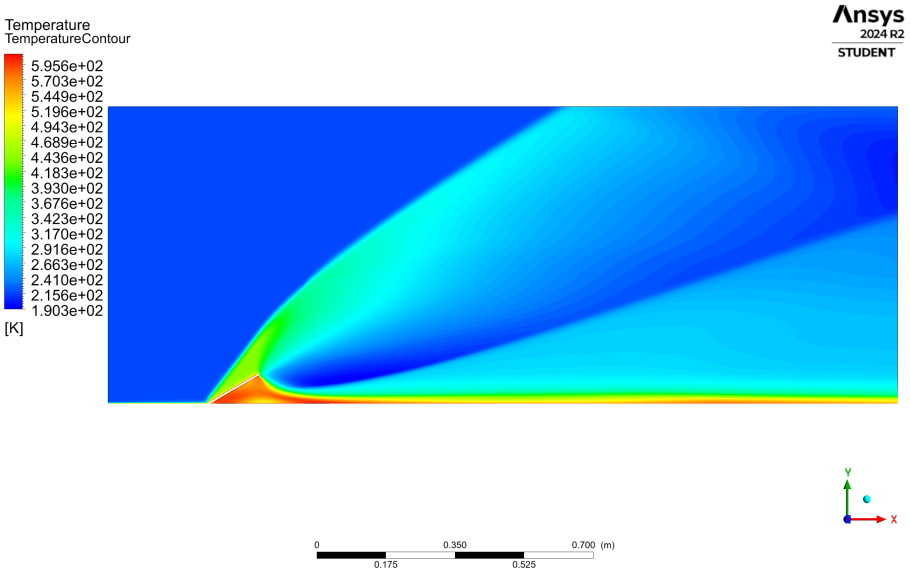

Figure 151: Linear Airbrake Temperature Contour

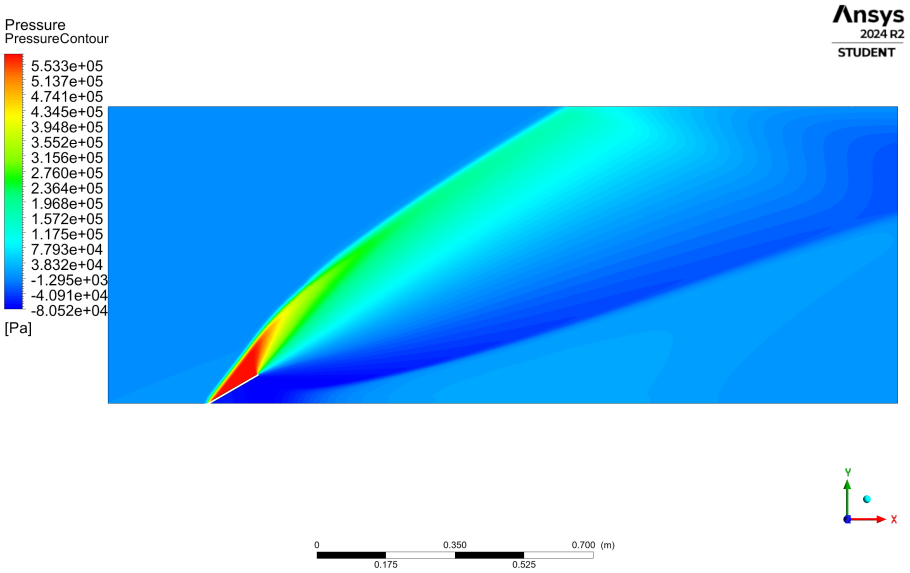

Figure 152: Linear Airbrake Pressure Contour

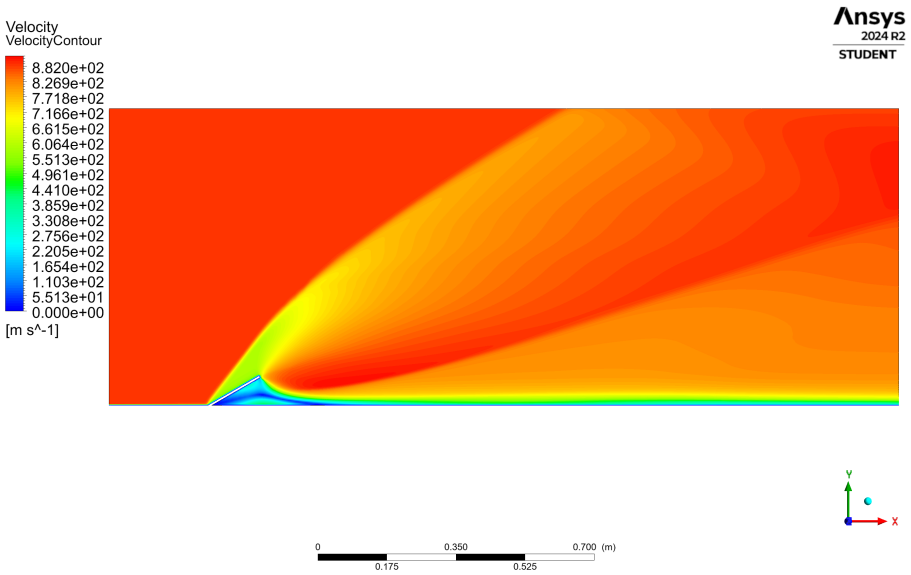

Figure 153: Linear Airbrake Velocity Contour

The CFD simulations also yielded the total drag values, which are tabulated below in Table 34. The drag values for both airbrake systems appear far too large than what is reasonable even with the solutions converging. Even as such, it is apparent that the linearly actuated airbrakes provide roughly twice as much braking force as the radially deploying system. This can be seen in the larger wake generated and the larger amount of recirculation present with the 'umbrella' style airbrake. The reference depth was set correctly to $132.9mm$, so the error is unknown and must still be investigated. As expected, the temperature at the leading edge of the linearly actuated airbrake is approximately 200^oC less than the radial deploying airbrakes. Additionally, the pressure is much lower on the linearly styled airbrakes compared to the radial. This would allow for a lighter and more conventional material to be used, as it would experience less thermal and pressure loads.

Table 34: CFD Determined Drag Force

CFD Setup	**Drag**	**Braking Force**
Flat Plate (N)	285	-
Radial Airbrake (N)	3,600	3,315
Linear Airbrake (N)	6,500	6,215

4.5.5 Conclusion and Future Work

With two proven viable designs, a decision must be made on which design to continue with. The radially deploying airbrakes seem more viable for a rocket body with its more compact shape, while the linearly deploying airbrakes appear better suited for the lifting body as they can be located on the top and bottom surfaces still allowing braking power, while not introducing a pitching moment. This design decision will be made by the preliminary design review in January 2025.

Future work includes analzying the error(s) in the current CFD models to determine a more reasonable drag value. Additional work includes determining the thermal loads and forces on the airbrakes and selecting an appropriate material. Once the airframe design decisions have been made, integration with the airframe, and supporting systems must also be completed.

4.6 Autopilot - Tristan Fernandes

Peer Reviewed By: Talha Nawaz
Peer Reviewed By: Xuan Nie

4.6.1 Abstract

The pitch-hold Autopilot system developed for the RPWT system serves as a critical component for maintaining stability and attitude control during the ascent and level-flight testing regimes of the flight path. While last year's implementation demonstrated the ability to achieve pitch stability during these conditions, it faced significant challenges in rapidly converging to the desired pitch angle. These limitations, primarily stemming from the system's response characteristics and controller tuning, which is one of the goal of this semester's work.

Following in the steps of the prior methodology, this work addresses the limitations of the modeling of the legacy Autopilot, and proposes methods to further develop this system to accurately model forces and moments acting on the vehicle. The method for determining the stability derivatives follows in the steps outlined in the legacy Autopilot. Results are consistent with last year's report, further verifying last year's model. However, when modeling the system, key limitations and assumptions were noted for future improvement. This semester's work also utilizes the framework from the legacy Trajectory Code as a foundation for determining Euler angles, rates and accelerations, velocities and distances as the vehicle is traveling during its desired modeled trajectory. Aerodynamic forces and moments are refereed directly from the legacy CFD data, along with key lengths and masses from other sections of last year's design [99]. To summarize, this semester's modeling has been solely been focusing on the design from the previous year, as information is readily available. Due

to the various design changes proposed this semester, some work has been done to demonstrate the effect of these proposed changes on stability and control of the vehicle.

Improvements have been made to the proportional-integral-derivative (PID) controller design. Specifically, the controller gains have been systematically determined to achieve a faster, less erratic response within the short period approximation. This ensures that the pitch angle aligns with the desired trajectory for the ascent and level-flight testing conditions. Additionally, this reduces the demand of the fin physical fin actuator, paving the road for further design in this aspect. This iterative tuning process incorporated both numerical simulations, and trajectory and transient specific constraints to optimize system performance.

The outcome of this semester's work analyzes the limitations in the previous Autopilot system the outlines the steps to achieving reliable, high-performance attitude control, with the goal of overcoming the previous limitations and settling a benchmark for future developments efforts. Additionally, effects of design changes are addressed to ensure that the rest of the team is on the same page, as stability and control of the vehicle is one of the critical aspects of this capstone design project and any flight vehicle in general.

4.6.2 Stability, Control, and Equilibrium

It is important to note key definitions before proceeding in the analysis of the Legacy Autopilot.

A body is in equilibrium when it is at rest or in uniform motion (i.e., constant linear and angular momenta)[100]. Equilibrium can be further categorized into the static and dynamic equilibrium:

- **Static Equilibrium** occurs when the body is at rest, with no net external forces or torques acting upon it. in this state, both the linear and angular accelerations are zero, indicating that the sum of all forces and the sum of all torques are balanced.
- **Dynamic Equilibrium** occurs when a body is in motion, but its velocity (both translational and rotational) remains constant. In this state, the net forces and torques acting on the body are balanced, allowing it to maintain a steady motion without acceleration. For example, an aircraft flying at a constant speed and altitude is in dynamic equilibrium, with forces like thrust, drag, lift, and weight perfectly balanced.

Stability is a property of an equilibrium state, where the equilibrium of a system is deemed stable if the body, when disturbed, returns to its initial states [100].

Stability can further categorized into static and dynamic stability.

- **Static Stability** refers to the initial tendency of a system to return to its equilibrium state when disturbed. If, after a small displacement, the forces or moments acting on the body naturally push it back toward its original position, the system is said to have positive static stability. For example, an aircraft that naturally aligns itself with the airflow after a small pitch displacement exhibits static stability. The requirement for static longitudinal stability is defined in terms of a neutral point, the boundary between stable and unstable CG positions [100].
- **Dynamic Stability** refers to the system's behavior over time after being disturbed. A dynamically stable system not only initially moves back toward equilibrium (indicating static stability) but also eventually settles back into its original state without oscillating excessively or diverging. For instance, an aircraft that experiences damped oscillations in response to a disturbance, ultimately returning to level flight, demonstrates dynamic stability. The requirement of dynamic stability is expressed in terms of the damping and frequency of a natural oscillation.

Control refers to the ability to manipulate the motion or orientation of a body to achieve a desired state or trajectory. Control systems are designed to generate forces or torques that counteract disturbances, maintain equilibrium, or guide the body along a specific path. Effective control relies on feedback mechanisms, where sensors measure the current state, compare it to the desired state, and adjust the control inputs accordingly. In the context of flight vehicles, control surfaces like ailerons, elevators, rudders and fins allow pilots or autopilots to manage an aircraft's orientation and stability dynamically.

4.6.3 Axes and Notation

Figure 154 below highlights the standard notation for describing the motion and aerodynamic forces acting on the body-axes system [101]. The body frame is fixed to the vehicle

- The variables x, y, z represent coordinates, with the origin at the center of mass of the vehicle [101]. The x-axis lies in the symmetrical plane of the vehicle and points towards the nose of the vehicle [101]. The z-axis lies in the plane of symmetry, perpendicular to the x-axis, pointing downwards [101]. The y-axis completes the triad, pointing out of the right wing [101].
- The variables u, v, w represent the instantaneous components of linear velocity in the directions of the x, y, z axes, respectively [101].
- The variables ϕ, θ, ψ represent the angular rotations, relative to the equilibrium state, about the x, y, z axes, respectively [101].
- The variables p, q, r represent the instantaneous components of angular velocity about the x, y, z axes, respectively [101]. Note, $p = \dot{\phi}, q = \dot{\theta}$ and

$r = \dot{\psi}$

- the variables X, Y, Z represent the components of aerodynamic force in the direction of the x, y, z axes, respectively [101].
- the variables L, M, N represent the components of aerodynamic moments about the x, y, z axes respectively [101].

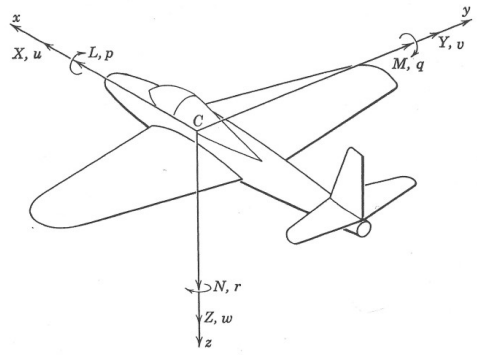

Figure 154: Standard Notation For Aerodynamic Forces and Moments, and Linear and Rotational Velocities in Body-Axis System[101] - missing RPY angles.

Terminologies depicted in Figure 155, highlights the key definitions the Guidance angles used for longitudinal dynamics modeling in aerospace engineering [102]. The body frame x is pointing forward at an angle of θ from the horizon x', Z is pointing down at an angle of γ from the vertical inertial plane z', and the velocity vector v points in the direction of motion at an angle of γ from the horizon. The pitch angle is defined by θ, the flight path angle is defined by γ, and the angle of attack is defined by α. The Flight Path angle is defined by the following notation, where the positive sign is used when the vehicle points upwards, while the negative is used when the vehicle is pointing downwards:

$$\gamma = \theta \pm \alpha \tag{165}$$

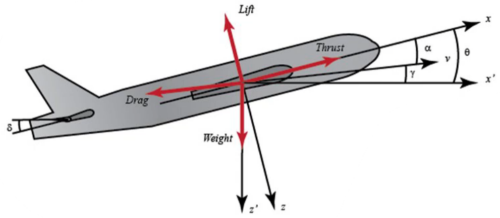

Figure 155: Standard Notation for Aerospace Guidance Angles [102].

4.6.4 Linearized Longitudinal Dynamics Model

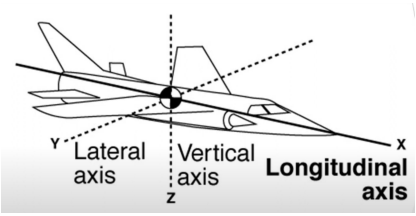

Figure 156: Standard Notation For Longitudinal Axis [101]

The foundation of the pitch-hold Autopilot system is the linearized representation of the longitudinal dynamics acting on the RPWT airframe using the short period approximation. Dynamics about the longitudinal axis (see Figure 156) are essential for characterizing trim maneuvers, which it critical for maintaining level-flight conditions during testing. This is an idealization, as the position of the control surfaces can be held fixed only to the extend of the maximum available control forces [101]. The aerodynamic forces and moments acting on the vehicle body are determined from non-dimensional coefficients that are linear functions of state and input variables.

Although the longitudinal dynamics of a flight vehicle are highly non-linear, they are simplified using the small angle and small rates assumptions as shown in the equations below:

$$\begin{aligned} &\sin\theta \approx \theta, \quad \cos\theta \approx 1 \\ &\dot{\theta} \text{ (angular rates) are small and linearization} \end{aligned} \tag{166}$$

4.6.5 State-Space Modeling

The state-space is modeled via non-dimensional variables and constant vehicle parameters.

4.6.5.1 Constant Vehicle Parameters

Constant vehicle parameters are values inherent to the airframe that do not change with time. These values are defined in the Table below:

Table 35: Aerodynamic Parameters and Calculations

Variable/Calculation	Value/Expression
Chord at root (wing)	$c_{\text{root}} = 0.1524\,\text{m}$
Chord at tip (wing)	$c_{\text{tip}} = 0.1016\,\text{m}$
Wingspan	$b = 3.5\,\text{m}$
Chord as a function of spanwise location (wing)	$c(y) = c_{\text{root}} + \left(\frac{c_{\text{tip}} - c_{\text{root}}}{2}\right) y$
Wing area (S)	$S = 2 \times \int_0^{\frac{b}{2}} c(y)\,dy = 0.4445\,\text{m}^2$
Mean aerodynamic chord ($\bar{c}$)	$\bar{c} = 2 \times \frac{1}{S} \int_0^{\frac{b}{2}} c(y)^2\,dy = 0.1287\,\text{m}$
Wing incidence angle	$i_{\text{wing}} = 0.0524\,\text{rad}$
Aspect ratio (wing)	$AR = \frac{b^2}{S} = 27.56$
Leading edge sweep angle (fin)	$\Lambda_{\text{LE,fin}} = 0.98$
Taper ratio (fin)	$\lambda_{\text{fin}} = 0.25$
Fin thickness	$t_{\text{fin}} = 0.010\,\text{m}$
Chord at root (fin)	$c_{\text{root,fin}} = 0.508\,\text{m}$
Finspan	$b_{\text{fin}} = 0.254 \times 2\,\text{m}$
Chord at tip (fin)	$c_{\text{tip,fin}} = \lambda_{\text{fin}} \times c_{\text{root,fin}} = 0.1270\,\text{m}$
Fin area (S_f)	$S_f = \left(\frac{c_{\text{root,fin}} + c_{\text{tip,fin}}}{2}\right) \times b_{\text{fin}} = 0.1613\,\text{m}^2$
Tail arm length (l_t)	$l_t = 2.2\,\text{m}$
Efficiency factor (η)	$\eta = 0.8$
Horizontal tail volume coefficient (V_H)	$V_H = \frac{S_f \times l_t}{S \times \bar{c}}$

4.6.5.2 Transient Vehicle Parameters

To ensure consistency with last year's Autopilot results, the values for the rocket parameters over time were used in this semester's modeling. It is important to note that these values are not representative of the final design parameters, a number of improvements can be made to the modeling of these transient conditions, which will be the goal of future work. These values and the algorithm used to calculate these values are shown in Figure 157 and Figure 158, respectively.

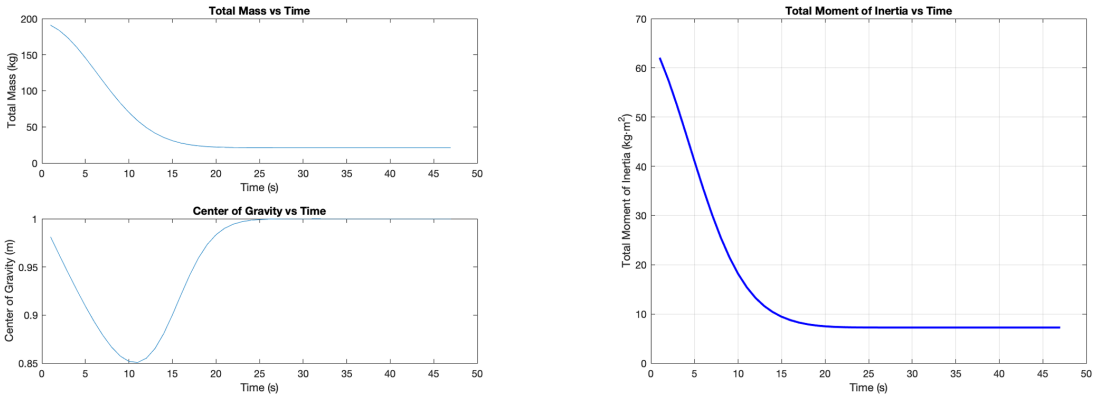

Figure 157: Transient Vehicle Parameters. [99]

Algorithm 4 Calculate Rocket Parameters Over Time

Initialize l_{casing}, r, $m_{\text{prolpellant}}$, m_{casing}, $I_{yycasing}$, $r_{\text{propellant}}$, cg_{Casing}
for $t = 1$ to t_b **do**
  $l_{\text{prop}} = l_{\text{casing}} - \text{burn\_rate} \times t$
  $m_{\text{propellant}} = m_{\text{propellant}} - ((l_{\text{casing}} - l_{\text{prop}})/l_{\text{casing}}) \times m_{\text{propellant}}$
  $x_{\text{cg}} = ((m_{\text{casing}} \times l_{\text{casing}}/2) + (l_{\text{prop}}/2) \times m_{\text{propellant}})/(m_{\text{propellant}} + m_{\text{casing}})$
  $m_{\text{tot}} = m_{\text{propellant}} + m_{\text{casing}}$
  $Iyy_{\text{propellant}} = (m_{\text{propellant}}/12) \times (3 \times r^2_{\text{propellant}} + l^2_{\text{prop}})$
  $Iyy_{\text{combined}} = I_{yycasing} + Iyy_{\text{propellant}}$
  $d_{\text{casing}} = |cg_{\text{Casing}} - x_{\text{cg}}|$
  $d_{\text{propellant}} = |l_{\text{prop}}/2 - x_{\text{cg}}|$
  $I_{\text{casing\_total}} = I_{yycasing} + m_{\text{casing}} \times d^2_{\text{casing}}$
  $I_{\text{propellant\_total}} = Iyy_{\text{propellant}} + m_{\text{propellant}} \times d^2_{\text{propellant}}$
  $Iyy_{\text{Parallel Axis Theorem}} = I_{\text{casing\_total}} + I_{\text{propellant\_total}}$
end for

Figure 158: Algorithm for Transient Vehicle Parameters. [99]

Considering these results, a number of issues can be pointed out. First, the total mass of the vehicle is not consistent with other sections of last year's report, which had the final loaded mass of the vehicle at 253.80, and an zero fuel weight of 80.34 kg [99]. It is clear here that the legacy Autopilot was working with outdated mass values. The CG (center of gravity) movement has been a point of great concern for the Controls team, as the CG is expected to move aft, towards the nose, as the propellant is ejected. Even following the steps outlined in the algorithm produced inconsistent results, further questioning the legitimacy of this transient parameter. Clearly, this is key model that must be improved. Lastly, just observing the method of calculating the principle 'YY' MOI (moment of inertia), clear limitations can be identified. Only the MOI of the propellant and casing were modeled. Evaluating the transient MOI of the

propellant is a good starting point, but only modeling the MOI of the casing (which had a mass of 21.20 kg [99]), is not a proper representation of vehicle. Sections such as the test section, wings and even fins are critical components that need to be modeled as well.

4.6.5.3 Non-Dimensional Aerodynamic Force and Moment Coefficients

Referenced from CFD results of the open rocket body from last year's work, the non-dimensional coefficients for lift, drag and pitching moments are defined below for changes in Mach number and changes in angle of attack.

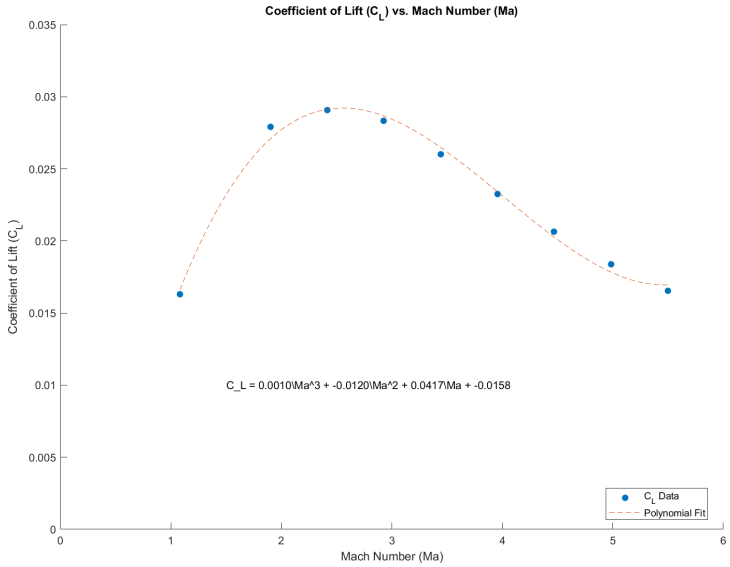

Figure 159: Coefficient of Lift VS Mach Number. [99]

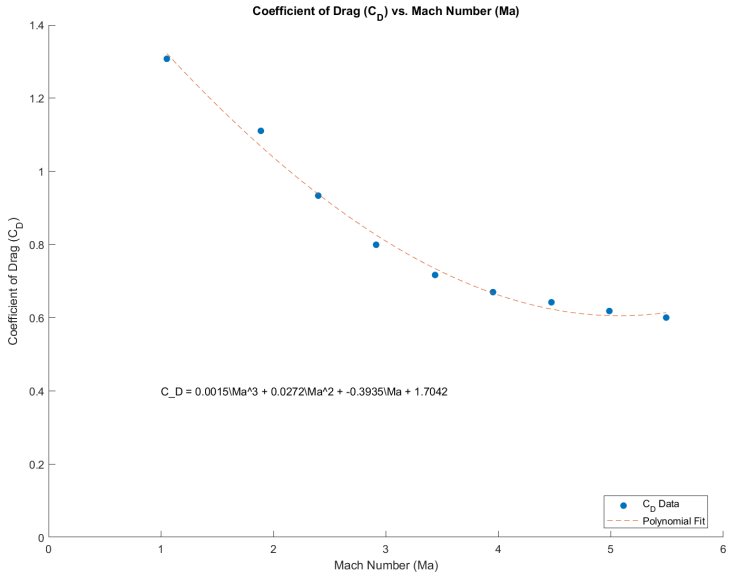

Figure 160: Coefficient of Drag VS Mach Number. [99]

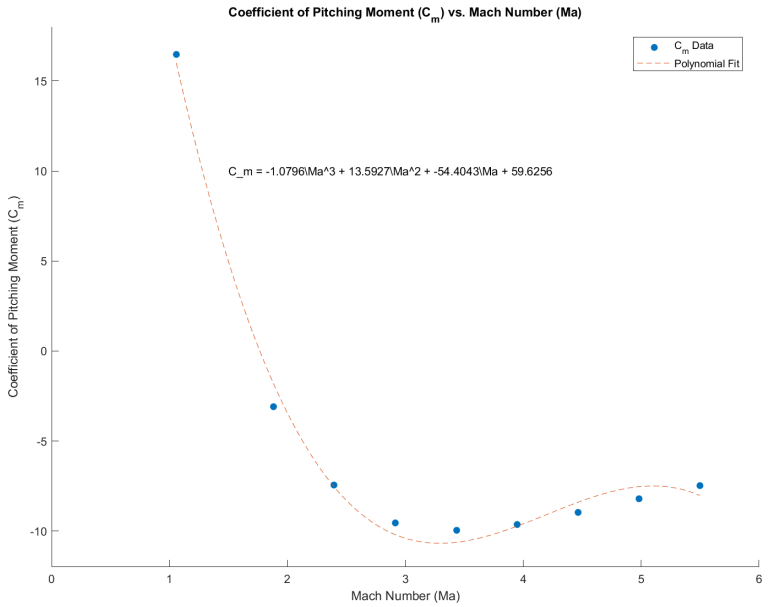

Figure 161: Coefficient of Pitching Moment VS Mach Number. [99]

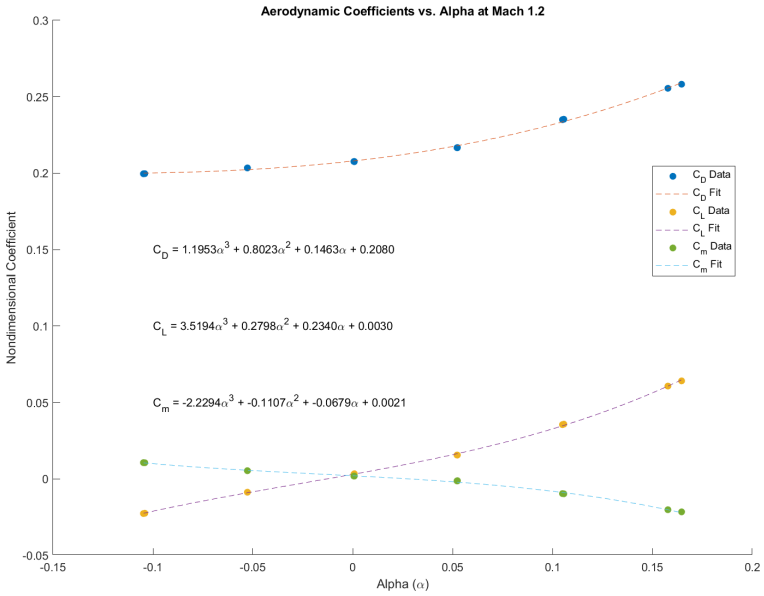

Figure 162: Aerodynamic Coefficients VS AOA - Mach 1.2. [99]

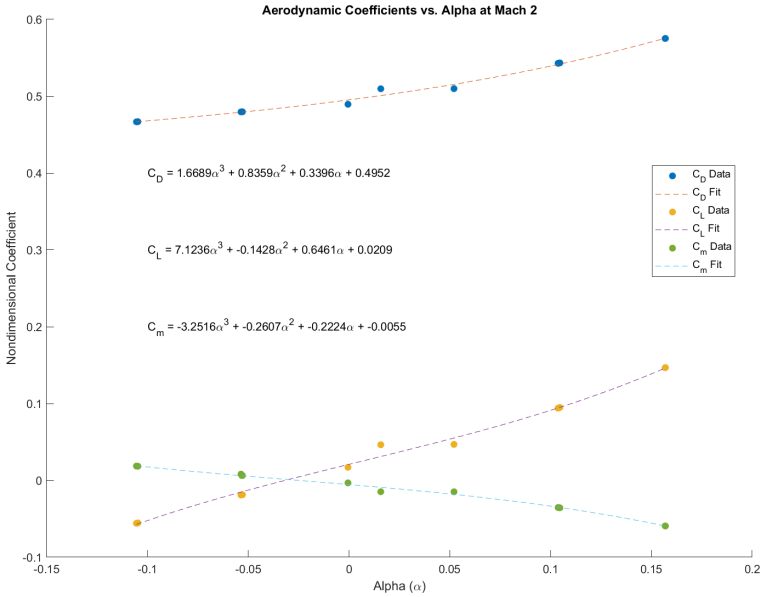

Figure 163: Aerodynamic Coefficients VS AOA - Mach 2. [99]

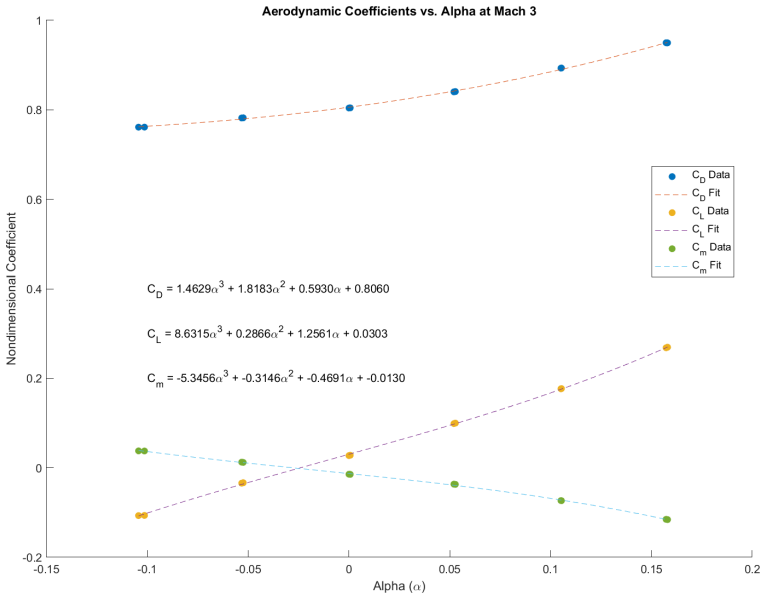

Figure 164: Aerodynamic Coefficients VS AOA - Mach 3 [99]

4.6.5.4 Longitudinal Stability Derivatives

Estimates for the X, Z, M longitudinal forces and moments with respect to the relevant variables u, w, q are covered in this section. These parameters are the longitudinal stability derivatives, which are dimensionless, as they expressed in terms of dimensionless aerodynamic coefficient derivatives.

Derivatives with respect to vertical velocity perturbations w are related to aerodynamic derivatives with respect to AOA (angle of attack), due to the small angles, small rates assumption:

$$\alpha = \tan^{-1}\left(\frac{w}{u}\right) \approx \frac{w}{u_0} \tag{167}$$

Axial force change with speed under constant thrust (X_u) focuses on the change in axial force under the condition of constant thrust, highlighting its impact on drag. It provides insight into how the rocket's drag characteristics vary with speed [99], [101].

$$X_u = -\frac{QS}{mu_0}\left(2C_{D_0} + MC_{D_M}\right) \tag{168}$$

Change in the aerodynamic force along the vertical axis of the aircraft (Z_u) with respect to changes in the aircraft's forward velocity dictates how the rocket's

flight characteristics change with speed, influencing its ability to maintain steady flight and recover from perturbations [99], [101].

$$Z_u = -\frac{QS}{mu_0}\left[2C_{L_0} + C_{Z_u}\right] \tag{169}$$

where

$$C_{Z_u} = -C_{L_u} \tag{170}$$

Change in the pitching moment with respect to changes in the rocket's forward velocity (M_u) dictates how the rocket's attitude will respond to changes in velocity. The importance of M_u lies in its impact on the aircraft's ability to maintain or return to a desired flight attitude following a disturbance [99], [101].

$$M_u = \frac{QS\bar{c}}{I_y u_0} C_{m_u} \tag{171}$$

Change in the aerodynamic force in the direction of the rocket's motion with respect to changes in the angle of attack (X_w) has direct implications for the rocket's ability to maintain or adjust its speed and trajectory. It affects flight stability, control responsiveness, and the ability to maintain desired speeds and altitudes in various flight conditions [99], [101].

$$X_w = \frac{QS}{mu_0}\left(C_{L_0} - \frac{2C_{D\alpha}}{\alpha}\right) \tag{172}$$

Change in vertical force with vertical speed (Z_w) is significant for understanding pitch damping and the rocket's stability in the vertical plane, affecting how the rocket responds to perturbations in its flight path [99], [101].

$$Z_w = -\frac{QS}{mu_0}\left(C_{D_0} + C_{L\alpha}\right) \tag{173}$$

Change in the pitching moment with respect to changes in the rocket's angle of attack (M_w) quantifies the moment that causes the rocket to pitch as the angle of attack changes. The significance of M_w is its influence on the rocket's ability to maintain a stable flight attitude in response to changes in the angle of attack [99], [101].

$$M_w = \frac{QS\bar{c}}{I_y u_0} C_{m\alpha} \tag{174}$$

Change in the aerodynamic force along the vertical axis of the aircraft with respect to changes in the pitch rate (Z_q) dictates the rocket's vertical lift and

aerodynamic forces affected by the rate at which the aircraft's nose moves up or down. It affects the rocket's ability to maintain or return to a level flight path after a pitch disturbance [99], [101].

$$Z_q = \frac{QS\bar{c}}{2mu_0} C_{Z_q} \tag{175}$$

where

$$C_{Z_q} = -2\eta V_H \alpha_t \tag{176}$$

Pitching moment change with pitch rate (M_q) provides insights into the pitch damping characteristics of the rocket. High pitch damping is crucial for the stability of the rocket's response to pitch control inputs and atmospheric disturbances [99], [101].

$$M_q = \frac{1}{I_y}\frac{\partial M}{\partial q} = \frac{QS\bar{c}^2}{2I_y u_0} C_{mq} \tag{177}$$

where

$$C_{mq} = -2\eta \frac{\ell_t}{\bar{c}} V_H a_t \tag{178}$$

Ignoring stability derivatives that are rates of change, the longitudinal state matrix is defined as:

$$A = \begin{bmatrix} X_u & X_w & 0 & -g\cos(\Theta_0) \\ Z_u & Z_w & u_0 + mZ_q & -g\sin(\Theta_0) \\ M_u & M_w & M_q & 0 \\ 0 & 0 & 1 & 0 \end{bmatrix} \tag{179}$$

Table 36: Table 4.1: Longitudinal Stablity Derivatives Summary.

Variable	**X**	**Z**	**M**
u	$X_u = \frac{QS}{mu_0}[2C_{X_0} + C_{X_u}]$	$Z_u = \frac{QS}{mu_0}[2C_{Z_0} + C_{Z_u}]$	$M_u = \frac{QS\bar{c}}{I_y u_0} C_{m_u}$
w	$X_w = \frac{QS}{mu_0} C_{X_\alpha}$	$Z_w = \frac{QS}{mu_0} C_{Z_\alpha}$	$M_w = \frac{QS\bar{c}}{I_y u_0} C_{m_\alpha}$
q	$X_q = 0$	$Z_q = \frac{QS\bar{c}}{2mu_0} C_{Z_q}$	$M_q = \frac{QS\bar{c}^2}{2I_y u_0} C_{m_q}$

Expressions for all the dimensional stability derivatives in terms of non-dimensional aerodynamic coefficient derivatives are summarized in the table above. Refer to the Autopilot Appendix for the unpacking of these equations and definitions of key parameters. Figure 165 below, shows the values of the longitudinal stability derivatives during the 30 second level-flight testing condition.

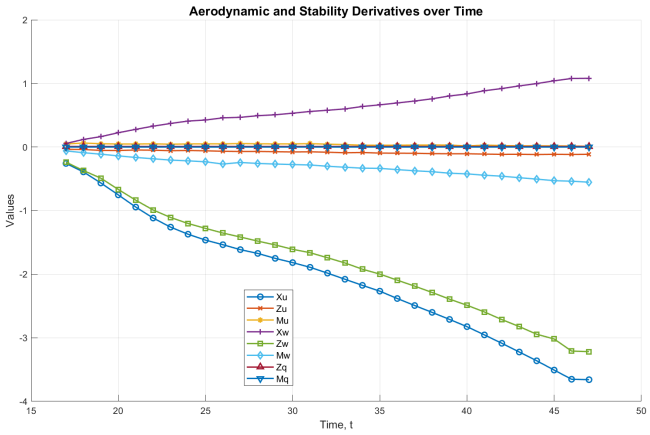

Figure 165: Stability Derivatives For Pitch Hold - 17 - 47 Second Burn Time.

By examining Figure 165, it is clear the most sensitive parameters are the axial speed derivatives X_u and X_w, and the vertical speed derivative Z_u. The negative stability derivatives suggest that the system is dynamically unstable. In the context of aerodynamics and flight dynamics, these derivatives indicate that any disturbance in the system will grow over time rather than diminish, leading to an unstable flight condition [100]. Positive stability derivatives indicate that the system is dynamically stable. In the context of aerodynamics and flight dynamics, these derivatives signify that any disturbance in the system will decay over time rather than grow, leading to a stable flight condition [100].

4.6.5.5 Controller Effectiveness

The control matrix is defined by the forces and moments due to fin deflection. The equations that govern the control matrix are defined below:

$$Z_{\delta_f} = \frac{\partial C_z}{\partial \delta_f} \tag{180}$$

$$M_{\delta_f} = \frac{\partial C_m}{\partial \delta_f} \tag{181}$$

A critical limitation of the state-space model is that the system does not integrate the non-dimensional coefficients of the equations above correctly. The method to properly model these parameters involves CFD simulation of a range control surface deflection at various Mach numbers, as defined in last year's report [99], but the following assumptions were made to model these values:

$$C_{m_{\Delta_f}}(i) = -2\eta(\frac{l_t}{\bar{c}})V_H a_t \tag{182}$$

$$C_{Z_{\Delta_f}} = -C_{L_q}(i) \tag{183}$$

4.6.6 Longitudinal Performance

To evaluate the proportional-integral-derivative gains of the PID controller, transient conditions of the system must be specified.

The table below provides the characteristics of the short period stick-fixed performance of the vehicle, specifically the natural frequency and damping ratio:

Table 37: Comprehensive Dynamics Performance Analysis

Short Period			
Parameter	**Formula**	**Initial Value**	**Final Value**
Frequency	$\omega_{nsp} = \sqrt{\frac{Z_\alpha M_q}{u_0} - M_\alpha}$	6.383	41.49
Damping Ratio	$\zeta_{sp} = -\frac{M_q + M_\alpha + \frac{Z_\alpha}{u_0}}{2\omega_{nsp}}$	0.0171	0.0388

Frequency refers to the amount of oscillations per unit time. In the context of aircraft stability and control, it is a measure of the period to complete one cycle of motion. Damping ratio is a dimensionless quantity that defines the oscillations in a system decay after a disturbance. This indicates how quickly the flight vehicle returns to steady flight after being disturbed [99], [103].

Period of the system refers to the time it take to complete one cycle of motion. Measured in seconds, it is inversely proportional to the frequency [99], [103]. The period of oscillation is defined by the following equation:

$$Period = \frac{2\pi}{\omega} \tag{184}$$

The period for the short period approximation is shown in the table below:

Table 38: Summary of Period Approximations for Short Period Dynamics

Approximation	**Initial**	**Final**
Short Period	0.9843	0.1514

The decrease in period for the short period approximation indicates that the vehicle's response to pitch disturbances improves as propellant is burned [99].

The characteristic equation for the short period longitudinal motion during the pitch-hold condition is defined by [99], [103]:

$$\lambda_{sp} = \frac{M_q + \frac{Z_\alpha}{u_0}}{2} \pm \frac{\sqrt{\left(M_q + \frac{Z_\alpha}{u_0}\right)^2 - 4\left(M_q \frac{Z_\alpha}{u_0} - M_\alpha\right)}}{2} \tag{185}$$

The characteristic equation represents the denominator of the open loop transfer function. The roots of the characteristic equation (λ) under the pitch-hold condition represents the vehicle's response to perturbations in pitch. Real roots represent a non-oscillatory response, which results in exponential decay or growth [103]. Complex roots represent oscillatory responses. The real part indicates the damping (stability) and the imaginary part indicates the frequency of oscillation [103]. The initial and final states of the roots for the short period longitudinal motion under the pitch-hold condition are shown in Table below.

Table 39: Longitudinal motion's characteristic of the Short Period Assumption

State	Initial	Final
Short Period	$-0.1092 \pm 6.3825i$	$-1.6104 \pm 41.4625i$

The initial roots indicate an oscillatory response due to the imaginary component. The real portion indicates that the system tends towards stability, as the negative sign indicates exponential decay. The final roots indicate a larger oscillatory response due to the larger imaginary component. The negative real portion indicates that the the system is stable and will lead to exponential decay of pitch perturbations.

Time to half amplitude ($t_{1/2}$) is a direct measure of the damping effect on the amplitude of the oscillation over time. This highlights the relationship between the damping coefficient and the rate of amplitude decay, with a larger damping coefficient resulting in a faster decay [99], [103]. It is determined using the following relation:

$$t_{1/2} = \frac{0.69}{|\eta|} \tag{186}$$

Table 40: Time to Half Amplitude

State	Initial	Final
Short Period	6.321	0.4287

The initial time to half amplitude for the short period approximation is relatively large, indicating a slow damping process. The demonstrates that the

system is less efficient at dissipating energy and stabilizing within a short period after being perturbed [99]. The final time to half amplitude indicates a drastic damping ratio, indicating a more rapid damping of oscillations. This demonstrates that the system is more effective at dissipating energy, leading to a faster stabilization after perturbations [99]. The transition from initial to final state indicates a significant improvement in the system's damping capacity as the propellant is burned.

Number of cycles to half amplitude ($N_{1/2}$) indicates the number of oscillations before the amplitude reduces to half of the initial value [99], [103]. It is defined by the following equation:

$$N_{1/2} = 0.110 \frac{\omega}{|\eta|} \tag{187}$$

Table 41: Number of Cycles to Half Amplitude for Short Period Dynamics

Approximation	Initial	Final
Short Period	6.432	2.834

4.6.7 Desired Pitch Angle Trajectory

The pitch hold autopilot is currently deriving the desired pitch trajectory from the legacy trajectory code [99] as the reference signal. The desired trajectory is computed based on the Euler integrator output, accounting for the 30-second level-flight testing interval. This trajectory ensures the rocket follows a controlled path while maintaining longitudinal stability. Figure 13 illustrates the desired pitch angle in degrees during the 30-second level-flight test. These values guide the autopilot to minimize deviation from the desired state, ensuring precision in maintaining the trajectory.

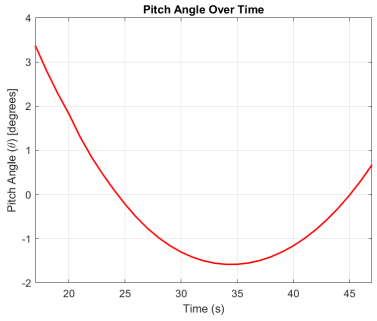

Figure 166: Desired Pitch Angle - From Legacy Trajectory Code

The desired pitch values are tabulated and are ready to be implemented in the Autopilot as the desired signal. Future work could aim to use the updated trajectory code discussed earlier, as it contains more accurate flight path data during the 30-second testing period.

4.6.8 Pitch Hold Autopilot

4.6.8.1 State and Input Variables

The state-space representation of a linear-time invariant (LTI) system is defined below. The longitudinal plant of the state equation is represented as:

$$\dot{\mathbf{X}} = \mathbf{AX} + \mathbf{BU} \tag{188}$$

And the output equation is defined as:

$$\mathbf{Y} = \mathbf{CX} + \mathbf{DU} \tag{189}$$

The state vector ($\mathbf{X}$) represents the state of the system at a given time. Each element of $\mathbf{X}$ corresponds to a state variable which is internal quantity of the system such as position, velocity or acceleration. The state vector for the longitudinal plant is defined as:

$$\mathbf{X} = \begin{bmatrix} \text{vertical velocity} \\ \text{pitch angle} \end{bmatrix} = \begin{bmatrix} w \\ \theta \end{bmatrix} \tag{190}$$

The input vector (U) represents the external inputs (control signals) applied to the system. The only input vector covered in this semester's Autopilot is the horizontal fin deflection (δ_f):

$$\mathbf{U} = \begin{bmatrix} \text{horizontal fin deflection} \end{bmatrix} = \begin{bmatrix} \delta_f \end{bmatrix} \tag{191}$$

The state matrix (A) defines how the state variables interact and evolve without external inputs. The dimensions are $n \times n$, where n is the number of states. The components of A are the stability derivatives which are defined in the subsequent sections.

$$\mathbf{A} = \begin{bmatrix} Z_w & u_0 \\ M_w & M_q \end{bmatrix} \tag{192}$$

The input matrix (B) defines how the inputs influence the state variables. The dimensions are $n \times m$, where m is the number of inputs. The components of the B are the actuator effectiveness which is defined in the subsequent sections.

$$\mathbf{B} = \begin{bmatrix} Z_{\delta_f} \\ M_{\delta_f} \end{bmatrix} \tag{193}$$

The output matrix (C) defines how the state variables contribute to the output. The dimensions are $p \times n$, where p is the number of outputs. The row vector

$\begin{bmatrix}0 & 1\end{bmatrix}$ selects the output from the state variables, specifically targeting the pitch rate to be integrated into the pitch angle [99].

$$\mathbf{C} = \begin{bmatrix}0 & 1\end{bmatrix} \tag{194}$$

The feedthrough matrix (D) directly relates the inputs to the outputs without involving states. In the case of the RPWT system, D is zero because the inputs do not directly influence the outputs without passing through the states.

$$\mathbf{D} = 0 \tag{195}$$

4.6.8.2 Transfer Open-Loop and Closed-Loop Transfer Functions

The open-loop (OL) transfer function takes fin deflection as an input and outputs the current pitch angle. The OL transfer function is represented using a state space integrator and the short period approximation [101]. At each time step this is calculated and thus the transfer function is time evolving [99]. The following OL transfer function describes the relationship between the pitch angle $\theta(s)$ and the fin deflection $\delta_f(s)$ [101]:

$$\frac{\theta(s)}{\delta_f(s)} = \frac{1}{s}\frac{q(s)}{\delta_f(s)} = \begin{bmatrix}0 & 1\end{bmatrix}(sI - A_{sp})^{-1}B_{sp} \tag{196}$$

The transfer function $\frac{q(s)}{\delta_f(s)}$ relates the elevator deflection to the pitch rate ($q(s)$). I is the identity matrix, A_{sp} is the short period approximation system matrix, and B_{sp} is the control matrix that describes how the fin deflection influences the state variables. The initial and final states of the governing state, control matrices, and the pitch hold transfer function are shown in Table 42.

Table 42: Short Period Fin Deflection Transfer Function between test time states

Equation	Initial	Final
$A_{sp} = \begin{bmatrix} Z_w & u_0 \\ M_w & M_q \end{bmatrix}$	$A_{sp} = \begin{bmatrix} -0.2172 & 839.5 \\ -0.0485 & -0.0012 \end{bmatrix}$	$A_{sp} = \begin{bmatrix} -3.208 & 3186.1 \\ -0.5404 & -0.0129 \end{bmatrix}$
$B_{sp} = \begin{bmatrix} Z_{\delta_f} \\ M_{\delta_f} \end{bmatrix}$	$B_{sp} = \begin{bmatrix} -2.206 \\ -15.087 \end{bmatrix}$	$B_{sp} = \begin{bmatrix} -1.237 \\ -6.375 \end{bmatrix}$
$\frac{\theta(s)}{\delta_f(s)} = \frac{1}{s}\frac{q(s)}{\delta_f(s)} = \begin{bmatrix}0 & 1\end{bmatrix}(sI - A_{sp})^{-1}B_{sp}$	$\frac{\theta(s)}{\delta_f(s)} = \frac{-0.1509s - 0.03169}{s^3 + 0.2183s^2 + 40.75s}$	$\frac{\theta(s)}{\delta_f(s)} = \frac{-6.375s - 19.78}{s^3 + 3.221s^2 + 1722s}$

The closed-loop (CL) transfer function $\frac{\theta}{\theta_c}$ represents the output response (pitch angle θ) to the command input (commanded pitch angle θ_c). $G_{\theta\delta_f}$ is the open-loop transfer function, and $\delta_f(s)$ is the Laplace transform of the fin deflection input. The term $1 + G_\theta \delta_f(s)$ represents the effect of feedback in the closed-loop system.

$$\frac{\theta}{\theta_c} = \frac{G_{\theta\delta_f}(s)}{1 + G_{\theta\delta_f}(s)} \tag{197}$$

$$\frac{\theta}{\theta_c} = \frac{C_{PID}(s)G_{\theta\delta_f}(s)}{1 + C_{PID}(s)G_{\theta\delta_f}(s)} \tag{198}$$

$C_{PID}(s)$ is the transfer function of the PID controller, which is added into the CL to improve the system's convergence to the desired Euler pitch angles. Using MATLAB's 'pidtune' command, the PID gains can be determined at each time step iteration of the state.

$$C_{PID}(s) = K_p + \frac{K_i}{s} + K_d s \tag{199}$$

K_p is the proportional gain, adjusting the control signal in proportion to the current error. $\frac{K_i}{s}$ is the integral term, adjusting the control signal based on the accumulation of past errors, aiming to eliminate steady-state errors. $K_d s$ is the derivative term, adjusting the control signal based on the rate of change of the error.

4.6.8.3 Closed-Loop Step Response

The closed-loop step response evaluates the effectiveness of the legacy Autopilot controller PI gains in tracking the desired pitch angle trajectory. This section also compares the behavior of the system using the improved PID controller against the legacy PI controller, using the same transient performance parameters outlined above.

Figure 167 displays the system's response with both the legacy PI controller and the proposed PID controller at the start of the level-flight test. The PI controller exhibits erratic oscillations due to insufficient damping, failing to settle quickly into a stable trajectory. In contrast, the PID controller introduces a derivative term that actively damps these oscillations. While there is a slightly larger overshoot in the pitch angle initially, this is followed by rapid convergence, highlighting the PID's capability to achieve faster and more stable settling behavior.

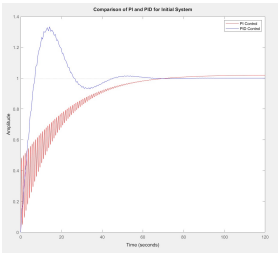

Figure 167: Comparison of PID and Legacy PI controller Step Response - Initial State.

For the final state of the level-flight interval, Figure 168 similarly shows the enhanced performance of the PID controller. The PI controller continues to display instability, with oscillations persisting across the duration. However, the PID controller, even as the system parameters evolve due to transient effects (e.g., fuel burn, CG shift), maintains its damping characteristics, providing consistent control performance. This reinforces the conclusion that the PID controller is more robust under varying flight conditions.

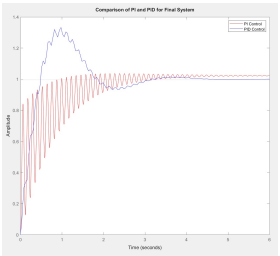

Figure 168: Comparison of PID and Legacy PI controller Step Response - Initial State.

While the PID controller significantly improves stability compared to the legacy PI controller, the response in the final state remains choppy. This is due to the dynamic variability of the system. As the vehicle progresses through the level flight path, changes in mass distribution, center of gravity (CG), and aerodynamic parameters influence the stability derivatives. These transient variations reduce the effectiveness of the fixed PID gain values used in the step input validation. Specifically, the derivative term can overreact to sudden changes in state variables, causing residual oscillations.

To improve this response is proposed to employ a similar gain scheduling strategy as last year, which adjusts the PID parameters based on real-time flight state data, such as Mach number, angle of attack, and mass distribution. Additionally the transient model can be refined to include comprehensive aerodynamic

effects and control surface interactions, providing a more accurate basis for the controller design.

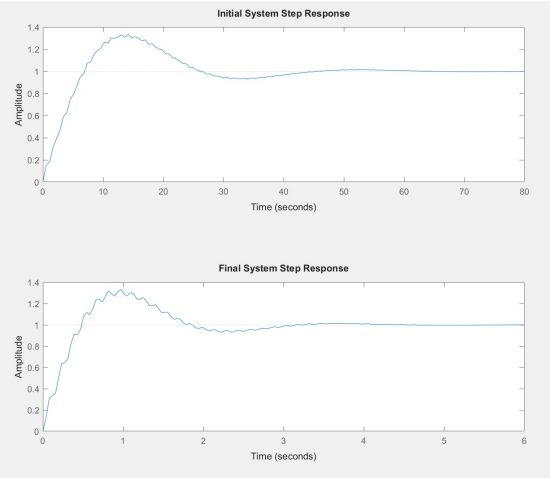

Figure 169: PID Step Response.

4.6.9 Conclusion and Future Work

This semester's work has focused on the analysis and refinement of the pitch-hold autopilot system, addressing the limitations of the legacy design while proposing critical improvements. The longitudinal dynamics model, rooted in the short-period approximation, provides a foundation for understanding the stability and control characteristics of the vehicle. By integrating transient domain characteristics and the trajectory-based desired vehicle pitch angles for level flight into the MATLAB-based autopilot code, the system must dynamically schedule PID gain coefficients to improve its response to changing flight conditions. The results demonstrate that a well-tuned PID controller significantly enhances the dynamically unstable response of the legacy PI design.

However, this semester's work also highlighted key challenges. The current control efficiency expressions, derived from theoretical models, fail to capture critical aerodynamic effects such as turbulence and downwash, limiting the accuracy of the state-space representation. Similarly, transient parameters like the center of gravity and moment of inertia remain inadequately modeled, which affects the precision of system predictions and controller performance. The findings from the step response analyses underscore the need for gain scheduling and potentially more advanced control methods to address the vehicle's time-varying dynamics.

Future efforts must focus on refining the state-space model with CFD-derived

data to account for the complexities of aerodynamic interactions, validating the updated models through simulations and experimental testing, and integrating these improvements into a comprehensive design framework. By addressing these areas, the goal of the Autopilot system is to achieve the reliability and precision required to meet the vehicle's stability and control demands throughout its testing flight regime. Additionally, as roll and yawing moments of the vehicle become more available, the Autopilot system could expand to a longitudinal and lateral model with the goal of simulated response using Matlab's Flight Gear software. This work serves as a step forward in achieving a robust and high-performance control system, setting the stage for further advancements in subsequent design iterations.

4.7 Lifting Body Control Surface Design - Lucas

This section of the midterm report focuses on the continued development of the control surfaces design of the lifting body. Following feedback from the previous report, additional analysis was performed on XFLR5 elevon simulations to evaluate their effectiveness under various operational conditions. The simulations were expanded to assess elevon performance in an envelope of speeds to compare with landing speeds, where control surface responsiveness and stability are critical. These findings provide deeper insight into the aerodynamic behaviour of the delta wing design and highlight refinements to ensure reliable control and maneuverability throughout the mission profile. This section will also present the CAD elevon design, which will be used in the CFD analysis. The same wing size and elevon configuration will be applied and compared with XFLR5, in addition to evaluating elevon effectiveness at supersonic speeds.

4.7.1 XFLR Design

It is important to note that these values are likely to change significantly once a lifting body design is introduced between the two delta wings. XFLR is limited to wing analysis and does not account for the effects that the aircraft's body would have between the wings. This is precisely why more accurate pitching moment calculations can be obtained through CFD simulations using a detailed CAD model. For now, values expressed in this section of the report will act as what we can expect at such airspeeds. Various revisions of the wing design were analyzed using XFLR5 to optimize the delta wing for the project's requirements. Initially, Revision 1 utilized a generic delta wing shape and size of 3.5$\mathbf{m^2}$ with minimal information regarding the necessary wing area, as detailed in the Fall Midterm Report [1]. Following further analysis, the airframe design team for the lifting body determined an approximate target wing area of 0.5 $\mathbf{m^2}$, prompting an XFLR5 elevon performance evaluation based on this specification, designated Revision 2. However, subsequent assessments revealed that this wing area was significantly underestimated. Ultimately, the wing design group finalized a wing area of approximately 2 $\mathbf{m^2}$, which was incorporated into the design of revision 3 to reflect the corrected specifications accurately. The third revision was also

further analyzed based on its simple triangular shape which will be a good starting point to analyze effectiveness rather than on a complex shaped delta wing. These results will be compared with CFD simulations later on. The following revisions can be seen in **Figure 170**

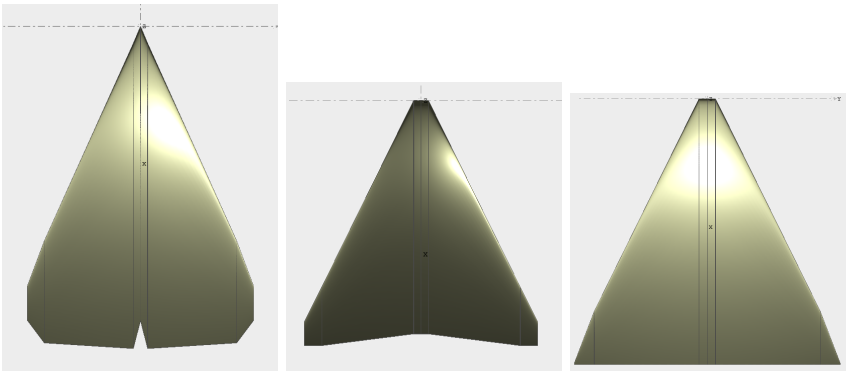

(a) Revision 1 (b) Revision 2 (c) Revision 3

Figure 170: Evolution of Wing Design Revisions Over Time.

4.7.1.1 Geometrical Specifications

Continuing analysis on revision 3, the exact specs of the shape and elevon size can be displayed in the table below.

Table 43: XFLR Geometrical Specifications

Specification	**Value**	**Unit**
Wing Span	2	m
Chord Length at Root	2	m
Exact Wing Area	2.2	mˆ2
Aspect Ratio	1.81	-
Elevon chord (% of Wing Chord Length)	20	%
Elevon Span (% of half a Wingspan)	80	%
Airfoil (NACA number)	0009	-

The elevon chord was set to 20% of the airfoil chord, as XFLR5 defines flaps as a percentage of the airfoil chord. While this approach is sufficient within the constraints of XFLR5, future CFD analyses will allow for more precise geometric lengths using CAD software. The elevon span was chosen as 80% of half the wingspan, drawing inspiration from historical supersonic aircraft such as the SR-71 Blackbird [104]. It is important to note that these initial elevon dimensions are subject to change as they are based on historical aircraft, as further analysis of elevon effectiveness is conducted, it will be adjusted to enhance overall efficiency. The wing area is slightly larger due to the gap between the two wings needing to be created to allow the elevons to deploy correctly and separate from each other.

Finally, the airfoil to be chosen was a symmetrical teardrop airfoil NACA 0009 to simplify our analysis for preliminary control surface effectiveness. Airfoil Selection from the airframe team will impact results however for now, the primary objective of the XFLR5 design is to ensure that the elevons are effective, with particular emphasis on their performance at lower speeds, such as during landing.

4.7.1.2 Environment Specifications

Table 44: XFLR Environment Specifications

Specification	Value	Unit
Altitude	200	m
Density	1.202	kg/mˆ3
Kinematic Viscosity	1.484e-05	mˆ2/s
Re Number	2,915,190	-

For the landing environment, an altitude of 200 meters was selected based on the 30-meter altitude above the CFB Valcartier ASL (168 meters)[105], with the assumption that the testing airspace is located near Ottawa. The figure below shows the clean configuration of the delta wing at an angle of attack (AOA) of 1 degree. One degree is chosen as a baseline for this analysis because a teardrop airfoil generates no left at 0 AOA, This behaviour is comparable to that of high-speed aircraft, which generate minimal lift at lower speeds where there wings must maintain a specific angle of attack (AOA) to produce sufficient lift. This concept is called the angle of incidence, where the wing relative to the aircraft body is at an angle to generate the required lift. As a result, analyzing controls at these speeds at AOA 1 can provide valuable insight into the likely configurations and performance of the elevons when deflected at low speeds, particularly under conditions where the AOA is not fully zero.

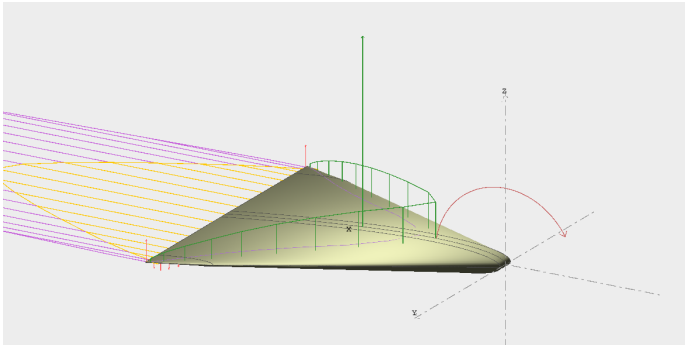

Figure 171: Clean configuration at AOA 1 degree

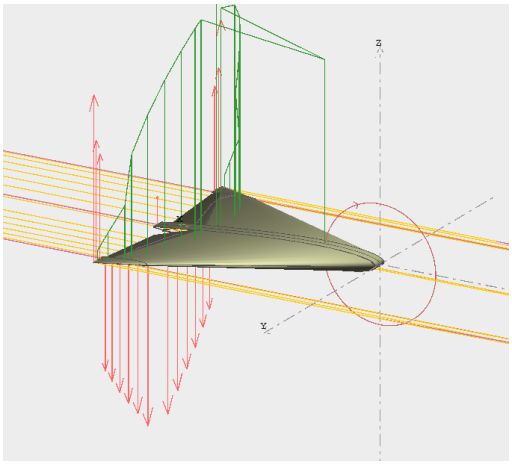

(a) Deflection down

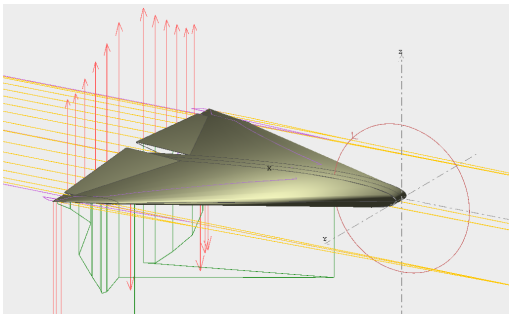

(b) Deflection up

Figure 172: Deflection 10 degrees at AOA 1 degree

As seen from **Figure 172** above, elevons effect pitch by creating a change in lift by changing the camber of the airfoil shape. When the elevons are deflected down the lift is increased as well as the center of lift moving further rearwards, as a result creating a large pitching moment downwards about the center of gravity. The lift can be visualized from the green lines, while downwash outlined in red, The downwash also contributes to pitch by pushing air flowing over the wing up or down, increasing the total pitching moment. A pitching moment coefficient table can be seen below with corresponding pitching moments assuming an approach speed of 100m/s. The next section will go into detail about pitching moment coefficients, it is important to note that C of G for these simulations was set to roughly 0.3 meters ahead of the aerodynamic center at AOA 1 degree. This was done to ensure stability as the wing would tend to pitch down slightly with 0 deflection.

4.7.1.3 Elevon Effectiveness (pitch)

Elevon Deflection (°)	Pitching Moment Coefficient (C_m)	Moment (Nm)
-10	-0.124	780
-5	-0.065	450
0	-0.006	120
5	0.054	-200
10	0.112	-500

Table 45: 100m/s Pitching Moments for Elevon Deflection at AOA = 1°

Table 45 demonstrates the effectiveness of elevon deflection at approach speed, where (-) value of deflection represents downward deflection and (+) value represents positive deflection. (-) for pitching moment coefficient indicates downward pitch and (+) indicates upward pitch. We will maintain this sign convention to ensure consistency with future work. The table above also shows that pitching the aircraft down will be slightly more sensitive than pitching up due to being larger in absolute value compared to the opposite pitching up. This is likely a result of the wing operating at an angle of attack (AOA) of 1 degree, a subtle effect stemming from the wing's non-zero angle of incidence. It is important to note that the pitching moment coefficient is unaffected by change in airspeed and moment is a function of airspeed as illustrated in the graph below. This helps illustrate that during approach control surface effectiveness will deplete.

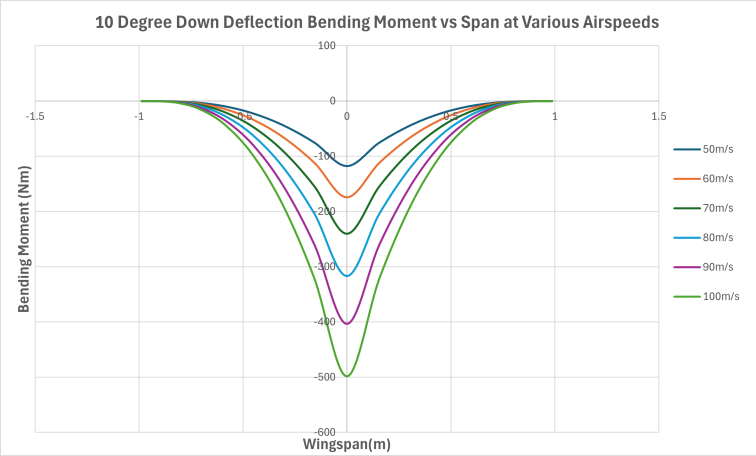

Figure 173: 10 Degrees Deflection Down Bending Moment vs Span at Various Airspeeds

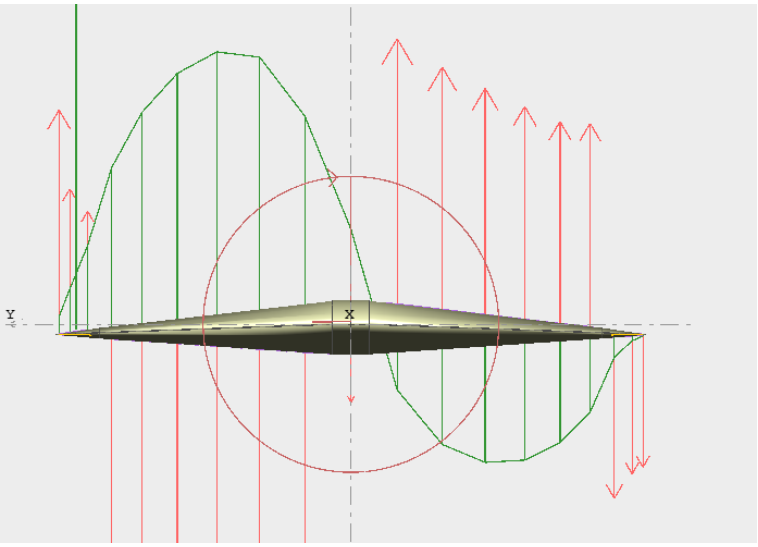

Figure 174: Elevon Deflection Rolling Left at 7.5 degrees

4.7.1.4 Elevon Effectiveness (Roll)

Regarding roll moments, the following coefficients can be expressed in the table below at the same landing environment.

Elevon Deflection (°)	**Rolling Moment Coefficient (C_l)**	**Moment (Nm)**
5	0.016	385
7.5	0.024	577

Table 46: 100m/s Rolling Moment Coefficient (C_l) and Corresponding Moments for Different Elevon Deflections at AOA = 1

Cl, not to be confused with lift coefficient CL, is the longitudinal moment coefficient. The value was computed by XFLR which was used to calculate the roll moment (L) using the equation below [106]:

$$L = cl \cdot q \cdot S \cdot b \tag{200}$$

Where

- L: Rolling moment (Nm),
- cl: Rolling moment coefficient,
- q: Dynamic pressure ($\frac{1}{2}\rho V^2$),
- S: Wing planform area (m^2),
- b: Wingspan (m).

The pressure distribution is observed to be uneven on either side, primarily due to the 1-degree angle of attack. However, this asymmetry does not adversely impact the pitching moment, indicating that pitch remains unaffected by roll in this instance. Further CFD analysis will be conducted to confirm whether this trend persists. These results are identical in magnitude for either roll direction, and have similar characteristics to pitch as airspeed is reduced. This is illustrated in the figure below

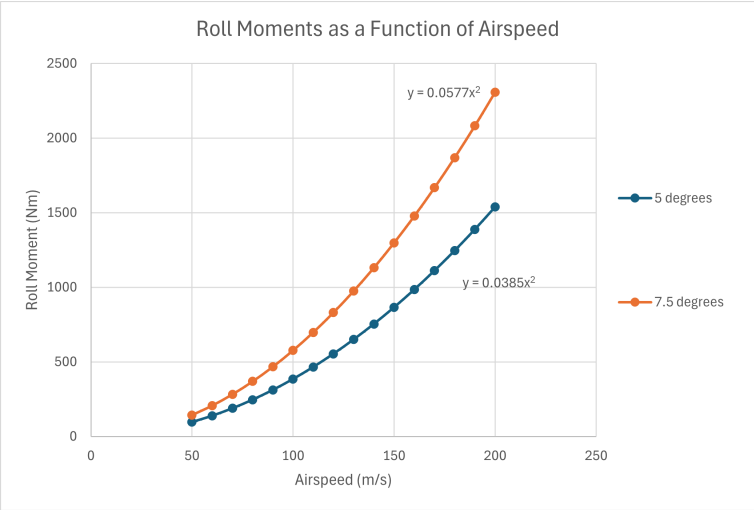

Figure 175: Elevon Deflection Rolling Left at 7.5 and 5 degrees

This demonstrates the effective force generated by the elevons increase by airspeed like that of pitch. The trendline equations for the rolling moment as a function of airspeed indicate a quadratic relationship between the airspeed and the rolling moment for different elevon deflections. For a 7.5-degree elevon deflection, the rolling moment increases with airspeed according to the equation

$$L = 0.0577x^2 \tag{201}$$

while for a 5-degree deflection, the relationship follows

$$L = 0.0385x^2 \tag{202}$$

This suggests that at higher airspeeds, the rolling moment grows more significantly for larger elevon deflections. The quadratic nature of these equations reflects the increasing sensitivity of the rolling moment to changes in airspeed, which is typical in aerodynamic behavior, as the dynamic pressure (q) rises with the square of the airspeed. This is also applicable to pitch and also indicates small deflections will likely be sufficient for maintaining pitch at supersonic flight. With (q) being represented by the equation below[106]:

$$q = \frac{1}{2}\rho v^2 \tag{203}$$

4.7.2 Elevon CAD

before CFD analysis to take place, a 3D model of the delta wing will need to be made with elevons modeled at different deflection angles.

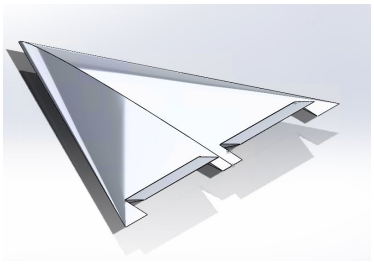

(a) 30 degrees up

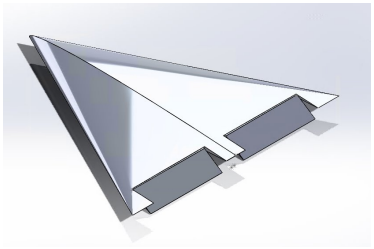

(b) 30 degrees down

Figure 176: Delta Wing Cad With Elevon Deflection

As seen in **Figure 176**, the elevons resemble that of the XFLR wing, they are taken to have the same area and same elevon size which is at the moment going to be modeled as square to simplify the CFD analysis, later its taper can be adjusted for different performance. Their size is roughly 0.21m by 0.69m and will be adjusted once aerodynamic forces are calculated from CFD analysis. The deflection angle maximum differs from previous XFLR analysis as the software was limited to smaller angles. CFD analysis will be able to find forces from higher deflection.

To make the pitching moments more accurate to what can be experienced on the lifting body design, a preliminary body has to be placed in between the two delta wings so pitching moments calculated in CFD will be applicable to our design. Pitching moments calculated on a symmetrical delta wing shape will not be accurate without including forces created by the lifting body. The second revision of this cad can be seen below with a basic lifting body shape for preliminary analysis. It consists of a half-cylindrical shape, flat body, and pointed nose. Dimensions of this can be adjusted as needed, and the test section can be incorporated later on for more detailed analysis. The described cad model can be seen in **Figure 177** on the following page

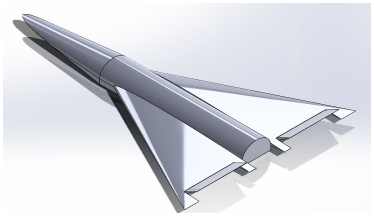

(a) Rear View

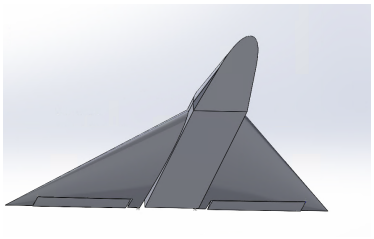

(b) Front view

Figure 177: Delta Wing Cad With Lifting Body

4.7.3 Subsection Conclusion

Future work will focus on analyzing this CAD model to evaluate elevon effectiveness with greater accuracy, particularly at supersonic speeds. The objective is to develop a preliminary assessment by late January, at which point it will become clear whether sticking with the elevon-delta wing configuration is feasible or if it requires a significant rework. This analysis will play a crucial role in determining whether the the preliminary design review will recommend continuing with a lifting body design or reverting to the rocket design from previous years.

4.8 Recovery and Landing - Xuan Nie

4.8.1 Summary

This section demonstrate a vehicle guidance and recovery system designed to ensure accurate navigation toward a waypoints using advanced control techniques. To achieve reliable and precise guidance, the system will integrate multiple control methods, including waypoint navigation, glide slope management, and sensor fusion. In this semester the focus is on the sensor fusion part of the flight control about how it was implemented, relate methods and calibration methods.

4.8.2 Introduction

In this report, various sensors are used for attitude detection to obtain accurate position data. Raspberry Pi Pico is used as a test platform for the primary

flight control computer and preliminary design of the flight control system. Components include MPU6050 IMU, HMC5883L magnetometer and BMP280 pressure sensor, Neo 8M GPS. The system is designed around the Raspberry Pi Pico microcontroller, which interfaces with multiple sensors to provide data for sensor fusion. Pi Pico collects sensor readings, executes AHRS algorithms, and derives metrics such as pitch, roll, yaw, and orientation in the form of quaternions.

4.8.3 System Overview

Microcontroller (Raspberry Pi Pico):

- The Raspberry Pi Pico acts as the central processor, completing data acquisition from all sensors via GPIO pins (I2C).
- It powers and communicates with each sensor, integrating and processing data to calculate pitch, roll, yaw, and orientation.

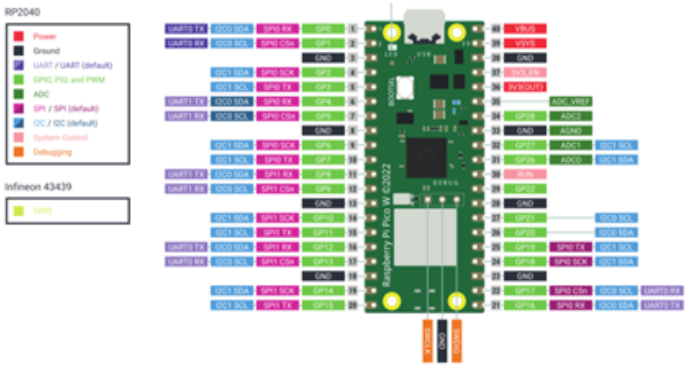

Figure 178: Pi Pico[107]

Inertial Measurement Unit (MPU6050):

- The MPU6050 integrates a 3-axis gyroscope and a 3-axis accelerometer, enabling the system to measure three-dimensional orientation and motion.
- The sensor provides real-time feedback on dynamics such as pitch, roll, and yaw.

Magnetometer (HMC5883L):

- The HMC5883L is a 3-axis digital compass that provides orientation data relative to the Earth's magnetic field.
- It complements the IMU by adding highly accurate magnetic field orientation information, helping to calibrate the gyroscope bias for greater accuracy.

Pressure/Temperature Sensor (BMP280):

- The BMP280 records atmospheric pressure and temperature, allowing altitude to be calculated from pressure changes.
- Also used to provide ambient temperature data, which can also be used for sensor calibration adjustments.
- Not currently integrated into the system; integration planned for next semester to facilitate altitude calculations.

Global Positioning System (Neo M8N):

- The Neo M8N GPS module provides latitude, longitude, and time data for location tracking.
- Combined with direction and altitude readings, GPS data enables positioning, allowing the system to plot its current position and movement.
- Not currently integrated into the system; integration planned for next semester to provide altitude, position, and fusion with IMU data for increased accuracy.

This setup is an initial prototype of a navigation sensor system for testing. While functional, its accuracy is limited by the the precision of the current sensors. To get more precise measurements, a higher-quality sensors are required.

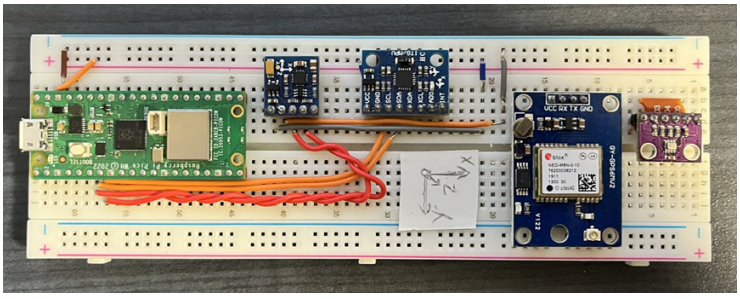

Figure 179: Pico assembly

4.8.4 Simulink Setup

The sensor fusion system was designed in Simulink, using the Sensor Fusion and Arduino libraries along with the hardware listed. We used I2C communication so Simulink can read sensor data in real-time and process it further. The next section gives a brief overview of each Simulink component and what it does.

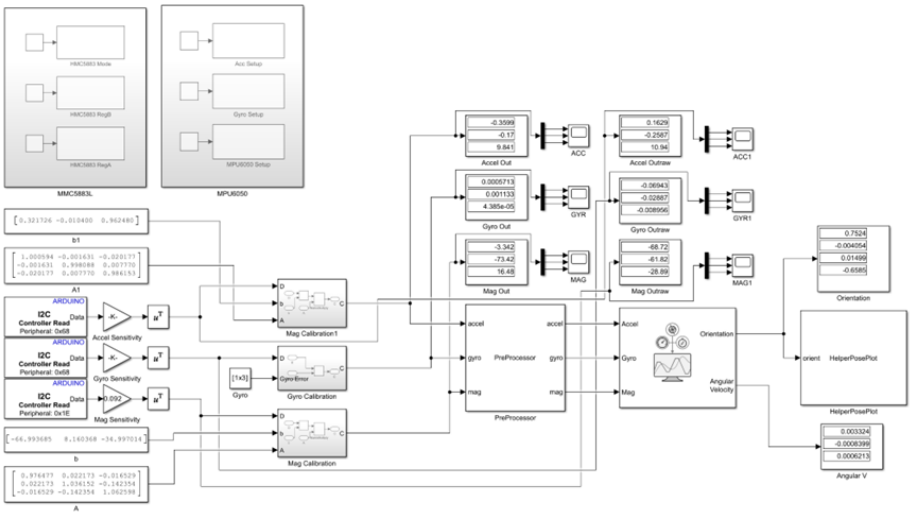

Figure 180: Pico assembly

The I2C write block is used to initialize the sensor, by writing configuration data to the sensor, which is used to enable data collection. Depending on the values written to the sensor registers, various configurations can be used by defining the maximum measurement range and sensitivity of the accelerometer and gyroscope. Provides the flexibility to modify the sensor configuration based on specific mission requirements. For current design, the maximum range of the accelerometer is configured to ± 4g, and the maximum range of the gyroscope is set to $\pm 500^{\circ}$/s. For future calculations of acceleration and turn rates for rocket designs, the maximum range may change.

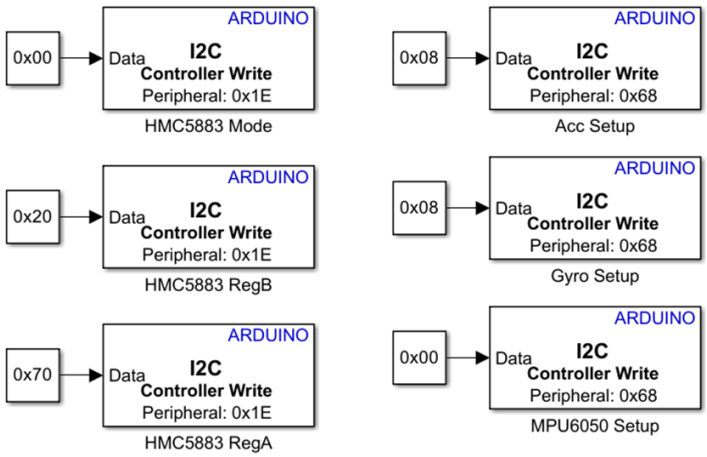

Figure 181: I2C Write

The I2C Read block check live data from the sensors and passes the readings to a sensitivity block, which converts the raw data into the correct units. As incorrect units will cause error in futher calculations. For computation in the AHRS (Attitude and Heading Reference System) algorithm, the input data must follow the correct units:

- Meters per second squared (m/s^2) for acceleration.
- Radians per second (rad/s) for angular velocity.
- Microtears (μT) for magnetic field strength.

The matrices in this figure represent calibration values, which will be explained in detail in the MAG/IMU Calibration section.

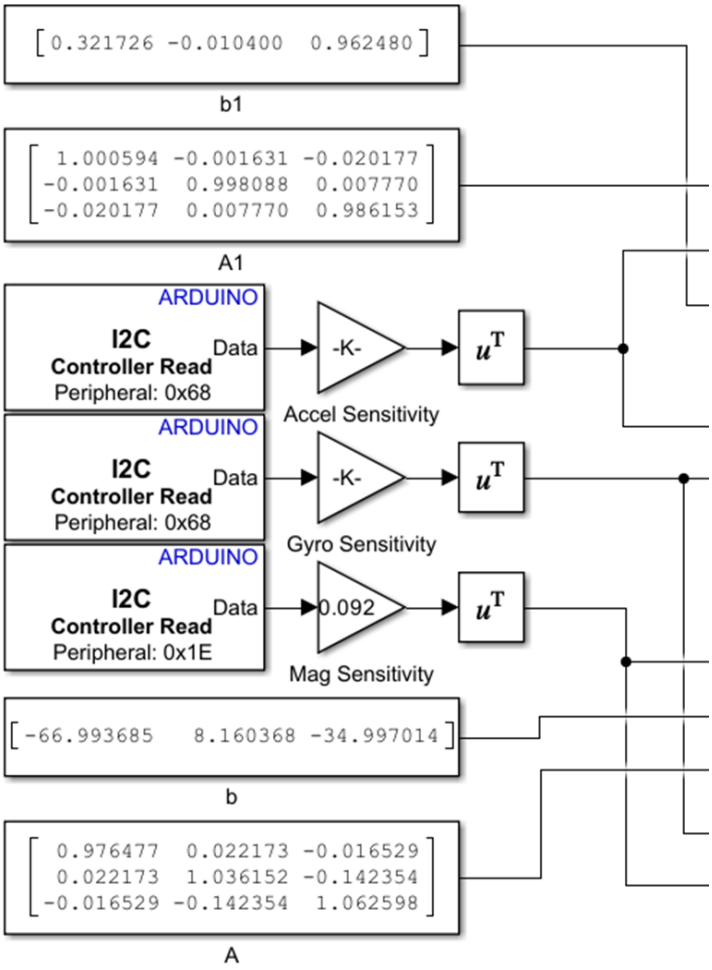

Figure 182: I2C read

The conversion formulas required to convert the raw data into the correct units based on the manufacturer's sensor datasheet are shown in Table 1.

Table 47: Data conversion

Sensors	**Conversion**
Accelerometer	$\left(\frac{1}{8192}\right) \times 9.81$
Gyroscope	$\left(\frac{1}{65.5}\right) \times \left(\frac{\pi}{180}\right) /3.6$
Magnetometer	0.092

4.8.5 MAG/ IMU Calibration

It is necessary to calibration of magnetometers and inertial measurement units (IMUs) for provide accurate and consistent sensor data. External sources like ferromagnetic materials, can cause measurement errors. or electrical cables near sensor that disrupt the magnetic field, as well as inherent flaws in the sensor itself. Magnetometers have two main error sources: hard and soft iron

effects. Since the Earth's magnetic north should always be the strongest magnetic field, a magnetometer should ideally generate readings of perfect sphere in three dimensions. However, in practical settings, external sources magnetic disturbances always affect sensor readings, producing an ellipsoidal form as opposed to a spherical one.

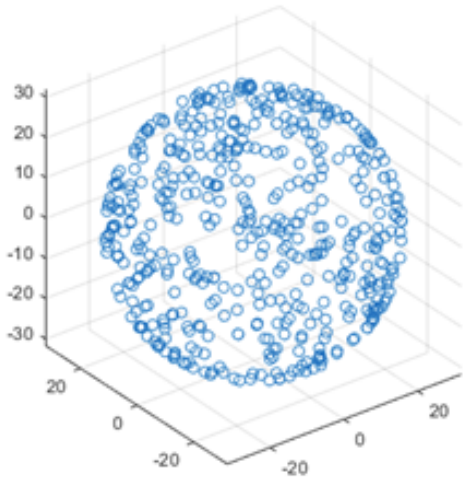

Figure 183: Ideal magnetometer data[108]

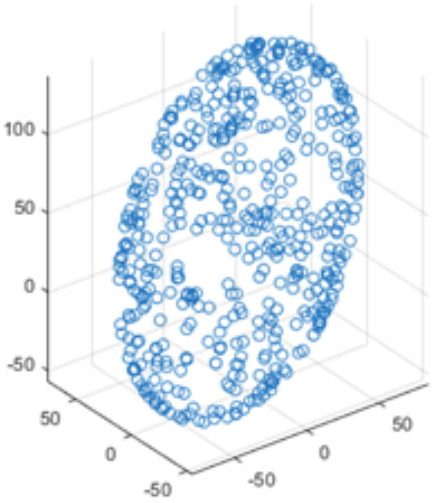

Figure 184: Real-world magnetometer data[108]

To address these distortions, a calibration model is used to adjust the magnetic field measurements in three-dimensional space. This model is expressed as:

$$\mathbf{m}_{cal} = A \cdot (\mathbf{m}_{raw} - \mathbf{b}) \tag{204}$$

Where $\mathbf{m}_{cal}$ is the calibrated magnetic field vector, and $\mathbf{m}_{raw}$ is the raw magnetometer reading vector, comprising measurements along the three axes.

$$m_{raw} = \begin{bmatrix} m_x \\ m_y \\ m_z \end{bmatrix}^T \tag{205}$$

$\vec{b}$ is the hard iron bias vector, representing the constant magnetic offset along the x, y, and z axes.

$$b = \begin{bmatrix} b_x \\ b_y \\ b_z \end{bmatrix}^T \tag{206}$$

A is the soft iron correction matrix, which is a transformation matrix used to reshape the ellipsoid into a sphere:

$$A = \begin{bmatrix} a_{11} & a_{12} & a_{13} \\ a_{21} & a_{22} & a_{23} \\ a_{31} & a_{32} & a_{33} \end{bmatrix} \tag{207}$$

After applying the calibration model, the corrected magnetometer reading should ideally form a perfect sphere.

$$m_{final} = \begin{bmatrix} a_{11} & a_{12} & a_{13} \\ a_{21} & a_{22} & a_{23} \\ a_{31} & a_{32} & a_{33} \end{bmatrix} \begin{bmatrix} m_x - b_x \\ m_y - b_y \\ m_z - b_z \end{bmatrix} \tag{208}$$

Where A and b represent the calibration factors derived from sensor readings. The calibrated result is:

$$m_{cali} = \begin{bmatrix} m'_x & m'_y & m'_z \end{bmatrix}^T \tag{209}$$

4.8.6 Calibration Procedure

In order to properly calibrate the magnetometer, the first step is to collect raw data by rotating the sensor in all possible directions to fully capture the magnetic field distortion. The following image shows the IMU data analysis setup in Simulink using the To Workspace block. Once data is recorded from all directions and Stop is pressed in Simulink, the data from all sensors will be saved and can be used for future analysis using Magneto software.

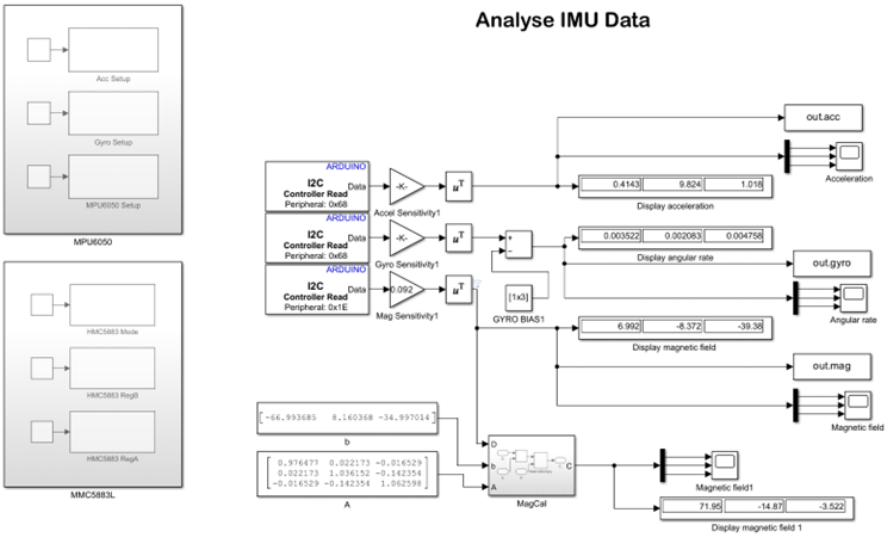

Figure 185: IMU Data Logging

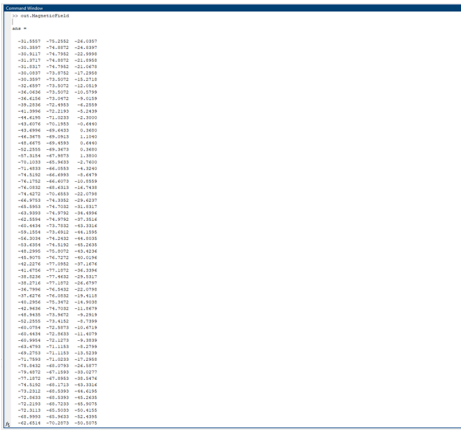

Figure 186: Recorded data

The calibration parameters are determined by Magneto software developed by Sailboatinstruments (Figure 10), which calculates the hard-iron and soft-iron correction factors. This process is applicable to both magnetometers and accelerometers, as they are similar. Once the calibration is complete, its effectiveness can be assessed by comparing the raw and corrected data using the Python plotting tools in Figures 11 to 19. However, to ensure the accuracy of the calibration values, the sensor outputs must be tested in Simulink to verify that all readings correspond to expected values.

Magnetometer:

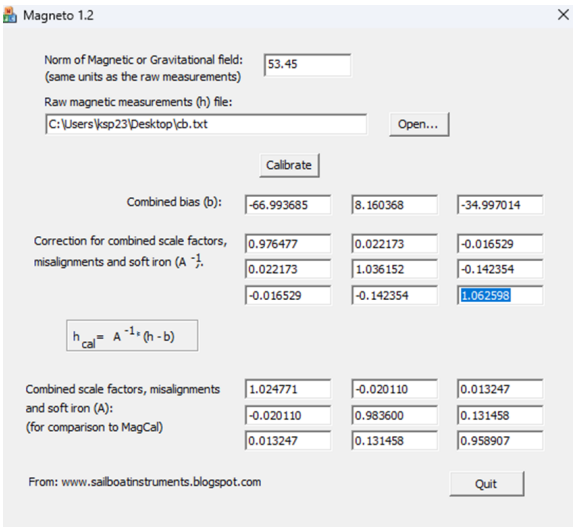

Figure 187: Magnetometer calibration values

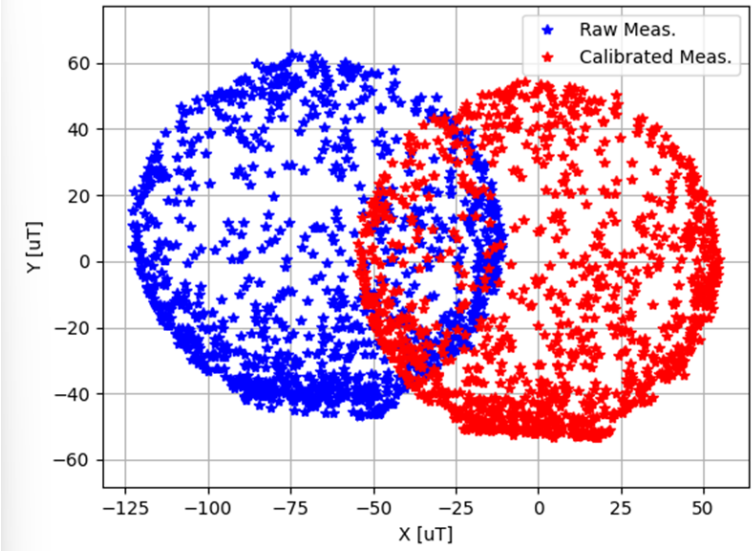

Figure 188: XY magnetometer data

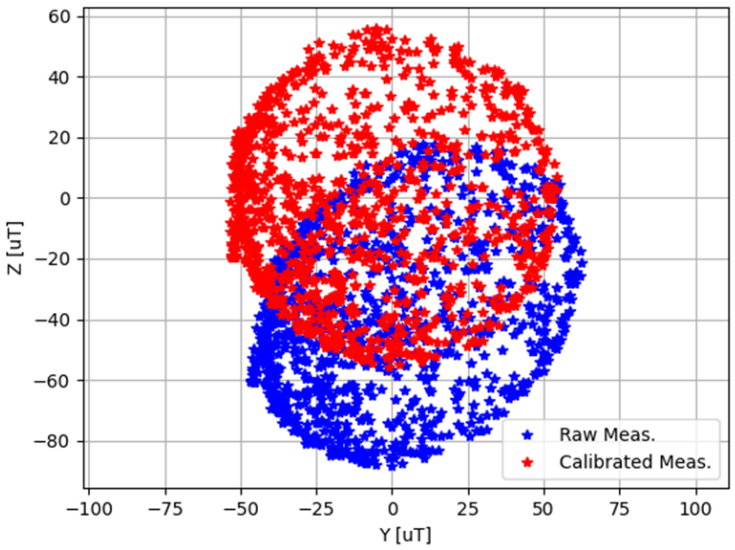

Figure 189: YZ magnetometer data

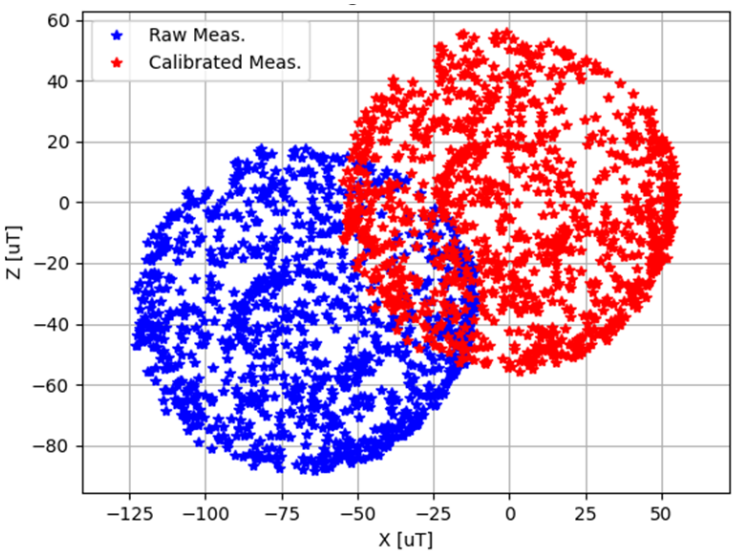

Figure 190: XZ magnetometer data

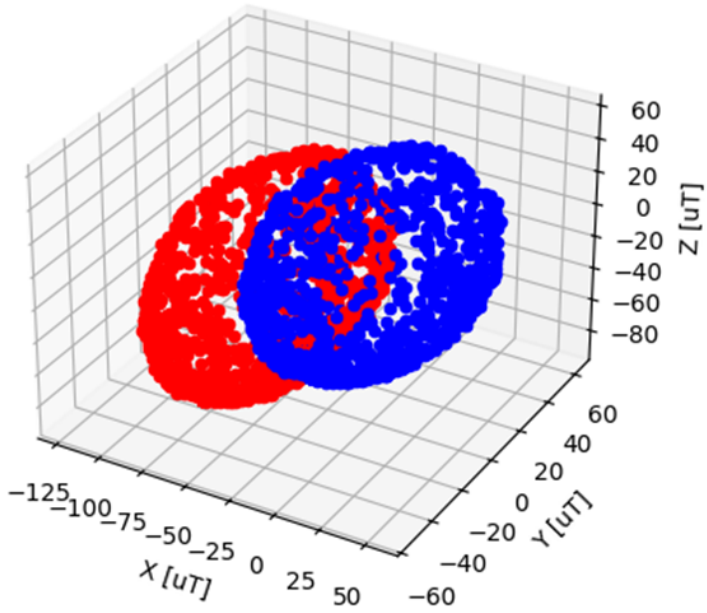

Figure 191: 3D magnetometer data

Accelerometer:

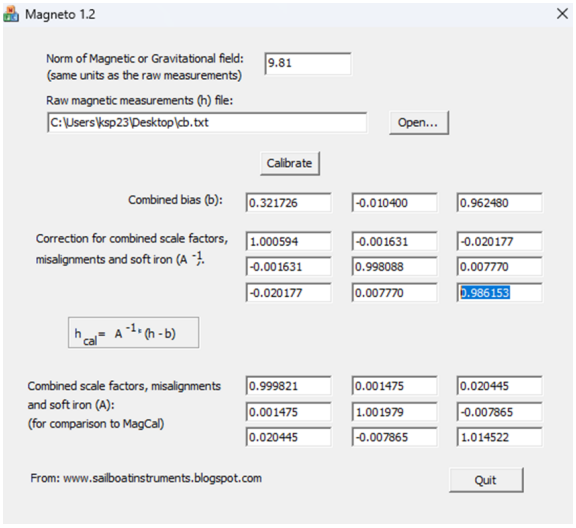

Figure 192: Accelerometer calibration values

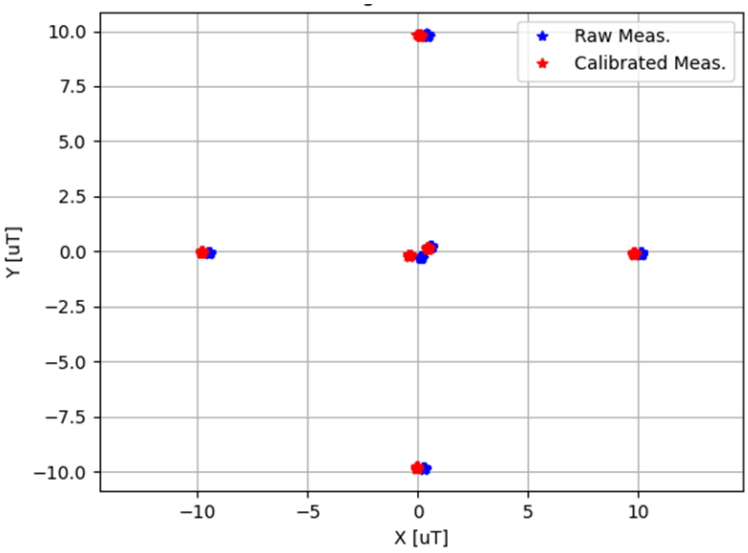

Figure 193: XY accelerometer data

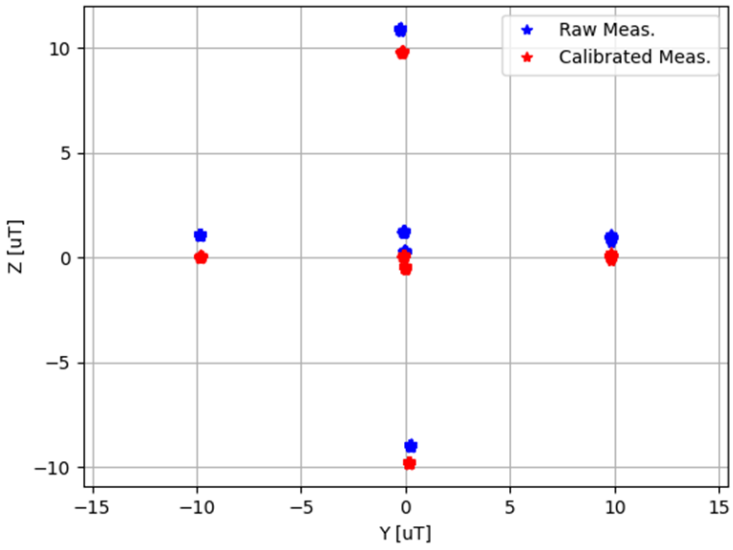

Figure 194: YZ accelerometer data

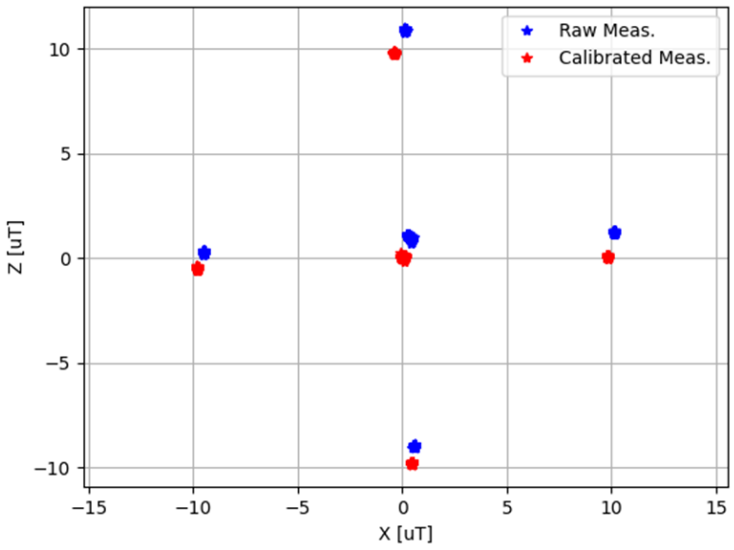

Figure 195: XZ accelerometer data

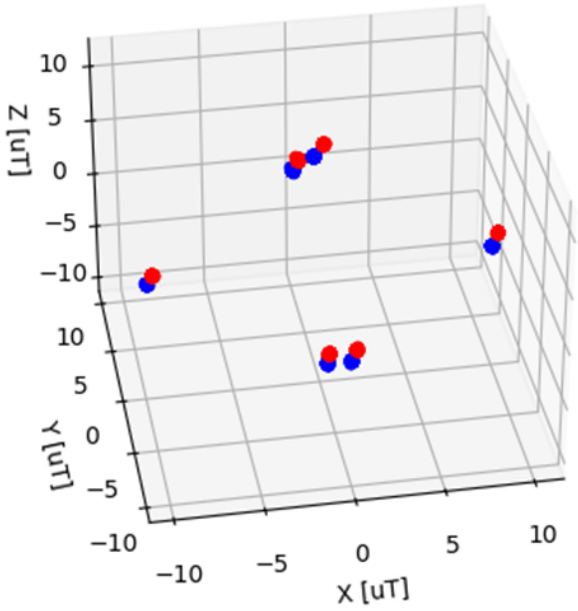

Figure 196: 3D accelerometer data

The graph highlights the difference between calibrated and uncalibrated data. The uncalibrated magnetometer data (shown in blue) shows the effects of hard and soft iron distortion, as indicated by the deviation from the origin zero point and the deformation of the spherical data into an ellipsoid. After applying the calibration parameters, both the magnetometer and accelerometer data are closer to the ideal spherical shape, which improves the accuracy of the system orientation. However, there is a significant error between the raw and calibrated data. To ensure that all sensors are outputting meaningful readings, all sensors must be tested in Simulink.

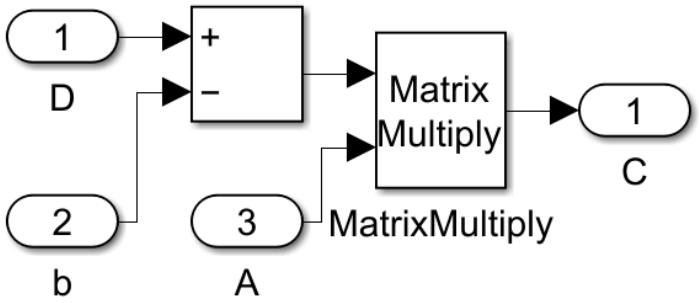

Figure 197: Calibration for IMU/MAG

The calibration of the accelerometer and magnetometer is done using a combination of offset correction and matrix multiplication[109], as shown in Figure 20. The raw sensor readings (D) are first adjusted by subtracting the bias (b) to correct for static offsets. This adjusted value is then multiplied by the calibration matrix (A) to account for scaling and alignment errors, resulting in the calibrated output (C). This approach ensures that both hard iron (bias) and soft iron (scaling and alignment) effects are properly corrected.

Gyro:

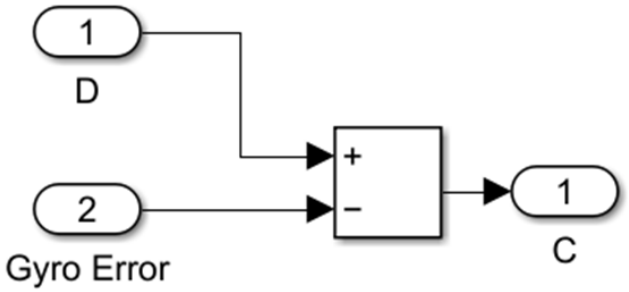

Figure 198: Calibration for gyro

The gyroscope calibration was performed by simply subtracting the observed error from the raw data, as the error is primarily a static offset that does not change with the sensor's orientation.

4.8.7 Calibration Testing

During the calibration test, the sensor was slowly rotate in Z axis for a full circle while recording all data in Simulink for analysis.

Magnetometer:

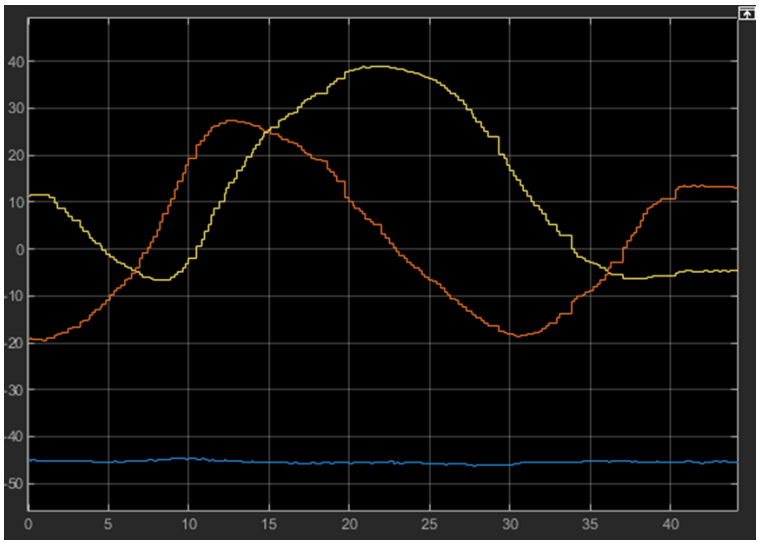

Figure 199: Calibrated magnetometer

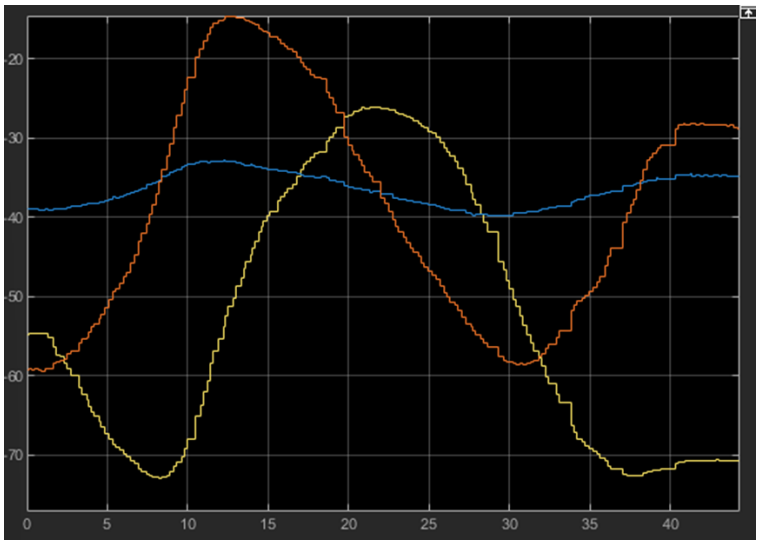

Figure 200: Uncalibrated magnetometer

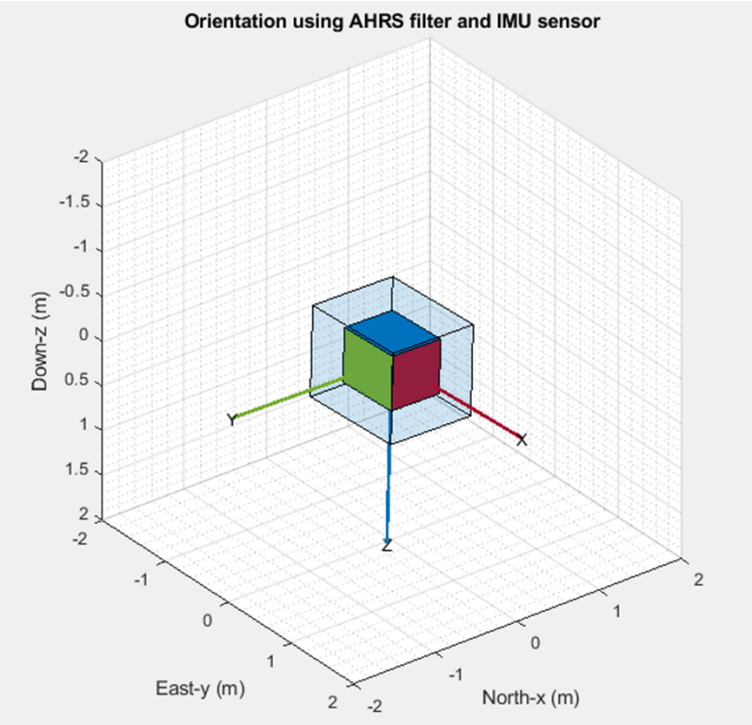

Figure 201: Orientation using AHRS

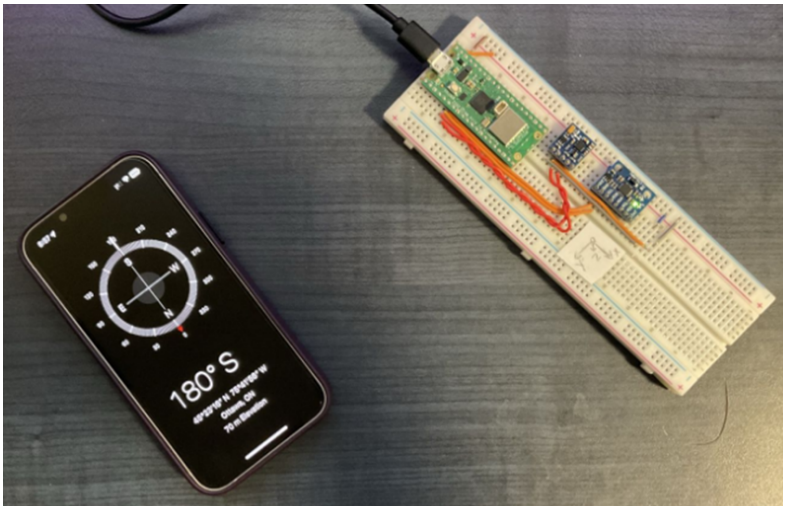

Figure 202: Compass comparison

From Figures 22 and 23, the calibration significantly improves the accuracy of magnetometer readings. In the calibrated plot (Figure 22), the data closely aligns with the expected ranges for all axes, reflecting a proper spherical distribution. On the other hand, the uncalibrated data (Figure 23) is consistently offset below zero and never reach above 0, which indicating there is offset of hard and soft iron effect that make the uncalibrated data useable for real-world applications.
Figure 24 demonstrates orientation tracking using the AHRS filter, providing a 3D visualization of orientation where the axis pointing north. Figure 25 compares the magnetometer-based compass reading to a phone compass, confirming that the calibrated system provides reasonable results.
The calibration process effectively adjusts the magnetometer output, making it reliable for use in positioning and navigation systems. However, some noise and errors still persist, showing the potential for further optimization using filters and better sensors.

Accelerometer:

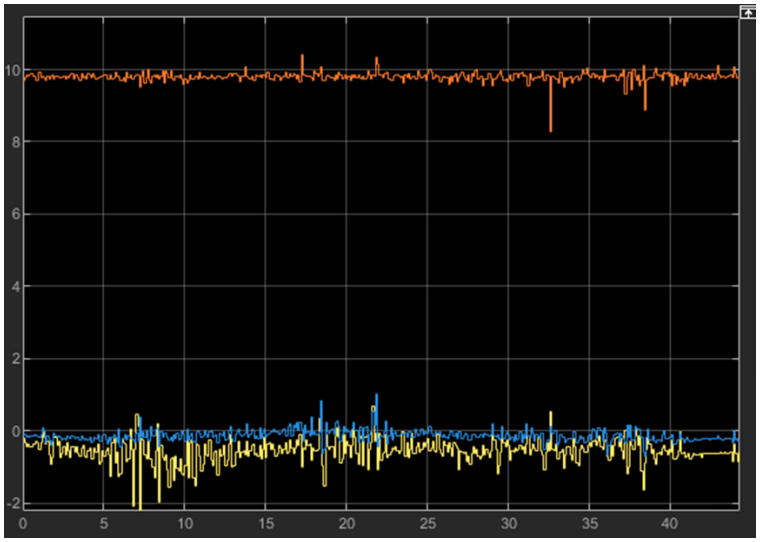

Figure 203: Calibrated accelerometer

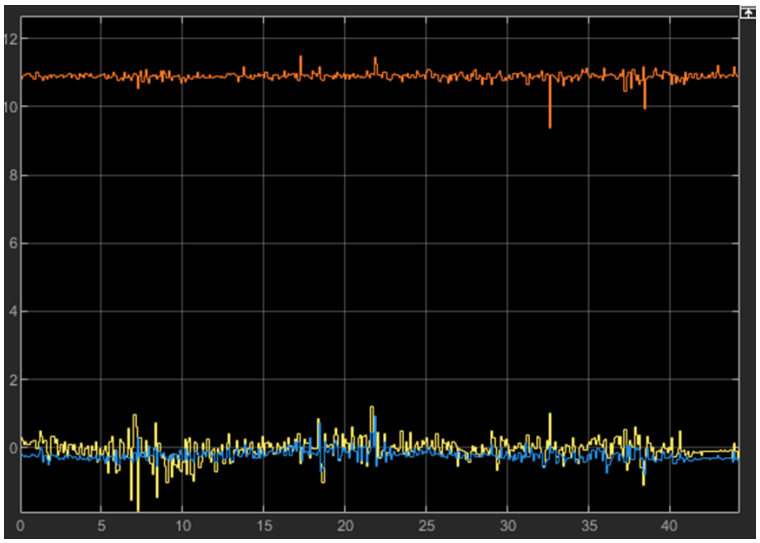

Figure 204: Uncalibrated accelerometer

From Figures 26 and 27, the calibration process significantly improves the accelerometer readings. In the calibrated plot (Figure 26), the data shows an expected value of 9.81 m/s^2 for acceleration on the Z-axis, while the X and Y axes show values closer to zero, in an ideal situation.
In contrast, the uncalibrated plot (Figure 27) shows the Z-axis output at approximately 11 m/s^2, significantly offset from the expected value, and other axes are less accurate as well. While calibration has improved accuracy, small errors remain in the X and Y axes since they are not zero all the time. This is likely due to the sensor not being in a perfectly centred rotation axis and the lack of data points during the recording process. As illustrated in Figures 16 to 19, precise calibration requires more data points and additional testing to further reduce errors.

Gyro:

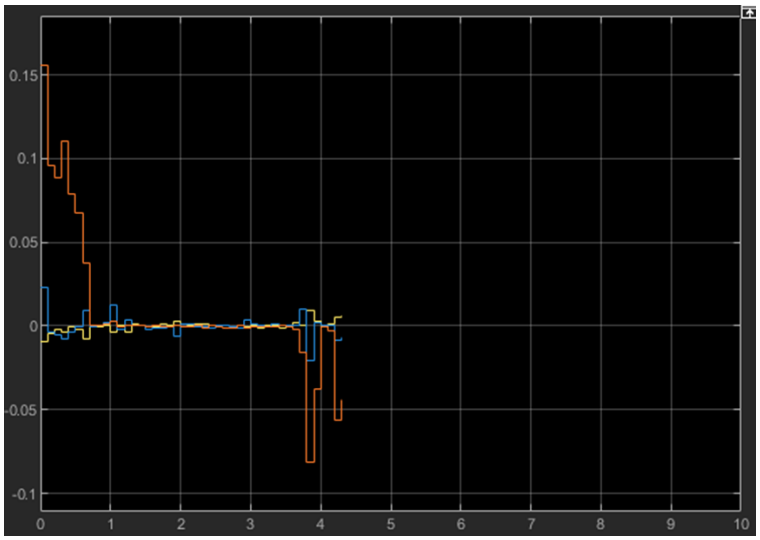

Figure 205: Calibrated gyro

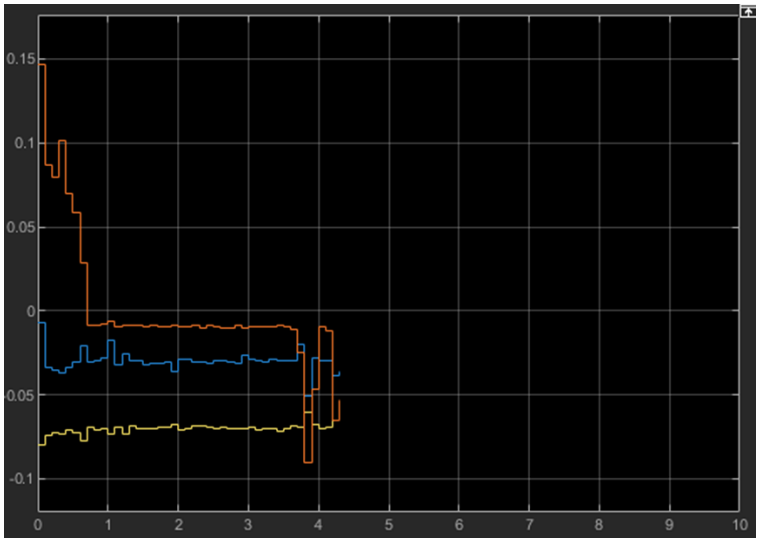

Figure 206: Uncalibrated gyro

From Figures 28 and 29, the gyroscope calibration appears to perform well enough. Most axes are close enough to near-zero values and the Z-axis shows correct angular acceleration, while the X and Y axes remain closer

to ideal values. Despite the calibration improvements, the data still contains significant noise, making it unsuitable for long-term operation
This issue is likely caused by sensor limitations and environmental noise. To address these problems, higher-quality sensors with additional signal processing techniques, such as implementing a high-pass filter will be considered in the next phase of development. These adjustments aim to improve the accuracy and reliability of the gyroscope data.

4.8.8 Sensor Fusion

In designing rocket propulsion and wind tunnel systems, sensor fusion is essential for measuring orientation and motion due to the limitations of individual sensors. While sensors like the IMU, magnetometer, and GPS provide valuable data to flight computers, each sensor has its limitations. For instance, GPS only offers location information and often has a margin of error of a few meters, causing slight shifts in location that may confuse the flight computer. Or accelerometer can provide pitch and roll angles, it may misinterpret acceleration as a change in angle, leading to incorrect pitch commands and potential errors. Sensor fusion addresses this by integrating data from multiple sensors. For example, motion data from the IMU and magnetometer can be compared with GPS readings, helping the system distinguish between actual movement and sensor error. Using an accelerometer and gyro combine to determine if the acceleration is from a change in angle or velocity. Sensor fusion also reduces the effect of noise, allowing the system to filter out sensor noise and validate data, preventing errors from external factors. Additionally, if one sensor fails, other sensors can still supply information to determine the vehicle's orientation and motion accurately based on a built-in motion model.

Several sensor fusion methods are commonly used in UAV, such as Kalman filters, complementary filters, and Madgwick filters. Alough each method handles data integration differently, but all can correct sensors drift and improve overall reliability. For this year's design, the AHRS algorithm[110] with Kalman filter in Simulink was chosen because of its high predictability, ease of use, and the ability to perform preliminary testing.

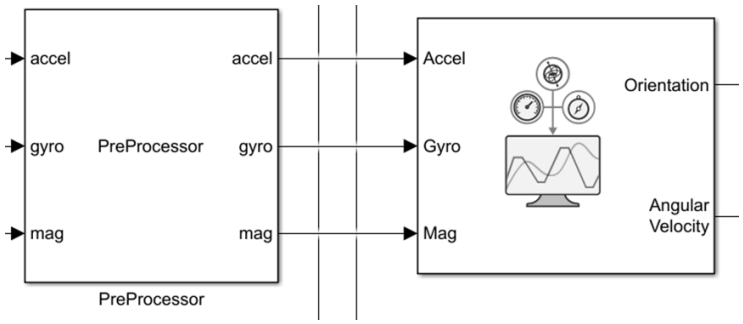

Figure 207: Pre Processor and AHRS[111]

4.8.9 Attitude Heading Reference System AHRS

The attitude heading reference system (AHRS) is an important component of navigation systems and is used to provide accurate orientation estimates, including roll, pitch, and yaw. It combines data from various sensors such as accelerometers, gyroscopes, and magnetometers. By integrating these sensor inputs, the AHRS algorithm provides orientation information while correcting for noise and bias in the sensors. This is achieved through the following components:

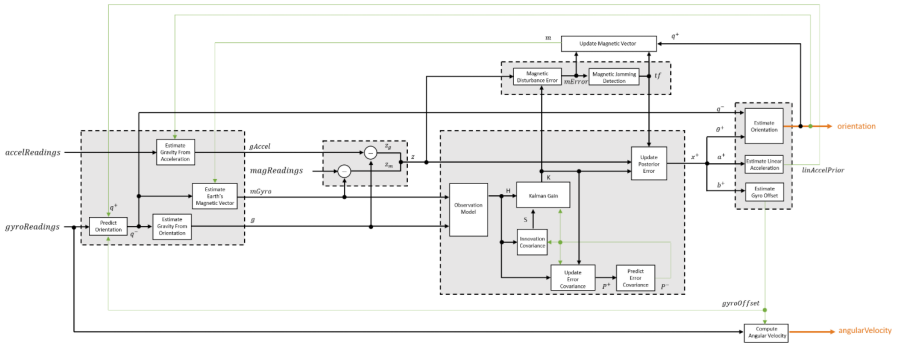

Figure 208: AHRS[112]

The first is a model that predicts the system orientation and supports sensor data fusion. Gyroscope readings are used to estimate changes in orientation, while accelerometer measurements are used to calculate the gravity vector. In addition, the model combines magnetometer data with the system orientation to estimate the Earth's magnetic field[112].

To improve the accuracy of these estimates, an error model is used. The model tracks bias and drift in sensor measurements in two main ways. First, it compares the estimated gravity vector (from the gyroscope and orientation data)

with the measurements from the accelerometer. This comparison helps identify and correct errors[112] caused by drift or noise in the sensors. Second, it evaluates the difference between the magnetic field vector predicted using the gyroscope and orientation data and the magnetometer readings[112].

The magnetometer correction step adds error correction by filtering out unrealistic readings. By examining the strength of the magnetometer data, the algorithm ignores unrealistic readings[112]. However, this correction alone is not enough to eliminate the effects of hard and soft iron. Properly calibrating the magnetometer remains critical to providing accurate and reliable heading data.

The main component of the AHRS is the Kalman filter. The Kalman filter is divided into two phases: prediction and update. In the prediction phase, gyroscope data is used to estimate changes in orientation in real time. The update phase then uses measurements from the accelerometer and magnetometer to improve this prediction. This process allows the algorithm to dynamically weight the contribution of each sensor based on its accuracy, effectively compensating for sensor noise and bias[112].

The correction process improves the orientation estimate. Magnetometer readings are used to adjust yaw (heading), while accelerometer data is used to correct tilt (roll and pitch) [112]. These corrections help maintain accuracy even if the sensors become noisy or drift over time.

Finally, angular velocity is calculated from gyroscope data, and applying corrections at an early stage helps minimize errors in these calculations.

4.8.10 Future Work

Navigation: During the launch phase in a rocket wind tunnel, GPS provides initial position data. However, as the vehicle accelerates to high speeds, GPS signals become unreliable. At this moment, the system will rely on data from the IMU and magnetometer to estimate the position. Once the speed decreases below approximately Mach 1.5, the GPS signal stabilizes and can once again provide accurate position information. Precise GPS data is essential for landing, as the flight computer needs reliable position input to ensure the vehicle reaches the designated recovery point.

To guide the vehicle to its recovery target, the system use position estimates through sensor fusion. The onboard computer determines the vehicle's current position relative to the designated waypoint and adjusts its trajectory accordingly. External factors such as wind and sensor noise are accounted for to optimize position and direction estimates, minimizing errors [113].

The navigation process can use both direct-to-waypoint (DTW) and track-to-waypoint (TTW) approaches[114]. TTW is generally preferred as it provides a smoother trajectory and avoids sudden directional changes which increase energy loss. This method helps reduce drag and minimizes lift loss during

course adjustments, therefore improving the efficiency of the vehicle's path to the recovery point.

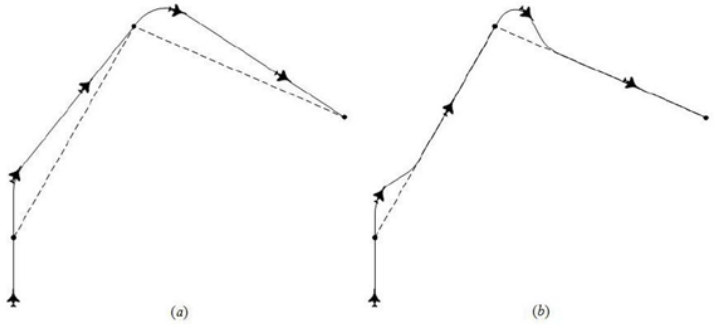

Figure 209: DTW and TTW[114]

The focus for next semester will be on reducing sensor errors and calculating and comparing positions through inertial navigation and GPS. This will provide complete and accurate data for the flight control system. Future work will be in collaboration with other members of the control group for flight control algorithms, hardware design, and implementation.

4.8.11 Conclusion

In conclusion, the attitude heading reference system (AHRS) and sensor fusion significantly improves data accuracy. This is achieved by integrating accelerometers, gyroscopes, and magnetometers with a Kalman filter. The system provides usable roll, pitch, and yaw estimates while reducing the effects of sensor noise and bias. Calibration of the magnetometer and accelerometers showed improvements in data accuracy by correcting for hard and soft iron effects and errors. However, analysis showed that further improvements are needed to address random noise issues. Implementing additional filtering techniques and incorporating higher quality sensors are key goals for future iterations.

4.9 Propulsion & Controls Subteam Recap

This semester, the subteam made significant progress in defining the rocket's propulsion and control mechanisms. The team focused on trajectory analysis, propulsion system preliminary design, and control system enhancements. A trajectory simulation was developed to replace and deprecate the legacy simulation work that was proven faulty. The propulsion system design was advanced with the preliminary sizing and configuration of a solid rocket motor tailored to meet the requirements of sustained Mach 3 velocity at 70,000 feet.

Control system developments included introducing and refining actuation mechanisms, such as airbrakes and fins, to ensure effective operation across various stages of flight. The fins were specifically analyzed for their contribution to pitch stabilization and trajectory correction. Furthermore, a first attempt at the pitch-hold autopilot system was modeled and simulated, providing precise attitude control throughout the flight. Sensor calibration, data fusion techniques, and data refinement techniques such as Kalman filtering were implemented to integrate gyroscope, accelerometer, and magnetometer data, ensuring accurate motion estimation and reducing system noise.

Looking ahead, the subteam plans to address thermal effects on the propulsion system to ensure control surface integrity under extreme operating conditions, refine the autopilot system for improved adaptability and response, and further advance and integrate the propulsion and control solutions into the broader vehicle design.

5 Test Section Design & Analysis

5.1 Test Section Subteam Introduction

The test section group was responsible for the data collection over the flight and the structures for the test specimen. Austin was exploring the option of creating a Schlieren system for supersonic flow visualization. This semester work was completed to design a tabletop version of the Schlieren system, which is currently waiting for component fabrication. Nathan focused on the original test section from last year's iteration of the rocket. Enhancing the inlet design to improve flow accuracy to the test specimen. By increasing the rocket's diameter and refining the inlet lip, the design maximized the axial distance for placing the enclosed test specimen before the initial shock convergence. Simulations ensured the test specimen size wouldn't choke the flow or create a bow shock. Colby examined the previous design of the load cell and looked at ways to account for temperature and improve reading. A redesign of the load cell's shape was completed with internal geometry requiring 3D metal printing to manufacture. The readings were improved by adding additional strain gauges for readings orthogonally to the tip in any direction. Temperature readings are now also taken to appropriately scale the measured force. Ryan was in charge of creating the wind tunnel and determining where the ideal location to place the test specimen. Flow analysis was completed resulting in a proposal of different test specimen locations based on the formation of shocks within the wind tunnel itself. Sebastian took the lead in creating a pylon to hang the test section under the airframe's body. The pylon allows for a pass-through wind tunnel and the installation of a traditional Schlieren system. Analysis was completed to determine the minimum 3.6 cm and maximum 80cm that the arm could be placed. The location chosen was 14.5cm.

5.2 Background on Test Section Goals

The test section is the payload of this mission making it the most important part of the project. The team looked at ways to improve last year's design. One of the main goals of this year's team was to have the test section as the leading edge allowing for free flow to flow over the specimen. The team also wanted to find a way to visualize the flow occurring in the test section previously there was only the load cell force balance of the subject.

5.3 Schlieren Imaging (Flow Visualization) - Austin Stubbs

Peer reviewed by Colby Jackson

The flow visualization type that has been chosen is Schlieren imaging. Schlieren imaging works by condensing light using convex mirrors to visualize the differences in densities within the test medium. This image is then captured by a high-speed camera to record the flow as it moves [115]. Note that for steady-

state conditions, a still frame can be enough. The goal for this semester was to get a tabletop Schlieren that can then be scaled down to fit within the parameters of the airframe.

5.3.1 Theory

Schlieren Imaging is used to see differences in density within air. This could be due to a temperature difference, such as a candle being lit, as shown in **Figure 210**. Shock waves from supersonic flow, as shown in **Figure 211** can be visualized using schlieren. The following section will discuss the theory of the single-pass and double-pass Schlieren systems and their advantages.

Figure 210: Example of Schlieren Without Color Filters Using a Single Mirror Setup [116]

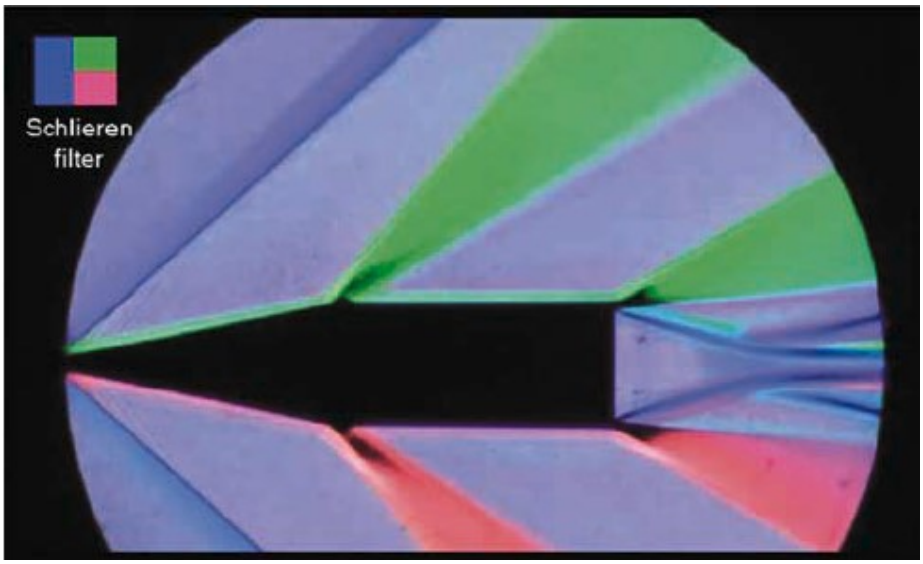

Figure 211: Schlieren Imaging Using Coloured Filters Instead of a Knife Edge to Visualize Shocks [117]

5.3.1.1 Single Pass

Two mirrors are used in a classic single-pass (Z-Type) Schlieren setup, as shown in **Figure 212**. In this setup, parabolic mirrors are superior because they focus all the light rays into a single point, resulting in a sharper image, as depicted in **Figure 213**, whereas the spherical mirrors collimated into a single point resulting in a dull image.

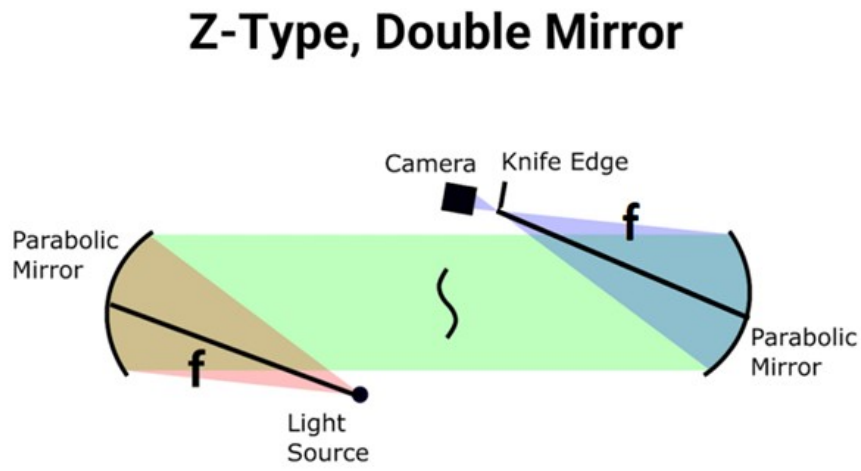

Figure 212: Schlieren Single Pass Example [118]

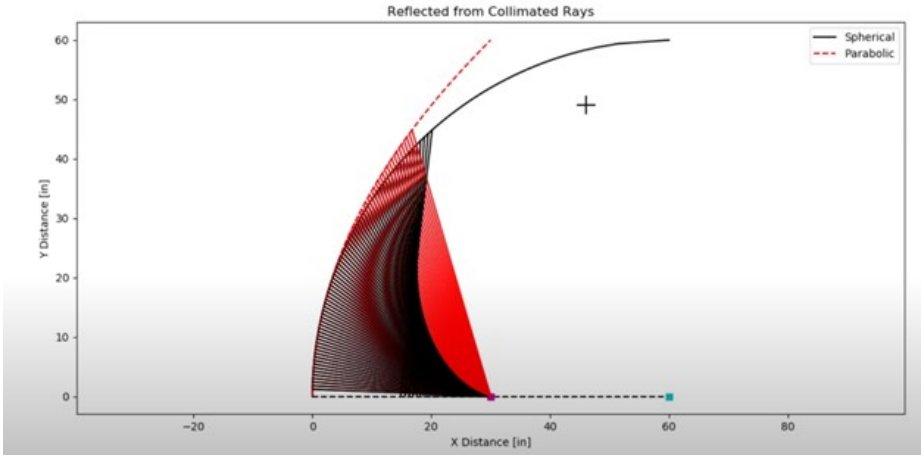

Figure 213: Comparison of Spherical vs Parabolic Mirrors in a Single-pass Schlieren [118]

In **Figure 214**, it's shown that the spherical mirror's light rays do not converge perfectly at the focal point. Since the tabletop setup is a proof of concept, this small discrepancy will not significantly impact imaging for the double pass (Z-type) setup.

The light passes over the test section (illustrated as the wavy line in **Figure 212**) and allows the camera to capture differences in density due to the refraction of light passing through regions of densities. The knife edge cuts off half of the light, enhancing contrast. The dark sections are a result of that portion of the light being cut off as shown in **Figure 210**. If the camera is shooting in colour, the knife edge can be replaced by a coloured filter, allowing the generation of heat maps. This can be especially useful for a non-technical audience to interpret, as demonstrated in **Figure 211**.

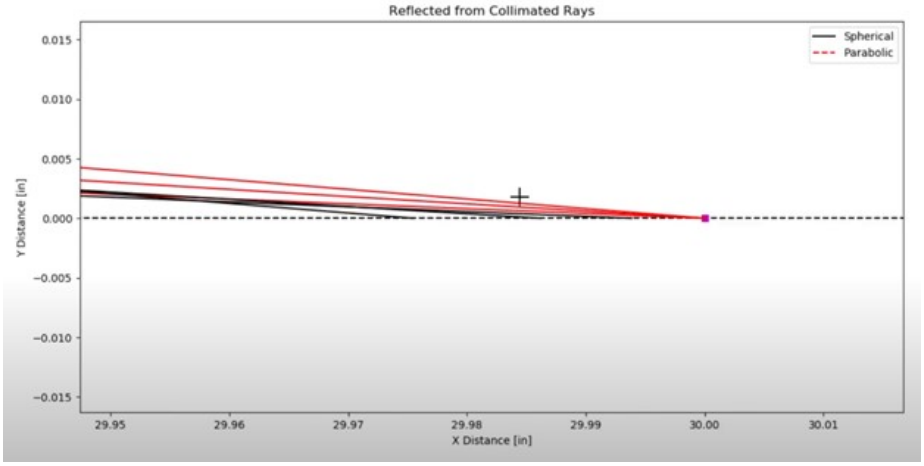

Figure 214: Zoomed-in image of the focal point for Spherical vs Parabolic mirrors [118]

5.3.1.2 Double Pass

In a double-pass Schlieren setup, a single spherical concave mirror is placed at two times its focal length, as depicted in **Figure 215**. The light from the source passes over the test section (shown as a wavy line), hits the mirror, and reflects back to the knife edge, where the camera captures the image. This setup is less sensitive to misalignment, uses fewer mirrors, and is more compact, making it ideal for rocket integration. However, it sacrifices image sharpness due to the double light pass.

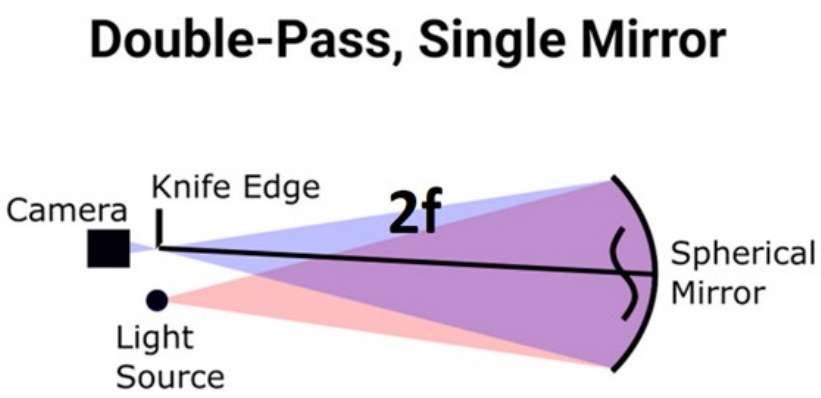

Figure 215: Schlieren Double Pass Example [118]

5.3.2 Preliminary Apparatus

The preliminary apparatus consists of stands to hold up the mirrors, lenses, and lights as shown in Figure 216 with the Bill of Materials (BOM) in Table 48. The mirror stands are to be constructed out of low-carbon steel, which was chosen for ease of manufacturing since drilling and welding are used in the design. The base of the apparatus is universal and will support all components except the camera, which will have its own tripod. After confirming the layout, the base mounts will be bolted into an 8-10 gauge aluminum sheet to secure the setup. Experiments will be held in the second semester to determine how much of a sacrifice the double pass system makes, ultimately with the goal of integrating the superior system.

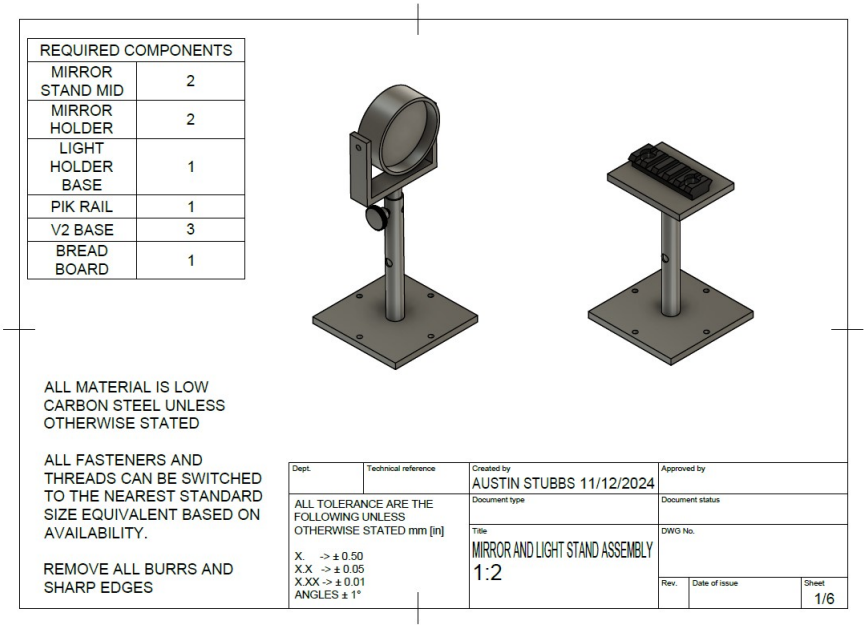

Figure 216: Mirror Stand (Left) and Light Stand (right) Assembly

Part Name	Qty	Description	Cost (CAD) each
Dielectric-Coated Concave Mirror, 400 - 750 nm, f = 500 mm, CM508-500-E02	2	Spherical convex mirrors best coating for visible light	$215.91
Streamlight 66133 Stylus Pro USB 350-Lumen Rechargeable LED Pen Light with 120-Volt AC Charge Cord & Nylon Holster Black	1	LED light source	$99.36
Solid Single razor blades (10 pack), other brands are fine as long as there is no hole in the blade	1	10 pk of black razor blades	$9.99
Black Electrical Tape (3 pack)	1	3pk Black electrical tape	$8.64
N-BK7 Plano-Convex Lens, Ø25.0 mm, f = 50 mm, AR Coating: 350 - 700 nm	1	Plano-convex lens	$48.64
Feyachi Green Laser Sight 532nm	1	Green laser 532nm	$42.55
Black cardstock	1	Cardstock to test different pin holes	$9.99
BokingOne 16 Pcs Color Correction Gel Filter for Lighting	1	Colored gel sheets for creating colored schlieren	$16.99
4mm threaded rod	2	d= 4mm L = +70 mm	Shop price
M4 nuts to match threaded rod	4	M4 nut matching threaded rod	Shop price
Hose pipe clamps	1	10 pk of Hose Clamps	$10.52
Patels Camera	1	Sony 1000fps	$0.00

Table 48: BOM for Schlieren Tabletop Apparatus

5.3.2.1 Mirror Stand

The mirror stand assembly can rotate 360 degrees about the y-axis and z-axis, as shown in **Figure 217**, which is critical for precise alignment during Schlieren imaging, improving image quality.

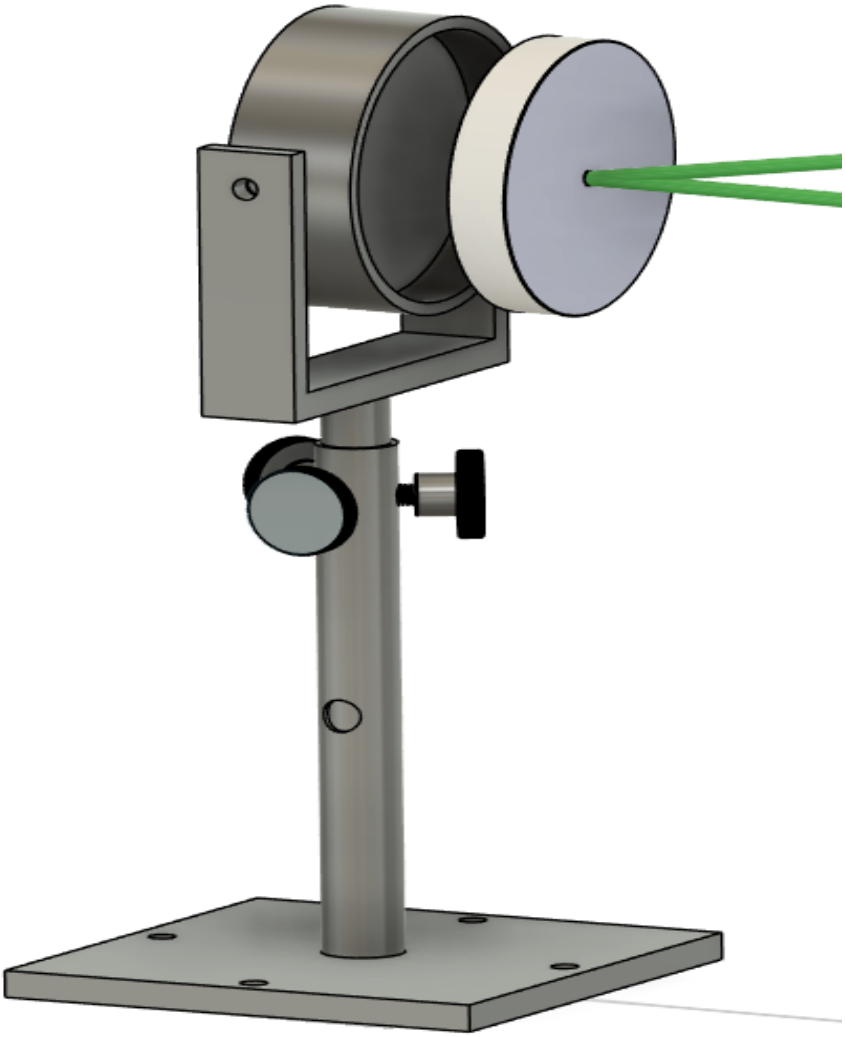

Figure 217: Assembled Mirror Housing with Light Incoming

The drawing for the Mirror holder is shown in **Figure 218**. This component holds the mirror in with just friction, as a foreseen issue set holes may need to be drilled and tapped for placement of set screws. Glue is to be avoided due to the risk of damaging the reflective surface. The hole is to be a clearance fit through hole so that a M4 threaded rod may be inserted having the clamping force prevent the mirror from unwanted rotation.

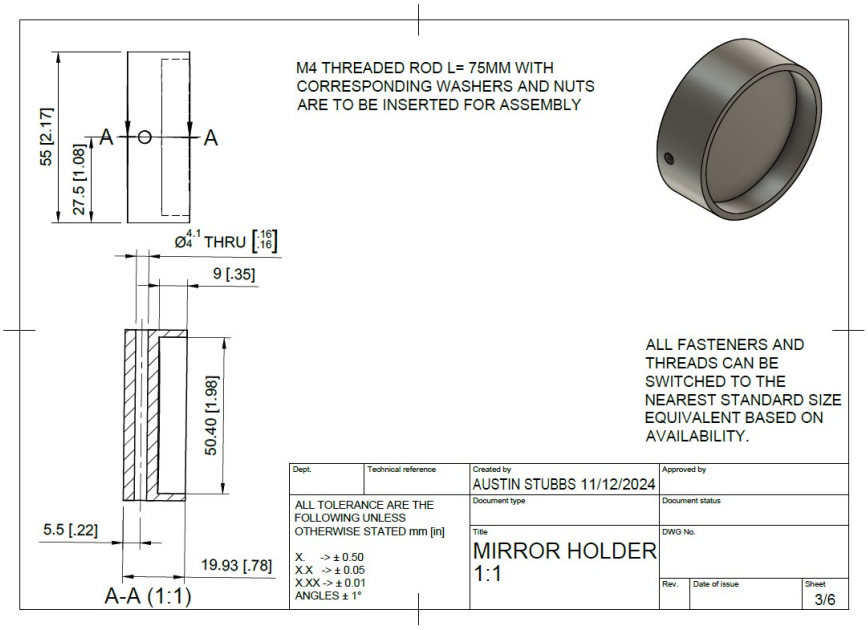

Figure 218: Drawing for Mirror Holder

The middle section of the mirror stand (resembling a field goal post) can be seen in **Figure 219**. This component features a 10mm round bar to be welded on the horizontal flat bar. The vertical flat bars are thinner to allow for bending, creating a clamping force that prevents the mirror holder from unwanted rotation. The holes on the vertical bars are the same-sized through holes as the mirror holder.

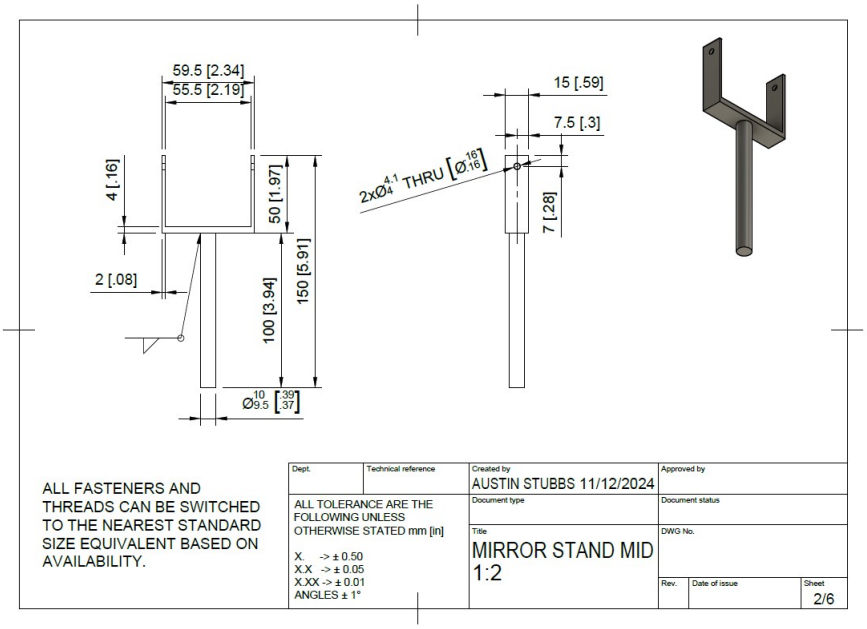

Figure 219: Drawing for Mirror Holder

The center through hole was placed to fit a No.2 Philips screwdriver in to allow for tightening the tube. Blue Loctite will be used if stand loosening becomes an issue. Height adjustments between 100 mm - 190 mm are made by sliding the mirror holder shaft and held in place by 3 thumb screws, as shown in **Figure 220**. The threads are placed externally on the pipe and internally on the plate to hold it upright. This design was changed from welding gussets for ease of manufacturing and to avoid warpage from welding.

Figure 220: Base for Schlieren Mirror Stand

An alternative design (as seen in **Figure 221**) omits the base, allowing the mirror to sit directly on a flat surface, although this design has less stability and fewer degrees of freedom. This component was not sent to be manufactured for the previous reasons.

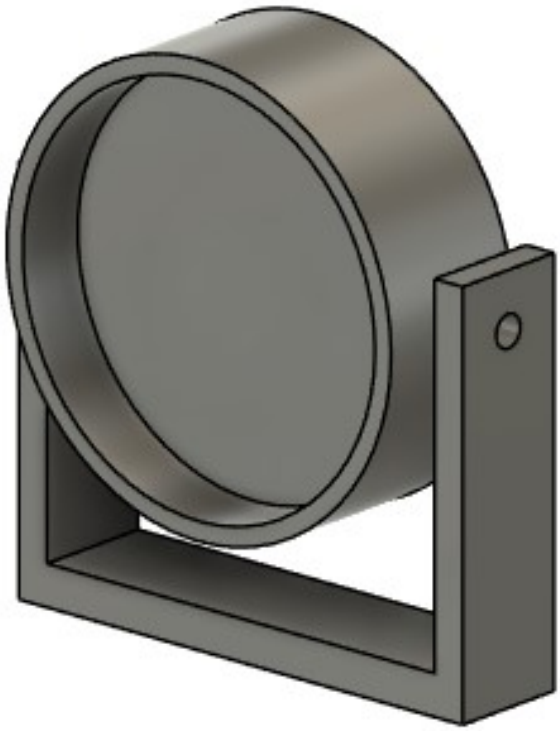

Figure 221: Alternative Design for Mirror Housing Without Base

5.3.2.2 Light Stand

The same base used for the mirror is used to mount the light, as shown in **Figure 222**. A Picatinny rail allows easy switching between the flashlight and laser mount. The laser came with a mount for a Picatinny rail. The extra material on the plate is to leave room for further attachments, such as a Plano-convex lessen holder. Future work includes a Plano-convex lens holder. The offset distance was calculated to be 54mm. However, validation of this number can be completed after the initial stand is set up.

Figure 222: Light Assembly Holder with Picatinny Rail

The light base shown in Figure 223 has a very similar construction to the midsection of the mirror holder in Figure 219. Featuring another d=10mm round bar welded to a flat plate. While there are 2 tapped holes to accept the Picatinny rail.

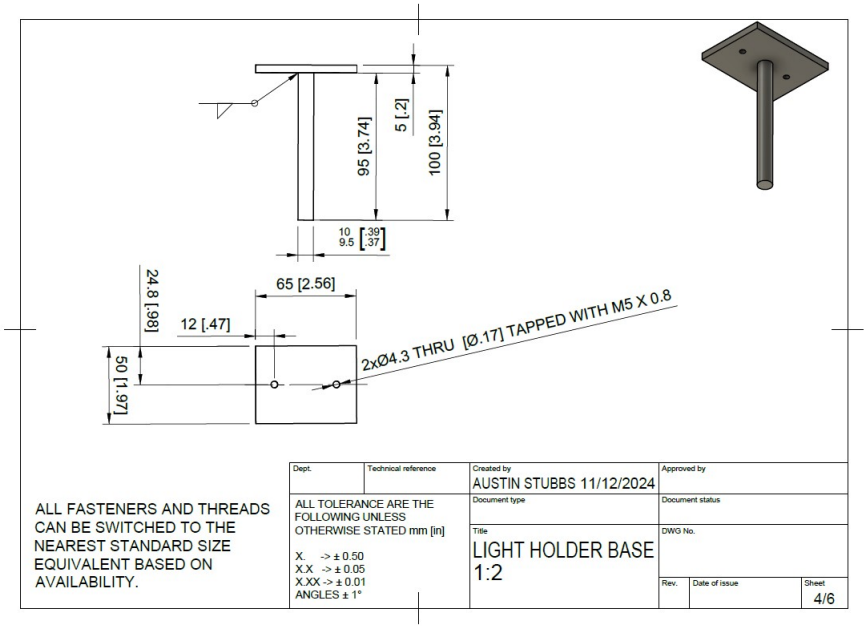

Figure 223: Middle Section for Light

The standard Picatinny rail shown in Figure 224 can be purchased online for likely much cheaper than the shop manufacturing it. Next semester KEFC funding should be requested to save the shop manufacturing a readily available part. The reason for using a Picatinny rail is that the laser mount came with a Picatinny rail mount. The system is reliable for precise instruments such as rifle scopes are often mounted to them. This part was submitted to the shop to avoid further delays in the event KEFC will not approve the Picatinny rail.

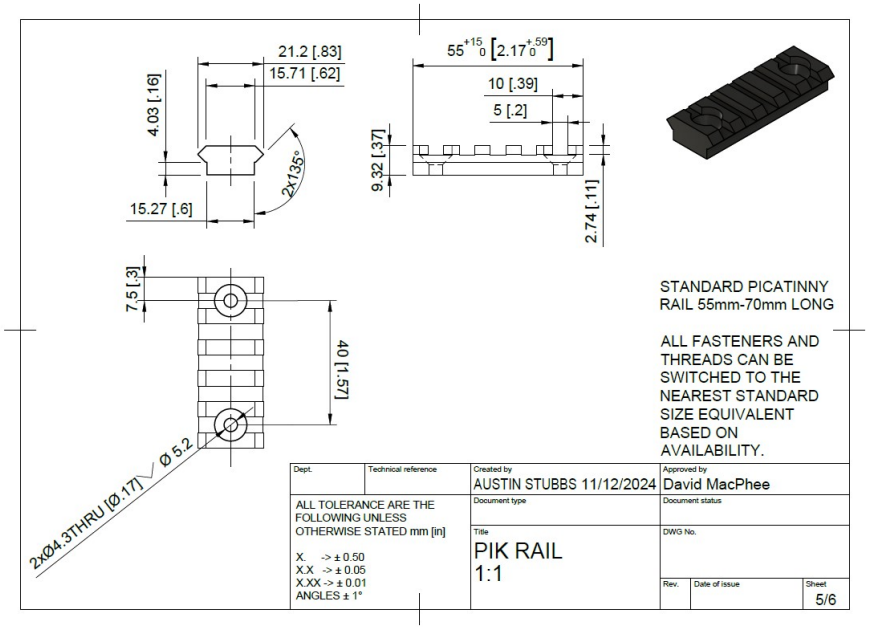

Figure 224: Drawing for Picatinny Rail

5.3.2.3 Breadboard

The Breadboard shown in Figure 225 consists of an 8 or 10-gauge aluminum sheet. This is the only aluminum part in the entire design. Aluminum was chosen for its corrosion resistance properties and weight savings so that one person can safely move it. A reason for considering the 8 gauge is because the shop has it on hand. This sheet is supported by 30 flush-fit screws placed in an 11 3/4"x 11 3/4" grid, starting 1/2" from each corner.

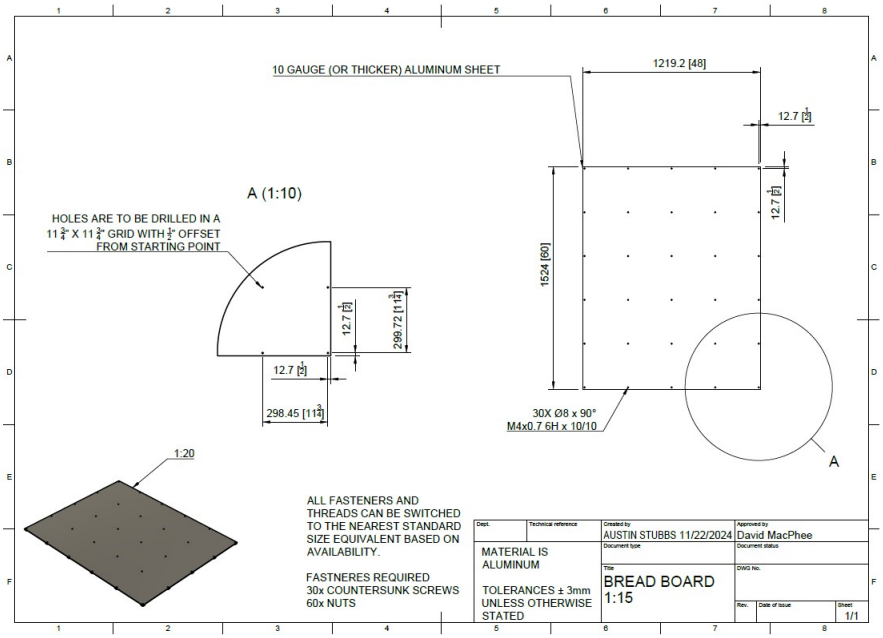

Figure 225: Breadboard Drawing

5.3.3 Calculations

In this section, calculations were completed for the distance of the Plano-convex lens and the thickness of the breadboard.

5.3.3.1 Plano-Convex lense

For the calculations of the plano-convex lens, clever geometry is used, as shown in **Figure 226**.

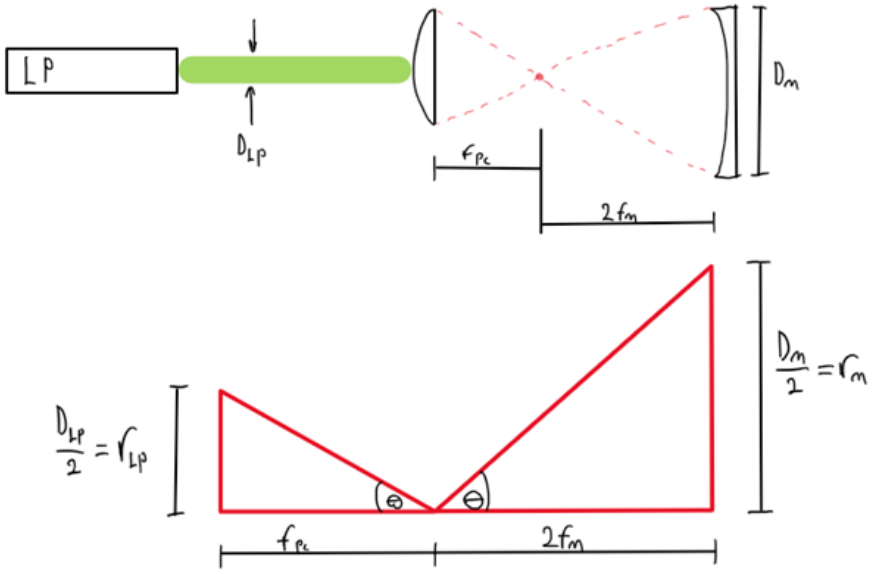

Figure 226: Geometry for Plano-Convex Calculation

The Laser diameter was measured using a pair of digital callipers, the mirror data was taken from the manufacturer's spec sheet [119].

Diameter Mirror Dm (mm)	Focal Distance Mirror Fm (mm)	Diameter of Laser Dlp (mm)	Focal Distance for Plano-Convex Lens Fpc (mm)	Theta Degrees
50.8 (2")	500.0	2.75	54	1.5

Table 49: Mirror and Lens Data (converted to millimetres)

Using **Equation 210**, Where Rm is the radius of the mirror, and Fm is the focal distance to the mirror,r we are able to obtain the angle $\theta = 1.5$:

$$\Theta = \tan^{-1}\left(\frac{R_m}{2F_m}\right) \tag{210}$$

Using **Equation 211** where Rlp is the radius of the laser and fm is the offset distance from the mirror to the Plano-convex lens to obtain F_{pc}:

$$\tan(\Theta) = \frac{R_{LP}}{F_m} \tag{211}$$

Equation 212 was obtained by rearranging **Equation 211** for Fm Finally, solving **Equation 212**, we obtain the value of $F_{pc} = 54\,\text{mm}$:

$$F_m = \frac{R_m}{\tan(\Theta)} \tag{212}$$

5.3.3.2 Breadboard Calculations

Calculations were completed to determine the thickness of the aluminum sheet. The first thing checked was to see if the 10-gauge sheet would not bend under its own weight.

The total weight is calculated using **Equation 213**:

$$W = w \cdot A \tag{213}$$

Substituting the values:

$$W = (291.16\,\text{in}^3) \cdot (0.0975\,\text{lbs/in}^3) = 28.4\,\text{lbs}.$$

Substituting the total weight into **Equation 214**, the weight per support point is given as:

$$W_{\text{point}} = \frac{W_{\text{sheet}}}{N} \tag{214}$$

Substituting $W_{\text{sheet}} = 28.41\,\text{lbs}$ and $N = 30$, we get:

$$W_{\text{point}} = \frac{28.41}{30} = 0.95\,\text{lbs/support}.$$

Finally, the distributed load w over the span can be calculated using **Equation 215**: Substituting $W_{\text{point}} = 0.95\,\text{lbs/support}$ and Span Length $= 16.6\,\text{in}$, we calculate:

$$w = \frac{W_{\text{point}}}{\text{Span Length}} \tag{215}$$

$$w = \frac{0.95}{16.6} = 0.057\,\text{lbs/in}.$$

Using the Moment of Inertia equation, where $b = 48$" and $h = 0.101$" (dimensions of the 10 gauge sheet), the moment of inertia I is calculated as shown in **Equation 216**:

$$I = \frac{bh^3}{12} \tag{216}$$

$$I = 1.01 \times 10^{-3}\,\text{in}^4$$

Substituting the given values into the deflection **Equation 217**:

Where $w = 0.101\,\text{lb/in}$, $L = 16.6\,\text{in}$, $E = 10 \times 10^6\,\text{psi}$, and $I = 0.00101\,\text{in}^4$, we calculate the deflection δ in inches.

$$\delta = \frac{5wL^4}{384EI} \tag{217}$$

$$\delta = \frac{5 \cdot (0.101) \cdot (16.6)^4}{384 \cdot (10 \times 10^6) \cdot 1.01 \times 10^{-3}} = 9.89 \times 10^{-3}\,\text{in}$$

For a worst-case scenario, a point load of 50 lbs was applied at the furthest distance between supports. This was to simulate someone putting their hand down and leaning slightly on the sheet. Using the point load deflection equation **Equation 218**: Substituting the given values into the point load deflection equation: Where $P = 50\,\text{lb}$, $L = 16.613\,\text{in}$, $E = 10{\times}10^6\,\text{psi}$, and $I = 0.00101\,\text{in}^4$, we calculate the deflection as:

$$\delta_{\text{point}} = \frac{PL^3}{48EI} \tag{218}$$

$$\delta_{\text{point}} = \frac{50 \cdot (16.613)^3}{48 \cdot (10 \times 10^6) \cdot 1.01 \times 10^{-3}} = 4.73 \times 10^{-4}\,\text{in}$$

The deflection is almost non-existent in both cases therefore the 10-gauge sheet of aluminum will be suitable for the Schlieren tabletop. 8 gauge has been permitted due to availability.

5.3.4 Conclusion

In conclusion, this semester included a lot of research then design work. A tabletop Schlieren system has been designed and is currently in queue to be manufactured. Next semester will begin with the assembly of the stands and breadboard. Experiments are planned to include testing the single vs double pass schlieren systems, replacing the razor blade with color filters to create gradients as seen in Figure 211, different types of glass will be experimented with as adjustments will need to be made for integration into the rocket.

5.4 Test Section Inlet (Rocket) - Nathan Bolduc

Peer Reviewed by: Phil Charapov - 101183161

5.4.1 Background

The test section inlet for the supersonic test vehicle, designed last year, aims to funnel incoming air to a test subject with minimal flow disturbance [1]. The main challenges are managing shocks and heat. At high speeds, shocks form along the inlet's leading edge, altering streamline direction and reducing flow velocity. A fine lip design, as used in last year's model, could theoretically prevent this, but it would overheat and melt [1]. Therefore, the lip must be rounded to avoid melting, which causes oblique shocks to form in the test section. The length of the test section for supersonic flow was chosen to balance two factors: it needed to be short enough to prevent a large boundary layer from forming, yet long enough to allow the flow to develop. This ensures accurate testing conditions by minimizing boundary layer effects while maintaining a stable flow. The length that was selected did not allow for full development of flow, but it did maintain an acceptable boundary layer and created adequate uniform flow for the test specimen [1].

5.4.2 Introduction

The main scope of this project is to offer accurate results of forces and flow visualization at high altitude and supersonic speeds. The working objective is Mach 3.0 at an altitude of 70,000 ft. To achieve flow visualization and maintain stability of the test vehicle, enclosing the test section was determined to be the best course of action [1].

The goal of this semester's work was to improve last year's inlet design, aiming to provide undisturbed flow to the test specimen. The main challenge is that any flow obstruction causes disturbances. To avoid this, the test specimen must either be unenclosed or placed before the initial oblique shock convergence. This section focuses on keeping the test specimen enclosed and therefore, improving the inlet to maximize the axial distance for placing the test specimen before the initial shock convergence. This was achieved by refining the lip and increasing the test section diameter relative to the increase in rocket diameter. Additionally, simulations were conducted to determine the acceptable size of the test specimen, ensuring the flow doesn't choke and create a bow shock in front of the inlet. These findings will be presented and discussed below.

5.4.3 Preliminary Design Work

Last year's design did not specify the geometry of the lip that they presented in their final report. Therefore, using data, graphs, and the Ansys assumptions from the report [1] an estimate of the model's geometry was obtained. It was determined that the inlet had a leading edge radius of approximately $R = 0.15in$ (Ref Figure 232).

5.4.4 Research

Research was conducted into potential inlet geometries to determine ways improve or potentially prevent shockwave development. While there are many supersonic and hypersonic inlet designs, such as those used in RAMJETS and SCRAMJETS, these rely on shock development and are less relevant to our needs. Therefore, supersonic geometry from existing supersonic vehicles were not considered as an option to improve the performance of the test section inlet. A more practical approach is to reduce the angle of the oblique shock, creating a larger axial distance within the inlet before the shocks converge. This allows the test subject to be positioned forward of the convergence point, ensuring undisturbed flow reaches the test subject.

5.4.5 CFD Setup

CFD was used to determine results due to the efficiency of being able to test different geometries quickly. The CFD model that was used for the results presented below is slightly different than what was used previously. The parameters were determined from direct comparison of the two models over simple geometry like a bluff body (sphere) and a wedge. The bluff body was used qualitatively to see if the CFD simulation would produce a detached shock (bow shock) in front of the bluff body. These results can be seen in Figure 227. The wedge was used qualitatively and quantitatively to see if the CFD results were similar visually and analytically to theoretical results. The results were compared in the following section. Table 50 below provides the key parameters that were used in the CFD to obtain the results throughout this report.

Table 50: CFD parameters

Parameter	Selected Parameter
Model	Density Based
Density	Ideal Gas
Viscosity	Sutherland
Turbulence Model	SST k-omega
Energy	On
Operating Pressure	4.688 kPa
Operating Temperature	219K

Ansys Fluent uses the finite volume method to discretize and solve the governing equations of fluid flow and heat transfer [1]. These finite volumes are dictated by the user defined mesh parameters, as the mesh gets finer the accuracy of the simulation is regarded to be more accurate, though not always the case. The geometry of the mesh also has an effect on the accuracy of the results. A **hex dominant method** with **face sizing** was chosen for the mesh parameters. The **hex dominant method** was selected due to improvement in accuracy over the default **triangular method** [120]. **Face sizing** was used to refine the size

of the mesh near the surfaces of the test section where the flow is changing the most. With the control volumes defined Ansys Fluent is able to solve the governing equations, calculated from the centroid of each cell using an iterative algorithm until it arrives at a converged solution. The Navier-Stokes Equations 219 through 223 represent the five governing equations: the continuity equation, the x, y, and z momentum equations, and the energy equation, respectively.

$$\frac{\delta \rho}{\delta t} + \nabla \ (\rho * \mathbf{V}) = 0 \tag{219}$$

$$\frac{\delta(\rho \ u)}{\delta t} + \nabla \ (\rho u * \mathbf{V}) = -\frac{\delta p}{\delta x} + \frac{\delta \tau_{xx}}{\delta x} + \frac{\delta \tau_{yx}}{\delta y} + \frac{\delta \tau_{zx}}{\delta z} + \rho f_x \tag{220}$$

$$\frac{\delta(\rho \ v)}{\delta t} + \nabla \ (\rho v * \mathbf{V}) = -\frac{\delta p}{\delta y} + \frac{\delta \tau_{yx}}{\delta x} + \frac{\delta \tau_{yy}}{\delta y} + \frac{\delta \tau_{zy}}{\delta z} + \rho f_y \tag{221}$$

$$\frac{\delta(\rho \ w)}{\delta t} + \nabla \ (\rho w * \mathbf{V}) = -\frac{\delta p}{\delta z} + \frac{\delta \tau_{xz}}{\delta x} + \frac{\delta \tau_{yz}}{\delta y} + \frac{\delta \tau_{zz}}{\delta z} + \rho f_z \tag{222}$$

$$\begin{aligned} \frac{\delta}{\delta t}\left[\rho\left(e + \frac{V^2}{2}\right)\right] + \nabla \ \left[\rho\left(e + \frac{V^2}{2}\right) * \mathbf{V}\right] &= \rho \dot{q} + \frac{\delta}{\delta x}\left(k \frac{\delta T}{\delta x}\right) \\ + \frac{\delta}{\delta y}\left(k \frac{\delta T}{\delta y}\right) + \frac{\delta}{\delta z}\left(k \frac{\delta T}{\delta z}\right) - \frac{\delta(u \ p)}{\delta x} - \frac{\delta(v \ p)}{\delta y} - \frac{\delta(w \ p)}{\delta z} \\ + \frac{\delta(u \ \tau_{xx})}{\delta x} + \frac{\delta(u \ \tau_{yx})}{\delta y} + \frac{\delta(u \ \tau_{zx})}{\delta z} + \frac{\delta(v \ \tau_{xy})}{\delta x} + \frac{\delta(v \ \tau_{yy})}{\delta y} \\ + \frac{\delta(v \ \tau_{zy})}{\delta z} + \frac{\delta(w \ \tau_{xz})}{\delta x} + \frac{\delta(w \ \tau_{yz})}{\delta y} + \frac{\delta(w \ \tau_{zz})}{\delta z} + \rho f * \mathbf{V} \end{aligned} \tag{223}$$

5.4.6 CFD - Validation

To validate the CFD model two tests were done and compared to theoretical knowledge. When a bluff body was simulated (sphere) the model produced a bow shock seen in Figure 227, which is to be expected in this scenario.

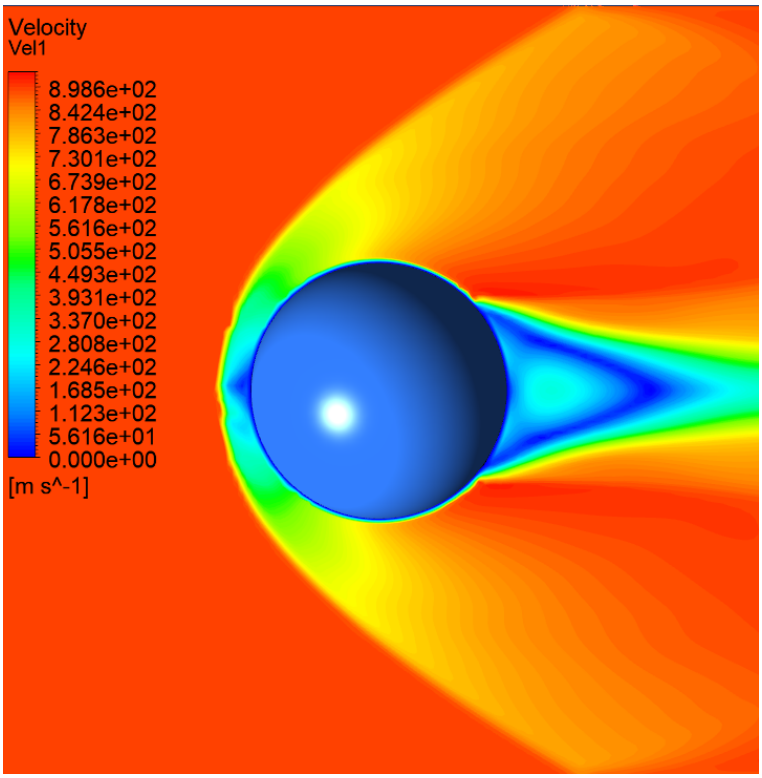

Figure 227: CFD simulation of a bluff body using parameters mentioned above

The colour index for corresponding velocities for the bluff body simulations was included in Figure 227 as supporting information. It can be seen in Figure 227 that a bow shock forms in-front of the bluff body with the leading surface perpendicular to the direction of flow having zero velocity.
The next scenario that was simulated is a wedge, which can be seen in Figure 228. The wedge was simulated and compared to analytical results, the results will be compared and discussed below. It should be noted that there is a purple line above the top surface of the wedge in Figure 228, this line corresponds to the data shown in Figure 230.

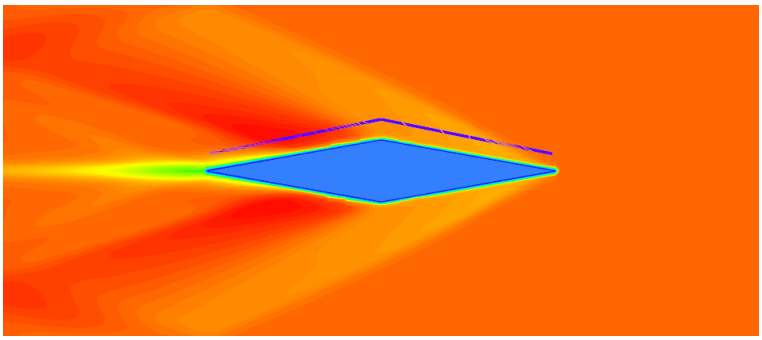

Figure 228: CFD simulation of a wedge using parameters mentioned above

Using theory learned from the textbook Fluid Mechanics - Ninth Edition [121] the mach number after the initial shock can be found. The wedge is $0.25m$ long with a 10 degree turn angle, the geometry of the wedge can be seen below in Figure 229.

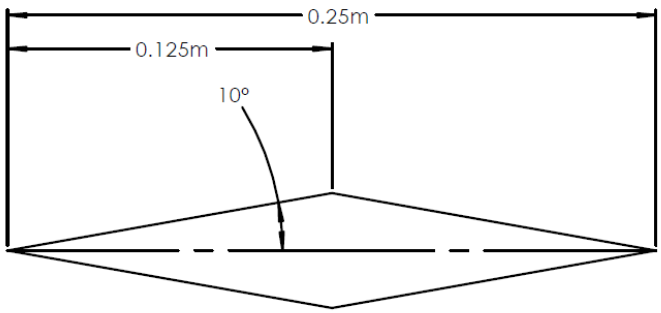

Figure 229: Critical dimensions for simulated wedge

In order to determine the downstream mach number after the oblique shock produced from the leading edge of the wedge, the following equations are required.

$$tan(\theta) = \frac{2\ cot(\beta)\ (Ma_1^2\ sin^2(\beta) - 1)}{Ma_1^2\ (k + cos(2\ \beta)) + 2} \tag{224}$$

$$Ma_{n_1} = Ma_1\ sin(\beta) \tag{225}$$

$$Ma_2 = \frac{Ma_{n_2}}{sin(\beta - \theta)} \tag{226}$$

Therefore, using Equations 224, 225, 226, and the Tables from Fluid Mechanics Ninth Edition textbook [121], the down stream mach number was found to be

$Ma = 2.50$. The corresponding temperature was determined to be $T = 272K$ which yields a downstream velocity of $826.5m/s$.

In addition to the mach number after the oblique shock, the mach number after the expansion fan (over the top point) was also calculated using Prandtl-Meyer supersonic expansion relations from Table B.5 [121]. Therefore, the Mach number after the expansion fan was determined to be $Ma = 3.54$ with a temperature of $T = 174.02K$, which corresponds to a velocity of $932m/s$.

Looking at Figure 230 below, the velocity of the fluid flowing along the upper surface of the wedge (Purple line in Figure 228) can be seen. The leading edge being at $0.25m$ and the trailing edge velocity being at $0m$. From Figure 230 it can be seen that the velocity after the shock wave and after the expansion fan is $829m/s$ and $963m/s$ respectively.

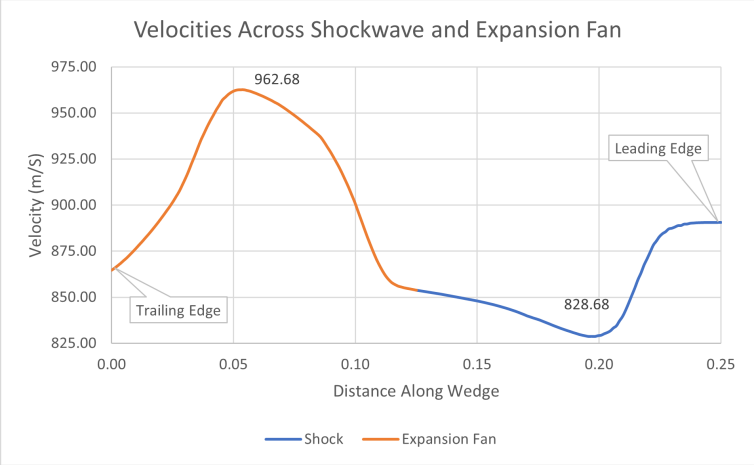

Figure 230: Velocity above the upper surface of the wedge

Table 51 below compares the theoretical results to the results obtained from the CFD simulation. It can be seen that there is a small difference between the values, with the larger difference being after the expansion fan.

Table 51: CFD simulation and theoretical values comparison

	Theoretical	**Simulation**	**% Difference**
Oblique Shock	826.5 m/s	828.7 m/s	0.27 %
Expansion Fan	932.0 m/s	962.7 m/s	3.3 %

Therefore, from the results presented above it can be concluded that the CFD model that is being used produces qualitative values that align with theoretical values and quantitative results that show key features like oblique shocks and

bow shocks. It should be noted that the quantitative results of shocks in CFD are different as there is a visible thickness when in reality it should be a discontinuity. Therefore, it will be assumed that the shock acts as a straight line from the lip of the obstruction to the visible convergence point (Ref Figure 231).

5.4.7 CFD - Oblique Shock Convergence

Figure 231 below gives a qualitative result of the internal flow into the test section. This figure provides the simulation results of how much axial distance there is before the oblique shocks produced from the leading edge converge. Figure 233 below shows the centerline velocity into the test section. This figure provides the axial distance for when the initial shocks converge. The results show that the shocks converge $180mm$ $(7in)$ into the test section (Ref Section Test Section Inlet Lip Refinement). It should be noted that the test section was increased to a diameter of $203.2mm$ $(8in)$ to maintain the $51mm$ $(2in)$ wall thickness and accommodate the overall diameter of the rocket being increased to a diameter of $305mm$ $(12in)$.

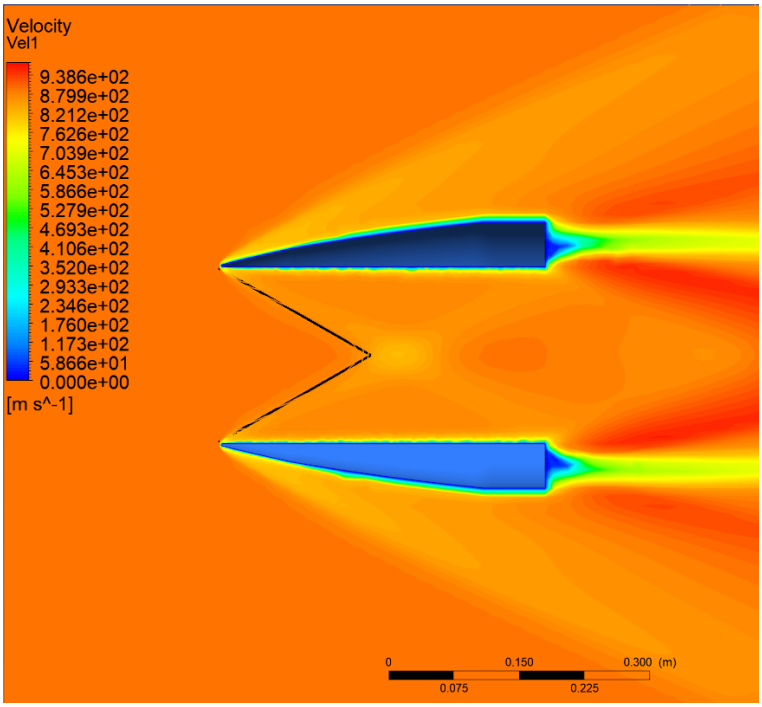

Figure 231: Simplified test section inlet CFD results

5.4.8 Test Section Inlet Lip Refinement

The test specimen will be placed before the initial shock convergence. Steps were taken to increase the axial distance in the test section before the shocks converge. Various inlet geometries were tested using CFD simulations in ANSYS. Figure 232 below shows the cross-section of the three lip geometries that were considered and simulated while Figure 233 shows the axial distance into the test section before the initial oblique shock converges.

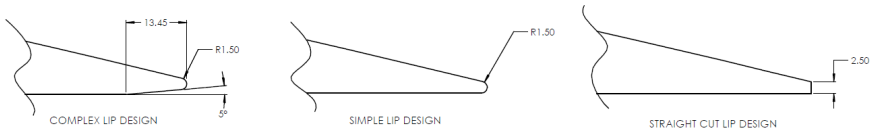

Figure 232: Test section inlet lips critical dimensions

The lip thickness and geometry were adjusted to see their effect on the oblique shock angle. As shown in Figure 233 below, the three lip geometries had little impact on the axial distance where the shocks converge, but the fineness of the lip did. Though little, the **simple lip** does create slightly more distance before the oblique shocks converge, and therefore it was selected to be used over the other two geometries.

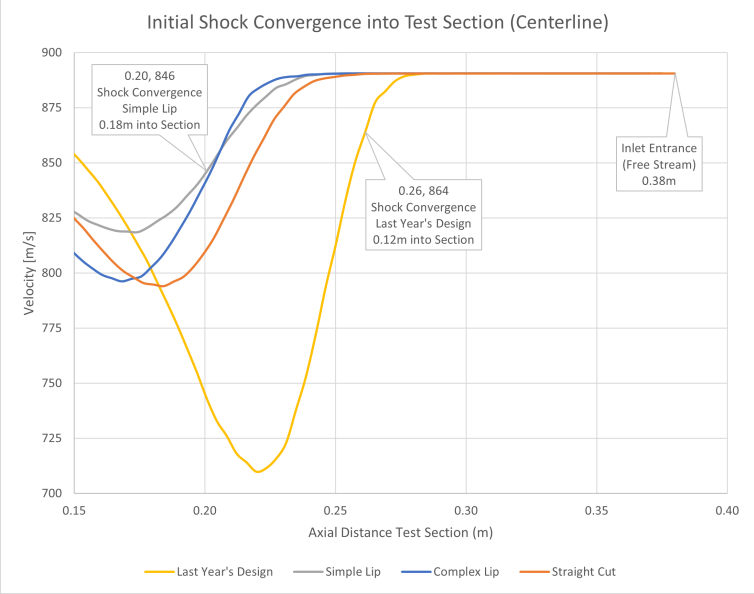

Figure 233: Centerline velocity of internal flow in test section

Last year's inlet design had a lip radius of approximately $3.8mm$ $(0.15in)$, while the current design has a lip radius of $1.5mm$ $(0.06in)$. From Figure 233 above, it can be seen that this change increased the axial distance from $12cm$ to $18cm$, a 50% increase. This increase allows adequate space for a test specimen to be positioned before the initial oblique shocks converge, subjecting the test specimen to the free-stream air at the desired conditions. This will allow the test section to be shortened significantly, as there is no longer a benefit to a longer section. Recall, the test section length was selected in the previous year to balance the boundary layer growth and the development of the flow. However, since the flow is unobstructed by positioning the test specimen forward of the oblique shocks, the length of the test section can be reduced.

5.4.9 Test Specimen Sizing

CFD simulations were conducted to find the largest test specimen that wouldn't obstruct the flow and cause a bow shock in front of the test section. A cylinder was chosen for these simulations because its circular cross-section and flat surface parallel to the flow create significant obstructions. This disk serves as a 'worst-case' scenario, ensuring that any other specimen would not produce worse results. Figure 234 shows a section view of the test section with the test specimen.

It should be noted that the test section does vary compared to previous' years design, the outer and inner profile of the test section were maintained, though the inner and outer diameter were both increased while maintaining the wall thickness. The load cell and connecting structure were adjusted to allow the simulations to converge and are currently arbitrarily designed, if the **rocket body** is selected over the **lifting body** than proper design and consideration will go into implementing the load cell and supporting structure into the shorter test-section.

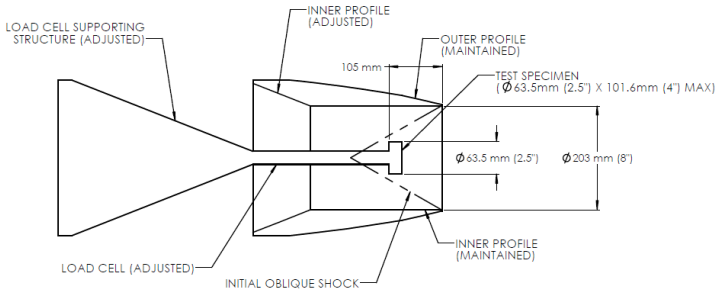

Figure 234: Section view of the test section and specimen

After numerous simulations the critical dimension of the cylinder was determined to be the diameter between $63.5mm$ $(2.5in)$ and $76.2mm$ $(3.0in)$. The

results for the 63.5mm diameter cylinder can be seen below in Figure 235. It should be noted that results would not converge with a cylinder diameter of 76.2mm, therefore no results can be presented and it is assumed that a 76.2mm diameter cylinder would result in the flow choking.

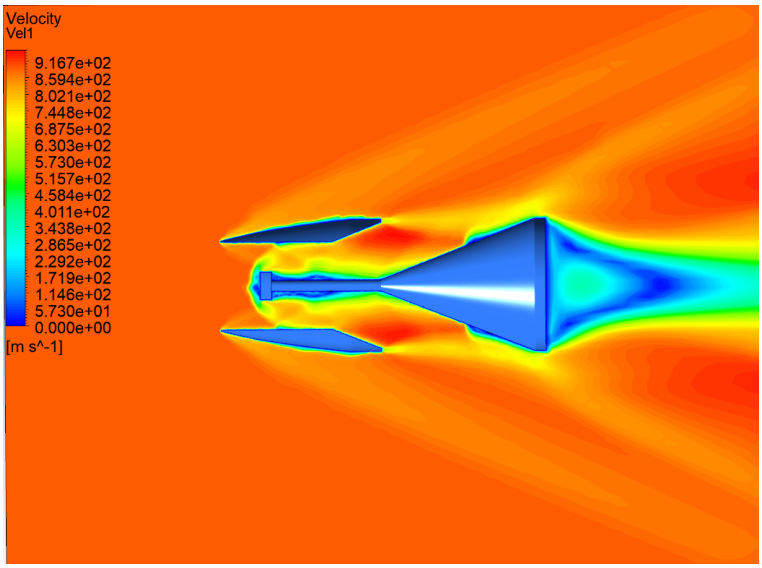

Figure 235: Section view of the test section and specimen

It can be seen in Figure 235 that there is a bow shock in-front of the cylindrical test specimen which is to be expected. Therefore, it can be seen that the CFD simulation shows that data could be collected on a specimen with a diameter of 63.5mm without choking the flow.

5.4.10 Conclusion

Improving the effectiveness of the test section for the rocket poses numerous difficulties, such as the inlet obstructing the flow, which creates shock waves that alter the flow contacting the test specimen. Therefore, to ensure the most accurate results it was determined that the best course of action was to move the test specimen in-front of the oblique shocks. A 63.5mm diameter by 101.6mm long cylinder was determined to be the largest specimen that could be positioned forward of the oblique shocks and still produce results without choking the flow through the test section. This was achieved by refining the lip geometry. The geometry that was selected was the simple lip design with a 1.5mm constant radius on the leading edge. This created an 18cm axial distance in the test section, allowing a test specimen to be placed in unobstructed flow. This was a 50% increase compared to last year's inlet lip design.

5.5 Force Balance Design - Colby Jackson

Peer Reviewed by: Austin Stubbs

5.5.1 Introduction

Accurate measurement of aerodynamic forces is crucial in wind-tunnel testing for validating aircraft designs and understanding flight characteristics [122]. The force balance apparatus quantifies these forces, specifically lift, drag, and all mechanical forces, which are essential for assessing performance. Previous designs of the vertical section were limited to single-axis force measurements, restricting comprehensive multi-directional force analysis with strain gauges [1].

This report focuses on redesigning the vertical section to a cylindrical geometry, ensuring it withstands specified forces while accommodating the strain gauges. These gauges are placed to capture forces in both vertical and horizontal planes, addressing the limitations of last year's designs. Implementing two half-bridge strain gauge circuits allows for temperature compensation, enhancing measurement precision and reliability [123], [124]. This setup enables more accurate force calculations by mitigating thermal effects on strain readings, which were previously not taken into account.

5.5.2 Theory

5.5.2.1 Governing Equations for Static Structural FEA

In performing static structural finite element analysis (FEA) using ANSYS, the governing equations are derived from the fundamental principles of mechanics, specifically the equilibrium equations, constitutive relations, and compatibility conditions [125]. The primary equation that describes the behaviour of the structure under static loading is [125]:

$$\mathbf{Ku} = \mathbf{F} \tag{227}$$

Where:

- $\mathbf{K}$ is the global stiffness matrix, representing the stiffness properties of the entire discretized structure.
- $\mathbf{u}$ is the displacement vector, containing the nodal displacements.
- $\mathbf{F}$ is the external force vector, representing the applied loads at the nodes.

Equation 227 represents the global equilibrium of the structure under static loading conditions [125].

The stiffness matrix $\mathbf{K}$ is assembled from the individual element stiffness matrices $\mathbf{K}_e$, which are derived from the element's material properties and geometry. The element stiffness matrix is given by [125]:

$$\mathbf{K}_e = \int_{V_e} \mathbf{B}$$

T D B dV (228)

Where:

- $\mathbf{K}_e$ is the element stiffness matrix.
- V_e is the volume of the element.
- $\mathbf{B}$ is the strain-displacement matrix, relating the element's nodal displacements to the strains.
- $\mathbf{D}$ is the constitutive matrix, relating the strains to the stresses according to Hooke's Law.

The strain-displacement relationship is given by [125]:

$$\boldsymbol{\varepsilon} = \mathbf{B}\mathbf{u} \tag{229}$$

Where:

- $\boldsymbol{\varepsilon}$ is the strain vector.
- $\mathbf{u}$ is the displacement vector.

The stress-strain relationship, according to Hooke's Law for linear elastic materials, is [125]:

$$\boldsymbol{\sigma} = \mathbf{D}\boldsymbol{\varepsilon} \tag{230}$$

Where:

- $\boldsymbol{\sigma}$ is the stress vector.
- $\boldsymbol{\varepsilon}$ is the strain vector.
- $\mathbf{D}$ is the constitutive matrix, which depends on the material's Young's modulus $\mathbf{E}$ and Poisson's ratio $\boldsymbol{\nu}$.

In static structural FEA, the goal is to solve for the displacement vector $\mathbf{u}$ by applying the known forces $\mathbf{F}$ and boundary conditions. Once the displacements are known, strains and stresses can be computed using Equations 229 and 230 [125].

Therefore, the overall process involves assembling the global stiffness matrix $\mathbf{K}$, applying boundary conditions, and solving the system of equations in Equation 227 to find $\mathbf{u}$.

5.5.2.2 Strain Gauges

Two half-Wheatstone bridges will be used in order to isolate the bending strain in the **X** and **Y** planes, which can be combined together to obtain the out-of-plane force [124]. A half-Wheatstone bridge circuit is shown in Figure 236.

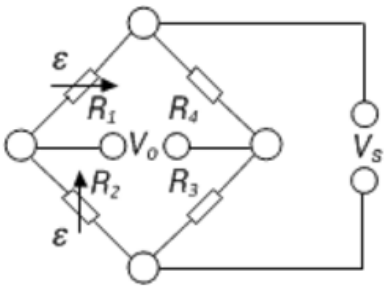

Figure 236: Strain Measurement on a Half-Bridge Bending Beam Circuit [124]

In the context of strain measurements using a Wheatstone bridge, the strain (ε) can be determined using bridge-specific equations that relate the output voltage ($\mathbf{V}_0$) to the excitation voltage ($\mathbf{V}_s$), accounting for the gauge factor ($\mathbf{k}$) of the strain gauge [123], [124]. For a bending strain scenario, where the strain gauge is arranged in a configuration sensitive to bending, the strain is given by [124]:

$$\varepsilon = \varepsilon_b = \frac{1}{2} \cdot \frac{4}{\mathbf{k}} \cdot \frac{\mathbf{V}_0}{\mathbf{V}_s} \tag{231}$$

Where:

- ε is the strain.
- ε_b is the bending strain.
- $\mathbf{V}_0$ is the output voltage of the bridge.
- $\mathbf{V}_s$ is the excitation voltage supplied to the bridge.
- $\mathbf{k}$ is the gauge factor of the strain gauge.

Here, the factor of $\frac{1}{2}$ accounts for the sensitivity of the bridge to bending effects [124].

To measure the torsion on the vertical section, a full bridge will be used in front of the two half bridges [124]. The full bridge circuit is shown in Figure 237.

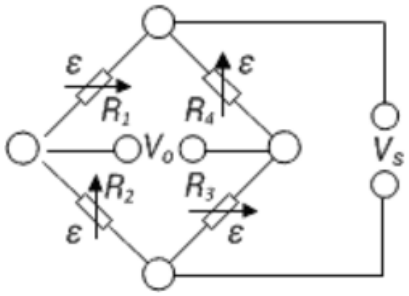

Figure 237: Torsion Measurement Full Bridge Circuit [124]

For torsional strain measurements, where the strain gauge arrangement isolates torsional effects, the strain is calculated as [124]:

$$\varepsilon = \varepsilon_d = \frac{1}{4} \cdot \frac{4}{\mathbf{k}} \cdot \frac{\mathbf{V}_0}{\mathbf{V}_s} \tag{232}$$

Where:

- ε_d is the torsional strain.
- $\mathbf{V}_0$, $\mathbf{V}_s$, and $\mathbf{k}$ are as previously defined.

The factor of $\frac{1}{4}$ represents the reduced sensitivity of the bridge to torsion [124].

The placement of the strain gauges is shown in Figure 238, where the red ovals are part of the two half-bridge circuits where the opposing strain gauges are connected, while the green ovals show the strain gauges that are part of the full bridge.

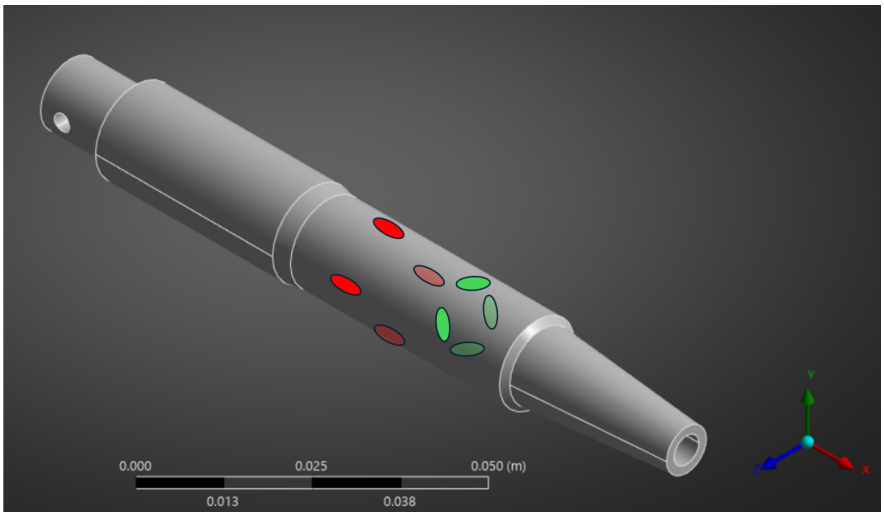

Figure 238: Placement of Strain Gauges Where Red is Part of the Half-Bridge Circuits While Green is Part of the Full Bridge Circuit. Opacity is Reduced on Strain Gauges Placed on the Non-Visible Side of the Body

5.5.3 Material Properties and Design Requirements

5.5.3.1 Material Properties

- **Materials**: Aluminum AlSi10Mg, SLA resin (Testing)
- **Yield Strength** (σ_{yield}): 240 ± 20 MPa [126]
- **Young's Modulus** (E): 70 GPa [126]

5.5.3.2 Material Selection

The material composition AlSi10Mg was selected for this project due to its compatibility with 3D printing processes and its mechanical properties, which closely resemble those of Aluminum 6061, the material used in last year's design. A key advantage of AlSi10Mg is its reduced coefficient of thermal expansion (CTE) compared to Al 6061, which minimizes issues like warping during Direct Metal Laser Sintering (DMLS). Additionally, the smaller solidification range ($\mathbf{\Delta T}$) of AlSi10Mg—approximately 40 K compared to the 70 K of Al 6061—reduces the likelihood of hot tearing and improves its processability in additive manufacturing [127].

5.5.3.3 Vertical Section Development

The final geometry of the vertical section was determined iteratively through trial and error of various geometries to determine the best for the specific case. A large outer diameter was desired due to the risks associated with applying

strain gauges to a tightly curved surface [123]. These risks include improper contact with the surface and potential damage to the strain gauge caused by excessive bending [123]. Due to this preference and the inherent constraints of one-axis load cell geometry, the use of internal geometry became unavoidable.

Load cells designed to measure forces orthogonal to a beam often incorporate specific internal geometries—such as dual cutouts flanking a central section—to concentrate strain and enhance measurement accuracy [124]. These cutouts, typically elliptical or rectangular, reduce the beam's cross-sectional area in targeted regions, thereby localizing deformation under applied loads [125]. This design ensures that strain is amplified in the central section where strain gauges are mounted, leading to more precise readings [123]. The strategic placement of these cutouts not only increases the sensitivity of the load cell but also minimizes the influence of extraneous forces, contributing to the device's overall accuracy and reliability [122].

In total, five main geometries were created and analyzed: rectangle, oval, conic curve, sphere, and parabolic, which were curves of the two cutouts concentrating the strain [128]. Each of the five curves had multiple sub-geometries where variables were changed, such as the width between cutouts, size of cutouts, and curves of cut-outs. Resulting in over 25 FEA files from these tests, it was found that two spheres with a 6 mm radius spaced 16 mm apart was the best geometry for this case.

Table 52: Effects of Varying Variables on Different Geometries

Geometry	**Spacing**	**Size**	**Distance from Edges**	**Strain Concentration**
Rectangular	Changed intensity of strain at cut-outs	Proportional to aspect ratio	High sensitivity near edges	Uniform distribution across cut out
Spherical	Changed intensity of strain at rear cut-out	Proportional to radius	Most insensitive to placement	Clear concentration
Conic	Minimal affect	Collapsed axially when too large and little strain when small	Minimal affect	High strain behind apex, high strain along section towards axial load cell
External Geometry	N/A	Strain concentration at edges	Edge geometry minimally affect location	Always on the edge of strain placement
Parabolic	Changed intensity of strain at rear cut-out	Sensitive to focal length	Tight parabolic shapes heavily influence while loose insensitive to edges	Concentration near vertex

5.5.4 Finite Element Analysis

Looking at the FEA from the chosen geometry, the concentration of strain around the cutouts can be visually observed, as shown in Figure 239.

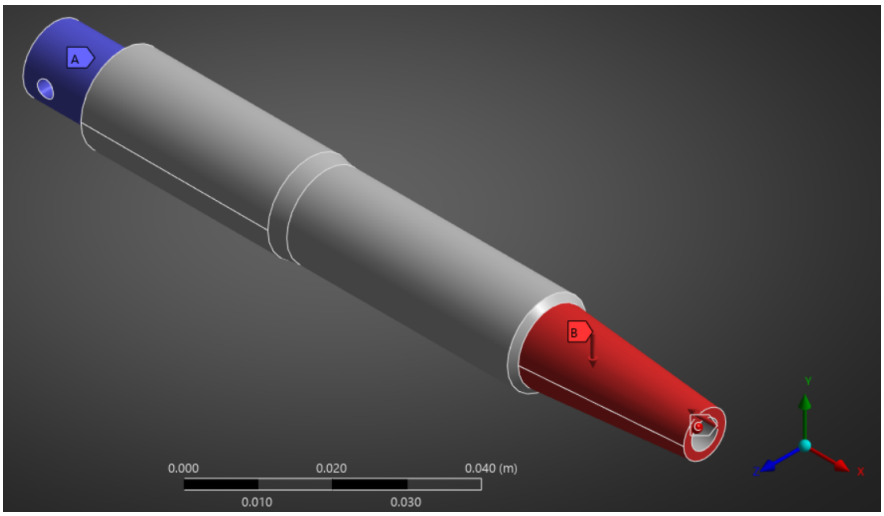

Figure 239: Engineering Drawing of the Vertical Section of the Force Balance Apparatus

Force A is applied to the tip surface in the negative **X**-direction with a magnitude of 2000 N, while Force B is applied to the side of the tip as a surface load with a magnitude of 500 N. These forces were derived from last year's report on the load cell [1]. The cutouts had to be designed to withstand both forces simultaneously without adversely affecting one another. Certain geometries proved problematic, as they allowed for a more concentrated strain area under the 500 N load but failed to withstand the 2000 N axial force. For example, conic curve cutouts created a highly concentrated strain area for orthogonal loads; however, they could not withstand the horizontal force and caused the structure to collapse. This limitation led to the rejection of the conic curve design.

In Figure 239, the fixed section of the vertical portion used for the FEA is highlighted in blue. While a bearing will eventually be incorporated somewhere along the thickness of this part, it is currently not possible to predict its exact placement, as the decision between the blended body and rocket test section has not yet been finalized. Both designs will influence the final dimensions of the load cell, as it will need to be scaled accordingly to match the chosen test section. For these reasons, the fixed section selected for the FEA was based on known fixed surfaces that will be connected to the axial section and secured in place with a pin. Both sections will then be mounted to the cone in a manner similar to last year's setup.

From the FEA, the amount of strain experienced at the gauge locations can be determined; the strain can be seen in Figure 240.

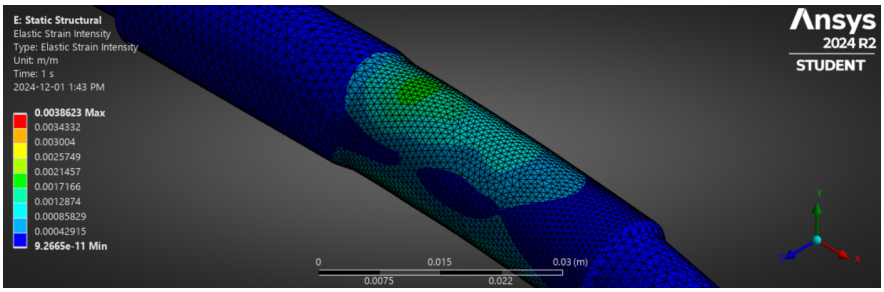

Figure 240: Strain Visualization With the 500 N Orthogonal Force and 2000 N Axial Force Acting on the Body

From Figure 240, the strain is concentrated right behind the cutout, which can be seen in Figure 243. The strain experienced at the two half-bridge locations is between 0.00172 and 0.00215, which, using the minimum value, will cause a resistance change of approximately 0.4284 Ω in one gauge. Since opposing strain gauges will be connected to the same half bridge, the resistance in the circuit will actually be closer to double that value. Whether this change is negative or positive dictates which direction the force is being applied [124].

In Figure 241, a 100 N·m moment force is acting in the positive **Z** direction.

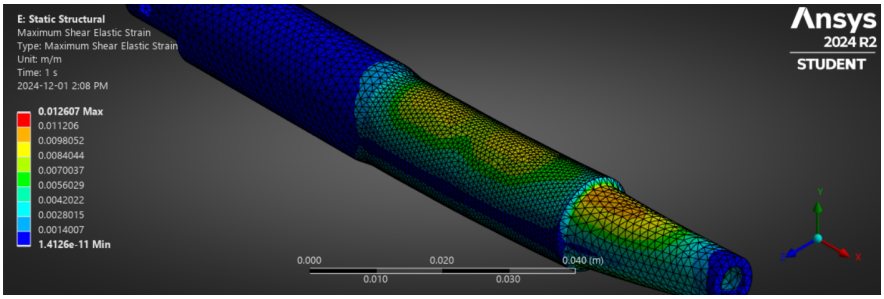

Figure 241: Strain Visualization With a 100 N·m Moment Force Acting on the Body in the **Z**-Axis Applied to the Same Surface as the 500 N Force

To ensure the above results could be accepted, a mesh convergence study was performed for the final geometry selected, as shown in Figure 242.

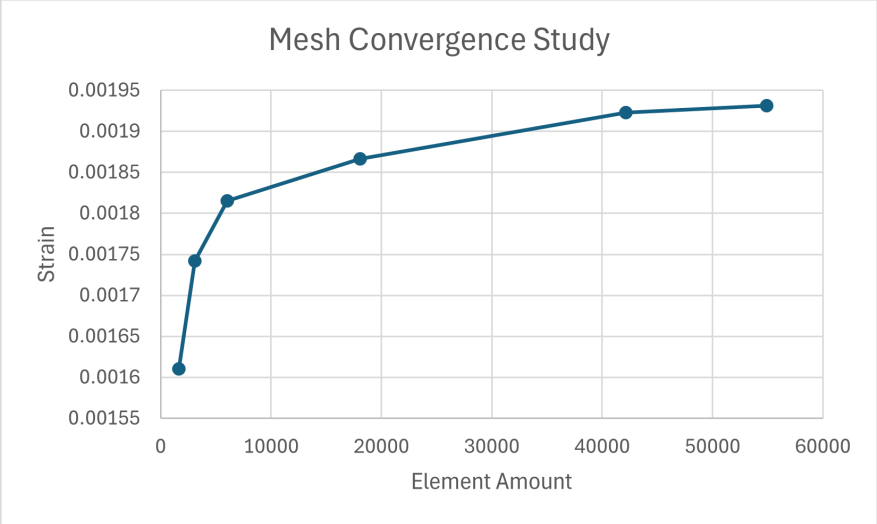

Figure 242: Vertical Load Cell Mesh Convergence Study

In Figure 242, the strain convergence around 0.001931 m/m can be observed. The strain was obtained by taking the average color over the strain placement location of the two half bridges in the same spot each time. The limit of the mesh was the ANSYS student license having a maximum number of nodes and elements; continuation of mesh convergence would likely not result in substantial changes. A detailed drawing of the final vertical section can be found in Figure 243.

5.5.5 Engineering Drawing

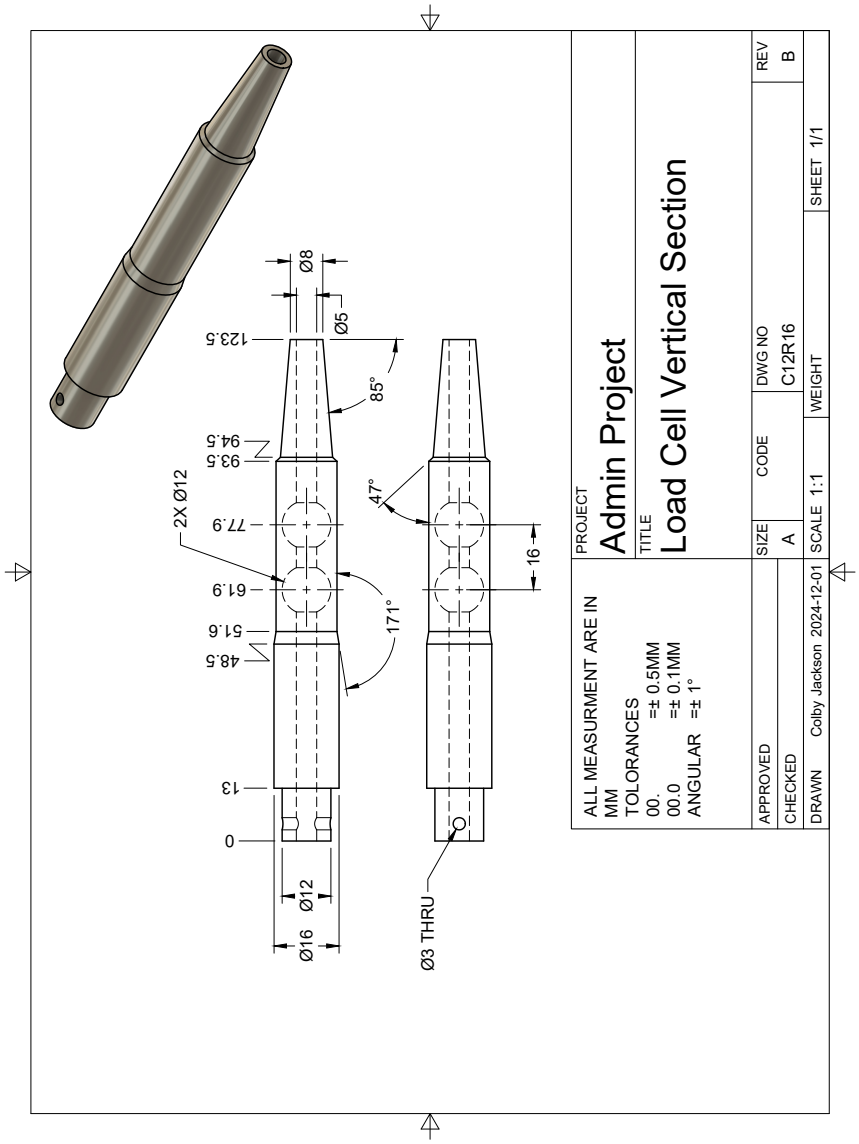

Figure 243: Engineering Drawing of the Vertical Section of the Force Balance Apparatus

5.5.6 Discussion

The initial design was limited to measuring forces along a single axis, which wasn't sufficient for analyzing multi-directional forces [1]. In the redesign, multiple strain gauges have been added in strategic positions to capture forces in both vertical and horizontal planes. This allows for a more comprehensive analysis of aerodynamic forces.

Through finite element analysis (FEA), significant strain concentrations were observed around the cutouts, confirming that the new design effectively amplifies strain where the gauges are placed. Various geometries were experimented with, and using two spherical cutouts with a 6 mm radius spaced 16 mm apart provided a good balance between concentrating strain and maintaining structural strength under the applied loads. The detailed engineering drawing can be found in Figure 243.

The FEA results indicated that the strain at the half-bridge locations ranged between 0.00171 and 0.00214 when subjected to combined axial and orthogonal forces. This amount of strain is sufficient to produce a measurable change in resistance in the strain gauges, enabling accurate detection of the applied forces [129]. The mesh convergence study supported the reliability of these FEA results, with strain values stabilizing around 0.00193.

The new design successfully withstands the specified forces—2000 N in the axial direction, 500 N in the orthogonal direction, and a 100 N·m moment force in the **Z**-axis—without compromising structural integrity. By carefully placing the strain gauges and utilizing both half-bridge and full-bridge circuits [124], accurate measurement of bending and torsional strains is achieved, which enhances the precision and reliability of the force balance apparatus.

5.5.7 Future Work

The next step involves 3D printing the redesigned vertical section using one of the listed materials, specifically the SLA resin for testing. The printed model will be tested to ensure that the design functions as intended before proceeding to manufacture with the final material.

After printing, experimental tests will be conducted to compare actual strain measurements with the FEA predictions and analytical calculations. By applying controlled loads to the apparatus and measuring the resulting strains, the accuracy and reliability of the design in real-world conditions will be verified.

Calibrating the strain gauge circuits will be an essential step to translate the electrical outputs into precise force measurements [124]. Calibration procedures will be developed, and accurate calibration curves will be established to improve the measurement precision of the apparatus.

A data acquisition system will be developed for real-time monitoring and recording of strain data. Software tools will process this data, converting strain mea-

surements into force vectors and providing visualizations of the aerodynamic forces during wind tunnel tests.

5.5.8 Conclusion

The vertical section of the force balance apparatus was redesigned to overcome the limitations of single-axis measurements and temperature effects. The next step is to print and test the design to confirm its effectiveness. Through iterative design and finite element analysis, a new geometry that concentrates strain at the gauge locations while keeping the structure strong under significant loads was designed.

By implementing multiple strain gauges and utilizing both half-bridge and full-bridge circuits, torsional strains and moments can now be accurately measured. The use of Wheatstone bridges minimizes the effects of temperature—a major source of error—thereby enhancing the overall accuracy of aerodynamic force measurements.

Successfully testing these elements will be a significant step forward in designing the force balance apparatus. Code will be written to reduce temperature-related errors, help us validate aircraft designs, and deepen our understanding of flight characteristics during wind tunnel testing.

5.6 Plane Body Test Section Design - Ryan Heywood

Peer Reviewed by: Nevan Bulitka

The newly proposed design choices of transitioning to a lifting body and integrating Schlieren imaging introduce significant design challenges for the vehicle's test section. These considerations necessitate a revised test section design that can support the Schlieren system setup without causing major concerns in other aspects of the vehicle design. The following subsection will elaborate on the proposed design solution for these new considerations.

5.6.1 Introduction

This subsection aims to establish a foundational understanding of flow dynamics within a planar test section, essential for effectively integrating a double-pass Schlieren imaging system into the design. In order to achieve an accurate visualization of the flow around a test subject using a Schlieren imaging system, it is crucial that the surrounding flow environment is relatively uniform. Since the basis of Schlieren imaging relies on changes in density to refract the light to obtain a useful image, the following analysis will focus on determining a suitable zone within the proposed test section with constant density. It should also be noted that the desired testing environment must have similar properties to that of the outside environment at the target altitude and Mach number of $70,000ft$ and 3.0 respectively. The analytical results will be compared with the Computational Fluid Dynamics (CFD) results from ANSYS Fluent to verify the design methodology and determine a suitable length along the test section for Schlieren integration.

Subsequent subsections detail the methodology, outlining the problem scope, modelling techniques, analytical and computational approaches, and validation methods. This is followed by the results section, presenting key findings, and the discussion, which explores the implications, limitations, and potential applications of the findings.

5.6.2 Methodology

The geometry of the proposed test section, shown below in Figure 244, consists of an opposed-wedge inlet that transitions to a flat, parallel-plate channel. For the flow analysis, a wedge angle of $\theta_w = 10°$ and a test section thickness of $t_w = 5cm$ was chosen. The initial internal test section height was set at $h_{\text{test}} = 30cm$, while the length of the test section was arbitrarily chosen as $l_{\text{test}} = 2.6m$ to ensure a desirable zone occurs within the test section. This geometry was selected not only for its symmetrical characteristics but also because the convex shape after the inlet will generate Prandtl-Meyer expansion fans, which will help reaccelerate the flow to conditions similar to the external environment.

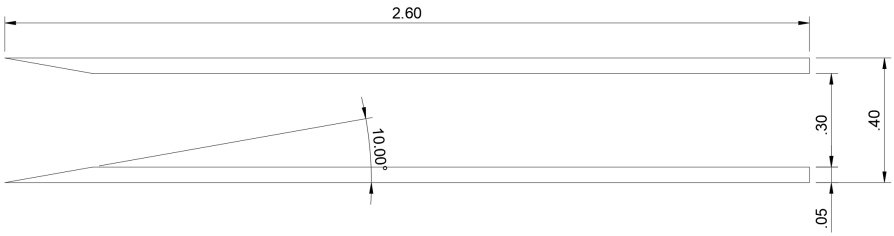

Figure 244: Proposed Planar Test Section Geometry in $[m]$

Before analyzing the flow through the test section, the initial flow parameters must be defined. Firstly, the flow in the test section is assumed to be inviscid and compressible, and boundary layer effects are assumed to be minimal up to the desired flow zone [130]. Additionally, the symmetrical geometry allows for the regular reflection of oblique shocks along the plane of symmetry to be analyzed similarly to reflections off of a solid boundary. To more clearly distinguish the different flow regions, the test section was divided into six zones, depicted in Figure 245 below, with orange lines representing shock waves, green lines representing Prandtl-Meyer expansion fans, and light blue arrows indicating flow direction.

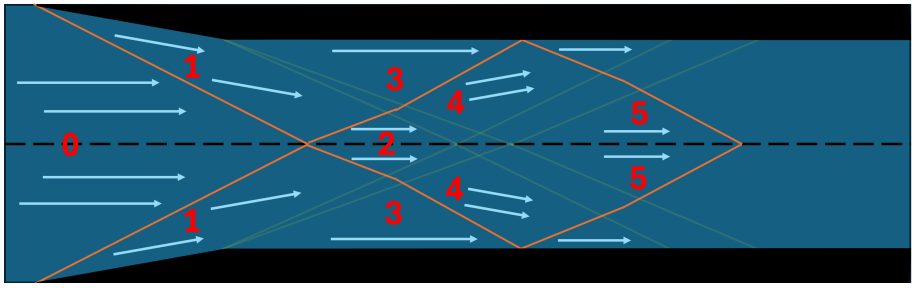

Figure 245: Analyzed Flow Zones in Proposed Test Section

As illustrated above, uniform flow should occur in zones 2 and 5. However, it is important to consider the thickness of the transition region between zones, as this will most likely not provide adequate space for Schlieren techniques to yield relevant results in zone 2. Additionally, the Mach number in zone 2 will be drastically reduced, as the flow has not been re-accelerated. Moreover, any flow after zone 5 is expected to have conditions that greatly deviate from the target conditions. Therefore, the conditions in zone 5 are expected to be the most desirable.

Throughout the test section, the flow interacts with weak oblique shock waves and Prandtl-Meyer expansion fans. The equations governing the flow properties across oblique shocks are derived from the conservation of mass,

energy, and momentum as shown in Equations 233-236 below [131].

Mach number (M) relation:

$$M_1 = \sqrt{\frac{(\gamma-1)M_0^2\sin^2(\beta_1)+2}{\sin^2(\beta_1-\theta_w)\left[2\gamma M_0^2\sin^2(\beta_1)-(\gamma-1)\right]}} \tag{233}$$

Static pressure (p) relation:

$$p_1 = p_0\left(\frac{2\gamma M_0^2\sin^2(\beta_1)-(\gamma-1)}{\gamma+1}\right) \tag{234}$$

Temperature (T) relation:

$$T_1 = T_0\left(\frac{\left[2\gamma M_0^2\sin^2(\beta_1)-(\gamma-1)\right]\left[(\gamma-1)M_0^2\sin^2(\beta_1)+2\right]}{(\gamma+1)^2M_0^2\sin^2(\beta_1)}\right) \tag{235}$$

Density (ρ) relation:

$$\rho_1 = \rho_0\left(\frac{(\gamma+1)M_0^2\sin^2(\beta_1)}{(\gamma-1)M_0^2\sin^2(\beta_1)+2}\right) \tag{236}$$

Where γ is the ratio of specific heats and is a constant value of 1.4, and β is the weak shock angle in $[Rad]$, and can be determined iteratively from the $\theta-\beta-Mach$ relation shown in Equation 237 below. The units for static pressure, temperature, and density are $[Pa]$, $[K]$, and $[kg/m^3]$ respectively.

$$\tan(\theta_w) = \frac{2\cot(\beta)\left(M^2\sin^2(\beta)-1\right)}{M^2(\gamma+\cos(2\beta))+2} \tag{237}$$

The value of β was determined using MATLAB[1] [133].

Next, the equations that govern the flow properties across the Prandtl-Meyer expansion fans are shown below in Equations 238-239 [134].

Prandtl-Meyer Angle (ν):

$$\nu(M_0) = \sqrt{\frac{\gamma+1}{\gamma-1}}\cdot\arctan\left(\sqrt{\frac{\gamma-1}{\gamma+1}\cdot(M_0^2-1)}\right)-\arctan\left(\sqrt{M_0^2-1}\right) \tag{238}$$

Where $\nu(M_0)$ is the Prandtl-Meyer angle, in $[Rad]$, for the first Mach region, and the second angle, in $[Rad]$, is defined as:

$$\nu(M_1) = \nu(M_0)+\Delta\nu \tag{239}$$

[1] See MATLAB Central File Exchange [132].

Where $\Delta\nu$ is based on the geometric change in the flow, and in this case is equivalent to θ_w in $[Rad]$. Once the second angle is obtained, the downstream Mach number can then be determined using the Prandtl-Meyer Mach Table by first converting to degrees and performing linear interpolation where required.[2]

Additionally, the stagnation pressures and temperatures of each zone can be computed using Equations 240 and 241 below.

$$P_{0_0} = P_{0_1}\left(1 + \frac{\gamma - 1}{2}M_1^2\right)^{\frac{\gamma}{\gamma-1}} \tag{240}$$

$$T_{0_0} = T_{0_1}\left(1 + \frac{\gamma - 1}{2}M_1^2\right) \tag{241}$$

Since the conditions in the test section at zone 5 are expected to change with respect to the initial conditions, the pressure drag of a diamond airfoil will also be evaluated such that the drag forces can be compared. A diamond airfoil with a chord length and half-wedge angle of $c = 10cm$ and $\delta_w = 10°$, shown below in Figure 246, was selected for analysis.

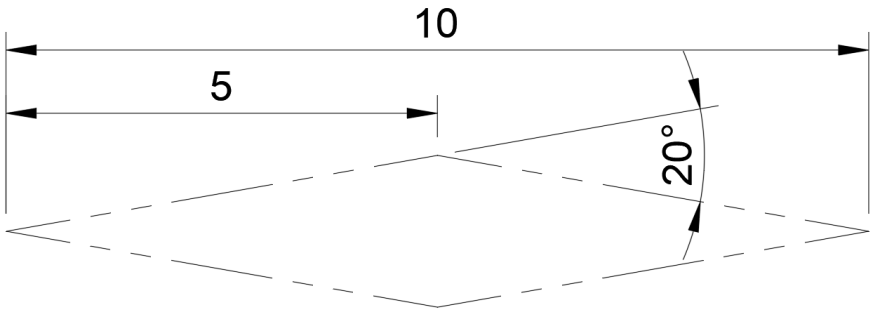

Figure 246: Dimensions of Diamond Airfoil in $[mm]$

The pressure drag of the diamond airfoil was calculated using Equation 242 below, derived from the airfoil shock expansion techniques [135].

$$D_p = c(p_1 - p_2)sin(\delta_w) \tag{242}$$

Where c is the chord length in $[m]$, δ_w is the half-wedge angle in $[deg]$, and p_1 and p_2 are the static pressures in $[Pa]$ after the oblique shock and expansion fans respectively. These pressures can be obtained using the same process

[2]See Appendix B

defined for the test section analysis above.

The test section geometry in Figure 245 was constructed in ANSYS Design Modeler with the mesh metrics shown in Table 53 below.

Table 53: Mesh Metrics of CFD Model

Metric	**Value**
Element Size (m)	0.01
Element Quality (Avg.)	0.989
Aspect Ratio (Avg.)	1.15
Skewness (Avg.)	5.68×10^{-3}
Orthogonal Quality (Avg.)	0.999

For the Fluent simulation, the energy model was turned on, and the SST k-omega viscosity model was used. This is not expected to significantly affect the simulation results at the desired flow zone. However, the result will be more accurate than the analytical solution and should yield a marginally lower Mach number than predicted. The fluid properties of air as an ideal gas were used, with the viscosity following the Sutherland model. The model for the diamond airfoil analysis uses identical simulation parameters, however, a finer mesh with an element size of $0.0025m$ and a thinner test section thickness of $t_w = 2.5cm$ was used. The thinner test section aims to reduce the thickness of the shock and expansion waves, allowing for a larger area within the test section to place the airfoil without interference.

5.6.3 Results

By employing Equations 233-236 from zones 0-1, 1-2, and 3-4, and Equations 238-239, from zones 1-3 and 4-5, the flow conditions for all zones can be calculated. Table 54 below compares the initial parameters, and the analytical and CFD results, with their associated percent errors.

Table 54: Comparison of Initial Conditions (Z0) and Zone 5 Conditions from Analytical and CFD Methods

Parameter	**Initial Conditions (Z0)**	**Zone 5 Conditions (Analytical)**	**Zone 5 Conditions (CFD)**	**% Difference (Z5: CFD vs. Analytical)**	**% Difference (Z0 vs. Z5 Analytical)**	**% Difference (Z0 vs. Z5 CFD)**
Static Pressure $[Pa]$	4488	4512	4813	6.7%	0.5%	7.2%
Stagnation Pressure $[Pa]$	164856	152947	157281	2.8%	7.2%	4.6%
Static Temperature $[K]$	218	223	226	1.4%	2.3%	3.7%
Stagnation Temperature $[K]$	610	610	612	0.3%	0.0%	0.3%
Density $[kg/m^3]$	0.0716	0.0704	0.0741	5.3%	1.7%	3.5%
Mach Number	3.00	2.95	2.92	0.8%	1.8%	2.6%

The results shown above indicate a high degree of accuracy between the analytical and CFD calculations, and validates the developed methodology. Furthermore, it is shown that the flow characteristics between zones 0 and 5 are also

very comparable, with the largest difference being the analytically calculated stagnation pressure yielding a percent difference of only 7.2%. The resulting density contour shown in Figure 247 below further illustrates that zone 5 has the potential to be an ideal position for Schlieren integration. To aid in visualization, the flow vectors have been overlaid, with red arrows representing Mach 3 flow, and yellow arrows indicating a reduced Mach flow.

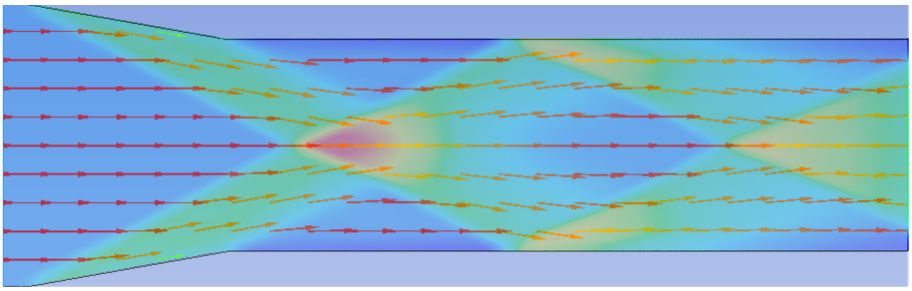

Figure 247: Analyzed Flow Zones with Density Contour and Flow Vectors in Proposed Test Section

Furthermore, by employing Equation 242 in both zones 0 and 5, the resulting pressure drag can be determined. Table 55 below compares the analytical and CFD pressure drags in zones 0 and 5.

Table 55: Comparison of Analytical and CFD Pressure Drag with Percentage Differences

Zone	**Analytical Pressure Drag (N)**	**CFD Pressure Drag (N)**	**% Difference**
0	126.2	125.0	1%
5	124.6	130.8	5%
% Difference	1%	5%	-

The pressure drags calculated above comparing zones 0 and 5 are in excellent agreement, with the analytical and CFD results varying by 1% and 5% respectively. Moreover, the CFD determined pressure drags are also in excellent agreement with the analytical values for each respective zone. The flow over the airfoil at each zone is depicted in Figure 248 below.

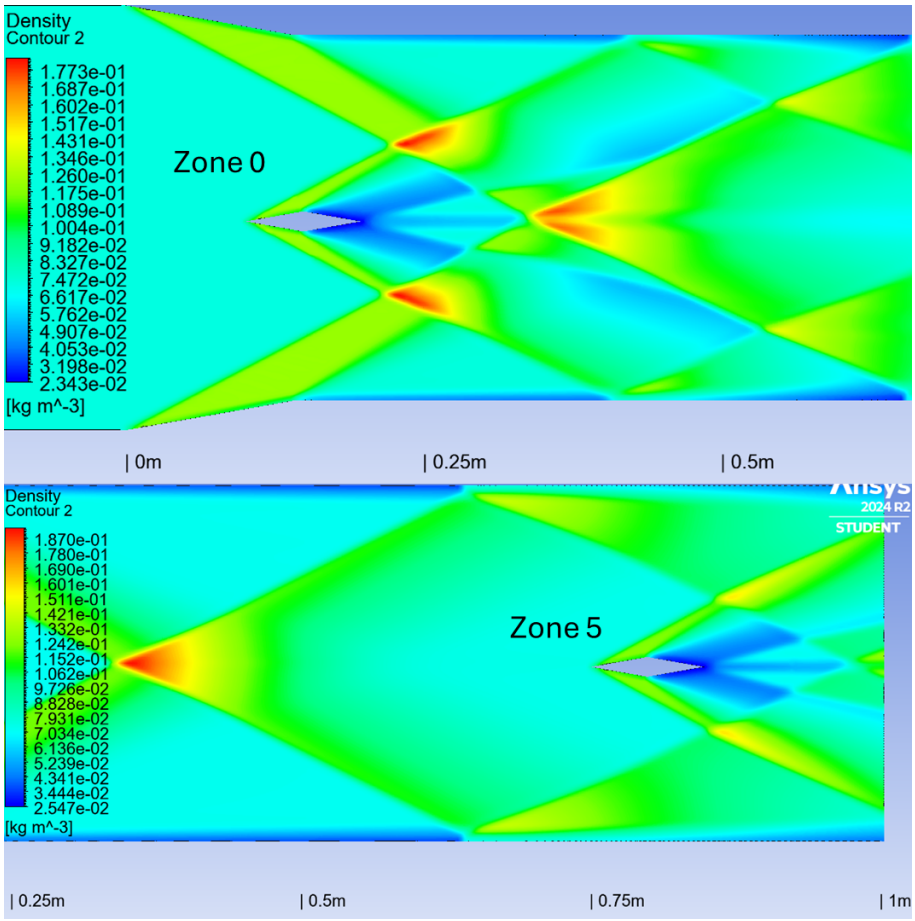

Figure 248: Density Contour of Flow Over Diamond Airfoil of Chord Length $0.1m$ in Zones 0 [Top] and 5 [Bottom]

In order to achieve meaningful results, the airfoil must be positioned before the converging shocks and the end of each zone, therefore, the position of the airfoil in zones 0 and 5 are $0.1m$ and $0.75m$ from the edge of the inlet respectively.

To obtain a comprehensive understanding of the difference in airfoil placement, it is important to compare the flow characteristics around the airfoil in both placements. Table 56 below compares the analytically computed flow characteristics for the airfoil in both zones.

Table 56: Comparison of Aerodynamic Parameters Between Zone 0 and Zone 5 Airfoils

2*Parameter	Zone 0 Airfoil		Zone 5 Airfoil		% Difference	
	Front Face	Rear Face	Front Face	Rear Face	Front Face	Rear Face
Static Pressure $[Pa]$	9220	1953	9155	1980	1%	1%
Stagnation Pressure $[Pa]$	158771	158771	149504	148431	6%	7%
Static Temperature $[K]$	271	174	276	178	2%	2%
Stagnation Temperature $[K]$	610	610	611	611	0%	0%
Density $[kg/m^3]$	0.118	0.0391	0.115	0.0387	3%	1%
Mach Number	2.51	3.55	2.476	3.49	2%	2%

All flow characteristics in Table 56 above are in excellent agreement. Once again, this strongly supports the robustness of the executed methodology.

5.6.4 Discussion and Future Recommendations

The density contours shown above enable a clearer visualization of the thickness of the transition regions between each zone, and more specifically, the fact that it is dependent on the area of the inclined face of the wedge inlet. Knowing this, it is beneficial to discuss the effects that minimizing this area has on both the size and flow quality of zone 5, and the size of the model that can be imaged within.

A similar model with nearly identical properties was constructed but with a wedge thickness of 1 cm. Figure 249 below shows the effect that decreasing the wedge thickness has on the size of zone 5.

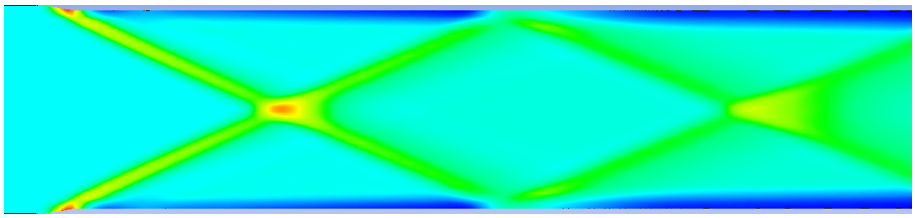

Figure 249: Analyzed Flow Zones with Density Contour in Test Section with 1cm Wedge Thickness

It is important to note that while the colour profile varies from the density contour in Figure 247, the density in zone 5 remains consistent with the inlet

density. The changes in Mach number and density along the center streamline were plotted for both geometries, as shown in Figures 250 and 251 below.

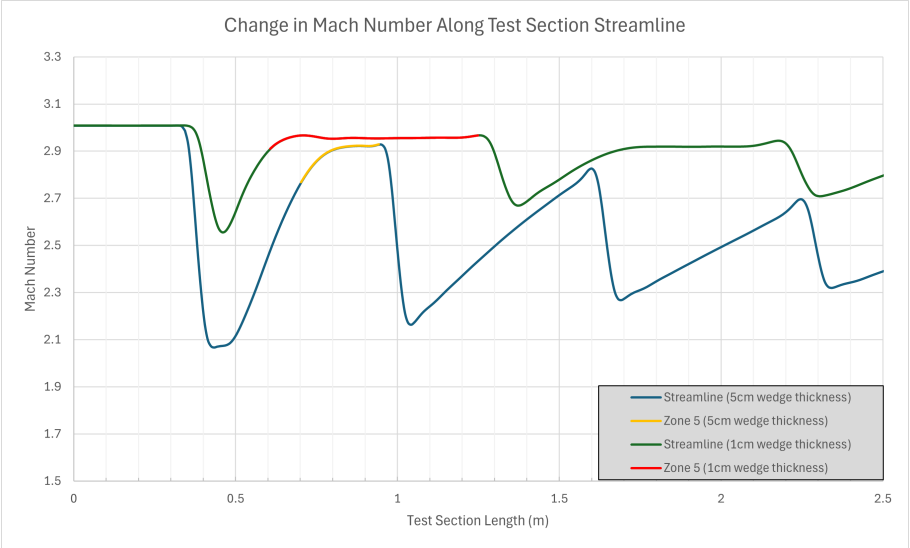

Figure 250: Mach Number Profile Along the Streamline of the 1cm and 5cm Wedge Geometries

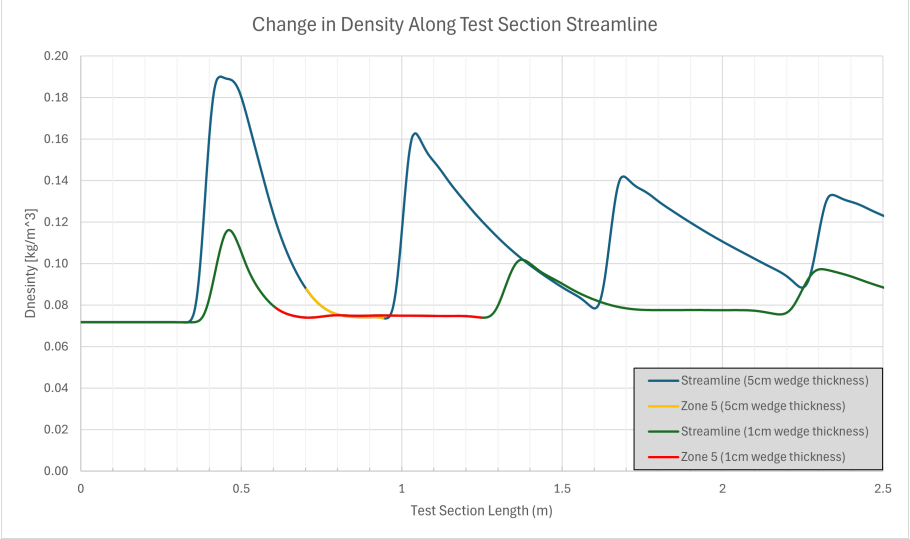

Figure 251: Density Profile Along the Streamline of the 1cm and 5cm Wedge Geometries

The result of decreasing the wedge thickness is a significant increase in the size of zone 5. Additionally, the feasibility of integrating Schlieren imaging into the test section of this geometry is also more plausible.

Nevertheless, since the position of the test section itself has not yet been determined, it is possible that many of the assumptions made for this analysis will no longer hold true. For example, if the test section is not the leading edge of the body, the incoming flow will have varying flow characteristics, and potentially varying angle of attack (AOA). Therefore, the placement of the test section on the body of the vehicle must be determined before advancing the analysis and determining the model placement for Schlieren integration. Thus, going forward, it will be beneficial to examine the changes in the flow characteristics of zone 5 with varying inlet Mach numbers. Additionally, expanding to a 3D analysis will be crucial in determining how the flow in zone 5 will affect the quality of the Schlieren imaging.

5.6.5 Conclusion

In conclusion, the analysis conducted in this subsection has demonstrated that the proposed planar test section can provide a suitable environment for Schlieren visualization of flow phenomena. By methodically designing the geometry with an opposed-wedge inlet and parallel-plate channel, it was shown that a uniform flow in specific zones within the test section were generated. Moreover, a comprehensive analysis of a diamond airfoil within these zones of uniform, similar flow further demonstrated the aerodynamical similarities between them. The analytical approach, validated against CFD results from ANSYS Fluent, highlighted the consistent flow conditions in zone 5, indicating that it is the most viable region for Schlieren imaging integration. The minimal discrepancies between the analytical and CFD results, as shown in the comparison of parameters, confirm the robustness of the design and methodology. Overall, this study establishes a solid foundation for future experimental studies in high-speed flow visualization using Schlieren techniques, which will allow for precise observations of flow dynamics around test subjects under conditions closely resembling those at the target altitude and Mach number. Ultimately, viability of this method, and position of the Schlieren system is dependent on the placement of the test section on the vehicle.

5.7 External Test Section - Sebastien Grondin

Peer Reviewed by: Chaanasya Gowda

An external test section design was selected for the plane due to the increased stability and size of a plane body. The advantage of an external test section is that it has the potential to avoid oblique shocks caused by the leading edge of the plane with its more open-concept design. The pylon design could also be applied to a wind tunnel design. In any case, the external test section will be supported by an extension arm/pylon mounted underneath the plane. The dimensions of the pylon will be determined using simplified analysis and engineering judgment. A few problems must be addressed to obtain the size and location of the extension arm. In the theory section, the boundary layer thickness will determine the minimum distance of the pylon. The viability of avoiding the shock caused by the nose of the plane will be determined as well as an approximation of the stresses experienced by the pylon. Once these values were obtained, a CAD of the extension arm, which integrates the force balance apparatus and load cell, was modelled.

5.7.1 Theory

The theory section aims to obtain a boundary for the height of the extension arm. The lower bound will be determined by the boundary layer thickness at the underside of the plane body. The upper bound is set by the minimum height among the leading shock or the vertical displacement of the landing gears. Additionally, the stresses induced by the drag will be estimated with simple geometry assumptions. The calculations for all equations in the theory can be found in Section 5.7.4

5.7.1.1 Boundary Layer Thickness

The lower bound of the height for the pylon will be determined in this section. This is due to the effects on speed from the boundary layer under the plane body. As the flow approaches a surface, its velocity tends towards what is known as the "no-slip condition". At the no-slip condition, the flow will attain zero bulk velocity relative to the plane. Therefore, the test section must extend past the boundary layer thickness to experience a true velocity of Mach 3. In the previous year's findings, the boundary layer thickness was 8.71 mm [136]. However, this value was obtained for an internal test section using CFD. The length 2.375 m (L), provided by the aircraft design team, is the distance where the wings meet for the most stable point with respect to the nose. Additionally, using atmospheric flight conditions for density (ρ), velocity (u), and viscosity (μ) from last year's report, the Reynolds number was calculated to be approximately $10.5 \cdot 10^6$ using Equation 243:

$$Re = \frac{\rho u L}{\mu} \tag{243}$$

The underside of the aircraft is flat and therefore, flat plate analysis can be used for boundary layer calculations. A Reynolds number that is above 500 000 on a flat plate is considered turbulent [137]. With this information, we can calculate the boundary layer (δ) thickness of a flat plate experiencing turbulent flow at x = L:

$$\delta = \frac{0.38x}{\sqrt[5]{Re}} \quad [138] \tag{244}$$

The boundary layer thickness over a flat plate travelling at a speed of Mach 3 at an altitude of 70 000 ft was calculated to be 3.6 cm using Equation 244. This will set a lower boundary on the height of the pylon. If the test section was placed anywhere less than 3.6 cm, the flow's velocity would decrease below Mach 3. The analysis for the boundary layer thickness does not take into account the gravitational pull because of its negligible effects compared to the dominant high-speed flow. This effect may increase the boundary layer thickness and thus the lower bound of the pylon shall be set at 5 cm based on engineering judgment until more accurate analysis can gauge a better estimate.

5.7.1.2 Leading Shock Effects

A problem with the extension arm design is that the leading edge of the plane will cause an oblique shock wave. This shock will cause a reduction in velocity as well as an increase in pressure and temperature. These changes in the flow properties will deviate from the readings otherwise found if we could avoid the shock wave. In this section, the viability of placing the test section below the shock is determined by using the theory for oblique shock angles. An estimated nose cone angle of 25°, determined by the plane body airframe team, will be used. Assuming a perfect wedge as the leading edge of the plane, we can use Figure 252 to determine the wave angle.

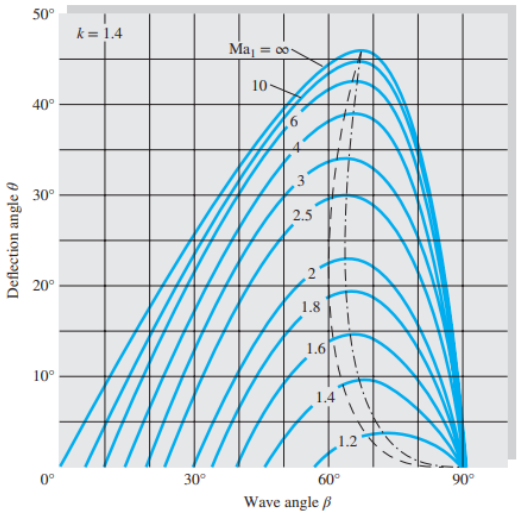

Figure 252: Deflection angle vs. wave angle for various Mach numbers [137]

Using Figure 252 at Mach 3 with a nose cone angle (θ) of 25°, the oblique shock wave angle (β) is approximately 42°. "L" is the distance of the test section which was determined earlier to be 2.375 m. With these values, we can determine how far the pylon should extend to avoid the shock. We can calculate the required pylon height (H) to avoid the shock wave by using the wave angle (β) and the distance from the nose cone (L).

$$H = L \tan \beta \tag{245}$$

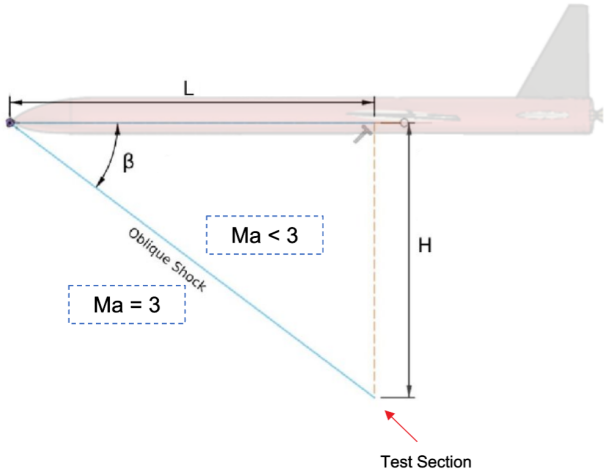

Figure 253: Extension of the pylon to avoid an oblique shock

Using Equation 245, "H" results in a value of 2.14 m. A large extension distance such as this could induce instability of the aircraft and is concluded to not be a viable option. This idea would require a novel system for the landing gears as the test section would be extending 2.14 m downwards. Furthermore, moving the test section closer to the nose cone would succeed in reducing the height requirement to avoid the leading shock. Consequently, there may be a point where the aircraft could experience adverse stability effects. The two main ways that the test section can successfully avoid the leading shock are by reducing the nose cone angle, incidentally lowering the wave angle, and placing the test section closer to the nose cone. It can be concluded that avoiding the leading edge's shock is inconclusive until further aircraft stability analysis is performed.

5.7.1.3 Bending Stress Analysis

In this section, an approximate maximum bending stress of the pylon will be determined. To obtain this value, we must make the geometrical assumption that the pylon will be modelled as a solid cylinder with a diameter of 100 mm and a length of 145 mm. The dimensions of the hypothetical cylinder come from the actual horizontal and vertical height of the pylon. This assumption is illustrated in Figure 254 below.

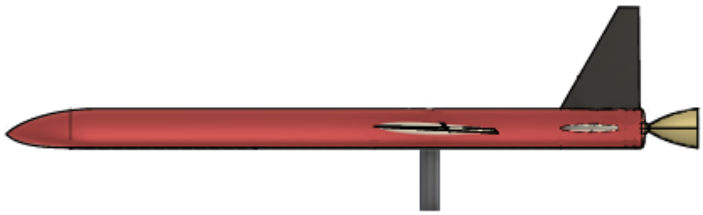

Figure 254: Rendering of the vertical cylinder assumption for analysis of the pylon (upscaled)

Firstly, the drag coefficient of the cylinder must be determined in order to calculate the drag force. Another assumption for this analysis is that the cylinder is perfectly smooth. We can now determine that the drag coefficient (C_d) is approximately 0.5 using Figure 255 below using the Reynolds number found earlier.

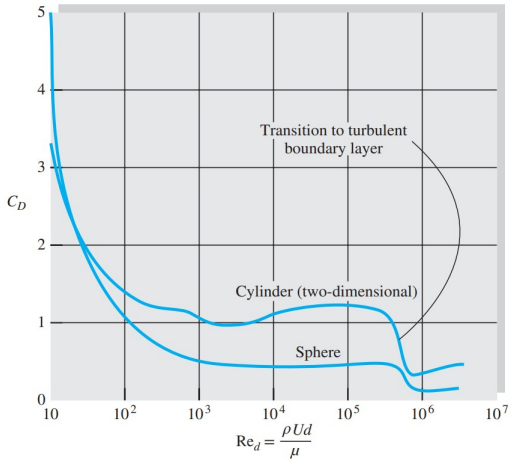

Figure 255: Drag coefficient of a cylinder and sphere at varying Reynolds numbers [137]

By inputting density (ρ) and velocity (v) for the flight conditions at Mach 3 into Equation 246, the drag force (F_d) experienced by the hypothetical cylinder with an area of A was calculated to be 206.4 N.

$$F_d = \frac{1}{2}\rho v^2 C_d A \tag{246}$$

The drag force is, according to NASA, applied at the center of pressure [139]. For this analysis, we will approximate the center of pressure to be at the halfway point of the cylinder. Using Equation 247, the maximum torque (M_{max}) on the modelled cylinder of height H is 14.96 $N \cdot m$.

$$M_{\max} = F_d \cdot \frac{H}{2} \tag{247}$$

With Equation 248, the maximum torque (M_{max}), distance from the neutral axis (NA, defined as half of the diameter, D), and the moment of inertia (I) of the cylinder allows us to obtain the maximum bending stress (σ_b).

$$\sigma_b = \frac{M_{\max} \cdot NA}{I} = \frac{M_{\max} \cdot \frac{D}{2}}{\pi \frac{D^4}{64}} \tag{248}$$

The resulting maximum bending stress (σ_b) is 152.4 kPa for the cylinder caused by the drag and can be compared to the yield strength of aluminum 6061-T6 (276 MPa) [140], a material used for many structural components in last year's design. This highlights a large margin of safety ensuring that the design meets the structural requirement.

5.7.2 External Test Section Design

The external test section's CAD was created with a predetermined boundary of the actual test section height (5 cm $< H <$ 24 cm) in mind. The lower bound was set from the boundary layer thickness. The upper bound was chosen based on the vertical displacement of 240 mm from last year's report [136]. The test section shall be closer to the upper bound to allow for more flexibility for a Schlieren system. However, a compact Schlieren system has not yet been designed to be integrated into the plane. This is why an extension distance of 145 mm was used in the test section design. The thickness, t, of the pylon (100 mm) is set to be larger than the horizontal width of the force balance apparatus (60 mm) with extra space for screws.

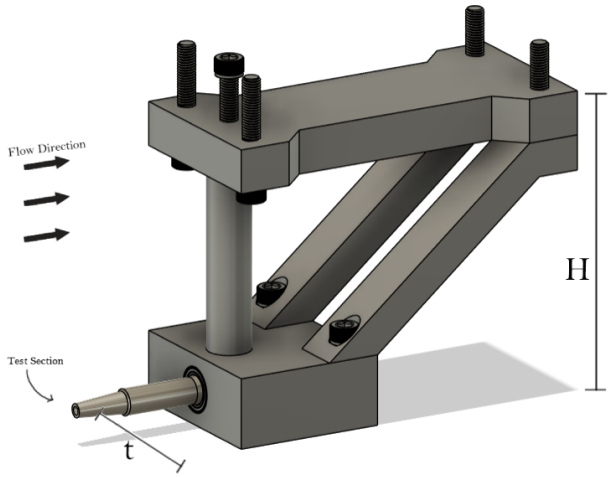

Figure 256: CAD of the external test section pylon

In Figure 256, the test section is the leading edge of the pylon and the rest of the force balance apparatus has been integrated inside a casing behind it. Arms have been added along with a cylinder, all fastened by alloy steel socket head screws, for structural integrity. This design will be fastened to the underside of the aircraft with 5 top screws onto the airframe. The setup for the aircraft with an implementation of an external test section can be visualized below in Figure 257.

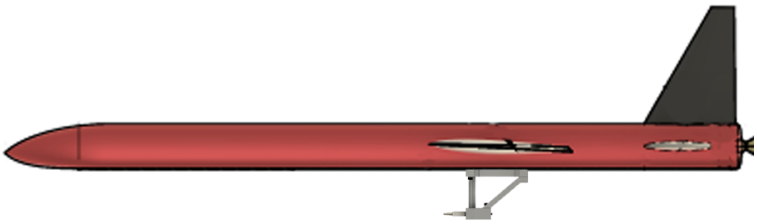

Figure 257: Conceptual attachment of the external test section pylon (upscaled)

The geometry of the current pylon is not designed to be aerodynamic and will,

in future iterations, resemble traditional supersonic pylons as seen in Figure 258.

Figure 258: AGM-88 HARM attached to a supersonic pylon [141]

5.7.3 Future Work

A high-priority task is to work with the aircraft design team to determine the instability caused by placing the test section closer to the nose cone. The goal of this task is to avoid the leading oblique shock from the nose cone while not having to resort to increasing the pylon height. In the bending stress analysis, the effects of the shock wave deflecting onto the pylon from the test specimen was not examined. This analysis would have to be performed for a range of test specimen leading edge angles from 0°to 90°. This is likely to require CFD analysis due to the complexity of shock waves. The CFD analysis will also give a more accurate "C_d" and center of pressure values. Another future task is the inclusion of an aerodynamic guard to cover the holding mechanism and divert the flow after the load cell. In addition, strain gauges will be integrated into the apparatus which will require channels to allow the wires to connect to the plane body.

5.7.4 Sample Calculations

$$v = \frac{\mu}{\rho} = \frac{1.44 \cdot\ 10^{-5} Pa \cdot\ s}{0.0722\ \frac{kg}{m^3}} = 20 \cdot 10^{-5} \frac{m^2}{s}$$

$$Re\ =\ \frac{UL}{v} = \frac{888\ \frac{m}{s} \cdot\ 2.375\, m}{20 \cdot\ 10^{-5}\, \frac{m^2}{s}} = 10.5 \cdot 10^6$$

$$\delta = \frac{0.38L}{\sqrt[5]{Re}} = \frac{0.38 \cdot 2.375\, m}{\sqrt[5]{6.73 \cdot 10^6}} = 3.6\, cm$$

$$H\ =\ L \cdot \tan\beta\ =\ 2.375\, m\ \tan 42^\circ = 2.14\, m$$

$$F_d = \frac{1}{2}\rho v^2 C_d A = \frac{1}{2}(0.0722\ \frac{kg}{m^3})(888\ \frac{m}{s})^2 \cdot 0.5 \cdot (0.1m \cdot 0.145m) = 206.4\ N$$

$$M_{\max} = F_d \cdot \frac{L}{2} = 206.4\ N \cdot \frac{0.145\, m}{2} = 14.96\ N \cdot m$$

$$\sigma_b\ =\ \frac{M_{\max}\ \cdot\ \frac{D}{2}}{\pi\ \frac{D^4}{64}} =\ \frac{14.96\ N \cdot m\ \cdot\ \frac{0.1m}{2}}{\pi\ \frac{0.1^4}{64}} = 152381.3\ Pa = 152.38\ kPa$$

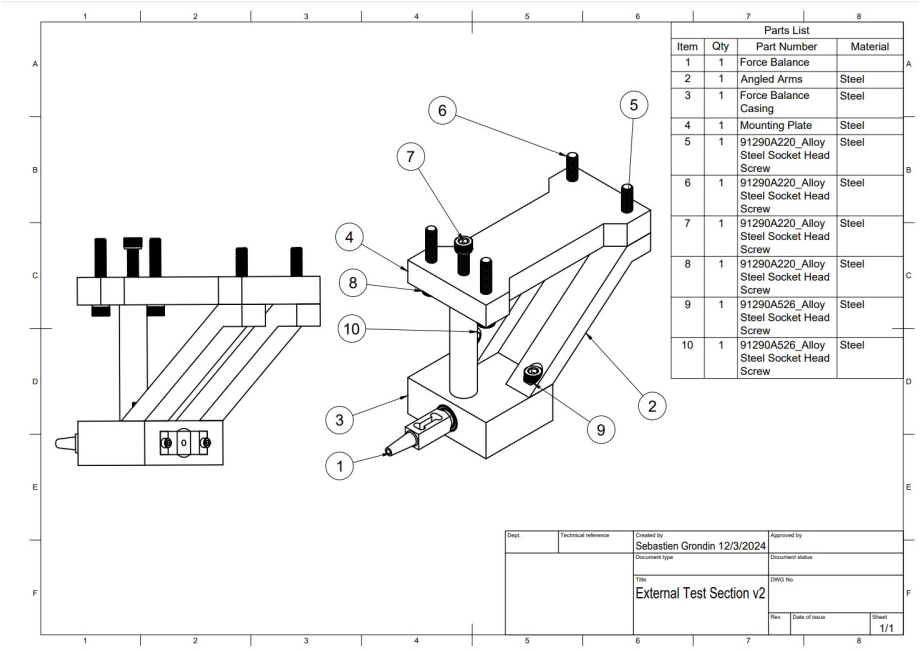

Figure 259: Assembly drawing of the pylon

5.8 Test Section Subteam Recap

This semester marked significant progress in research and design efforts. A tabletop Schlieren system was developed and prepared for manufacturing, with next semester focused on assembling the stands and breadboard. Planned experiments include comparing single and double-pass Schlieren systems, exploring the use of color filters to generate gradients, and testing various glass types for integration into a rocket. Addressing challenges in the rocket's test section led to critical design improvements. The test specimen was repositioned ahead of oblique shocks to avoid flow disruptions, and a refined lip geometry with a 1.5 mm radius on the leading edge enabled an 18 cm unobstructed axial distance. This redesign increased the effective test section length by 50% compared to prior configurations, accommodating larger specimens without choking the flow. The force balance apparatus was redesigned to overcome limitations in single-axis measurements and temperature effects. A new geometry was developed through iterative design and finite element analysis, focusing strain at gauge locations while maintaining structural integrity. Enhanced accuracy was achieved using 'Wheatstone bridges to minimize temperature-induced errors, enabling precise aerodynamic force measurements. Future steps include testing the apparatus and writing code to validate aircraft designs and improve wind tunnel testing accuracy. Analysis of the planar test section confirmed its suitability for Schlieren visualization. A uniform flow zone was achieved through a well-designed opposed-wedge inlet and parallel-plate channel. Validation against CFD results demonstrated consistent flow conditions, particularly in zone 5, identified as ideal for Schlieren imaging. This establishes a foundation for future high-speed flow visualization experiments, enabling precise observations of flow dynamics around test subjects under realistic flight conditions. Key considerations for the external test section design included ensuring accurate velocity readings at Mach 3. While maintaining pylon stability was a challenge due to boundary layer and oblique shock interactions, calculations confirmed the structural reliability of the aluminum 6061-T6 pylon. Future efforts will optimize stability, refine shock wave interactions through CFD, and enhance the aerodynamic profile for improved performance.

6 Conclusion

There has been considerable design work completed by the RPWT team in the Fall 2024 term. Each of the four sub-teams - Ascent System Design, Airframe Design, Propulsion & Control Systems Design, and Test Section Design - developed their respective designs to align with the mission of the launch vehicle. In particular, the adoption of a plane-body and Schlieren imaging system were considered. The supersonic flow achieved in the test section will allow for aerodynamic testing and imaging for longer durations than currently available on the ground.

For the upcoming Winter 2025 term, the integration of the design work completed this term will be a priority. Specifically, the preliminary design and location of the test section will aim to be completed by the end of January, so the control surfaces and systems can be designed and tuned accordingly. In addition, a go/no-go decision on the adoption of the plane-body will be made by the end of January. This decision will consider the aerodynamic benefits of the plane-body, as well as the flexibility in test section design the plane-body configuration offers.

Despite difficulties faced by the team regarding initial direction and progress, there is a lot of pride held by the team in the work done this semester. The team worked hard to come up with tasks that would improve the design of the launch vehicle, and those results are showcased in this report. The team is excited for the road ahead and future design work.

6.1 Acknowledgements

The RPWT team would like to acknowledge the support of the lead engineers on the project, Dr. David MacPhee, Dr. Oren Petel, and Dr. Jason Etele. They have provided guidance regarding the analysis and decisions of the team over the course of the semester. They also kindly provided coffee and donuts for the team at each of the weekly Friday meetings.

The RPWT team would like to thank PhD student Zack Milani for the support he offered to members of the team regarding their Computational Fluid Dynamics simulations. The team would also like to thank Gabriel Lamont, the co-op student in the Carleton engineering machine shop, for his support regarding manufacturing of Schlieren system fixtures.

References

[1] 4907P Capstone Team, *Rocket propelled wind tunnel - winter design report 2024*, (Accessed: 2024-09-07), 2024.

[2] B. M. F. F. Khoury J. M. Crissman, "The structure and properties of polyethylene films using in heavy lift balloons," 1985.

[3] Y. Saito, T. Yamagami, Y. Matsuzaka, *et al.*, "High altitude balloons with ultra-thin polyethylene films," *Advances in Space Research*, vol. 30, no. 5, pp. 1159–1165, 2002, ISSN: 0273-1177. DOI: 10.1016/S0273-1177(02)00527-6. [Online]. Available: https://www.sciencedirect.com/science/article/pii/S0273117702005276.

[4] M. V. Vasilescu, *Research on choosing the best gas for the flettner balloon: An unconventional power generator energy device*, Available on ResearchGate, 2023. [Online]. Available: https://www.researchgate.net/profile/Mihail-Vlad-Vasilescu/publication/369133903_RESEARCH_ON_CHOOSING_THE_BEST_GAS_FOR_THE_FLETTNER_BALLOON_AN_UNCONVENTIONAL_POWER_GENERATOR_ENERGY_DEVICE/links/655c4517ce88b87031fb88d0/RESEARCH-ON-CHOOSING-THE-BEST-GAS-FOR-THE-FLETTNER-BALLOON-AN-UNCONVENTIONAL-POWER-GENERATOR-ENERGY-DEVICE.pdf.

[5] M. OpenCourseWare, *Drag coefficient for a sphere*, Accessed: November 28, 2024, 2016. [Online]. Available: https://ocw.mit.edu/courses/8-01sc-classical-mechanics-fall-2016/66d953b5091e8e1c05219ec56ce8efba_MIT8_01F16_chapter8.6.pdf.

[6] A. Godeamer, *International standard atmosphere*, https://agodemar.github.io/FlightMechanics4Pilots/mypages/international-standard-atmosphere/, Accessed: November 28, 2024.

[7] TranslatorsCafe.com, *Altitude conversion calculator*, https://www.translatorscafe.com/unit-converter/en-US/calculator/altitude/?a=35000&au=ft&to=10&tu=C#altidude-scheme-big, Accessed: November 28, 2024, 2024.

[8] E. C. for Medium-Range Weather Forecasts (ECMWF). "Climate data store (cds)." Accessed: 2024-11-29. (n.d.), [Online]. Available: https://cds.climate.copernicus.eu/.

[9] "Weather balloon." (2020), [Online]. Available: https://www.weather.gov/media/key/KEY%20-%20Weather%20Balloon%20Poster.pdf. [Accessed Oct. 20, 2024].

[10] H. D. et al. "Energy management strategy design and station-keeping strategy optimization for high altitude balloon with altitude control system." (2019), [Online]. Available: https://www-sciencedirect-com.proxy.library.carleton.ca/science/article/pii/S1270963819318164. [Accessed Oct. 1, 2024].

[11] F. M. White, "Pressure distribution in a fluid," in *Fluid Mechanics*, McGraw-Hill Education, 2016, ch. 2, p. 87.

[12] P. V. et al. "Altitude control of long-duration balloons." (2005), [Online]. Available: https://arc.aiaa.org/doi/pdf/10.2514/1.7481. [Accessed Nov. 3, 2024].

[13] "Horizontal asme-code compressed air storage tank with mounting plate, powder-coated steel, 80 gallon capacity." (2024), [Online]. Available: https://www.mcmaster.com/4377K34/. [Accessed Nov. 17, 2024].

[14] "Industrial air 4.7-hp single-stage hi-flo 3-cylinder replacement air compressor pump (16.1 cfm @ 40 psi)." (2024), [Online]. Available: https://www.aircompressorsdirect.com/Industrial-Air-040-0348RP/p57812.html. [Accessed Nov. 17, 2024].

[15] "Gx200." (2024), [Online]. Available: https://engine.honda.ca/en/GX/gx200. [Accessed Nov. 17, 2024].

[16] S. Gudmundsson, "Selecting the powerplant," in *General Aviation Aircraft Design: Applied Methods and Procedures*, Elsevier, 2022, ch. 7, p. 208.

[17] "Oasis 12-volt extended duty tankless air compressor." (2024), [Online]. Available: https://www.aircompressorsdirect.com/Oasis-Manufacturing-XDM3000-12-Air-Compressor/p3942.html?srsltid=AfmBOor4I3cVviWY7U0HOml21C4nlA_0dQFtDhBptXbLeSkR9qEAxGy1. [Accessed Nov. 17, 2024].

[18] "Idealpower 12v 180ah sealed lead acid battery (elhr-12v-180ah)." (2024), [Online]. Available: https://www.emergencylighting.ca/Catalog/sealed-lead-acid-batteries/voltage/idealpower-12v-180ah-sealed-lead-acid-battery.aspx. [Accessed Nov. 17, 2024].

[19] F. M. White, "Compressible flow," in *Fluid Mechanics*, McGraw-Hill Education, 2016, ch. 9, pp. 597–623.

[20] M. H. Sadraey, "Engine performance," in *Aircraft Performance: An Engineering Approach*, CRC Press, 2024, ch. 4, p. 143.

[21] "What's the difference between psi and cfm?" (2019), [Online]. Available: https://www.matteigroup.com/en-us/blog/whats-the-difference-between-psi-and-cfm. [Accessed Nov. 23, 2024].

[22] M. Basarab, "Rocket propelled wind tunnel," Carleton University, Tech. Rep., 2024.

[23] D. Morin, "The lagrangian method," 2007. [Online]. Available: https://scholar.harvard.edu/files/david-morin/files/cmchap6.pdf.

[24] V. Hirvonen, "Lagrangian mechanics," [Online]. Available: https://profoundphysics.com/lagrangian-mechanics-for-beginners/.

[25] "Swivel-under-load hoist rings." (2023), [Online]. Available: https://www.mcmaster.com/catalog/130/1802/4137N22.

[26] "2d rigid body dynamics: Impulse and momentum." (2007), [Online]. Available: https://ocw.mit.edu/courses/16-07-dynamics-fall-2009/67ff6b0726f53d06285e21f0261fe94e_MIT16_07F09_Lec23.pdf.

[27] A. Arndt, "Allowable stress design and plastic design," in *Specification for Structural Steel Buildings*, American Institute of Steel Construction, 1989.

[28] "Asm material data sheet – aluminum 6061." (2001), [Online]. Available: https://asm.matweb.com/search/specificmaterial.asp?bassnum=ma6061t6.

[29] "Structural mechanics lecture 11: Buckling of plates and sections." (2013), [Online]. Available: https://ocw.mit.edu/courses/2-080j-structural-mechanics-fall-2013/345c462fe40421ea0f795bd35d2e4af1_MIT2_080JF13_Lecture11.pdf.

[30] C. Modlin. "The 1.5 1.4 ultimate factors of safety for aircraft and spacecraft." (2014), [Online]. Available: https://ntrs.nasa.gov/api/citations/20140011147/downloads/20140011147.pdf.

[31] "Main stainless steel grades and grades chart." (2024), [Online]. Available: https://steelprogroup.com/stainless-steel/grades/.

[32] Wikipedia, "Aircraft principal axes," in Wikipedia, 2024.

[33] J. Dubeau *et al.*, "Rocket propelled windtunnel," Carleton University, Tech. Rep., 2024.

[34] McMaster-Carr, "Mcmaster-carr," in McMaster-Carr, 2024.

[35] I. M. Plastics, "Drylin® e stepper motor, stranded wires with molex connector and brake, nema34," in Igus Motion Plastics, 2024.

[36] CANBAT, "Cli12-24 specifications," in CANBAT, 2024.

[37] S. et al., "Air-launch experiment using suspended rail launcher for rockoon," in Aerospace Journal, 2021.

[38] J. Lane, "Design processes and criteria for the x-51a flight vehicle airframe," in NATO Research & Technology Organisation (RTO), 2007.

[39] T. R. J. Maj Christopher M Rondeau, "X-51a scramjet demonstration program: Waverider ground and flight test," in Society of Flight Test Engineers (STFE), 2013.

[40] NASA. "Buckling of thin-walled circular cylinders." (Accessed: 31 October 2024), [Online]. Available: https://shellbuckling.com/papers/classicNASAReports/NASA-SP-8007-2020Rev2FINAL.pdf.

[41] M. S. S. B. Bartdorf M. Schildcrout. "Critical stress of thin walled cylinders." (Accessed: 31 October 2024), [Online]. Available: https://ntrs.nasa.gov/api/citations/19930082161/downloads/19930082161.pdf.

[42] A. A. U. Ltd. "15.4.1. buckling of thin cylindrical shells." (Accessed: 31 October 2024), [Online]. Available: https://www.abbottaerospace.com/aa-sb-001/15-local-stability-isotropic-materials/15-4-buckling-specific-cases/15-4-1-buckling-of-thin-cylindrical-shells/.

[43] R. G. B. W. C. Young. "Roark's formulas for stress and strain, 7th ed." (Accessed: 31 October 2024), [Online]. Available: https://jackson.engr.tamu.edu/wp-content/uploads/sites/229/2023/03/Roarks-formulas-for-stress-and-strain.pdf.

[44] R. D. Finck. "Usaf (united states air force) stability and control datcom (data compendium)." (Accessed: 6 December 2024), [Online]. Available: https://apps.dtic.mil/sti/citations/ADB072483.

[45] NASA. 1976. [Online]. Available: https://ntrs.nasa.gov/api/citations/19770009539/downloads/19770009539.pdf.

[46] "Atmospheric properties calculator." (Accessed: 6 December 2024), [Online]. Available: https://aerospaceweb.org/design/scripts/atmosphere/.

[47] G. R. Center. "Mach number." (Accessed: 6 December 2024), [Online]. Available: https://www.grc.nasa.gov/www/k-12/airplane/mach.html.

[48] C. Harris, *NASA NASA Supercritical Airfoils A Matrix of Family-Related Airfoils*. 1990. [Online]. Available: https://ntrs.nasa.gov/api/citations/19900007394/downloads/19900007394.pdf.

[49] L. R. Cente. "Turbulence model numerical analysis 3d onera m6 wing validation." (Accessed: 6 December 2024), [Online]. Available: https://turbmodels.larc.nasa.gov/onerawingnumerics_val_sa.html.

[50] A. Lamsal, A. Mishra, S. Prajapati, and J. William. "Theoretical and computational study on swept back wing for variable." (Accessed: 6 December 2024), [Online]. Available: https://www.researchgate.net/publication/364644125_Theoretical_and_Computational_Study_on_Swept_Back_Wing_for_Variable_Mach_Ranges.

[51] NASA. "Ad-1 oblique wing." (Accessed: 6 December 2024), [Online]. Available: https://www.nasa.gov/reference/ad-1/.

[52] 2024. [Online]. Available: https://www.grc.nasa.gov/www/k-12/VirtualAero/BottleRocket/airplane/sound.html.

[53] 2024. [Online]. Available: http://airfoiltools.com/airfoil/details?airfoil=sc20706-il.

[54] *Matweb material property data: Aluminum 6061-t6*, 2024. [Online]. Available: https://asm.matweb.com/search/specificmaterial.asp?bassnum=ma6061t6.

[55] J. Bailey and H. Wessel, "A survey of aluminum alloys for aerospace applications," NASA, Tech. Rep., 1972, Accessed: 2024-12-01. [Online]. Available: https://ntrs.nasa.gov/api/citations/19720022808/downloads/19720022808.pdf.

[56] K. Niemeyer, *Oblique shocks*, Accessed: December 4, 2024, n.d. [Online]. Available: https://kyleniemeyer.github.io/gas-dynamics-notes/compressible-flows/oblique-shocks.html.

[57] *Supercritical airfoil (coordinates from raymer w/ one correction) (nasasc2-0714-il)*$_2$024, 2024. [Online]. Available: http://airfoiltools.com/airfoil/details?airfoil=nasasc2-0714-il#polars.

[58] *Disadvantages of delta wing aircraft: A comprehensive analysis*, Accessed: 2024-12-01, 2024. [Online]. Available: https://orbitshub.com/disadvantages-of-delta-wing-aircraft-a-comprehensive-analysis/.

[59] *Naca 63010 airfoil (coordinates)*, 2024. [Online]. Available: http://airfoiltools.com/airfoil/details?airfoil=n63010a-il.

[60] *Openvsp: Nasa's open source parametric geometry tool*, Accessed: 2024-12-01. [Online]. Available: https://openvsp.org/.

[61] 2024. [Online]. Available: https://www.grc.nasa.gov/www/k-12/VirtualAero/BottleRocket/airplane/lifteq.html.

[62] E. Toolbox, *Standard atmosphere*, Accessed: 2024-12-01, 2024. [Online]. Available: https://www.engineeringtoolbox.com/standard-atmosphere-d_604.html.

[63] E. Edge, *Speed of sound - engineers edge*, Accessed: 2024-12-01, 2024. [Online]. Available: https://www.engineersedge.com/physics/speed_of_sound_13241.htm.

[64] *Mean aerodynamic chord - airfield models*, Accessed: 2024-12-01. [Online]. Available: https://www.airfieldmodels.com/information_source/math_and_science_of_model_aircraft/formulas/mean_aerodynamic_chord.htm.

[65] N. G. R. Center, *Reynolds number*, Accessed: 2024-12-01, 2024. [Online]. Available: https://www.grc.nasa.gov/www/k-12/airplane/reynolds.html.

[66] "Falcon 9." (2024), [Online]. Available: https://www.spacex.com/vehicles/falcon-9/.

[67] "How the 4 types of landing gear struts work." (2016), [Online]. Available: https://www.boldmethod.com/learn-to-fly/systems/how-the-4-types-of-landing-gear-struts-work/.

[68] "Effects of spring and damper elements in aircraft landing." (2020), [Online]. Available: https://www.ijrte.org/wp-content/uploads/papers/v8i5/D9247118419.pdf.

[69] "Worm gears explained." (2007), [Online]. Available: https://www.machinerylubrication.com/Read/1080/worm-gears.

[70] "Trapezoidal threads: Characteristics and applications." (2007), [Online]. Available: https://www.univiti.it/en/approfondimenti/product-information/trapezoidal-threads-characteristics-and-applications.

[71] "Industrial gear reducer,gear motor manufacturer - sdt transmission." (2021), [Online]. Available: https://www.sdtgear.com/worm-gearbox-efficiency/.

[72] "U.s. standard atmosphere supplements, 1966." (1966), [Online]. Available: Available:%20https://ntrs.nasa.gov/api/citations/19670028571/downloads/19670028571.pdf. [Accessed Oct. 24, 2024].

[73] "Rocket propelled wind tunnel fall midterm report." (2024). [Accessed Dec. 1, 2024].

[74] "Dm-1." (), [Online]. Available: Available:%20https://www.haascnc.com/machines/vertical-mills/drill-tap-mill/models/dm-1.html. [Accessed Oct. 24, 2024].

[75] E. R. G. Eckert and M. Minn, "Engineering relations for heat transfer and friction in high-velocity laminar and turbulent boundary-layer flow over surfaces with constant pressure and temperature," *American Society of Mechanical Engineers*, 1956.

[76] C. J. Schroeder, R. J. Parrington, J. O. Maciejewski, and J. F. Lane, *ASM Handbook*. ASM International, 2024.

[77] G. P. Sutton and O. Biblarz, *Rocket Propulsion Elements, 9th Edition*. Wiley, 2016.

[78] A. Zamboulis, E. A. Nakiou, E. Christodoulou, *et al.*, "Polyglycerol hyperbranched polyesters: Synthesis, properties and pharmaceutical and biomedical applications," *International Journal of Molecular Sciences*, 2019.

[79] E. W. Price and R. K. Sigman, "Combustion of ap-based propellants," *Journal of Applied Polymer Science*, 2000.

[80] J. W. Arblaster, "Selected values of the crystallographic properties of elements," *International Metallographic Society*, 2018.

[81] S. Shi, Y. Wang, T. Jiang, *et al.*, "Carbon fiber/phenolic composites with high thermal conductivity reinforced by a three-dimensional carbon fiber felt network structure," *American Chemical Society*, 2022.

[82] "Report 1135." (), [Online]. Available: https://ntrs.nasa.gov/api/citations/19930091059/downloads/19930091059.pdf. [Accessed Dec. 1, 2024].

[83] Z. Li, Z. Lin, M. Han, Y. Mu, and J. Yu, "Electrospun carbon nanofiber-based flexible films for electric heating elements with adjustable resistance, ultrafast heating rate, and high infrared emissivity," *Springer Nature*, 2021.

[84] "Chapter 3 notes." (), [Online]. Available: https://brightspace.carleton.ca/d2l/le/content/145980/viewContent/2805687/View. [Accessed Dec. 1, 2024].

[85] J. Etele, *Fundamentals of Transatmospheric & Space Propulsion*. Aldanox Group Inc., 2022.

[86] P. Kuentzmann, "Introduction to solid rocket propulsion," Office National d'Etudes et de Recherches Aérospatiales, Tech. Rep., 2004. [Online]. Available: https://apps.dtic.mil/sti/pdfs/ADA425146.pdf.

[87] O. B. George P. Sutton, *Rocket Propulsion Elements*. Wiley, 2017.

[88] A. Manash and P. Kumar, "Comparison of burn rate and thermal decomposition of ap as oxidizer and pvc and htpb as fuel binder based composite solid propellants," *Defence Technology*, vol. 15, no. 2, pp. 227–232, 2019, ISSN: 2214-9147. DOI: https://doi.org/10.1016/j.dt.2018.08.010. [Online]. Available: https://www.sciencedirect.com/science/article/pii/S2214914718301946.

[89] "Marotta control actuation systems." (2020), [Online]. Available: https://marotta.com/products/control-systems/control-actuation-systems/.

[90] "Parker csdemmcas control actuation system." (2024), [Online]. Available: https://ph.parker.com/us/en/product/electromechanical-missile-control-actuation-systems-cas/csdemmcas.

[91] "Mps control actuation system (cas)." (2024), [Online]. Available: https://www.mpsag.com/en/aerospace-defence/control-actuation-system-cas.

[92] A. Pektas, U. Haciabdullahoglu, N. Ejder, Z. Demircan, and C. Tola, "Effects of different fin shapes on apogee and stability of model rockets," in *2019 9th International Conference on Recent Advances in Space Technologies (RAST)*, Jun. 2019, pp. 193–199. DOI: 10.1109/RAST.2019.8767439.

[93] S. M. Harmon and I. Jeffreys, *Theoretical lift and damping in roll of thin wings with arbitrary sweep and taper at supersonic speeds : Supersonic leading and trailing edges*, May 1950. [Online]. Available: https://ntrs.nasa.gov/citations/19930082815.

[94] J. Hansen, *Mechanics of materials: Lesson 55 - tresca, von mises, and rankine failure theories explained*, Nov. 2022. [Online]. Available: https://www.youtube.com/watch?v=QV6xB0bLJwM&t=375s.

[95] R. E. Wallace, "Low-speed investigation of a double wedge airfoil with leading-edge slat," Ph.D. dissertation, California Institute of Technoology, 1952. DOI: 10.7907/NJPD-HF21.

[96] P. M. Sforza, "Quasi-one-dimensional flow equations," *Theory of Aerospace Propulsion*, 2012.

[97] *Is there any specific location on airframe for gaining higher drag?* https://aviation.stackexchange.com/questions/79650, Accessed: 2024-10-25.

[98] J. D. A. Jr., *Fundamentals of Aerodynamics*. McGraw-Hill, 2010.

[99] U. E. Students, "Rocket propelled wind tunnel," Carleton University, Tech. Rep., 2024.

[100] B. Etkin and L. D. Reid, *Dynamics of Flight: Stability and Control*, 3rd. New York, Chichester, Brisbane, Toronto, Singapore: John Wiley & Sons, Inc., 1996.

[101] D. A. Caughey, "Introduction to aircraft stability and control course notes," Cornell University, Tech. Rep., 2011. [Online]. Available: https://courses.cit.cornell.edu/mae5070/Caughey_2011_04.pdf.

[102] N. Academy, "Nasa engineering safety center," NASA, Tech. Rep. [Online]. Available: https://nescacademy.nasa.gov.

[103] R. C. Nelson, *Flight Stability and Automatic Control, 2nd ed.* Boston, MA: WCB Publishers, 1998.

[104] P. Kucher, "Sr-71 online - blackbird diagrams gallery," in www.sr-71.org, 1998. [Online]. Available: https://www.sr-71.org/blackbird/diagrams/.

[105] allmetsat, "Airport : Valcartier cfb valcartier quebec canada," in Allmetsat.com, 2024. [Online]. Available: https://en.allmetsat.com/airports/southern-quebec.php?icao=CYOY..

[106] D. Raymer, "Aircraft design : A conceptual approach," in S.L.: Amer Institute Of Aerona, 2019.

[107] Matt, "Pi pico pinout and power pins," in *Raspberry Pi Collection*, Accessed: 31 Oct. 2024, Raspberry Pi Spy, 2021. [Online]. Available: https://www.raspberrypi-spy.co.uk/2021/01/pi-pico-pinout-and-power-pins/.

[108] MathWorks, "Magnetometer calibration - matlab & simulink," in *MATLAB & Simulink Documentation*, Accessed: 31 Oct. 2024, MathWorks, 2021. [Online]. Available: https://www.mathworks.com/help/fusion/ug/magnetometer-calibration.html.

[109] MathWorks. "Magcal: Magnetometer calibration." Accessed: 31 Oct. 2024. (2024), [Online]. Available: https://www.mathworks.com/help/fusion/ref/magcal.html.

[110] MathWorks. "Estimate orientation using ahrs filter and imu data in simulink." Accessed: 31 Oct. 2024. (2024), [Online]. Available: https://www.mathworks.com/help/fusion/ug/estimate-oientation-using-ahrs-filter-and-imu-data-in-simulink.html.

[111] MathWorks. "Estimate orientation through inertial sensor fusion." Accessed: 31 Oct. 2024. (2024), [Online]. Available: https://www.mathworks.com/help/fusion/ug/estimate-orientation-through-inertial-sensor-fusion.html.

[112] MathWorks. "Ahrs system object." Accessed: 31 Oct. 2024. (2024), [Online]. Available: https://www.mathworks.com/help/nav/ref/ahrs.html.

[113] Ines, "Kalman filter example python," in *Kalman Filter Blog*, Accessed: 31 Oct. 2024, Netlify, 2021. [Online]. Available: https://kalmanfilter.netlify.app/post/kalman-filter-example-python/.

[114] U. of Sydney, "Advanced flight systems research," in *Research Reports*, Accessed: 31 Oct. 2024, University of Sydney, 2024. [Online]. Available: https://web.aeromech.usyd.edu.au/JabLab/Research/SyntheticGuidance/index.html.

[115] A. Mazumdar. "Principles and techniques of schlieren imaging systems." Accessed: Oct. 23, 2024. (2011), [Online]. Available: https://academiccommons.columbia.edu/doi/10.7916/D8TX3PWV.

[116] "Schlieren optics." Accessed: Oct. 23, 2024. (), [Online]. Available: https://sciencedemonstrations.fas.harvard.edu/presentations/schlieren-optics.

[117] "Color schlieren photograph of the supersonic flow around the wedge-plate model." Accessed: Oct. 23, 2024. (), [Online]. Available: https://www.researchgate.net/figure/Color-Schlieren-photograph-of-the-supersonic-flow-around-the-wedge-plate-model_fig1_225743260.

[118] "Schlieren mirrors: Spherical vs. parabolic." Accessed: Oct. 23, 2024. (), [Online]. Available: https://www.researchgate.net/publication/285743260_schlieren_mirrors.AS_Spherical_vs_Parabolic.

[119] "Dielectric-coated concave mirror, 400 - 750 nm, f = 500 mm, cm508-500-e02." Accessed: Dec. 2, 2024. (), [Online]. Available: https://www.thorlabs.com/thorproduct.cfm?partnumber=CM508-500-E02.

[120] Engineer Your Sound, *Hex mesh vs tet mesh (which is better and why?) - loud speaker acoustic speaker design*, (Accessed: 2024-12-05), 2023. [Online]. Available: https://engineeryoursound.com/hex-mesh-vs-tet-mesh-which-is-better-and-why/.

[121] Frank White and Henry Xue, *Fluid mechanics - ninth edition*, (Accessed: 2024-11-30), 2022.

[122] N. T. R. S. (NTRS). "Strain gauge application." (2020), [Online]. Available: https://ntrs.nasa.gov/api/citations/20200002944/downloads/20200002944.pdf (visited on 10/28/2024).

[123] O. Engineering. "How to position strain gauges." (2015), [Online]. Available: https://www.omega.co.uk/techref/pdf/Strain-gauge-application-info/how-to-position-strain-gauges.pdf (visited on 10/28/2024).

[124] H. World. "Wheatstone bridge circuit." (2024), [Online]. Available: https://www.hbkworld.com/en/knowledge/resource-center/articles/strain-measurement-basics/strain-gauge-fundamentals/wheatstone-bridge-circuit (visited on 10/28/2024).

[125] J. M. Gere and B. J. Goodno, *Mechanics of Materials*, 8th. Cengage Learning, 2012.

[126] AIDRO. "Alsi10mg datasheet." (2022), [Online]. Available: https://aidro.it/wp-content/uploads/2022/01/AlSi10Mg-1.pdf (visited on 12/05/2024).

[127] B. A. Fulcher, D. K. Leigh, and T. J. Watt. "Comparison of alsi10mg and al 6061 processed through dmls." (2014), [Online]. Available: https://utw10945.utweb.utexas.edu/sites/default/files/2014-035-Fulcher.pdf (visited on 11/30/2024).

[128] X. Jiang, X. Sun, F. Li, *et al.*, "Sla 3d printing resin for high-temperature applications," *Sensors*, vol. 22, no. 19, p. 7508, 2022. [Online]. Available: https://www.mdpi.com/1424-8220/22/19/7508 (visited on 10/28/2024).

[129] DAOKI. "Daoki bf120-3aa 120 ohm high-precision pressure resistance strain gauge." (2024), [Online]. Available: https://tinyurl.com/3rwhbj7x (visited on 10/28/2024).

[130] A. Pope and K. Goin, "High speed wind tunnel testing," in Wiley, 1965.

[131] N. G. R. Center. "Oblique shock waves." Accessed: 2024-10-31. (2024), [Online]. Available: https://www.grc.nasa.gov/WWW/k-12/airplane/oblique.html.

[132] MathWorks. "Theta-beta-mach analytic relation." Accessed: 2024-10-31. (2024), [Online]. Available: https://www.mathworks.com/matlabcentral/fileexchange/32777-theta-beta-mach-analytic-relation.

[133] L. Rudd and M. J. Lewis, "Comparison of shock calculation methods," *AIAA Journal of Aircraft*, vol. 35, no. 4, pp. 647–649, 1998.

[134] H. Li and G. Ben-Dor, "Oblique-shock/expansion-fan interaction - analytical solution," *AIAA Journal*, vol. 34, no. 2, pp. 418–421, Feb. 1996. DOI: 10.2514/3.13081.

[135] "Shock-expansion techniques for aerofoils." Accessed: 2024-12-03. (2024), [Online]. Available: https://www.aerodynamics4students.com/gas-dynamics-and-supersonic-flow/gasdynamics_w.php?page=8&.

[136] Z. Morin-Barich, "Rocket propelled wind tunnel," Carleton University, Tech. Rep., 2024, p. 57.

[137] F. M. White, *ISE Fluid Mechanics*, 9th. McGraw-Hill Education, 2021, ISBN: 9781260575545.

[138] J. G. Leishman. "Introduction to boundary layers." Accessed: 2024-10-31. (2023).

[139] NASA Glenn Research Center, *Center of pressure*, Accessed: 2024-12-02.

[140] A. M. D. Sheet, *6061-t6 aluminum properties*, Accessed: 2024-12-02, 2024.

[141] D. N. Updates, *Explained: What is agm-88 harm, a new anti-radar missile that the us has given to ukraine?* Accessed: 2024-12-04, 2022.

A Autopilot Appendix

Table 57: Explanation of Non-Dimensional Variables in Stability Derivatives

Variable	Representation	Obtained From
$C_{D_{M/\alpha}}$	Change in drag coefficient with respect to Mach number and angle of attack	Experimental data (wind tunnel tests) or CFD simulations
$C_{L_{M/\alpha}}$	Change in lift coefficient with respect to Mach number and angle of attack	Experimental data (wind tunnel tests) or CFD simulations
$C_{m_{M/\alpha}}$	Change in pitching moment coefficient with respect to Mach number and angle of attack	Experimental data (wind tunnel tests) or CFD simulations
C_{D_0}	Zero-lift drag coefficient	Wind tunnel tests or CFD simulations at zero angle of attack
C_{L_0}	Lift coefficient at zero angle of attack	Wind tunnel tests or CFD simulations at zero angle of attack
C_{m_0}	Pitching moment coefficient at zero angle of attack	Wind tunnel tests or CFD simulations at zero angle of attack
u_0	Reference or free-stream velocity	Predefined in design specifications or measured during flight tests or simulations

Table 58: Explanation of Non-Dimensional Variables in Controller Effectiveness

Variable	Representation	Obtained From
$C_{Z_{\delta_f}}$	Change in the aerodynamic force along the vertical axis with respect to fin deflection (δ_f)	Derived from the lift coefficient changes due to fin deflection, $C_{L_{\delta_f}}$
M_{δ_f}	Change in the pitching moment with respect to fin deflection (δ_f)	Derived from the moment coefficient changes due to fin deflection
$C_{m_{\delta_f}}(\theta)$	Coefficient of the pitching moment due to fin deflection at a given mean aerodynamic chord	Derived from tail efficiency η, tail arm length l_t, mean aerodynamic chord $\bar{c}$, horizontal tail volume V_H, and tail lift curve slope a_t
$C_{Z_{\delta_f}}$	Coefficient of the aerodynamic force along the vertical axis due to fin deflection	Negative of the lift coefficient changes due to fin deflection, $C_{L_{\delta_f}}(\theta)$
l_t	Tail arm length	Distance from the aerodynamic center of the wing to the aerodynamic center of the horizontal tail
V_H	Horizontal tail volume coefficient	$\frac{S_t l_t}{S\bar{c}}$, where S_t is the area of the horizontal tail, l_t is the tail arm length, S is the wing area, and $\bar{c}$ is the mean aerodynamic chord

Longitudinal Dimensional Stability Derivatives
Defined in terms of non-dimensional aerodynamic coefficient derivatives, the equations are unpacked for the reader to understand the parameters considered in the stability derivatives.

- **Aerodynamic Derivatives:**
  The dimensionless derivative are related to the aerodynamic derivatives. The axial and normal force coefficients are expressed in terms of the lift and drag coefficients, and AOA with respect to to the body axis. The AOA is the angle between the instantaneous vehicle velocity vector and the x-axis, and assumed that the propulsive thrust is aligned with the x-axis. Thus, the axial and normal force coefficients are:

$$\begin{aligned} C_X &= C_T - C_D \cos\alpha + C_L \sin\alpha \approx C_T - C_D + C_L\alpha \\ C_Z &= -C_D \sin\alpha - C_L \cos\alpha \approx -C_D\alpha - C_L \end{aligned} \tag{249}$$

  Thrust coefficient is defined as:

$$C_T \equiv \frac{T}{QS} \tag{250}$$

  Where T is the net propulsive thrust, assumed to be aligned with the x-axis of the body reference frame.

- **Speed Derivatives:**
  Derivatives with respect to u. Speed damping represented in derivative below:

$$C_{X_u} = C_{T_u} - C_{D_u} \tag{251}$$

  The contribution of compressibility effects are defined below:

$$C_{D_u} = M\frac{\partial C_D}{\partial M} \tag{252}$$

The contribution of the derivative of the coefficient of thrust is defined as:

$$C_{T_u} = \frac{\partial}{\partial(u/u_0)}\left(\frac{T}{QS}\right) = -2C_{T_0} \tag{253}$$

The equilibrium thrust coefficient is define as:

$$C_{T_0} = C_{D_0} + C_{L_0}\tan\theta_0 \tag{254}$$

Which gives:

$$C_{X_u} = -2C_{D_0} - 2C_{L_0}\tan\Theta_0 - MC_{DM} \tag{255}$$

Substituting into nondimensional stability derivative gives:

$$X_u = -\frac{QS}{mu_0}[2C_{D_0} + MC_{DM}] \tag{256}$$

The derivative of the normal force coefficient C_Z with respect to the vehicle speed u is defined below:

$$C_{Z_u} = -C_{L_u} \tag{257}$$

Ignoring the dependence of aeroelastic effects on lift coefficient on speed only considering compressibility effects:

$$C_{D_u} = M\frac{\partial C_L}{\partial M} \tag{258}$$

Where M is the flight Mach number. The Prandtl-Glauert similarity law for supersonic flow is:

$$C_L = \frac{C_L|_{M=0}}{\sqrt{1-M^2}} \tag{259}$$

Which shows:

$$\frac{\partial C_L}{\partial M} = \frac{M}{1-M^2}C_{L0} \tag{260}$$

Where:

$$C_{Zu} = -\frac{M^2}{1-M^2}C_{L0} \tag{261}$$

The dimensional stability derivative is defined as:

$$Z_u = -\frac{QS}{mu_0}\left[2C_{L_0} + \frac{M^2}{1-M^2}C_{L_0}\right] \tag{262}$$

The pitching moment coefficient with speed u is generally depends on aeroelastic deformation (ignored) and as shown below:

$$C_{m_u} = M\frac{\partial C_m}{\partial M} \tag{263}$$

Thus:

$$M_u = \frac{QS\bar{c}}{I_y u_0}MC_{m_M} \tag{264}$$

- **Angle-of-Attack Derivatives:** The derivatives with respect to vertical velocity w are expressed in terms of derivatives with respect to angle of attack α:

$$C_X = C_T - C_D + C_{L\alpha} \tag{265}$$

Where:

$$C_{X\alpha} = C_{T\alpha} - C_{D\alpha} + C_{L\alpha}\alpha + C_L = -C_{D\alpha} + C_{L0} \tag{266}$$

Since propulsive thrust is independent of the AOA ($C_{T_\alpha} = 0$). Using the parabolic approximation for the drag polar:

$$C_D = C_{Dp} + \frac{C_L^2}{\pi e A R} \tag{267}$$

And:

$$C_{D\alpha} = \frac{2C_L}{\pi e A R} C_{L\alpha} \tag{268}$$

And:

$$X_w = \frac{QS}{mu_0}\left(C_{L_0} - \frac{2C_{L_0}}{\pi e A R} C_{L_\alpha}\right) \tag{269}$$

Similarly, the z-force coefficient is defined as:

$$C_Z = -C_D\alpha - C_L \tag{270}$$

Where:

$$C_{Z\alpha} = -C_{D0} - C_{L\alpha} \tag{271}$$

So:

$$Z_w = -\frac{QS}{mu_0}\left(C_{D0} + C_{L\alpha}\right) \tag{272}$$

Thus, the dimensional derivative of pitching moment with respect to vertical velocity w is given by:

$$M_w = \frac{QS\bar{c}}{I_y u_0} C_{m\alpha} \tag{273}$$

- **Pitch-rate Derivative:**
The principal contribution to pitch damping is from the horizontal tail defined by:

$$C_{m_q} = -2(0.8 - 1.1)\eta \frac{l_t}{\bar{c}} V_H a_t \tag{274}$$

Also:

$$C_{L_q} = 2\eta V_H a_t \tag{275}$$

So:

$$C_{Z_q} = -C_{L_q} = -2\eta V_H a_t \tag{276}$$

The value for C_{m_q} is multiplied by a factor of 0.8-1.1 to account for contributions of other components such as the wings.

The derivative C_{X_q} is usually assumed to be negligibly small.

B Additional Materials

B.1 MATLAB Code

The following code was used to determine β, with $n = 0$ specified for the weak oblique shock:

```
% This function returns the oblique shock wave angle (beta) for a
    given
% deflection angle (theta) in degrees and ratio of specific heats (
    gamma).
% and Mach number M. Specify 0 for the weak oblique shock
% or 1 for the strong shock.
%
% Syntax:
% beta(M,theta,gamma,n)     where n specifies weak or strong shock
    returned
%
% NOTE: Angles supplied and returned from this function are in
    DEGREES.
%
% Based on an analytical solution to the theta-beta-Mach relation
    given in
% the following reference:  Rudd, L., and Lewis, M. J., "Comparison
     of
% Shock Calculation Methods", AIAA Journal of Aircraft, Vol. 35, No
    . 4,
% July-August, 1998, pp. 647-649.
%
% By Chris Plumley, undergraduate, University of Maryland.
clc;
clear;
clear all;

function Beta=beta(M,theta,gamma,n)
theta=theta*pi/180;             % convert to radians
mu=asin(1/M);                   % Mach wave angle
c=tan(mu)^2;
a=((gamma-1)/2+(gamma+1)*c/2)*tan(theta);
b=((gamma+1)/2+(gamma+3)*c/2)*tan(theta);
d=sqrt(4*(1-3*a*b)^3/((27*a^2*c+9*a*b-2)^2)-1);
Beta=atan((b+9*a*c)/(2*(1-3*a*b))-(d*(27*a^2*c+9*a*b-2))/(6*a*(1-3*
    a*b))*tan(n*pi/3+1/3*atan(1/d)))*180/pi;
end
```

B.2 Prandtl-Meyer Mach Table

Table A.1: Values of M, ν, and μ

M	ν **(deg)**	μ **(deg)**
2.00	26.38	30.00
2.02	26.93	29.67
2.04	27.48	29.35
2.06	28.02	29.04
2.08	28.56	28.74
2.10	29.10	28.44
2.12	29.63	28.14
2.14	30.16	27.86
2.16	30.69	27.58
2.18	31.21	27.30
2.20	31.73	27.04
2.22	32.25	26.77
2.24	32.76	26.51
2.26	33.27	26.26
2.28	33.78	26.01
2.30	34.28	25.77
2.32	34.78	25.53
2.34	35.28	25.30
2.36	35.77	25.07
2.38	36.26	24.85
2.40	36.75	24.62
2.42	37.23	24.41
2.44	37.71	24.19
2.46	38.18	23.99
2.48	38.66	23.78

M	ν **(deg)**	μ **(deg)**
2.50	39.12	23.58
2.52	39.59	23.38
2.54	40.05	23.19
2.56	40.51	22.99
2.58	40.96	22.81
2.60	41.41	22.62
2.62	41.86	22.44
2.64	42.31	22.26
2.66	42.75	22.08
2.68	43.19	21.91
2.70	43.62	21.74
2.72	44.05	21.57
2.74	44.48	21.41
2.76	44.91	21.24
2.78	45.33	21.08
2.80	45.75	20.92
2.82	46.16	20.77
2.84	46.57	20.62
2.86	46.98	20.47
2.88	47.39	20.32
2.90	47.79	20.17
2.92	48.19	20.03
2.94	48.59	19.89
2.96	48.98	19.75
2.98	49.37	19.61
3.00	49.76	19.47